Dissertation zur Erlangung des Doktorgrades

der Fakultät für Chemie und Pharmazie

der Ludwig-Maximilians-Universität München

In-vitro reconstitution and structural analysis of integrin-proximal adhesome complexes

Patricia Lieselotte Kammerer

aus Naila

2017

Erklärung

Diese Dissertation wurde im Sinne von § 7 der Promotionsordnung vom 28. November 2011 von Herrn Prof. Dr. Reinhard Fässler betreut.

Eidesstattliche Versicherung

Diese Dissertation wurde eigenständig und ohne unerlaubte Hilfe erarbeitet.

München, 10.01.2018

Patricia Kammerer

Dissertation eingereicht am	31.08.2017
1. Gutachter:	Prof. Dr. Reinhard Fässler
2. Gutachterin / 2. Gutachter:	Prof. Dr. Axel Imhof
Mündliche Prüfung am	04.12.2017

Widmung

Für meine Eltern und Lucas

Table of contents

Abbreviations

AA	Amino acid
ABD	Actin binding domain
ADA	N-(2-Acetamido)iminodiacetic acid
AIEX	Anion exchange chromatography
BC	Bent-closed conformation
BS3	Bis-sulfo-succinimidylsuberate
CD	Circular dichroism spectroscopy
CH	Calponin homology domain
CIEX	Cation exchange chromatography
ddH_2O	Double distilled (ultrapure) water
DLS	Dynamic light scattering
DMPC	1,2-dimyristoyl-sn-glycero-3-phosphocholine
DMPG	1,2-dimyristoyl-sn-glycero-3-phospho-(1'-rac-glycerol)
DOL	Degree of labeling
DSF	Differential scanning fluorimetry
EC	Extended-closed conformation
ECM	Extracellular matrix
EM	Electron microscopy
EO	Extended-open conformation
EPLIN	Epithelial protein lost in neoplasm
ERK	Extracellular signal-regulated kinase
FA	Focal adhesion
FAK	Focal adhesion kinase
FAT	Focal adhesion targeting domain
FBS	Fetal bovine serum
FERM	4.1, ezrin, radixin, moesin domain
FPLC	Fast protein liquid chromatography
HEK293	Human embryonic kidney cells
HEPES	N-2-hydroxyethylpiperazine-N-2-ethane sulfonic acid
ILK	Integrin-linked kinase
IMAC	Immobilized metal ion affinity chromatography
IPP	ILK-PINCH-α-parvin trimeric complex
IPTG	Isopropyl β-D-1-thiogalactopyranoside
IR	Infrared
LC-MS/MS	Liquid chromatography-tandem mass spectrometry
LIM domain	Structure first described in Lin11, Isl-1 and Mec-3
LRR	Leucine-rich repeat
Lys	Lysine
MSP	Membrane scaffold protein
MST	Microscale thermophoresis
NA	Nascent adhesion
NHS	N-Hydroxysuccinimide
NPxY motif	Asn-Pro-X-Tyr motif
NTA	Nitrilotriacetic acid
NxxY motif	Asn-X-X-Tyr motif

PBS	Phosphate buffered saline
PCR	Polymerase chain reaction
PEI	Polyethyleneimine
PINCH	Particularly interesting Cys-His-rich protein
PIP2	Phosphatidylinositol 4,5-bisphosphate
PIP3	Phosphatidylinositol 3,4,5-trisphosphate
PKD	Pseudokinase domain
PMSF	Phenylmethylsulfonyl fluoride
PTB	Phosphotyrosine binding domain
RSU-1	Ras suppressor protein 1
RT	Room temperature
SAXS	Small-angle x-ray scattering
SDS-PAGE	Sodium dodecyl sulfate poly-acrylamide gelelectrophoresis
SEC	Size-exclusion chromatography
SH2/3	Src homology domain 2/3
SLIC	Sequence- and ligation-independent cloning
SN	Supernatant
THD	Talin head (FERM) domain
TCA	Trichloroacetic acid
TCEP	Tris(2-carboxyethyl)phosphine
T_m	Melting temperature
TM	Transmembrane
TMCyto	Intergrin transmembrane and cytosolic domains
Tris	Tris(hydroxymethyl)-aminomethane
Trp	Tryptophane
Tyr	Tyrosine
WCL	Whole cell lysate

1 Introduction

1.1 Integrin-mediated cell adhesion

For cells in higher organisms it is essential to control their attachment to other cells and to the extracellular matrix (ECM) in order to form tissues or control cell migration. Integrins are heterodimeric cell surface receptors that mediate cell adhesion to the extracellular matrix and thereby control cell polarity, motility, proliferation, differentiation and survival. These molecules are ubiquitously expressed, consist of α and β subunits and require an activation step before they can mediate adhesion and signaling. By simultaneously binding the ECM and the actin cytoskeleton via adapter proteins in the cytoplasm, integrins transduce forces across the plasma membrane. This enables the cell to attach tightly to substrates and also to detect stiffness and biochemical composition of their surroundings.

1.1.1 Integrin subtypes and structures

Integrins represent a family of 24 adhesion molecules that have specific and overlapping functions. Each integrin consists of one α and one β subunit, which are highly glycosylated and non-covalently linked. In mammals, 18 different α subunits and 8 β subunits are expressed in a tissue-specific manner and mediate the interaction with different ECM components. Integrins can be divided into four groups according to their ligand specificity for either RGD- (Arg-Gly-Asp) containing proteins such as Fibronectin or Vitronectin (a), for Collagens (b), for Laminin (c) or for LDV- (Leu-Asp-Val) containing proteins (d) (Hynes, 2002). Among the most closely studied integrins are the Fibronectin-binding α5β1 and the Fibrinogen-binding platelet integrin αIIbβ3.

Each integrin subunit is composed of a large ectodomain of up to 1104 amino acids (AA) for α and up to 778 AA for β, a single span transmembrane (TM) domain of 25-29 AA and a short cytoplasmic tail of 13-70 AA (Arnaout et al., 2005). The crystal structure of the extracellular part of $\alpha_V\beta_3$ integrin was solved in 2001 and provided crucial insights into the architecture and the interplay of the two subunits (Xiong et al., 2001). A ligand-binding “head” structure is formed by the N-terminal β-propeller structure in the α subunit and the N-terminal βA domain of the β subunit. In 8 of the α integrin subunits, ligand binding occurs via an αA domain inserted into the β-propeller domain, which is homologous to the βA domain of the β-integrin

subunit. αV further consists of three β-sandwich domains with an immunoglobulin-like fold, which form so-called “thigh” and “calf” modules. In β3, the “head” domain is supported by an immunoglobulin-like “hybrid” domain followed by a plexin-semaphorin-integrin (PSI) domain, four domains with an epidermal growth factor (EGF)-like fold and a β-tail domain (Xiong et al., 2001). Integrins can adopt three different conformations, a compact, bent-closed (BC) state, in which the α and β extracellular domains are folded back onto themselves, an extended-closed (EC) state, where the two subunits are no longer bent but display low affinity towards their ligand, and an extended-open (EO) conformation, where the α and β cytoplasmic, transmembrane and ectodomains are separated and the ligand binding pocket within the β headpiece is opened up (Moser et al., 2009, Chen et al., 2010, Nishida et al., 2006).

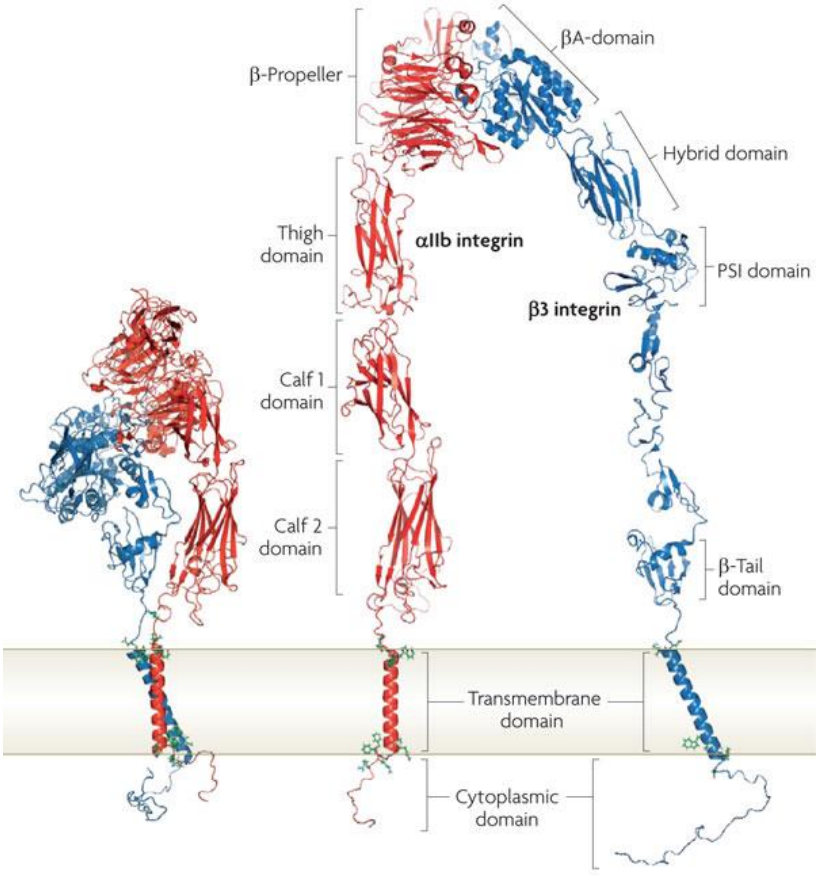

Figure 1: Structural model of an αIIbβ3 heterodimer in bent-closed (left) and extended-open (right) conformation (Shattil et al., 2010). The model shows the domain structure of integrins as well as the spheroid “head” piece formed by the N-terminal domains of the α and β subunit, which mediates ligand binding. The bent conformation is the state observed in crystal structures of integrin extracellular domains (PDB ID: 4G1M), while the model of the extended-open conformation was derived by separating and rearranging the domains of the crystal structure. Both conformations were fused to structures of the integrin transmembrane domains resolved by NMR spectroscopy (PDB ID: 2K9J) and to unstructured integrin tail peptides.

1.1.2 Integrin activation and clustering

The shift from the BC to the EO conformation is referred to as integrin activation. It can be induced by numerous external cues, which lead to the binding of intracellular activators such as talin and kindlin to the β-tail (Shattil et al., 2010, Vicente-Manzanares and Horwitz, 2011). This “inside-out” signaling controls ligand binding and is followed by the assembly of diverse signaling hubs that associate with the F-actin cytoskeleton and signal into the interior of the cell (“outside-in” signaling). Signal propagation inside the cell is achieved via the phosphorylation of specific substrates, the generation of phosphatidylinositol (3,4,5)-trisphosphate (PI(3,4,5)P3) by phosphoinositide 3-kinase (PI3K) at the plasma membrane, and by rearrangements of the actin cytoskeleton (Qu et al., 2011, Pasquali et al., 2007).

In two recent studies, the three different activation states of integrins and the transitions between these conformations were characterized thermodynamically (Li et al., 2017b, Li and Springer, 2017). These studies revelaed that K562 cell expressing α5β1 integrins have a 4,000-fold higher affinity towards fibronectin in the EO conformation than in the BC or EC states and the energetically limiting step in integrin activation is the extension of the extracellular domains, as it requires a free energy of about 4 kcal/mol (Li et al., 2017b). Due to this energy barrier, the three activation states are distributed on the cell surface in a thermodynamic equilibrium where 99.75 % of the integrins are in the BC, 0.10 % in the EC and 0.15 % in the EO state. The high-affinity EO state is stabilized by the binding of adapter proteins such as talin and kindlin to the cytoplasmic tail and the application of relatively weak pulling forces (0-4 pN) from the actin cytoskeleton (Li and Springer, 2017).

Since the adhesive force generated by a single integrin is insufficient to firmly link a region of the cell membrane to the ECM, several integrins need to assemble into micro- or even macro-clusters and thus provide stronger adhesion (van Kooyk and Figdor, 2000). Although the exact mechanisms for integrin clustering have not been resolved, there are two hypotheses how these assemblies could be initiated (Carman and Springer, 2003). The presence of multivalent ligand has been shown to recruit integrin clusters, thereby increasing adhesion strength by 6-fold (Roca-Cusachs et al., 2009). This indicates that integrin clustering can be induced by extracellular cues such as high ligand density. Another hypothesis focuses on intracellular adaptor proteins such as talin and kindlin as potential mediators of integrin clustering. Talin is

able to form dimers via its C-terminal dimerization domain and a recent study demonstrated that kindlin-2 dimerizes via the N- and C-terminal halves of its F2 domain (Goult et al., 2013, Li et al., 2017a). It could be imagined that both mechanisms play a role and potentiate each other, especially considering the aforementioned distribution of integrin activation states. One integrin in the EO state could bind to its ligand, become stabilized in this conformation by talin or kindlin binding to its cytoplasmic domain, who then in turn increase their respective local concentrations by forming homodimers. This increase in local concentration leads to a higher probability of kindlin or talin binding to another integrin, stabilizing it in the EO state as well. The accumulation of several active integrins and adaptor proteins could trigger the recruitment of other adhesome proteins and the formation of mature focal adhesions. Finally, it is alos possible that transmembrane domaine association of integrin subunits contributes to clustering.

1.1.3 The integrin transmembrane domain and cytoplasmic tail

Once activated, integrins assemble into small clusters and recruit adaptor and signaling proteins, the entirety of which has been termed the integrin adhesome (Zaidel-Bar and Geiger, 2010). Nucleation of adhesome assembly occurs at the short cytoplasmic tails of integrins. Of particular importance are the integrin β-subunits, which control the activation of integrins. The tail sequences of the different β subunits show a high degree of similarity, especially in the membrane proximal region (Moser et al., 2009). Most integrin β-tails contain two canonical NxxY-motifs, which serve as binding sites for phosphotyrosine binding (PTB) domains including the integrin activators, talin and kindlin (Calderwood et al., 2003). While the membrane-proximal NPxY motif has been shown to bind the FERM domain of talin (Calderwood et al., 1999), the membrane-distal NxxY motif binds the FERM domain of kindlin (Moser et al., 2008, Nikolopoulos and Turner, 2000b).

The canonical model for integrin activation, established mainly through studies on αIIbβ3 dimers, states that in the inactive, low-affinity conformation, the transmembrane domains of integrin α and β subunits are tightly associated through GxxxG dimerization motifs (termed the outer membrane clasp), and through a salt bridge in the region closer to the cytoplasm (inner membrane clasp). In this state, the αIIb helix is aligned with the plasma membrane, while the β3 helix is tilted in a 25° angle relative to the α helix (Yang et al., 2009, Lau et al., 2009).

It has been proposed that, upon binding of activating molecules like talin, the tilt is reduced, destabilizing the inner membrane clasp and leading to a separation of the helices, which converts the integrin extracellular domain into an active state and probably promotes clustering (Ye et al., 2014). However, it remains unclear how universally applicable this mechanism is to other types of integrins, since it has lately been shown that in β1-containing integrins, lysine-752, which appears to be conserved in β1 and β3, displays opposite roles (Lu et al., 2016). Despite their high sequence homology, β1 and β3 transmembrane and cytoplasmic domains (TMCyto) display differences in biological functions and potentially in the structures they form.

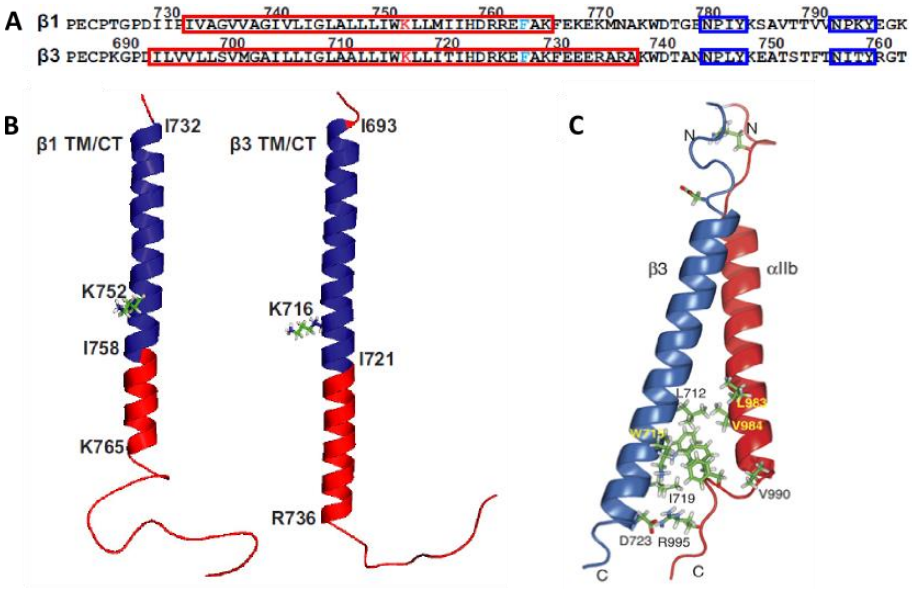

Figure 2: Sequences and structures of β1 and β3 transmembrane and cytosolic domains (TMCyto) (A,B (Lu et al., 2016), C (Lau et al., 2009)). (A) Within the amino acid sequences, the NxxY motifs (blue boxes) and the helical parts of the structures (red boxes) are highlighted, as well as the conserved lysine residue(red) and the residue at which the structure depicted in (C) ends (blue). NMR structures of the monomeric β TMCyto domains (B) reveal that the helical parts span the plasma membrane (blue) and extend well into the cytosol (red), while the remainders of the cytoplasmic tails are unstructured. An NMR structure of the transmembrane domains of an αIIbβ3 dimer (C) shows the orientations and interactions of the two subunits. Notably, the β3 helix is tilted in a 25° angle relative to the αIIb helix PDB 2K9J).

1.2 The integrin-proximal adhesome complex

Integrin tails lack enzymatic and actin-binding activities and hence rely on the recruitment of adhesome components acting as adaptor and signaling molecules for signal propagation. Initially, these signaling hubs (termed the adhesome) are small (<0.25 µm) and short-lived (<1 min). They are called nascent adhesions (NA) and can eventually mature into larger and

longer-lived focal adhesions (FAs) (Vicente-Manzanares et al., 2009). While most NAs dissolve, a few associate with the F-actin cytoskeleton and recruit further adhesion proteins like tensin or α-actinin, EPLIN and other LIM domain containing proteins, which reinforce their attachment to the actin fibers. High-resolution quantitative mass spectrometry has revealed that a set of core proteins leads to the formation of NAs and the tension-dependent recruitment of further proteins including 24 LIM domain-containing proteins. This recruitment finally results in the maturation of NAs into FAs (Schiller et al., 2011, Kuo et al., 2011). To date, a minimum of 245 proteins are recruited to integrin adhesion sites (Schiller et al., 2013). They form an intricate protein network necessary for signaling, cytoskeletal organization and mechanotransduction, thereby inducing downstream functions such as cell migration, differentiation, proliferation and survival (Engler et al., 2006, Wozniak and Chen, 2009).

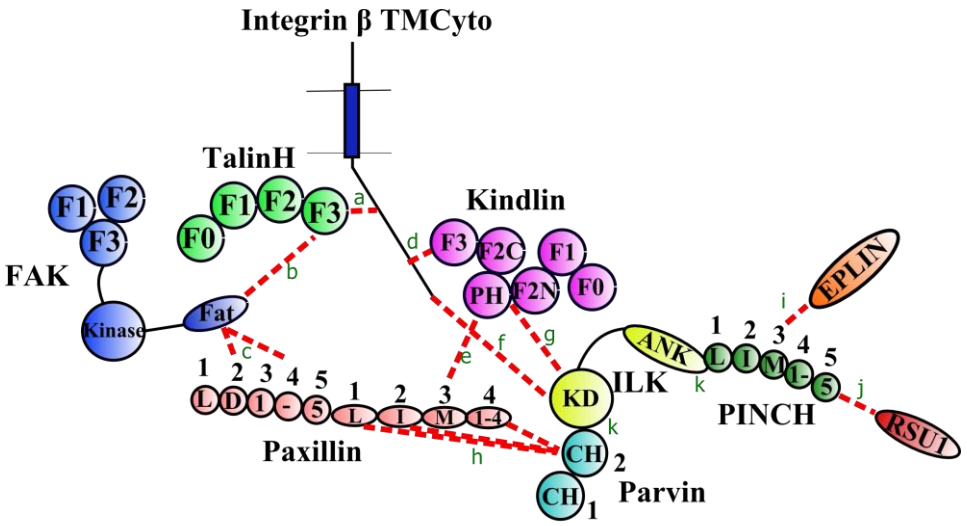

Figure 3: Overview of central integrin adhesome components and their reported interactions. THD (only the head domain is depicted for simplicity) and kindlin interact directly with the integrin β cytoplasmic domain and recruit other proteins to the adhesion site. Among these are paxillin, focal adhesion kinase (FAK), the IPP complex (ILK, PINCH, parvin), EPLIN (epithelial protein lost in neoplasm) and RSU-1 (ras-suppressor protein). The dashed lines represent reported interactions between individual components, the green letters indicate the references. a (Anthis et al., 2009), b (Lawson et al., 2012), c (Hoellerer et al., 2003), d (Moser et al., 2009), e (Theodosiou et al., 2016), f (Fukuda et al., 2009), g (Huet-Calderwood et al., 2014, Fukuda et al., 2014), h (Wang et al., 2008, Lorenz et al., 2008), i (Karakose et al., 2015), j (Dougherty et al., 2005), k (Stiegler et al., 2013)

Due to the high complexity, dynamics, size and co-existence of various adhesion sites, it is difficult to determine and characterize the protein-protein interactions in NAs and FAs using conventional means such as microscopy of fluorescently tagged FA components or pull-down experiments. Therefore, most attempts at structural analysis have been conducted on a set of proteins identified as “key components” for integrin activation and signaling. Among these

are talin, kindlin, paxillin, focal adhesion kinase (FAK), the IPP (integrin-linked kinase (ILK), PINCH, parvin) complex, EPLIN, RSU1, vinculin, zyxin, CAS, α-actinin and tensin (Hoffmann et al., 2014).

1.2.1 Talin and kindlin activate integrins through interactions with the integrin cytoplasmic tail

Among the proteins composing the integrin adhesome, talin and kindlin are the two components most crucial for integrin activation by directly interacting with the cytoplasmic tail. Talin acts not only as an integrin activator, which has been shown in knockout and knockdown experiments, but also connects the integrin with the actin cytoskeleton and mediates force transduction (Priddle et al., 1998). In vertebrates, there are two talin isoforms, the ubiquitously expressed talin1, and talin2, which is the prevailing form in muscle cells (Debrand et al., 2009). The kindlin protein family comprises three members in mammals, kindlin-1 which is mainly expressed in epithelial cells of skin, intestine and kidney, kindlin-2, which is ubiquitously expressed, and kindlin-3, which is only found in cells of hematopoietic lineages (Ussar et al., 2006). Like talin, kindlin binds directly to integrin tails, but neither is sufficient to activate fibronectin-binding integrins on its own (Theodosiou et al., 2016). Furthermore, integrins which where “forced” into the EO state by the addition of Mn^{2+} ions did not display full adhesive capacity when either talin or kindlin were depleted, indicating that the aforementioned stabilization of the EO state by the two adaptor proteins is essential for integrin activation. Therefore, it can be assumed that kindlin and talin act synergistically for maintaining the high-affinity EO state of integrins and thus form the “inner core” of the adhesome.

1.2.1.1 Talin structure and interactions with the integrin tail

Talin is a large (~270 kDa) protein comprised of a C-terminal rod domain of about 220 kDa and an N-terminal head domain (THD) of about 47 kDa, which are connected via a long and probably unstructured linker (Rees et al., 1990). THD consists of a FERM (4.1, ezrin, radixin, moesin) domain that contains three subdomains (F1, F2, F3) and an additional F0 subdomain, which has a ubiquitin-like structure. The large rod domain encompasses 13 R-domains composed of 4-5 α-helices each and an actin binding and dimerization domain (DD) at the C-terminus.

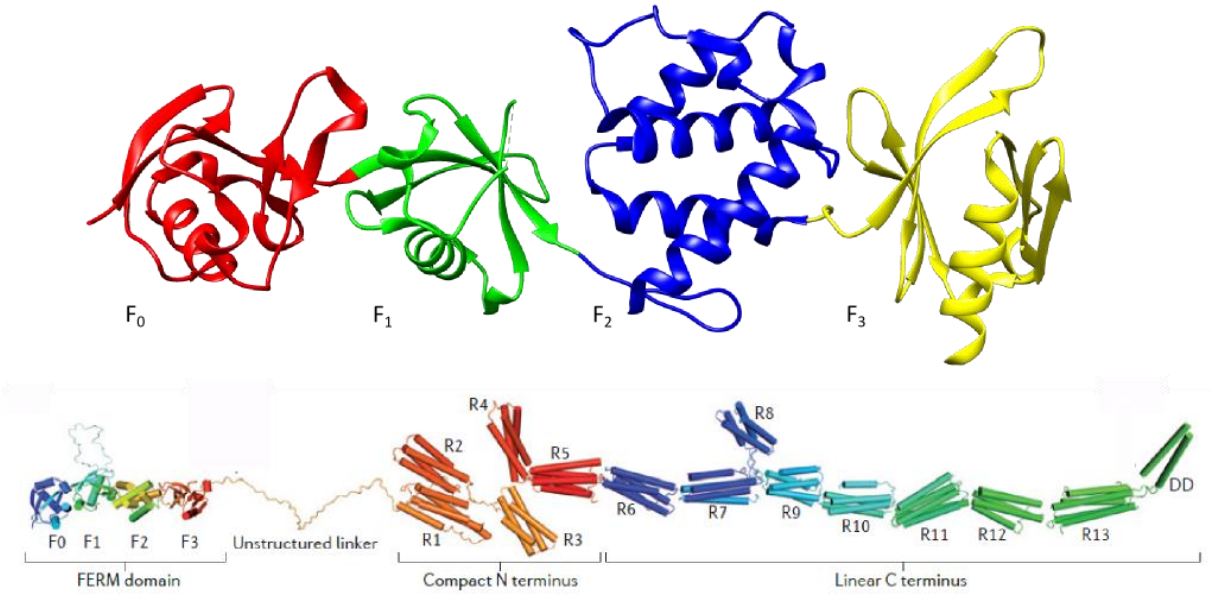

Figure 4: Crystal structure of the tain-1 head domain (PDB 3IVF) and model of full-length talin (Elliott et al., 2010, Calderwood et al., 2013). The talin head domain comprises an elongated FERM domain (F1, F2, F3) and an N-terminal F0 domain. A flexible, unstructured loop in the F1 domain was deleted for crystallization and is missing in the structure. THD is connected via a long, unstructured linker with the rod consisting of 13 helical bundle domains (R1-13) and the C-terminal dimerization domain (DD). There are two integrin binding sites in the F3 domain and in R11-R12, three actin binding sites in the FERM domain, in R4-R8 and in R13-DD.

Binding to β-integrin tails is accomplished via the F3 subdomain, which forms a PTB domain, and via a proposed second integrin binding site within the rod domain (Calderwood et al., 2003). When talin function is not required, it is believed to be in an autoinhibited state where its C-terminus interacts with the PTB domain, preventing β-tail binding by the FERM domain (Goksoy et al., 2008). The second integrin binding site, however, should still be accessible in this conformation. Talin connects to F-actin via three proposed binding sites in the FERM domain, in the rod domains R4-R8 and in the actin binding and dimerization domain (Calderwood et al., 2013). Further reinforcement of actin binding is accomplished through interaction with actin-binding adapter molecules such as vinculin, for which there are several binding sites in the rod domain (Schiller and Fässler, 2013). Most vinculin binding sites are cryptic and only become exposed when talin is extended and under force (del Rio et al., 2009). Furthermore, talin F3 domain has been shown to interact with the focal adhesion targeting (FAT) domain of FAK. The FAK binding site largely overlaps with the integrin binding surface in F3, probably excluding the binding of both partners at the same time (Lawson et al., 2012).

Due to the size of full-length talin and the corresponding difficulties in its recombinant production, the much smaller THD domain is used in most experiments that study integrin functions. After deletion of an unstructured loop in the F1 domain, the head domain of talin-1 was successfully crystallized and structurally characterized (Wegener et al., 2007, Elliott et al., 2010). Furthermore, the structure of the talin-2 F2F3 domains in complex with β1D integrin tail has been solved, shedding light on the binding mode and important residues for interactions (Anthis et al., 2009). The reason for choosing the talin-2/β1D pair for crystallization is that at a K_D of 36 µM it displays the highest affinity and thus the most stable complexes of all the talin-1/-2 and β1A, β1D, β3 combinations (see Fig. 5). The talin-1/β1A interaction in solution is extremely weak with a K_D of 490 µM, which is surprising, since this talin-integrin pair is prevailing in most cell types. Talin F3 forms a narrow groove, which binds to the membrane-proximal NPxY motif, and additionally forms a salt bridge with the N-terminus of the cytoplasmic tail, close to the plasma membrane (Anthis et al., 2009).

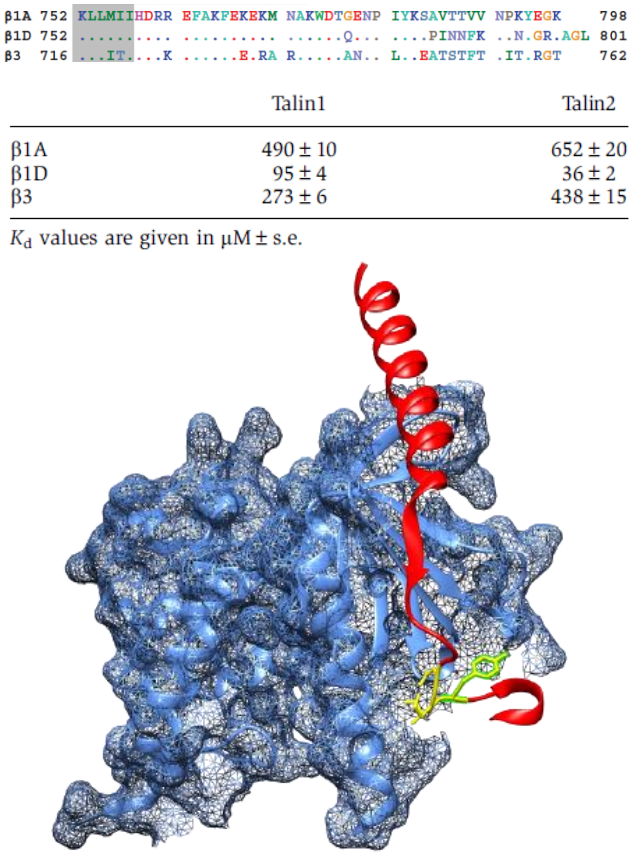

	Talin1	Talin2
β1A	490 ± 10	652 ± 20
β1D	95 ± 4	36 ± 2
β3	273 ± 6	438 ± 15

K_d values are given in µM ± s.e.

Figure 5: Crystal structure of the talin-2 F2 and F3 domains in complex with the β1D tail peptide (PDB 3G9W) (Anthis et al., 2009). Talin-2 and β1D are the prevailing variants in muscle tissue and display higher affinities than other talin-integrin tail pairs. The sequence variations between β1A, β1D and β3 are displayed, as well as the binding affinities for the different variants. The crystal structure shows the binding pocket of talin-2 F3 (blue) with β1D peptide (red). The membrane-proximal NPxY motif essential for the interaction is highlighted in yellow.

In β1A and β1D, the NPxY motif displays different conformations, resulting in higher binding affinity in the talin-2/β1D pair, which appears to be required in muscle tissue (Anthis et al., 2010). Yet even this highest affinity indicates a surprisingly weak bond (36 µM), considering that it must withstand the traction forces from the actin cytoskeleton via the integrin tail.

1.2.1.2 Kindlin structure and functions

The kindlin family encompasses three different members, kindlin-1, -2 and -3. While kindlin-1 is mainly expressed in epithelial cells and kindlin-3 in hematopoietic cells, kindlin-2 is almost ubiquitously expressed (Meves et al., 2009). Despite the high degree of similarity, the three kindlins also fulfill non-redundant functions, indicated by the observations that in the absence of one isoform, the other two cannot compensate for the loss (Karakose et al., 2010).

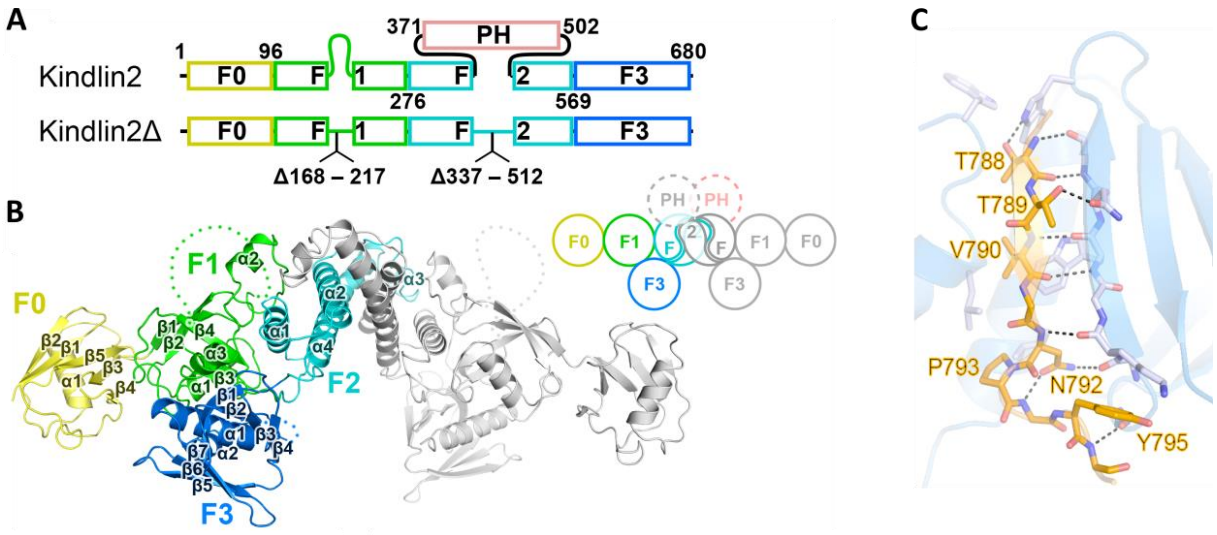

Figure 6: Crystal structure of a kindlin-2 dimer in complex with the integrin β cytoplasmic tail (Li et al., 2017a). (A) For crystallization, a kindlin-2 construct was chosed in which the flexible loop inserted into the F1 domain as well as the PH domain were deleted. (B) Unlike talin, which displays an unusual, elongated structure of the FERM domain, kindlin adopts a classical, cloverleaf-like conformation. In the crystal structure, as well as in solution, kindlin-2 forms homodimers through the N- and C-terminal parts of the F2 domains. The cartoon in the upper right corner depicts the orientation of the domains as well as the potential position of the PH domain. (C) Similar to talin, kindlin-2 binds the membrane-distal NPxY motiv of the integrin β1 tail through a narrow groove in the F3 domain. Additionally, the TTV-motif directly upstream of the NxxY motif and the C-terminal EGK-motif are essential for kindlin-2 binding to the tail. (orange: integrin β1 cytoplasmic domain, blue: kindlin-2 F3 domain)

Structurally, the kindlins are closely related to THD, sharing the 3-subunit FERM domain and the F0-subdomain, yet lack a rod domain. Like THD, kindlin also has a large unstructured region within the F1 domain. The most striking difference in comparison to THD is the pleckstrin homology (PH) domain, which is inserted into the F2 subdomain and binds phosphatidylinosotides in the plasma membrane. Like talin, kindlin interacts directly with β-tails via the PTB fold in their F3 domains (Bottcher et al., 2009). Besides the membrane-distal NxxY motif, a TTV (β1) or STF (β3) motif upstream of it are crucial for kindlin binding. Furthermore, it has been shown that the β1 tail's COOH terminus is essential for kindlin binding and that the deletion of these residues reduces the affinity (Harburger et al., 2009). Recently, the crystal structure of kindlin-2 has been solved, using a construct in which the

flexible F1 linker and the PH domain had been deleted (Li et al., 2017a). This structure shows that in kindlin-2, as opposed to the elongated THD, the F0-F3 domains are arranged in a classical cloverleaf-like shape. Binding to the TTV or STF motif as well as to the membrane-distal NxxY motif occurs in a narrow groove within the F3 domain and the Glu-796 residue of the C-terminal EGK motif in β1 is bound through backbone-backbone interactions (Figure 6C). Furthermore, the crystal structure as well as biophysical studies showed that kindlin-2 forms dimers through the N- and C-terminal parts of the F2 domain (Figure 6B). The formation of these dimers in solution is slow and occurs over several days, therefore the proposed function of the dimers in integrin clustering will have to be assessed in future studies.

It has been shown that reduced levels of kindlin-2 cause disruption of the actin cytoskeleton and that, like talin, kindlin not only associates with F-actin indirectly through adapter proteins like α-actinin and migfilin, but also binds actin directly through its F0 domain (Tu et al., 2003, Has et al., 2009, Bledzka et al., 2016). Furthermore, kindlin-2 binding to ILK has been intensively studied, mapping the interaction surface with the ILK pseudokinase domain to a 38-AA linker sequence between the N-terminus of the F2 domain and the PH domain in kindlin-2. It has been proposed that the interaction with ILK might be crucial for recruiting kindlin to focal adhesions and for enhancing kindlin-mediated integrin activation (Fukuda et al., 2014, Huet-Calderwood et al., 2014). Recently, direct interaction of kindlin-2 and paxillin has been demonstrated, revealing a mechanism through which paxillin is recruited to focal adhesions by kindlin (Theodosiou et al., 2016).

1.2.1.3 Importance of the plasma membrane for talin- and kindlin-mediated integrin activation

The plasma membrane plays an important role in focal adhesion assembly, as several adhesome proteins, including talin, kindlin, ILK and FAK interact with phosphatidylinositol-phosphates (PIPs) in the inner leaflet of the plasma membrane. These interactions are thought to recruit the proteins to the membrane and to ensure their correct orientation towards the integrin tail and each other. For talin-mediated integrin αIIbβ3 activation, the mechanism has been determined in great detail and demonstrates the importance of interactions with the membrane. Talin in its autoinhibited form, where positively charged residues in the F3 domain are bound to a negatively charged surface in the R9 domain, is located in the cytoplasm. The

same residues can bind to negatively charged phosphatidylinositol-4,5-bisphosphate (PIP_2) in the plasma membrane, which probably disrupts its autoinhibition and orients talin towards the plasma membrane and the integrin tail (Legate et al., 2011, Goksoy et al., 2008). Mutations, which disrupt the F3-R9 interaction, have been shown to increase the rate of focal adhesion assembly (Kopp et al., 2010). Furthermore, experiments using β3-tails coupled to large unilamellar vesicles (LUVs) showed that PIP_2 as well as the presence of negatively charged membrane lipids enhances talin affinity towards the tail (Moore et al., 2012). After disruption of the autoinhibited state, most likely mediated by interactions of the talin FERM domain with PIP_2, talin F3 binds to the first NPxY motif and to the membrane-proximal region of the β tail, extending its transmembrane helix (Ye et al., 2016). Through the formation of a salt bridge with a conserved Asp residue, F3 domain binding reduces the tilt angle of the β3 TM helix by 20° and disrupts the interaction of the integrin α and β TM domains (Anthis et al., 2009, Ye et al., 2014).

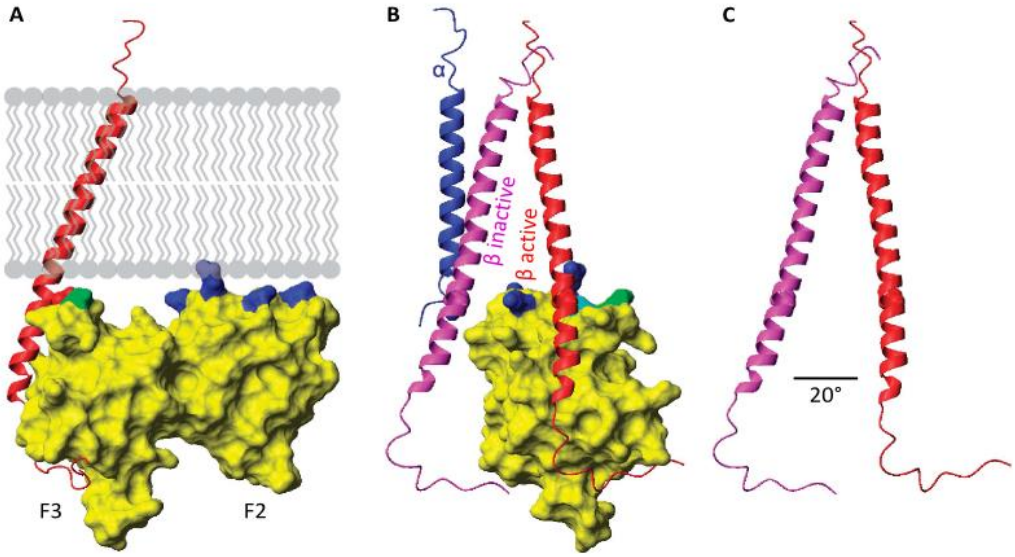

Figure 7: Mechanism of talin-mediated integrin activation (Anthis et al., 2009). (A) By interacting with negatively charged phosphatidylinositol-phosphates in the plasma membrane via positively charged residues in F2 and F3 (blue), THD is recruited and correctly oriented towards the integrin tail. Through the formation of a salt bridge with the β tail, talin reduces its tilt by 20° (C) and unclasps the α and β TM domains (B). The model is based on the NMR structure of the TM domains of αIIbβ3 (PDB 2K9J) overlaid with the x-ray structure of the talin-2 F2F3-β1D fusion construct (PDB 3G9W).

Kindlins recognize PIP_2 and phosphatidylinositol-3,4,5-trisphosphate (PIP_3) via their F0 and PH domains and via an unstructured loop in the F1 domain. Moreover, there are indications of a conformational change in the PH domain following PIP_3 binding which might be important for anchoring kindlin to the plasma membrane (Liu et al., 2011, Liu et al., 2012, Yates et al., 2012,

Bouaouina et al., 2012). These interactions with the plasma membrane have been shown to be essential for full co-activation of integrins by kindlin. NMR data suggests that, unlike talin, kindlin alone is not sufficient to unclasp αIIbβ3 TM domains. Instead, it enhances activation by talin, however neither by increasing talin binding to the tail nor by facilitating talin localization to the membrane (Kahner et al., 2012). Also, no direct interaction of kindlin and talin has been reported so far, therefore the co-activating effect of kindlin might be derived from events occurring after talin binding to the integrin tail. It has been proposed that kindlin might also be involved in integrin clustering and to increase focal adhesion assembly via avidity effects. This might be achieved through kindlin dimerization, which bind to two integrin tails and thus initiate cluster formation, or through the recruitment of other adhesome components such as paxillin, ILK or migfilin (Das et al., 2013, Li et al., 2017a).

1.2.2 FAK

FAK, a highly conserved non-receptor tyrosine kinase, plays a pivotal role in focal adhesions as a signaling switch and as a scaffolding molecule. It is ubiquitously expressed and essential for embryonic development (Ilic et al., 1995). FAK is composed of an N-terminal FERM domain, a 40 AA linker, a kinase domain, a long proline-rich low-complexity region and a C-terminal focal adhesion targeting (FAT) domain (Lietha et al., 2007). In its autoinhibited conformation, the FERM domain and the catalytic domain interact, keeping FAK inactive. Recent studies have shed some light on the proposed mechanism of FAK activation (Goni et al., 2014, Brami-Cherrier et al., 2014).

A patch of basic amino acids (KAKTLR) in the FERM F_2 domain has been shown to bind PIP2 in the plasma membrane, inducing a “relaxed” conformation as well as transient FAK dimerization. Formation of dimers occurs via FERM:FERM as well as FERM:FAT or FAT:FAT contacts and facilitates phosphorylation of Y397 in the linker region between the FERM and kinase domain *in trans*. Together with three nearby PxxP motifs, phosphorylated Y397 leads to Src recruitment and activation by binding to its Src homology (SH2 and SH3) domains. Src in turn phosphorylates the Y576 and Y577 residues in the activation loop of the FAK kinase domain, which leads to further activation of FAK (Calalb et al., 1995). This FAK-Src complex then phosphorylates substrates such as paxillin and induces structural changes in the actin cytoskeleton (Schaller et al., 1995, Mitra et al., 2005).

The FAT domain is composed of a four-helix bundle and has been shown to bind to the LD (Leu-Asp-rich) motifs in paxillin (Hayashi et al., 2002). Of these five LD motifs at the N-terminus of paxillin, characterized by the consensus sequence LDXLLXXL, LD2 and LD4 have been shown to bind the FAT domain, which contains two paxillin binding sites (Scheswohl et al., 2008). NMR structures show that paxillin LD2 and LD4 peptides can bind simultaneously to the FAT domain (as displayed in Figure 8B), yet it is not clear whether this is a mechanism to recruit two paxillin molecules or whether one paxillin molecule binds both sites.

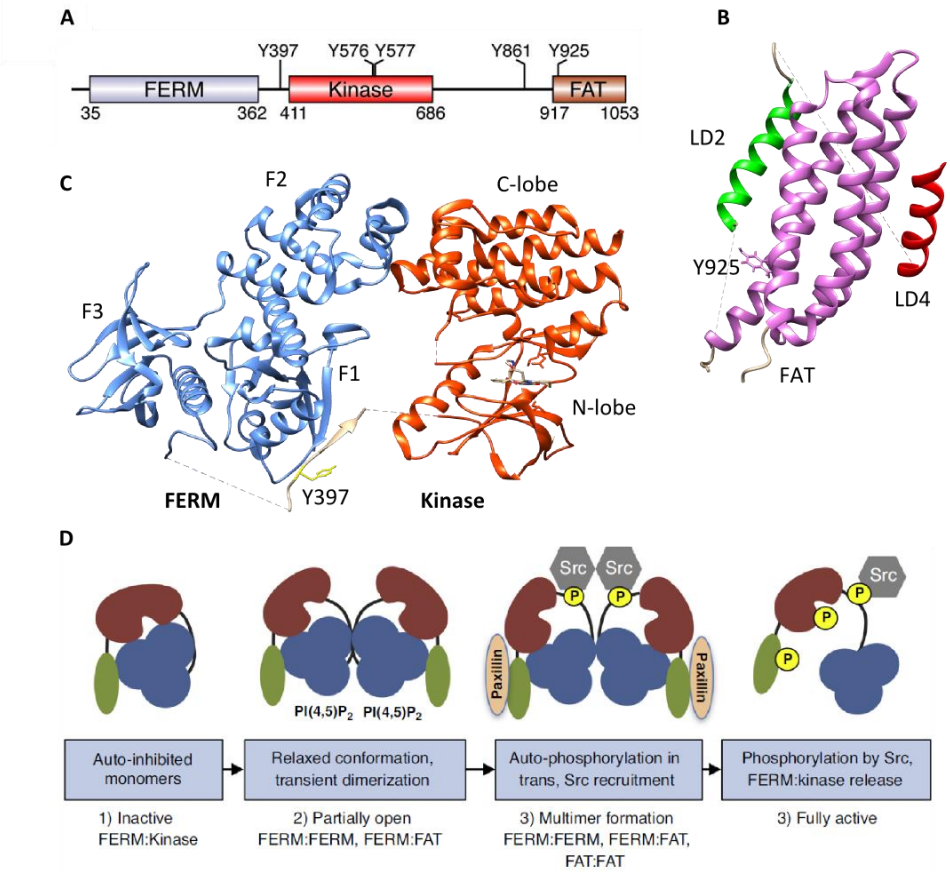

Figure 8: Structure and proposed mechanism of activation of FAK (Lietha et al., 2007, Kleinschmidt and Schlaepfer, 2017). (A) FAK is composed of a FERM domain, a kinase domain and a FAT domain, which are connected via long linker regions. The C-terminal FAT domain contains two binding sites for the LD2 and LD4 motifs of paxillin. Phosphorylation of Y925 creates a binding site for Grb2, which activates the MAPK pathway (B, PDB 2L6F). In its inactive, autoinhibited state, FERM and kinase domains are bound (C, PDB 2J0K). (D) Upon binding to PIP2 in the plasma membrane, FAK adopts a relaxed conformation and forms transient dimers through FERM:FERM and FAT:FAT contacts. This allows for Y397 autophosporylation in trans and a FERM:FAT interaction can be stabilized by paxillin. Phosphorylation of Phosphorylation of 397 creates a binding site for Src, which attaches via its SH2 and SH3 domains to phosphor-Y397 and three neighboring PxxP motifs. Src phosphorylates Y576 and Y577, which leads to full activity of FAK.

For the latter case, a model has been proposed that suggests paxillin bending around the FAT domain to occupy both binding sites (Bertolucci et al., 2005). Both paxillin binding sites are necessary for full activity of FAK, yet one site is sufficient for FA localization and even mutation of both sites still allows for FA targeting at 10 % efficiency compared to the wild type (Scheswohl et al., 2008). It appears that FAK is recruited to FA sites in part through complexes of integrin tails, kindlin and paxillin (Theodosiou et al., 2016). Paxillin facilitates recruitment of FAK to focal adhesions, yet it is not sufficient, since the deletion of other FAT binding partners prevents FAK recruitment to FAs (Miller et al., 2013). Therefore, the exact mechanism of FAK recruitment to FAs has yet to be resolved. It has further been proposed that the application of force induces detachment of the FERM and kinase domains and increases Y397 phosphorylation (Zhou et al., 2015).

1.2.3 Paxillin

Paxillin is an essential component of focal adhesions and functions as an adaptor or scaffold protein for focal adhesion components. Its N-terminus is composed of five Leu-Asp rich regions, referred to as LD1-5, which are heavily phosphorylated upon integrin activation and which mediate binding to kindlin, vinculin, ILK, FAK and parvin at defined and non-overlapping binding sites (Turner, 2000, Deakin and Turner, 2008). These LD motifs form amphipathic helices, as was shown in NMR structures (see Fig. 8B). Phosphorylation on Y31 and Y118 enhances binding of FAK to the nearby LD2 and LD4 domains in an indirect manner and seems to play a role in focal adhesion maturation (Zaidel-Bar et al., 2007).

NMR structures of the paxillin LD1, LD2 and LD4 motifs each in complex with the CH2 domain of α-parvin have been solved (Wang et al., 2008), showing that the CH2 domain displays the canonical CH fold with the unusual variation of the N- and C-terminal helices packing together to form a hydrophobic surface which allows LD1 binding. Through this interaction, paxillin recruits parvin to early focal adhesions (Nikolopoulos and Turner, 2000a). Due to large linker regions in between the LD motifs, the N-terminal half of paxillin appears to be largely unstructured, making the determination of a crystal structure difficult. It stands to reason that paxillin undergoes conformational changes upon binding to its interactors, resulting in a more defined structure.

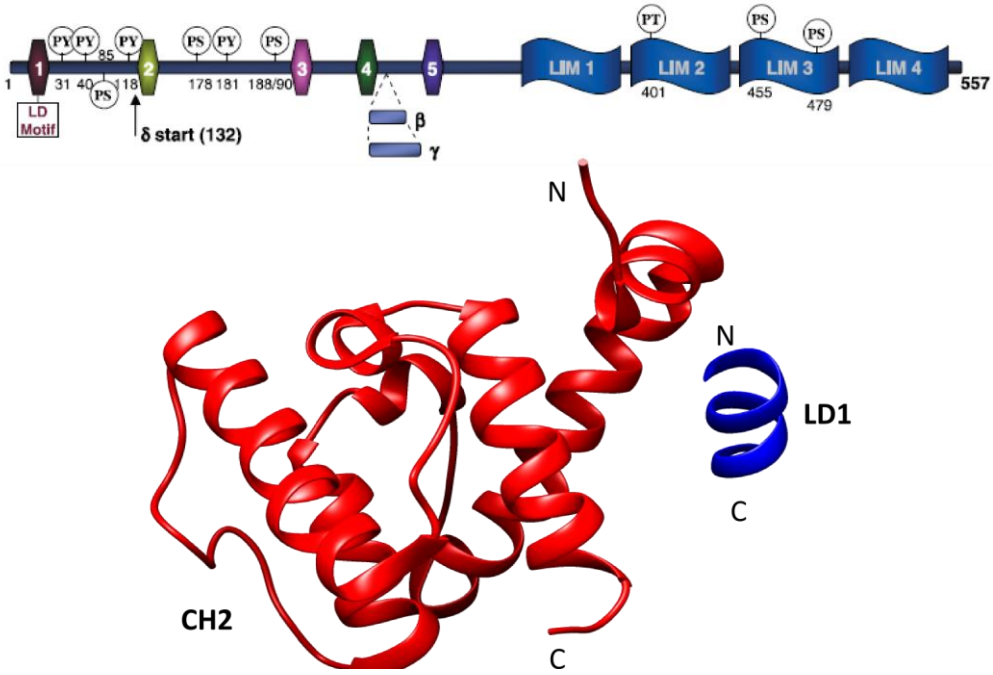

Figure 9: Domain structure of paxillin and NMR structure of paxillin LD1 domain in complex with α-parvin CH2 domain (PDB 2K2R) (Brown and Turner, 2004). Paxillin is composed of 5 LD-motifs at its N-terminus and of four Zn^{2+}-binding LIM domains at its C-terminus, which mediate binding to many different adhesome components. There is no crystal structure yet of full-length paxillin, but the structures of different LD motifs have been determined in complex with interaction partners, like parvin CH2 domain.

The C-terminal half of paxillin contains four LIM domains, which are each composed of two zinc-finger domains and a tight turn and which mediate protein-protein interactions (Schmeichel and Beckerle, 1994). The LIM2 and LIM3 domains play an important role in focal adhesion targeting, which can be regulated through their phosphorylation (Brown et al., 1998). It has recently been demonstrated that the LIM3 domain of paxillin binds to kindlin-2 in a Zn^{2+}-dependent manner (Theodosiou et al., 2016). This binding poses a mechanism for paxillin recruitment to integrin tails, where it then carries out its role as central focal adhesion adapter molecule.

1.2.4 The IPP complex

The heterotrimeric ILK/PINCH/parvin (IPP) complex has been shown to be pre-assembled in the cytoplasm of mammalian cells and is recruited to focal adhesions after integrin activation by talin and kindlin (Zhang et al., 2002, Hoffmann et al., 2014). The chief component of the IPP complex is Integrin-linked kinase (ILK), which, contrary to its name, contains a pseudoactive site and is incapable of catalyzing phosphorylation (Wickstrom et al., 2010). Instead, it plays an important role as scaffolding protein in a heterotrimeric complex with PINCH and parvin (IPP complex) and links integrins to the actin cytoskeleton and to adaptor

and signaling molecules (Qin and Wu, 2012). Of ILK, there is only one isoform in vertebrates, while there are two members of the PINCH family (PINCH-1 and -2) and three parvin isoforms (α-, β-, γ-parvin). PINCH-1 and -2 are equally expressed in adult tissues, as well as α- and β-parvin, while γ-parvin is the predominant form in hematopoietic cells (Korenbaum et al., 2001, Legate et al., 2006). ILK can form complexes with different PINCH and parvin isoforms, which mediate varying downstream signaling effects.

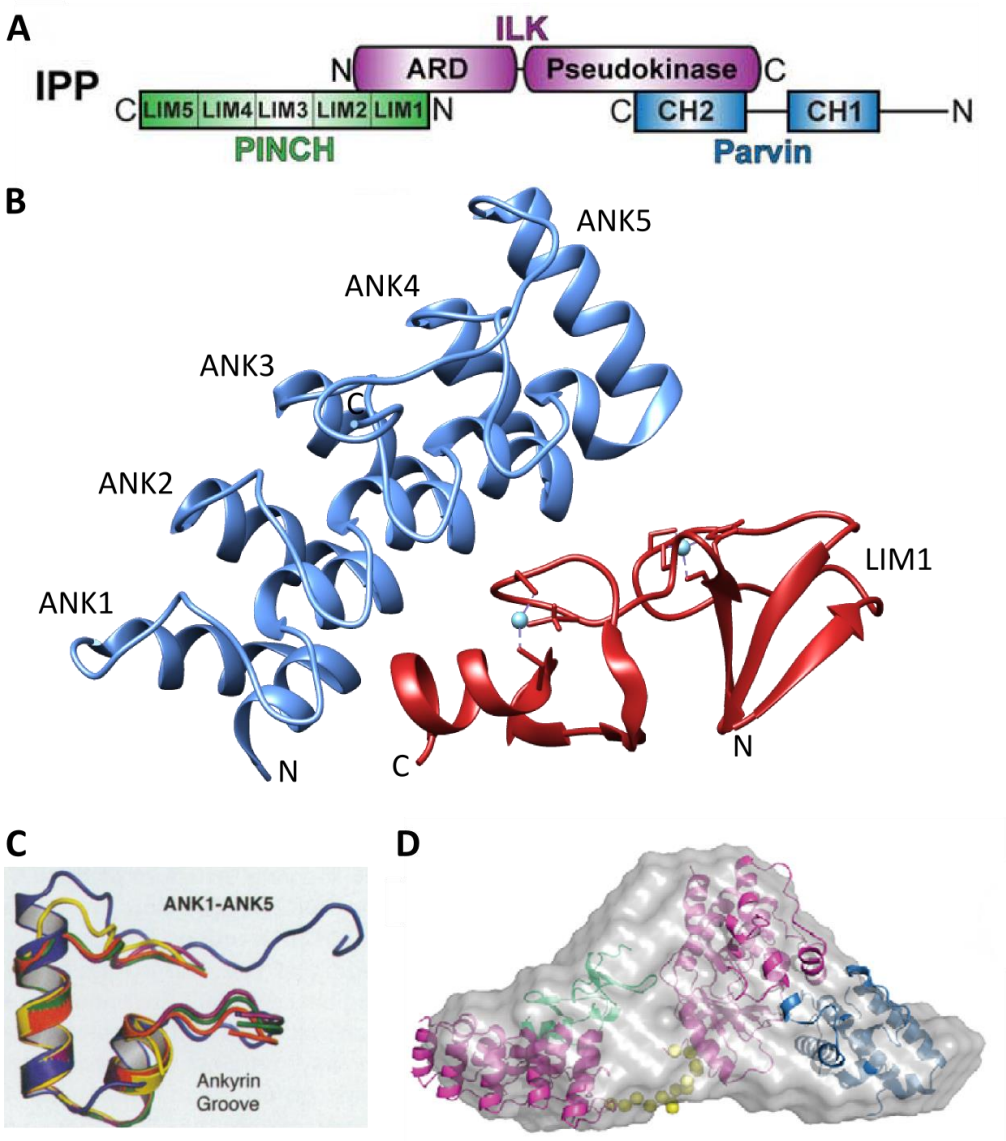

Figure 10: Structural properties of the IPP complex (Stiegler et al., 2013, Chiswell et al., 2008). (A) The heterotrimeric IPP complex is composed of ILK, PINCH and parvin. ILK Ankyrin repeat domain (ARD) binds to PINCH LIM1 domain, while the pseudokinase domain associates with the parvin CH2 domain. (B) The crystal structure of ILK-ARD/PINCH-LIM1 (PDB 4HI8) reveals that the five Ankyrin repeats in ILK are almost identically folded (C) and stack via α-helix contacts, leading to a concave, superhelical structure. The inside of this structure is termed "Ankyrin groove" and interacts with the Zn^{2+} binding side of PINCH LIM1, which is composed of a tandem-Zn-finger motif. (D) A SAXS analysis of a minimal IPP complex composed of full-length ILK, PINCH LIM1

domain and α-parvin CH2 domain revealed and envelope into which the two partial structures of ILK-ARD/PINCH-LIM1 and ILK-PKD/parvin CH2 (determined by crystallization) were modeled, suggesting a compact structure.

The 52 kDa protein ILK is composed of five N-terminal Ankyrin repeats (ANK), a short linker sequence and a C-terminal pseudokinase domain (PKD). The Ankyrin repeat domain binds to the first LIM domain of PINCH, which has been characterized by crystallization (Chiswell et al., 2008). Ankyrin repeats consist of 33 AA stretches, which fold into hairpin-helix-turn-helix structures and which pack against each other through their α-helices, stacked in an antiparallel manner. In the overall structure, this leads to the formation of helical bundles arranged in a left-handed superhelical spiral, which resembles a cupped hand with the so-called "Ankyrin groove" on the concave side (Mosavi et al., 2004, Sedgwick and Smerdon, 1999). This groove contains the binding surface through which ILK attaches to PINCH (Chiswell et al., 2008).

PINCH comprises five LIM domains, each composed of 55 AA tandem-Zn-fingers, which bind Zn^{2+} ions for stabilization. The Zn^{2+} binding sites in PINCH LIM1 are on the side that is facing the Ankyrin groove, allowing both zinc fingers to bind to ILK, while the C-terminal one has been shown in mutagenesis studies to be the more important one for binding (Velyvis et al., 2001). In ILK, the Ankyrin repeats 2-5 directly interact with LIM1, with ANK4 providing the most important interactions. ANK1 is not directly binding to LIM1, yet mutagenesis studies showed it to be important for PINCH binding, suggesting that it might associate with LIM2 domain, which is absent in the crystal structure. NMR structures of PINCH LIM1-4 have been determined (PDB: 1G47 (LIM1), 2D8X (LIM2), 2COR (LIM3), 1NYP/1U5S (LIM4)).

Parvin consists of an N-terminal polypeptide stretch followed by two calponin-homology (CH) domains, of which the second binds the pseudokinase domain (PKD) of ILK. The ILK-PKD/α-parvin-CH2 crystal structure (PDB 3KMW) not only revealed the structural basis for the interaction but also helped resolve the strongly debated question whether ILK is a real kinase or a pseudokinase (Fukuda et al., 2009). While the ILK PKD shows the conserved kinase domain fold with an ATP bound at the expected location, the catalytic loop is severely degraded and the key Asp and catalytic Lys and Asn residues are missing. Furthermore, the topologies of ATP and Mg^{2+} are altered and the activation segment is unusually short and lacks a conserved phosphorylation site. Finally, the fact that the crystal structure contains non-hydrolyzed ATP strongly indicates catalytic inactivity (Qin and Wu, 2012). *In vitro*, using the purified ILK

variants, no catalytic activity was observed, neither could a previously proposed interaction with PIP3 be verified (Fukuda et al., 2009).

The binding site for α-parvin CH2 domain is formed by two conserved helices (αEF and αG) and part of the P+1 loop, which is the substrate binding site in active kinases (Fukuda et al., 2011). The binding interface between ILK-PKD and parvin CH2 is large, which is typical for high-affinity complexes (Lo Conte et al., 1999).

The binding interface for paxillin in the CH2 domain is not compromised by ILK binding suggesting that simultaneous binding of ILK and paxillin is possible (Wang et al., 2008). Furthermore, the ILK-PKD/α-parvin CH2 complex was shown to interact with integrin β1 and β3 tails in pull-down experiments, indicating that the integrin binding site on ILK is also non-overlapping with the parvin binding site (Fukuda et al., 2009, Hannigan et al., 1996). Besides binding to ILK, α-parvin has been shown to interact with paxillin and F-actin simultaneously (Nikolopoulos and Turner, 2000a).

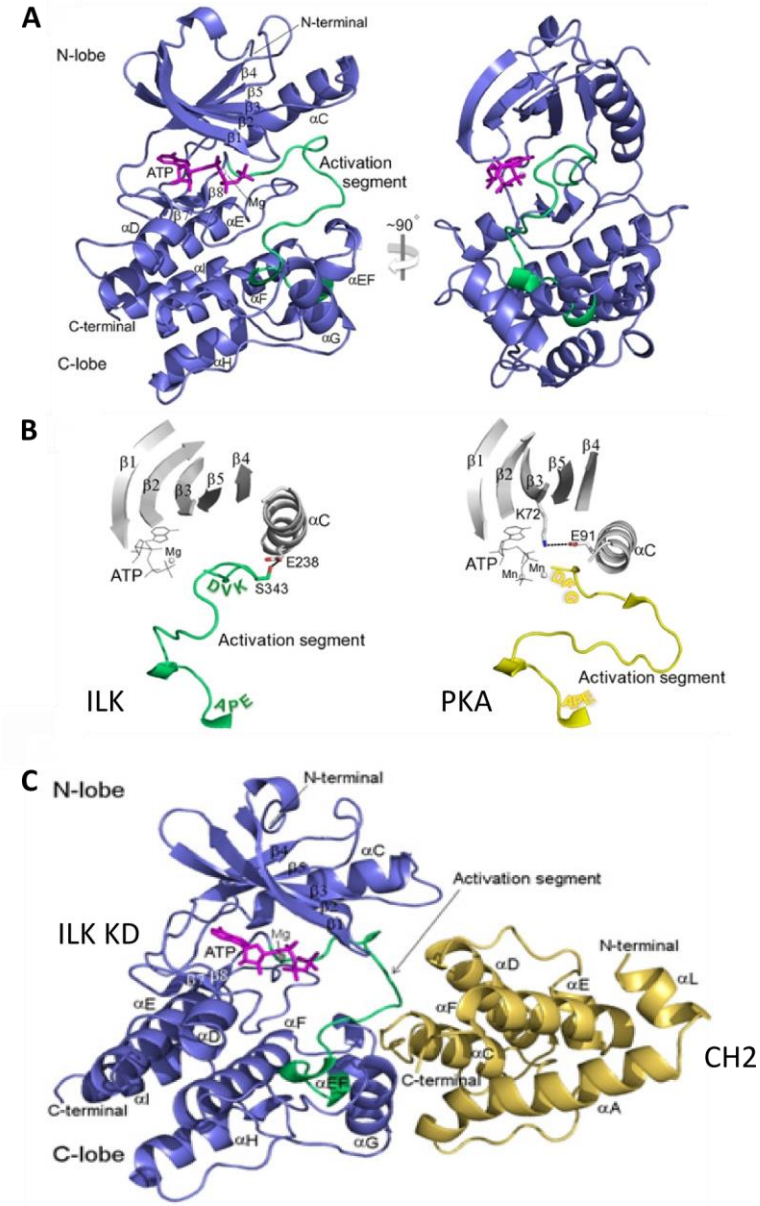

Figure 11: Crystal structure of the ILK pseudokinase domain in complex with α-parvin CH2 domain (Fukuda et al., 2009). (A) The ILK kinase domain displays a classical kinase structure, yet it has no catalytic activity. (B) The activation segment (displayed in green) is shorter and the conformation of the non-hydrolyzed ATP in the crystal structure is unusual, compared to the catalytically active protein kinase A (PKA). (C) The parvin CH2 domain binds to the helices αEF and αG and to part of the activation loop.

The structure of the full-length heterotrimeric complex has not been solved yet due to problems in producing the components recombinantly. Even the pseudokinase domain of ILK, if produced alone in *E. coli*, is largely insoluble, while co-expression of the second parvin CH domain leads to soluble complexes (Fukuda et al., 2009). Stiegler *et al.* reported the successful production of a "minimal IPP complex" in *E. coli*, composed of full-length ILK, the α-parvin CH2 domain and the LIM1 domain of PINCH1, facilitating SAXS analysis (Stiegler et al., 2013). Modeling of the two existing structures determined by X-ray crystallography (PDB 3F6Q,

3KMU) into the obtained envelope suggests a compact conformation of the complex, with dimensions of 120x60x40 Å.

A possible mechanism for the recruitment of the IPP complex to integrin tails is through binding to kindlin-2. In cells lacking kindlin-2, ILK and PINCH do not localize to adhesion sites (Montanez et al., 2008). This indicates that the direct interaction of ILK with the integrin tail might not be enough to recruit ILK from the cytoplasm, yet it is possible that IPP, which has been recruited to the focal adhesion through kindlin-2 or paxillin or a complex of both, might interact with the tail during later stages of adhesion maturation (Wickstrom et al., 2010).

1.2.5 The IPP-binding proteins EPLIN and RSU-1

Epithelial protein lost in neoplasm (EPLIN) and ras suppressor protein 1 (RSU-1) has been identified as interaction partners of PINCH and also localize to FAs (Karakose et al., 2015). EPLIN was first found to be of interest in a screen for proteins downregulated in human cancer cells, as its name implies (Maul and Chang, 1999). It is composed of a central LIM domain and two actin-binding domains (ABD) at the N- and C-termini and exists in two splice variants, the 90 kDa EPLIN-α and the 110 kDa EPLIN-β. EPLIN has been shown to bundle F-actin fibers via its two ABDs and also to influence nucleation of G-actin (Maul et al., 2003).

Extracellular signal-regulated kinase (ERK) phosphorylates EPLIN at S362 and S604, thereby inhibiting F-actin binding and relocating EPLIN to the cell periphery (Han et al., 2007). There, it has been shown to co-localize with paxillin and to potentially stabilize FAs (Tsurumi et al., 2014). The localization to adhesome complexes is probably mediated through interaction with PINCH, which was identified by interactome studies on PINCH as well as in assays with cells depleted of PINCH, where EPLIN did not localize to FAs any more (Karakose et al., 2015). Furthermore, depletion of EPLIN significantly reduces cell adhesion, spreading and migration. Recently, the phosphatase CDC14A has been shown to de-phosphorylate EPLIN, thereby controlling the actin-bundling effect of EPLIN (Chen et al., 2017).

Ras suppressor protein 1 (RSU-1) was originally identified as a protein, which can inhibit transformation by Ras (Cutler et al., 1992). It is highly conserved, expressed in various mammalian cells and comprises 7 leucine-rich repeats (LRR) (Ito et al., 2010). These LRR motifs can be found in various proteins and have been shown to mediate protein-protein interactions (Kobe and Kajava, 2001). RSU-1 interacts with the LIM5 domain and the short C-terminal part

of PINCH-1, which are both required for binding (Dougherty et al., 2005). Since the short C-terminal region is only present in PINCH-1 but not PINCH-2, the interaction of RSU-1 is restricted to PINCH-1.

Studies on cells depleted of either RSU-1 or PINCH-1 indicated that RSU-1 localization to focal adhesions is dependent on PINCH-1 while depletion of RSU-1 had no effect on PINCH-1 recruitment (Ito et al., 2010). Therefore, the LIM1 domain of PINCH appears to be crucial for localization to focal adhesions through binding to ILK and for cell attachment, while LIM5 through binding of RSU-1 is required for cell spreading. Furthermore, RSU-1 has been reported to regulate PINCH-1 levels and stability, which thereby affects and regulates the stability of the IPP complex as well (Gonzalez-Nieves et al., 2013).

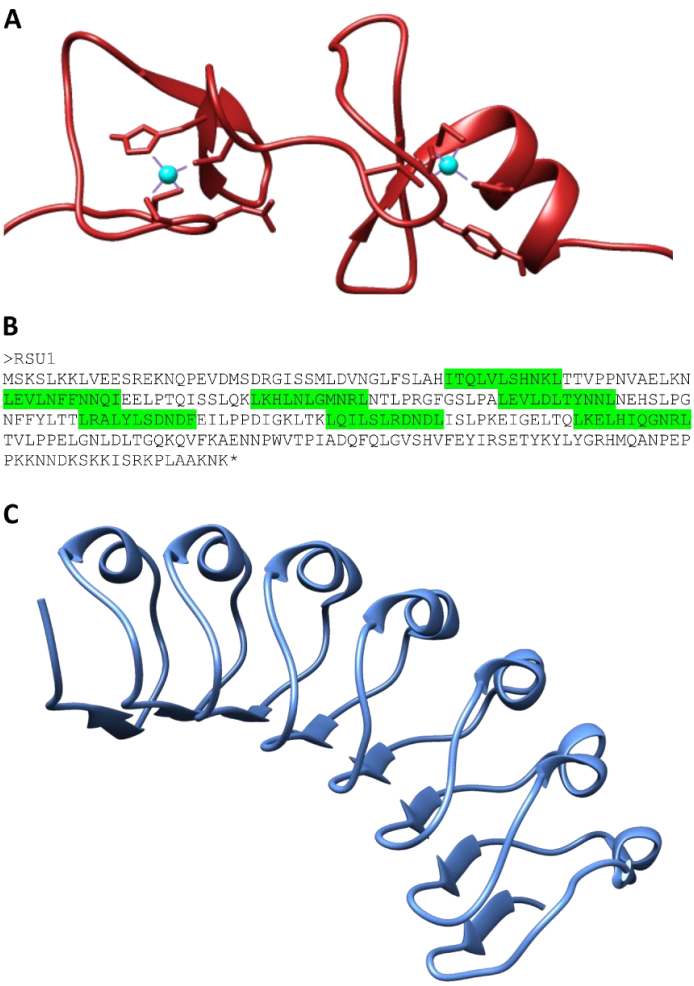

Figure 12: Structural details of EPLIN and RSU-1. (A) EPLIN consists of a central LIM domain and two actin binding domains at the N- and C-terminus. So far, only a solution structure of the Zn^{2+}-binding LIM domain has been resolved (PDB 2D8Y), the remaining parts of the molecule are probably intrinsically disordered when not bound to a ligand. (B) RSU-1 has been shown to bind to PINCH-1 and contains 7 leucine-rich repeat (LRR) motifs of the consensus sequence LxxLxLxxN/CxL, where x can be any amino acid and L can also be replaced by I, F or V (LRR motif indicated in green). (C) Of RSU-1 there is no crystal structure known so far, but it can be expected to assume a similar fold as other LRR motif-containing proteins, like the internalin b leucine rich repeat domain (PDB 1D0B). Each LRR consists of one α helix and one β strand, which are each stacking to form a bent, arc-like structure.

1.3 Experimental approaches for studying protein-protein interactions *in vitro*

Assembly of the integrin adhesome is based on various protein-protein interactions, with individual components exerting catalytical or scaffolding functions, or both, as is the case for FAK. Therefore, understanding which proteins interact with each other to form the large multi-protein adhesome complexes or smaller subcomplexes is essential for reconstructing the events that lead to FA assembly and function. There are several well-established methods to study protein-protein interactions *in vitro* using recombinant proteins. Which of these methods is best suited for studying an interaction depends on the characteristics of the recombinantly produced proteins. As a first indication whether two proteins interact, pull-down assays are used in which one potential binding partner is immobilized on a surface (e.g. beads) and incubated with the potential binding protein. If there is an interaction, both proteins can later be co-eluted. Although this method is very crude and prone to non-specific interactions with the bead material, it is a good screening tool to find interactions which merit further study. Classical biophysical methods for detecting and quantifying protein-protein interactions are surface plasmon resonance spectroscopy (SPR), isothermal titration calorimetry (ITC), microscale thermophoresis (MST) or analytical ultracentrifugation (AUC). These approaches allow not only the detection of an interaction but also the determination of biniding affinities and in some cases also stoichiometry and kinetic parameters such as on- and off-rates. All of these methods possess advantages and caveats, such as the high sample consumption in ITC or the occurrence of non-specific interactions with the chip surface in SPR. Therefore, it is difficult to predict which method will be best suited for measuring a specific protein-protein interaction and ideally, several orthogonal methods should be applied to identify potential artifacts.

The aforementioned methods are well suited for studying the binding modes and affinities of protein-protein interactions, however they do not provide structural information, like interfaces involved in the interaction, orientation of the proteins in the complex or conformational changes. These questions are classically answered through X-ray crystallography, NMR spectroscopy or Cryo-electron microscopy (Cryo-EM). Recently, another approach to gain information on the native structure of protein complexes by chemical crosslinking and subsequent mass spectrometric analysis has been developed (Herzog et al., 2012, Leitner et al., 2010). After assembly or isolation of protein complexes with several

components, the structures are fixed by chemically crosslinking lysine residues, which are a specific distance (25-30 Å, dependent on the crosslinker) apart from each other. The crosslinked sample is proteolytically cleaved into peptides, which retain the crosslinks and can thus be identified by mass spectrometric analysis. This allows the identification of protein surfaces, which are located in close proximity within the complex, as well as conformational changes in single components, induced by binding to other proteins. The crosslinks can be displayed in existing partial structures of the proteins in the complex and allow the generation of a model.

1.4 Aims of the thesis

The integrin adhesome is a highly complex and versatile assembly of proteins with signaling, scaffolding and force-transducing properties. The innermost components, whose deletion causes severe defects in cell adhesion and migration, have been identified in numerous studies, yet little is known regarding the architecture of the complex. Due the high amount of different proteins in focal adhesions in cells it is difficult to pinpoint which components interact directly and in which sequence and stoichiometry. One way to investigate direct binding can be done by reconstructing adhesome complexes *in vitro* using recombinant proteins.

The **first aim** of my thesis was the recombinant production and purification of the innermost components of the integrin adhesome. I established protocols for obtaining purified and active full-length FAK, EPLIN and the heterotrimeric IPP complex at >90 % purity. Recombinant THD, kindlin-2 and paxillin were purified according to already established protocols.

The **second aim** was the detection and characterization of protein-protein interactions among these adhesome components and towards the integrin tail. Furthermore, I assembled complexes of adhesome proteins in order to gain structural information via chemical crosslinking and LC-MS/MS analysis.

For the **third aim** of my thesis I established a platform for studying the interactions of adhesome components with integrin tails embedded into a lipid bilayer. For this, I incorporated integrin transmembrane and cytoplasmic domains, which can be selectively

inserted into Nanodiscs composed of varying lipid compositions. This system can be used to test the binding of individual components as well as complex assembly around integrin tails by pull-down experiments as well as single-molecule microscopy.

The **fourth aim** was to express and purify talin-integrin fusion constructs, which can be used in optical tweezer experiments. This set-up simulates the traction force on the talin-integrin bond as it is inside the cell, including a so-far neglected element of integrin dynamics. Furthermore, it can be used to study and characterize the bond in presence of kindlin-2 and a lipid bilayer.

2 Material and Methods

2.1 Materials

2.1.1 Buffers and gels

Buffers for recombinant protein purification

Kindlin, talin, PINCH, paxillin, EPLIN

A1 20 mM Tris, 500 mM NaCl, 1 mM TCEP, pH 7.5

A2 20 mM Tris, 500 mM NaCl, 500 mM imidazole, 1 mM TCEP, pH 7.5

A3 20 mM Tris, 200 mM NaCl, 1 mM TCEP, pH 7.5

IPP complex

B1 50 mM HEPES, 150 mM NaCl, 10 µM $ZnCl_2$, 0.1 % Tween-20, 1 mM TCEP, 1 mM PMSF, pH 7.5

B2 50 mM HEPES, 150 mM NaCl, 10 µM $ZnCl_2$, 0.05 % Tween-20, 1 mM TCEP, pH 7.5

B3 50 mM HEPES, 150 mM NaCl, 500 mM imidazole, 10 µM $ZnCl_2$, 0.05 % Tween-20, 1 mM TCEP, pH 7.5

B4 50 mM HEPES, 150 mM NaCl, 1 µM $ZnCl_2$, 0.05 % Tween-20, 1 mM TCEP, pH 8.5

B5 50 mM HEPES, 150 mM NaCl, 500 mM imidazole, 1 µM $ZnCl_2$, 0.05 % Tween-20, 1 mM TCEP, pH 8.5

FAK

C1 50 mM Na-phosphate, 350 mM NaCl, 5 % glycine, 5 % mannitol, 1 mM TCEP, pH 7.5

C2 50 mM Na-phosphate, 350 mM NaCl, 500 mM imidazole, 5 % glycine, 5 % mannitol, 1 mM TCEP, pH 7.5

TMCyto constructs

D1 50 mM HEPES, 150 mM NaCl, 0.1 % Triton-X100, pH 7.5

D2 50 mM HEPES, 150 mM NaCl, 3 % EMPIGEN, 1 mM TCEP, pH 7.5

D3 50 mM HEPES, 150 mM NaCl, 1.5 % EMPIGEN, 1 mM TCEP, pH 7.5

D4 50 mM HEPES, 150 mM NaCl, 500 mM imidazole, 1.5 % EMPIGEN, 1 mM TCEP, pH 7.5

D5 20 mM MES, 60 mM NaCl, 1.5 % EMPIGEN, 1 mM TCEP, pH 5.5

D6 20 mM MES, 1 M NaCl, 1.5 % EMPIGEN, 1 mM TCEP, pH 5.5

Nanodiscs

Cholate buffer	20 mM Tris, 100 mM NaCl, 100 mM Cholate, pH 7.5
Nanodisc buffer	20 mM HEPES, 150 mM NaCl, 0.5 mM EDTA, pH 7.5
Cytobuffer	139 mM K_2HPO_4, 8.8 mM NaH_2PO_4, 0.4 mM $MgCl_2$, 3.2 mM NaCl, pH 7.5
PBS	10 mM Na_2HPO_4, 1.8 mM KH_2PO_4, 137 mM NaCl, 2.7 mM KCl, pH 7.4
NHS labeling buffer	20 parts PBS + 1 part 200 mM $NaHCO_3$, pH 9.0

Agarose Gel electrophoresis

1x TAE buffer	40 mM Tris, 20 mM acetic acid, 1 mM EDTA
6x DNA sample buffer	0.2 % (w/v) Orange G, 60 % (w/v) glycerol, 60 mM EDTA
Agarose gel	1 % (w/v) agarose in 1x TAE buffer, 1 µl ethidium bromide per 10 ml gel volume

SDS-PAGE

1x SDS running buffer	25 mM Tris, 192 mM Glycine, 0.1 % (w/v) SDS
1x Tricine running buffer	25 mM Tris, 25 mM Tricine, 0.05 % (w/v) SDS
5x SDS sample buffer (reducing)	250 mM Tris/HCl, pH 8.0, 7.5 % (w/v) SDS, 25 % (v/v) glycerol, 0.25 mg/ml bromophenol blue, 12.5 % (v/v) 2-mercaptoethanol
4x Lower Tris	1.5 M Tris/HCl, pH 8.8
4x Upper Tris	0.5 M Tris/HCl, pH 6.8
Tricine Tris	2.5 M Tris-HCl, pH 8.8
Coomassie staining solution	10 % (v/v) acetic acid, 25 % (v/v) isopropanol, 0.1 % (w/v) Coomassie Brilliant Blue R-250
Coomassie destaining solution I	10 % (v/v) acetic acid, 25 % (v/v) isopropanol
Coomassie destaining solution II	10 % (v/v) acetic acid

Table 1: Composition of gels used for SDS-PAGE. The amounts given are sufficient for 2 separating gels (10 ml total) and 2 stacking gels (5 ml).

SDS gels						
Separating gel	**ddH_2O (ml)**	**30 % Acrylamide/Bis (ml)**	**Lower Tris (ml)**	**20 % SDS (µl)**	**10 % APS (µl)**	**TEMED (µl)**
10 %	4.15	3.3	2.5	50	50	5
12 %	3.45	4.0	2.5	50	50	5
15 %	2.45	5.0	2.5	50	50	5
Stacking gel	**ddH_2O (ml)**	**30 % Acrylamide/Bis (ml)**	**Upper Tris (ml)**	**20 % SDS (µl)**	**10 % APS (µl)**	**TEMED (µl)**
4 %	3.1	0.65	1.25	50	37	7.5
Tricine gels						
% gel	**ddH_2O (ml)**	**30 % Acrylamide/Bis (ml)**	**Tricine Tris (ml)**	**-**	**10 % APS (µl)**	**TEMED (µl)**
16 %	0.22	5.33	4.3		50	6
4 %	3.42	0.66	0.76		50	6

Silver staining

Fixing solution	13.5 % (v/v) formalin, 40 % (v/v) methanol
$Na_2S_2O_3$ solution	0.02 % (w/v) $Na_2S_2O_3$ in H_2O
$AgNO_3$ solution	0.1 % (w/v) $AgNO_3$ in H_2O
Developing solution	3 % (w/v) Na_2CO_3, 0.05 % (v/v) formalin, 0.000016 % (w/v) $Na_2S_2O_3$
Stop solution	50 % (v/v) ethanol, 15 % (v/v) acetic acid
100 % TCA solution	1 g/ml TCA in ddH_2O

Western Blotting

Western Blot transfer Buffer	25 mM Tris, 192 mM Glycine, 10 % (v/v) methanol
PBS	4 mM KH_2PO_4, 16 mM Na_2HPO_4, 115 mM NaCl, pH7.4
PBS-T	PBS, 0.1 % (v/v) Tween-20
Blocking solution	4 % (w/v) non-fat dried milk powder in PBS-T

2.1.2 Media and cell culture materials

DMEM, 4.5 g/l Glucose, GlutaMax	Gibco, 31966-021
Fetal bovine serum	Gibco, 10270-106
FreeStyle 293 Expression Medium (HEK293E suspension culture)	Thermo Fisher, 12338001
EX-CELL 405 Serum-Free Medium (High Five Insect cells)	Sigma-Aldrich, 14405C
LB medium	1 % (w/v) tryptone/peptone, 1 % (w/v) NaCl, 0.5 % (w/v) yeast extract
LB-agar plates	LB medium with 5 g/l agar
5ml Costar Stripette	Corning, 4487
15ml Costar Stripette	Corning, 4488
25ml Costar Stripette	Corning, 4489
15ml tube	Corning, CLS430791
50 ml tube	Corning, CLS430829
75 cm^2 Falcon Tissue Culture Treated Flask	Corning, 10-126-11
175 cm^2 Falcon Tissue Culture Treated Flask	Corning, 10-126-13
Cellfectin II	Invitrogen, 10362100
Geneticin (G418 Sulfate, 50 mg/mL)	Gibco, 10131027
Penicillin/ Streptomycin (100x)	PAA, P11-010
PEI (linear, 1 mg/ml in ddH_2O)	Polysciences, 23966
PEI MAX 40000 (Polyethylenimine HCl MAX, Linear, Mw 40,000)	Polysciences, 24765-2
Pluronic F-68 Non-ionic Surfactant (100X)	Gibco, 24040032
Trypsin / EDTA (10x)	Gibco, 15400-054
Vi-CELL XR	Beckman Coulter, 383556

2.1.3 Antibodies

All antibodies used (except anti-$His_6$and anti-GST) were directed against the focal adhesion components from mouse.

Table 2: Antibodies used for detection of recombinant focal adhesion components in Western Blot

Protein detected	Host	Dilution for WB	Source
FAK	rabbit	1 : 1000	Cell signaling, 3285S
GST	mouse	1 : 2500	Novagen, 71097-3
ILK	mouse	1 : 5000	Transduction laboratories, 611803
kindlin 2	mouse	1 : 1000	Merck Millipore, MAB2617
α-parvin	rabbit	1 : 1000	Cell signaling, 8190
paxillin	mouse	1 : 1000	Transduction laboratories, 610051
PINCH	mouse	1 : 1000	Transduction laboratories, 612710
RSU-1	rabbit	1 : 1000	“self-made” by Fässler department
THD	rabbit	1 : 1000	“self-made” by Fässler department
phospho-Tyr	mouse	1 : 1000	Merck Millipore, 4G10, 05-321
phospho-pax-Y31	rabbit	1 : 1000	Thermo Fisher, 44-720G
phospho-pax-Y118	rabbit	1 : 1000	Thermo Fisher, 44-722G
Src (pan)	rabbit	1 : 1000	Thermo Fisher, 44-656G

2.1.4 Instruments

Avanti J-25 centrifuge	Beckman Coulter
Avanti J-26S XP centrifuge	Beckman Coulter
CD spectrometer Jasco J-715	Jasco
Dynamic Light Scattering (DLS) DynaPro Nanostar	Wyatt
EasyPure II LF ultrapure water system	Barnstead
Eppendorf 5424R centrifuge	Eppendorf
Eppendorf 5804R centrifuge	Eppendorf
Epson Perfection V550 Photo scanner	Epson
ImageQuant LAS4000 Luminescent image analyzer	GE Healthcare
Infors HT Minitron incubator	Infors
JA-10 fixed-angle rotor	Beckman Coulter
JA-25.50 fixed-angle rotor	Beckman Coulter
microTOF mass spectrometer	Bruker
Mini-PROTEAN Tetra Vertical Electrophoresis Cell	BioRad, 1658004
Mini Trans-Blot Cell	BioRad, 1703930
Monolith NT.115 Instrument, red-blue	Nanotemper, MO-G007

NGC Quest 10 Plus Chromatography system	BioRad, #7880003
Nanodrop 1000	Thermo Fisher
Optima XL-100K ultracentrifuge	Beckman Coulter
Prometheus NT.48 NanoDSF device	Nanotemper, PR001
Sonopuls HD 2070 Sonicator with MS 73 Microtip	Bandelin
SW 41 Ti Rotor, Swinging Bucket	Beckman Coulter, 331362
T3 Thermocycler (PCR cycler)	Biometra

2.1.5 Organisms

E. coli One Shot® ccdB Survival™ 2 T1R cells	Thermo Fisher, A10460
E. coli DH10EmBacY	*Multi*Bac^{Turbo} kit, A. Craig & I. Berger
E. coli Rosetta Bl21 (DE3) (F- ompT hsdSB (rB- mB-) gal dcm (DE3) pRARE (CamR))	Merck Millipore, 70954-3
HEK293E-EBNA1	Obtained from Y. Durocher, Biotechnology Research Institute, National Research Council Canada, Montréal
High Five insect cells	Thermo Fisher, B85502
OmniMax cells	One Shot OmniMAX™ 2 T1R Chemically Competent *E. coli*, Thermo Fisher
pirHC cells	pir^{+} cells, high copy number, *Multi*Bac^{Turbo} kit, A. Craig & I. Berger
SF9 insect cells	Merck Millipore, 71104-3

2.1.6 Enzymes and commercial proteins

(All restriction enzymes used for cloning were acquired from New England Biolabs)

Benzonase Nuclease	Merck Millipore, 71205-3
Calf intestinal alkaline phosphatase	NEB, M0290S
Cre recombinase	NEB, M0298S
Fast-Link DNA ligation kit	Lucigen, LK6201H

His-PreScission protease	GE Healthcare, 27-0843-01
His-SenP2 (Sumo-protease)	MPIB Microchemistry Core Facility, (Reverter and Lima, 2004)
His-TEV protease	MPIB Microchemistry Core Facility, (Kapust et al., 2001)
LysC	Wako, LAL3933
MSP1E3D1	Cube Biotech, 26156
MSP2N2	Cube Biotech, 26176
PfuUltra II Fusion HS DNA Polymerase	Agilent, 600670
RecA	NEB, M0249S
SUMOstar Protease	Life Sensors, 4110
T4-DNA polymerase	NEB, M0203S
Trypsin	Promega, V5111

2.1.7 Columns for purification

DextraSEC PRO2 desalting columns	AppliChem, A8710,0050
ENrich SEC70	BioRad, 780-1070
ENrich SEC650	BioRad, 780-1650
HiLoad 16/600 Superdex 200 pg	GE Healthcare, 28989335
HisTrap FF, 1 ml	GE Healthcare, 17-5319-01
HisTrap HP, 5ml	GE Healthcare, 17-5248-02
HiTrap Q HP, 1 ml	GE Healthcare, 17-1153-01
HiTrap SP HP, 1 ml	GE Healthcare, 17115101

2.1.8 Fluorophores

Alexa 488 NHS ester	Thermo Fisher, A20000
Alexa 647 NHS ester	Thermo Fisher, A37573
Alexa 647 Maleimide	Thermo Fisher, A20347
Atto 565 NHS ester	Atto tec, AD 565-31

NT647 labeling kit	Nanotemper, L001

2.1.9 Miscellaneous

1 kb plus DNA ladder	Thermo Fisher, 10787018
BS3-H12/D12 crosslinker	Creative Molecules Inc., 001SS
Cell scrapers	Sarstedt, 83.1830
Dounce tissue grinder, 25 ml	Blaessig Glas
Gel Filtration Standard	BioRad, 151-1901
Immobilon P, PVDF membrane	Merck Millipore, IPVH00010
MST capillaries, premium coated (hydrophilic)	Nanotemper, MO-K005
nanoDSF Grade Standard capillaries	Nanotemper, PR-C002
Ni-NTA Agarose beads	Qiagen, 30210
Ni-NTA Sepharose High Performance	GE Healthcare, 17-5268-01
Precision plus protein standard Kaleidoscope	BioRad, 1610375
Whatman Chromatography paper	GE Healthcare, 3030917

Concentrators

Amicon Ultra 4, 10 K	Merck Millipore, UFC801024
Amicon Ultra 15, 10 K	Merck Millipore, UFC901024
Amicon Ultra 15, 30 K	Merck Millipore, UFC903024
Amicon Ultra 0.5 ml, 10 K	Merck Millipore, UFC501096

Sterile filters

Ultrafree-MC-GV, PVDF, 0.22 µm	Merck Millipore, UFC30GV00
Millex GV, 0.22 µm PVDF	Merck Millipore, SLGV033RS
Millex HA, 0.45 µm MCE	Merck Millipore, SLHA033SS
Stericup and Steritop, 0.22 µm, GP	Merck Millipore, SCGPT05RE

Dialysis devices

SnakeSkin Dialysis membranes, 10.000 MWCO	Thermo Fisher, 68100
SnakeSkin Dialysis membranes, 3.500 MWCO	Thermo Fisher, 68035
Slide-A-Lyzer Mini dialysis devices, 10K MWCO, 0.5 ml	Thermo Fisher, 88401

DNA purification

QIAquick Gel Extraction Kit	Qiagen, 28706
QIAprep Spin Miniprep Kit	Qiagen, 27106
QIAquick PCR Purification Kit	Qiagen, 28106
NucleoBond BAC 100	Macherey-Nagel, 740579
NucleoBond Xtra Midi Plus	Macherey-Nagel, 740412.50

Lipids and detergents

DDM (n-Dodecyl-β-Dmaltopyranoside)	Anatrace, D310-25GM
DMPC lipid (1,2-dimyristoyl-sn-glycero-3-phosphocholine)	Corden Pharma, LP-R4-B58
DMPG lipid (1,2-dimyristoyl-sn-glycero-3-phospho-(1'-rac-glycerol)	Avanti Polar Lipids, 240796
EMPIGEN BB (30.3 %)	Sorachim, EMP-100
PI(4,5)P2 (1,2-dioctanoyl-sn-glycero-3-phospho-(1'-myo-inositol-4',5'-bisphosphate))	Avanti polar lipids, 850185P
POPS (1-palmitoyl-2-oleoyl-sn-glycero-3-phospho-L-serine)	Avanti polar lipids, 840034P

2.1.10 Chemicals

Acetic acid	Sigma-Aldrich, 33209
Acetonitrile	Fluka, 34967
Agarose, Ultra pure	Invitrogen, 16500-500
$AgNO_3$	Riedel-de Haen, 31630
Ammonium bicarbonate	Fluka, 40867-50G-F
Ammonium peroxodisulfate (APS)	Merck Millipore, 1.01201.0500
Ampicilin	Sigma-Aldrich, A9518

Brilliant Blue R	Sigma-Aldrich, B0149
Chloramphenicol	Sigma-Aldrich, C0378
Chloroform	Merck Millipore, 1.02445.1000
Chromosulfuric acid (2-5% $Na_2Cr_2O_7$ in 90% H_2SO_4)	Sigma-Aldrich, 27174
Ethanol	Sigma-Aldrich, 32205
Ethidium bromide	Roth, 2218.2
Formaldehyde, 37 %	Merck Millipore, 1.04003.1000
Formic acid (FA)	Fluka, 56302
Gentamicin solution (50 mg/ml)	Sigma-Aldrich, G1397
Glycerol, 86 %	Roth, 4043.1
Glycine	Sigma-Aldrich, 33226
HCl, 37 %	VWR Chemicals, 20252.335
HEPES	Biomol, 05288.100
Imidazole	Merck Millipore, 1.04716.0250
Immobilon Western chemiluminescent HRP substrate	Merck Millipore, WBKLS0500
Iodoacetamide	Sigma-Aldrich; I6125-5G
IPTG (Isopropyl β-D-1-thiogalactopyranoside)	Thermo Fisher, R0392
Isopropanol	Sigma-Aldrich, 33539
Kanamycin	Sigma-Aldrich, K1876
K_2HPO_4 * 3 H_2O	Roth, 6878.1
D-Mannitol	Sigma-Aldrich, M4125
2-Mercaptoethanol	Merck Millipore, 805740
MES	Merck Millipore, 1.06126.0025
Methanol	Sigma-Aldrich, 32213
$MgCl_2$ * 6 H_2O	Merck Millipore, 1.05833.1000
NaCl	Roth, 3957.2

Na_2CO_3	Merck Millipore, 1.06392.1000
$NaHCO_3$	Merck Millipore, 6329.1000
$NaH_2PO_4 * H_2O$	Merck Millipore, 1.06346.1000
NaOH	VWR Chemicals, 28245.298
$Na_2S_2O_3 * 5\ H_2O$	Merck Millipore, 0077695
$NiSO_4 * 6\ H_2O$	Sigma-Aldrich, 31483
Non-fat dried milk	AppliChem, A0830,0500
Orange G	Roth, 0318.1
PMSF	Sigma-Aldrich, P7626
Rotiphorese Gel 30	Roth, 3029.1
SDS pellets	Roth, CN30.3
Sodium azide	Merck Millipore, 1.06688.0100
Sodium cholate hydrate	Sigma-Aldrich, C6445
Spectinomycin	Sigma-Aldrich, S2647
Sucrose	Sigma-Aldrich, S7903
TCEP	Roth, HN95.2
TCEP (for crosslinking)	Perbio Science Germany; 0020490
Trifluoro acetic acid	Thermo Scientific, 28904
Titriplex III (EDTA)	Merck Millipore, 1.08418.1000
Trichloroacetic acid TCA)	Merck Millipore, 1.00807.1000
Tricine	Sigma-Aldrich, T0377
Triton-X100	Roth, 3051
Trizma base (Tris)	Sigma-Aldrich, T1503
Tryptone/peptone	Roth, 8952.2
Tween-20	Serva, 37470.01
Urea	Sigma-Aldrich, U6504
Yeast extract	Roth, 2363.3
$ZnCl_2$	Merck Millipore, 8816.0250

2.1.11 Expression vectors and primers

Table 3: List of expression vectors used, indicating expression system, resistance markers and purification tags.

Name	System	Resistance	Tag/Protease site
pCoofy17-EPLIN	*E. coli*	Kanamycin	N-His_{10}-SUMO3
pCoofy17-Kindlin2	*E. coli*	Kanamycin	N-His_{10}-SUMO3
pCoofy17-Paxillin	*E. coli*	Kanamycin	N-His_{10}-SUMO3
pCoofy17-THD	*E. coli*	Kanamycin	N-His_{10}-SUMO3
pCoofy55-FAK	HEK293	Ampicillin	N-His_{10}-SUMOstar
pET15b-TMCyto-b1-wt	*E. coli*	Ampicillin	N-His_6
pET15b-TMCyto-b1-NPIA	*E. coli*	Ampicillin	N-His_6
pET15b-TMCyto-b1-NPKA-TTAA	*E. coli*	Ampicillin	N-His_6
pET15b-TMCyto-a5-wt	*E. coli*	Ampicillin	N-His_6
pACEBac1-IPP	Insect cells	Gentamycin	N-His_6-PreScission
pACEBac1-IPP-dLIM5	Insect cells	Gentamycin	N-His_6-PreScission
pIDS-K2-IntBeta-Pax	Insect cells	Spectinomycin	N-GST-PreScission
pIDK-RSU-EPLIN	Insect cells	Kanamycin	/
pIDC-FAK-Talin	Insect cells	Chloramphenicol	/
pCoofy17-Talin1-F3-b1A_long_link	*E. coli*	Kanamycin	N-His_{10}-SUMO3
pCoofy17-Talin2-F3-b1D_long_link	*E. coli*	Kanamycin	N-His_{10}-SUMO3
pCoofy17-Talin2-Head-b1D-2ybbR-N-link	*E. coli*	Kanamycin	N-His_{10}-SUMO3
pCoofy17-Talin2-Head-b1D-2ybbR-F3-link	*E. coli*	Kanamycin	N-His_{10}-SUMO3

Table 4: List of primers used for the construction of expression vectors

Name	Sequence	Purpose
PaKa53_SLIC_ FAK_rev	5’- CCCCAGAACATCAGGTTAATGGCGTCAGTG TGGCCGTGTCTG -3’	Amplification of FAK from pCoofy18-mFAK
PaKa135_SLIC_ FAK_pCoofy55_fwd	5'- CTCATCGCGAACAGATTGGAGGAATGGCAG CTGCTTATCTTGACC -3’	Amplification of FAK from pCoofy18-mFAK
PaKa81_LP2_ ccdB_fwd	5’- CGCCATTAACCTGATGTTCTG -3’	Amplification of the pCoofy55 backbone
PaKa136_SLIC_ SUMOstar_rev	5'- TCCTCCAATCTGTTCGCGATGAG -3’	Amplification of the pCoofy55 backbone
PaKa137_EPLIN_ planB_fwd	5'- GGGATCCATGGAAAACTGTCTGGGAGATTCC -3’	Amplification of EPLIN from pET15b-EPLIN
PaKa138_EPLIN_ PlanB_rev	5’- CCCTCGAGTCATTCTTCATCCTCGTCCTC -3’	Amplification of EPLIN from pET15b-EPLIN

PaKa182_Insert_ TMCyto_pGEX_fwd	5'- CCTGGGATCCGGTGGCGGTAGCGGCGG TGGCAGCCATGACAGAAGGGAATTTGCTA -3’	MultiBAC cloning
PaKa183_Insert_ TMCyto_pGEX_rev	5'- CAGCCTCGAGCTCATTTTCCCTCATACTTC -3’	MultiBAC cloning
PaKa184_IPP_ Insect_PINCH_fwd	5’- CACCGTCGACGTGTTCCAGCAGCAG -3’	MultiBAC cloning
PaKa185_IPP_ Insect_PINCH_rev	5’- TCGGCGGCCGCTCATTTCTCGAACTGCGGGTGGC TCCAACCGCTGCCTTCCTTCCTAAGGTCTCAGATAG -3’	MultiBAC cloning
PaKa187_ ILK_pIDK_fwd	5’- CTGTTCTCGAGGCCCATGGACGACATTTTCAC -3’	MultiBAC cloning
PaKa188_ ILK_pIDK_rev	5’- TCAGGCTAGCGGCGTTACTTGTCCTGCATC -3’	MultiBAC cloning
PaKa189_Parva_ pIDK_fwd	5’- GTGCCCTCGAGCGCCCCCATGGGATCCC -3’	MultiBAC cloning
PaKa190_Parva_ pIDK_rev	5’- TGATGCTAGCGCTCTTATATTCCCCAGAAC ATCAG -3’	MultiBAC cloning
PaKa191_K2_ pIDK_fwd	5’- GCAGCTCGAGGGAATGGCTCTGGACGGG -3’	MultiBAC cloning
PaKa192_K2_ pIDK_rev	5’- CAGGGCTAGCGCGTCACACCCAACCACTG -3’	MultiBAC cloning
PaKa193_PAX_ pIDC_fwd	5’- GTTCAGGCCTCCCATGGACGACCTCGATG -3’	MultiBAC cloning
PaKa194_PAX_ pIDC_rev	5’- TCAGTCTAGAGGCGTTAGCAGAAGAGCTTC -3’	MultiBAC cloning
PaKa195_pIDK_ EPLIN_fwd	5’- GTTCCTCGAGCAGACCGGTGGATCCATG -3’	MultiBAC cloning
PaKa196_pIDK_ EPLIN_rev	5’- GGTGGCTAGCTGCGAGTCATTCTTCATCCTCG -3’	MultiBAC cloning
PaKa197_pIDK_ RSU_fwd	5’- GGAGGCTAGCGACGAGGACACCATCGAC -3’	MultiBAC cloning
PaKa198_pIDK_ RSU_rev	5’- AGCTATGCATCCCCAGAACATCAGGTTAATGG -3’	MultiBAC cloning
PaKa199_pIDC_ Talin_fwd	5’- CAGCAGCGCTCCGGTGGAATGGTTGCGC -3’	MultiBAC cloning
PaKa200_pIDC_ Talin_rev	5’- TGGTTCTAGACGAGTGCGGCCGCTCAGC -3’	MultiBAC cloning
PaKa201_pIDC_ FAK_fwd	5’- GTTCGGATCCCCCATGGCAGCTGCTTATC -3’	MultiBAC cloning
PaKa202_pIDC_ FAK_rev	5’- GGTTTCTAGAGTCAGTGTGGCCGTGTCTG -3’	MultiBAC cloning
PaKa203_pIDK_ IntBeta_fwd	5’- GGAACTCGAGTTCATGTCCCCTATAC -3’	MultiBAC cloning
PaKa204_pIDK_ IntBeta_rev	5‘- TGCGCCATGGCGAGCTCATTTTCCCTCATAC -3’	MultiBAC cloning
PaKa242_Mut_ LIM5_fwd	5’- CTGTTTGGTGATGTTTGATTCCATTGCAACCGTG -3‘	Deletion of PINCH-LIM5
PaKa243_Mut_ LIM5_rev	5’- CACGGTTGCAATGGAATCAAACATCACCAAAC AG -3‘	Deletion of PINCH-LIM5
PaKa231_SLIC_ linker1_Talinforce_fwd	5’- GCTAGCGGTGGTGGTAGTGCCGGTG -3‘	Amplification of longer linker sequence for talin-integrin fusions
PaKa232_SLIC_ linker1_Talinforce_rev	5’- GCTACCTCCGCCAGATCC -3‘	Amplification of longer linker sequence for talin-integrin fusions
PaKa233_SLIC_ Talin2_247_fwd	5’- GGTGGTGGATCTGGCGGAGGTAGCTGTGG CCATGATCGTCGCG -3‘	Amplification talin2-integrin fusion backbone
PaKa234_SLIC_ Talin2_247_rev	5’- CACCGGCACTACCACCACCGCTAGCGCTTT GTTTCTTCTTAAGGATG -3‘	Amplification talin2-integrin fusion backbone
PaKa235_SLIC_ Talin1_239_rev	5’- CACCGGCACTACCACCACCGCTAGCGCTTT TTTTCTTCTTAAGGATG -3‘	Amplification talin1-integrin fusion backbone
PaKa236_Insert_ ybbR_N_AgeI_fwd	5’- CCGGTGGAGACTCTCTGGAATTCATCGCTT CTAAACTGG -3‘	Cloning of talin-intergin fusion construct
PaKa237_Insert_ ybbR_N_AgeI_rev	5’- CCGGCCAGTTTAGAAGCGATGAATTCCAGA GAGTCTCCA -3‘	Cloning of talin-intergin fusion construct

PaKa238_Insert_ ybbR_tail_MscI_fwd	5‘- CGACTCTCTGGAATTCATCGCTTCTAAACTG GCTGG -3‘	Cloning of talin-intergin fusion construct
PaKa239_Insert_ ybbR_tail_MscI_rev	5‘- CCAGCCAGTTTAGAAGCGATGAATTCCAGAG AGTCG -3‘	Cloning of talin-intergin fusion construct
PaKa240_SLIC_Talin_ ybbR_fwd	5’- GGTGGTGGATCTGGCGGAGGTAGCGACTCTC TGGAATTCATCGC -3‘	Cloning of talin-intergin fusion construct

2.1.12 Software

Bruker Compass DataAnalysis 4.2	Bruker
Dynamics 7	Wyatt Technology
Inkscape 0.92	https://inkscape.org/en/
ChromLab 4.0	BioRad
MO-S001A MO.Affinity Analysis	Nanotemper
MO-S001C MO.Control	Nanotemper
PR-S01 PR.ThermControl	Nanotemper
ProtParam tool	http://web.expasy.org/protparam/
Serial Cloner 2-6-1	SerialBasics
Spectra Manager II	Jasco
UCSF Chimera 1.10.2	http://www.cgl.ucsf.edu/chimera/

2.2 Methods

2.2.1 Molecular Biology Methods

2.2.1.1 Generation of chemically competent *E. coli* cells (OmniMax™, Rosetta™, pirHC)

50 ml of LB medium were inoculated with an overnight culture of *E. coli* cells at a ratio of 1:100 (v/v) and incubated at 37 °C while shaking, until an $OD_{600\ nm}$ of 0.5 was reached. Then, the culture was centrifuged (4,000 x g, 4 °C, 10 min) and the pellet was resuspended in 40 ml 0.1 M $MgCl_2$ solution. After another centrifugation step, the pellet was resuspended in 20 ml 50 mM $CaCl_2$ solution and incubated on ice for 30 min. After centrifugation, the cells were resuspended in 2 ml 50 mM $CaCl_2$, 15 % (v/v) glycerol and 100 µl aliquots were flash-frozen in liquid nitrogen. All reagents were passed through a 0.22 µm sterile filter prior to use.

2.2.1.2 Transformation of chemically competent *E. coli* cells

Either 1 µl of purified plasmid DNA or 10 µl of a ligation, SLIC, or mutagenesis reaction were added to one 100 µl aliquot of competent cells. After 25 min incubation on ice, the cells were subjected to a 45 sec "heat shock" at 42 °C, then cooled down again on ice. 500 µl of LB medium were added and the bacteria were incubated for 45 min at 37 °C and 650 rpm shaking in a heat block. Afterwards, the cells were pelleted (3 min, 4000 x g), resuspended in 50 µl LB and plated on LB-agar plates with the desired antibiotics for selection. The plates were incubated over night at 37 °C.

2.2.1.3 Analytical and preparative agarose gel electrophoresis

1 % (w/v) agarose in 150 ml TAE buffer was heated in a microwave, until the agarose had been completely dissolved. The homogeneous solution was cooled down to 50-60 °C under running tap water, then mixed with 15 µl ethidium bromide and cast into a casting platform with a comb for either narrow or broad pockets (10 µl vs. 30 µl sample volume). After cooling down, the solid gel was placed in a running chamber filled with TAE buffer and loaded with the DNA samples. Prior to application on the gel, the DNA was mixed with 6x DNA sample buffer. The gel run was conducted at 150 V for approximately 1 h and the bands visualized on a UV light transilluminator at 366 nm.

When a preparative gel electrophoresis was conducted, the desired bands were cut out of the gel using a scalpel and extracted from the agarose using a QIAquick PCR purification kit, according to the manual. This method is based on the immobilization of the desired DNA fragments on an ion exchange column, removal of unbound contaminants and elution of the purified DNA.

2.2.1.4 Preparation of plasmid DNA from bacterial cultures

For small-scale preparation of plasmid DNA from 5 ml culture volume, the QIAprep Spin Miniprep kit was used. It combines alkaline lysis of the bacteria cells with ion exchange chromatography on spin columns, where only the DNA is bound. Contaminating proteins or RNA pass through the column, the DNA is washed and eluted in buffer of alkaline pH.

For transient transfection of HEK293 cells, high amounts of plasmid DNA are necessary. Therefore, DNA was extracted from 500 ml cultures using the NucleoBond Xtra Midi Plus kit. The underlying purification principle is the same as for the Miniprep kit.

2.2.1.5 Restriction digest of dsDNA

For the insertion of DNA fragments into expression vectors, PCR products or vector DNA were digested with restriction endonucleases. These enzymes recognize specific DNA sequences and cut both strands, creating either blunt or cohesive ends, which can then be specifically joined with the desired complementary fragment. For a preparative digest, 2-3 µg of DNA were mixed with 10-20 units of restriction enzyme (or enzymes) and 10x reaction buffer (as recommended by the supplier). The samples were the incubated at the optimal reaction temperature (usually 37 °C) for 1-2 h and the desired fragments separated by agarose gel electrophoresis. These fragments were the extracted, purified and used for ligation. For analytical digests, 300-500 ng of DNA were digested with 5 units of restriction enzyme(s).

2.2.1.6 Polymerase chain reaction (PCR)

For amplifying DNA fragments while optionally manipulating the flanking regions (inserting restriction sites, creating homologous regions for SLIC cloning etc.), PCRs were conducted.

PCR reaction (50 µl):

50 ng	Template-DNA	
5 µl	Pfu Ultra II reaction buffer	(10x)
1 µl	Pfu Ultra II DNA Polymerase	(2.5 U/µl)
1 µl	Primer fwd	(10 µM)
1 µl	Primer rev	(10 µM)
1 µl	dNTPs	(10 mM)
x µl	ddH_2O	

Program thermo-cycler:

95 °C	2 min	
95 °C	20 s	⎫
50-55 °C	20 s	⎬ 30 x
72 °C	20 s per 1 kb	⎭
72 °C	3 min	
4 °C	hold	

The PCR reactions were analyzed by agarose gel electrophoresis and the desired bands were cut out and purified.

2.2.1.7 Site-directed mutagenesis using QuikChange mutagenesis

In order to introduce point mutations or to delete gene fragments, mutagenesis PCR was used. For this reaction, primers were designed with the desired mutation in the middle of the oligonucleotide, flanked by 15-20 bp complementary sequences on both sides.

PCR reaction (50 µl):

70 ng	Template-DNA	
5 µl	Pfu Ultra II reaction buffer	(10x)
1 µl	Pfu Ultra II DNA Polymerase	(2.5 U/µl)
1 µl	Primer fwd	(10 µM)
1 µl	Primer rev	(10 µM)
1 µl	dNTPs	(10 mM)
x µl	ddH_2O	

Program thermo-cycler:

95 °C	2 min	
95 °C	20 s	⎫
50-55 °C	20 s	⎬ 18 x
72 °C	60 s per 1 kb	⎭
72 °C	10 min	
4 °C	Hold	

The PCR reaction was digested with *Dpn*I for 1 h at 37 °C. This enzyme cleaves only the methylated template DNA, but not the newly synthesized, mutated DNA strands, reducing the number of negative clones in the following transformation and selection process. 10 µl of the digested PCR reaction were added to one aliquot of chemically competent OmniMax cells.

2.2.1.8 DNA sequencing

In order to confirm the successful generation of the desired expression constructs and to check for unwanted point mutations, the plasmid DNA was sequenced using one or more specific sequencing primers. The sequencing reaction and evaluation was carried out by the Microchemistry Core Facility of the MPI for Biochemistry or by Eurofins Genomics. The sequences were aligned using the Serial Cloner software.

2.2.1.9 DNA ligation

DNA fragments were joined using Fast-Link DNA ligase. 100 ng of vector backbone DNA were mixed with a three-fold excess of insert DNA, calculated by formula (1).

$$m_{insert}\,[ng] = 3 * m_{backbone}\,[ng] * \frac{Length\ insert\ [bp]}{Length\ backbone\ [bp]} \quad \textbf{(1)}$$

After addition of 2 µl 10x reaction buffer, 1 µl ATP (10 mM), 1 µl Fast-Link Ligase (2 U) and ddH_2O to a final volume of 20 µl, the sample was incubated at RT for 20 min. 10 µl of the ligation reaction were added to 1 aliquot of chemically competent cells.

2.2.1.10 SLIC (Sequence- and ligation-independent cloning) (Li and Elledge, 2012)

For insertion of DNA fragments into expression vectors with no suitable restriction sites at the desired location, SLIC cloning was used. The underlying principle of this method is the generation of identical sequences at the ends of two DNA fragments, followed by a homologous recombination event, which fuses the two fragments into one vector. The identical sequences that mediate the homologous recombination reaction have to be between 15-25 bp long.

The desired DNA fragments or vector backbones were amplified by a PCR reaction using primers with the identical sequences at the termini. The bands of the correct sizes were excised from agarose gels, and then the SLIC reaction was carried out.

100 ng	Backbone DNA
x µl	Insert DNA (calculated using formula (1))
1 µl	RecA buffer (10X)
1 µl	RecA
y µl	ddH_2O (fill up to 10 µl)

The reaction was incubated for 30 min at 37 °C and then the 10 µl were added to one aliquot of competent OmniMax cells.

2.2.1.11 De-phosphorylation of DNA

In order to reduce re-ligation of vector backbones, the DNA was de-phosphorylated using calf intestinal alkaline phosphatase (CIP).

30 µl	Vector DNA (after gel extraction)
4 µl	CutSmart buffer (10X)
1 µl	CIP (10 U)
5 µl	ddH_2O
40 µl	

After 30 min incubation at 37 °C, the DNA was used for ligation.

2.2.1.12 T4-DNA polymerase fill-in reaction

For ligation of DNA fragments with non-compatible ends, i.e. blunt ends and 5'- overhangs, a fill-in reaction with T4-DNA polymerase was carried out. This enzyme recognizes 5'- overhangs and synthesizes the recessed strand in 5' -> 3' direction to form double stranded DNA with blunt ends.

50 µl	digested sample (5'- overhang)
1 µl	NEB Buffer (CutSmart or 3.1)
2.4 µl	dNTPs (10 mM)
1 µl	T4 DNA Polymerase (3U)
5.6 µl	dH_2O
60 µl	

The reaction was incubated for 20 min at 12 °C, followed by a heat inactivation step at 75 °C for 20 min. The remaining enzyme and excess dNTPs were removed using a PCR purification kit according to manufacturer's protocol.

2.2.1.13 Vector fusion using Cre recombinase

The enzyme Cre recombinase recognizes *loxP* sites in dsDNA and mediates site-specific recombination between two of these elements. Therefore, two vectors containing one single *loxP* site each can be fused into one large vector by Cre-mediated recombination. This method can be used for the fusion of up to four vectors simultaneously.

1.5 µg	Vector A
1.5 µg	Vector B
(1.5 µg	Vector C) optional
(1.5 µg	Vector D) optional
2 µl	Cre recombinase Buffer
1.5 µl	Cre recombinase (1.5 U)
20 µl	

The reaction mix was incubated at 37 °C for 1 h and then used for the transformation of 200 µl OmniMax cells. Clones carrying vector fusions were selected using a combination of the antibiotic resistance markers on the vectors used.

2.2.2 Cell biology methods

2.2.2.1 Adherent cell culture

Adherent HEK293T cells were maintained in DMEM, supplemented with 10 % (v/v) FBS and 1 % (v/v) Penicillin/Streptomycin in a humidified atmosphere at 37 °C and 5 % CO_2. For passaging, the cells were washed once with PBS, then incubated for 5 min at 37 °C with trypsinization solution (1x Trypsin/EDTA solution in PBS). The cells were detached by tapping on the culture flask, mixed with 3 parts culture medium, centrifuged at 300 x g, 5 min, 20 °C and resuspended in culture medium. The desired amount of cells was transferred to a new culture vessel and supplemented with culture medium.

2.2.2.2 Transient transfection of adherent HEK293T cells

Cells were cultured to ~90 % confluence. 3 h prior to transfection (Tom et al., 2008a), the medium was changed to DMEM + 1 % FBS. For every 1 cm^2 of growth area, 0.3 µg vector DNA was mixed with 17 µl PBS and 0.4 µl PEI solution (1 mg/ml), resulting in a DNA : PEI ratio of 1.5 : 2. After 15 min incubation at RT, the transfection mixture was distributed dropwise across the growth area and the cells incubated for up to 7 days at 37 °C. Recombinant protein production was monitored by SDS-PAGE or western blotting after 3, 5 and 7 days.

2.2.2.3 Suspension culture of cells

Protein production in suspension cells was carried out by Judith Scholz from the Microchemistry Core facility of the Max-Planck Institute for Biochemistry.

For large-scale protein production, suspension-adapted HEK293E-EBNA1 (Durocher et al., 2002) cells were used. These cells stably express the Epstein-Barr virus nuclear antigen 1 (EBNA1), which amplifies episomal DNA containing an Epstein-Barr virus origin of replication. Plasmid DNA is thus retained throughout the production phase, increasing the yield of recombinant proteins.

The HEK293E cells were cultivated in serum-free Freestyle medium, supplemented with 1 % (v/v) Pluronic and 50 µg/ml G-418, in shaker flasks at 37 °C, 5 % CO_2 and 110 rpm. Cell number and vitality was determined using a Vi-CELL XR analyzer. For maintenance and expansion, the cells were grown to a density of 1.5 * 10^6 cells/ml and diluted with fresh medium to a density of 2-2.5 * 10^5 cells/ml.

2.2.3 Recombinant protein production

2.2.3.1 Transient transfection of HEK293E cells in suspension

For recombinant protein production, HEK293E cells were grown to a density of 1.0 * 10^6 cells/ml and then transiently transfected using PEI MAX (Tom et al., 2008b). 1 µg vector DNA per ml culture volume was mixed with PBS (1/10 to 1/100 of the culture volume) and 2 µg PEI MAX per ml culture volume, yielding a DNA : PEI ratio of 1 : 2. After 15 min at RT, the transfection mix was added drop-wise to the HEK293E cells. Recombinant protein production was maintained for 72 h post transfection and then the cells were harvested (200 x g, 5 min). The pellet was flash-frozen in liquid nitrogen and stored at -80 °C until protein purification was performed.

2.2.3.2 Recombinant protein production in High Five insect cells

Multi-protein complexes were produced in High Five insect cells using the *Multi*BAC^{Turbo} expression system (Bieniossek et al., 2012). Chemically competent *E.coli* DH10EmBacY cells were transformed with a single pACEBAC1 vector containing expression cassettes for all desired proteins. The transformation was carried out as usual, with an extended incubation phase at 37 °C after the heat-shock (over night instead of 45 min). The bacteria were then plated on an LB agar plate containing kanamycin (50 µg/ml), gentamycin (7 µg/ml), tetracyclin (10 µg/ml), BluoGal (100 µg/ml) and IPTG (40 µg/ml). If the vector DNA has been inserted correctly into the mini-attTn7 site via T7 transposition, the LacZ gene in the baculoviral DNA is disrupted and BluoGal is no longer degraded to the blue product. Colonies containing the desired Bacmids thus remain white after 48 h incubation at 37 °C and are selected for Bacmid preparation.

Two positive colonies were used for a 2 ml pre-culture and incubated at 37 °C and 250 rpm until cells started growing. 50 – 200 ml medium were then inoculated in a ratio of 1:100 with the pre-culture and incubated at 37 °C, 250 rpm for up to 24 h. The cells were harvested by centrifugation (2800 x g, 15 min) and the Bacmid DNA was isolated using the Nucleobond BAC100 kit according to manufacturer's protocol.

For production of sufficient amounts of baculovirus for liter-scale production of recombinant protein complexes, Sf9 insect cells were transfected with Bacmid DNA. For 1 ml culture volume, 1 µg Bacmid DNA was mixed with 100 µl PBS and 2 µg PEI MAX and vortexed 3 x 3 s.

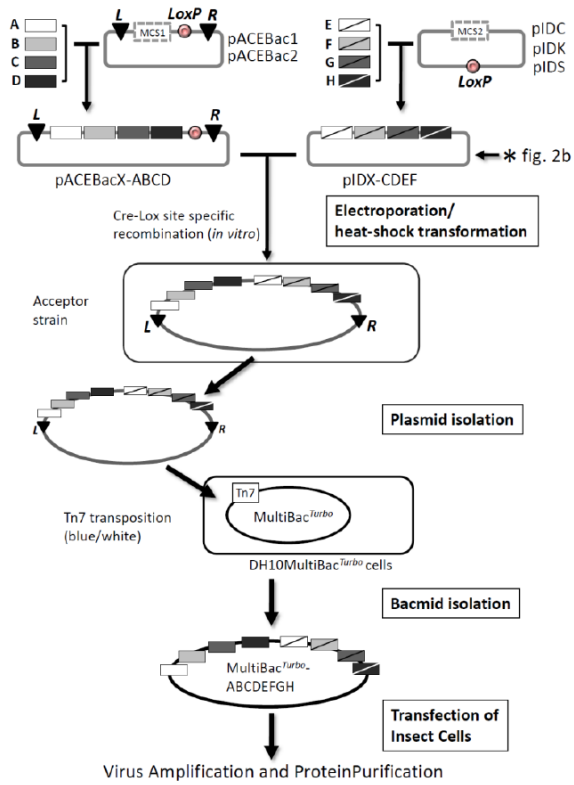

Figure 13: Workflow for the expression of multi-protein complexes in insect cells using the *Multi*BAC^{Turbo} system. All expression cassettes for the individual proteins are combined into one large acceptor vector, which is then transformed into DH10EmBacY cells. After Tn7 transposition, the expression cassettes are integrated into a baculovirus shuttle vector (Bacmid), which can be isolated from the bacteria and used for transfection of insect cells. These cells will then start producing baculovirus, which is used for large-scale infection of insect cells and recombinant protein production. Image from (Berger, 2012)

The cell density was adjusted to 0.8 * 10^6 cells/ml and the transfection mixture was added dropwise to the culture. After 5 d at 26 °C and 150 rpm, cell vitality and shape was assessed using a ViCell counter and microscopical fluorescence control. In case of successful transfection, the cells are larger than the non-transfected control and show green fluorescence signal in more than 90 % of the cells, due to a GFP reporter gene on the EmBacY Bacmid DNA. Successfully transfected cultures were harvested by centrifugation (2800 x g, 15 min), the supernatant was cleared by sterile filtration (0.22 µm) and used either directly for recombinant protein production or for further virus amplification.

In order to generate larger amounts of baculovirus particles, the supernatant generated by transfection was used for infection of a larger culture of SF9 cells. For this purpose, cell density was adjusted to 0.5 * 10^6 cells/ml and transfection supernatant was added in dilutions ranging from 1:1000 to 1:5000, depending on the transfection efficience (determined in small-scale cultures beforehand). 48 h post infection, the cell number had doubled approximately and the cells had grown in size, indicating virus production. The culture was then diluted to 1 * 10^6 cells/ml, incubated at 26 °C for 48 h and then the supernatant was harvested as before.

For large-scale protein production, High Five insect cells were adjusted to a density of 1 * 10^6 cells/ml and infected with supernatant from either transfection or P1 amplification. Again, the optimal virus titer for infection, as well as its influence on the production of the desired recombinant proteins was determined using small-scale production and then

expanded to 1-5 l cultures. When the transfection supernatant was used, 10 ml of supernatant were added to 1 l culture volume. 72 h post-transfection, cells were harvested (2800 x g, 15 min). The pellet was flash frozen in liquid N_2 and stored at -80 °C until protein purification was performed.

2.2.3.3 Recombinant protein production in *E. coli* Rosetta BL21 (DE3)

One day prior to recombinant protein production, expression vectors were transformed into chemically competent *E. coli* Rosetta BL21 (DE3). Positive clones were selected on LB agar plates containing the vector's selection marker as well as chloramphenicol (34 µg/ml), to retain the Rosetta cells' pRARE plasmid. For production, 1.5 l LB medium containing the respective selection antibiotics were inoculated with all the colonies on the LB agar plate. For this purpose, the plate was covered with 2 ml LB medium and the colonies were harvested using a cell scraper. This rather unusual inoculation method was chosen especially for pCoofy-vectors since in overnight cultures, a high percentage of cells were dead or dying and took 4-5 hours after inoculation to recover and start dividing. Cultures inoculated with the colonies on the agar plate recovered much more quickly and yielded higher amounts of protein.

Cells were grown at 37 °C to an $OD_{550\ nm}$ of 0.6, then cooled down to 18 °C for overnight production or to 12 °C for 72 h production. For LIM-domain proteins like PINCH or paxillin, $ZnCl_2$ was added to a final concentration of 0.466 mM. Gene expression was then induced by addition of IPTG to a final concentration of 0.2 mM. Cells were harvested the following day or after 72 h by centrifugation (5000 x g, 10 min) and resuspended in 30 ml Buffer A1. The cells were flash-frozen in liquid N_2 and stored at -80 °C until protein purification.

2.2.4 Recombinant protein purification

All buffers, ddH_2O and 20 % ethanol used for purification were prepared freshly (maximum one week prior to purification) and passed through a 0.22 µm bottle-top filter to remove particles or microorganisms. Buffers used on the FPLC system were additionally degassed by stirring them under vacuum for 1-2 h. The detergents were added after filtration and degassing to avoid foaming. TCEP was added freshly on the day of usage. All purification steps were carried out at 4 °C on the FPLC system or on ice for batch purification to avoid temperature-dependent protein degradation or aggregation.

2.2.4.1 Cell disruption and preparation of lysates for purification

The *E. coli* cell pellets were thawed slowly in a water bath at RT and supplemented with 1 mM TCEP, 1 mM PMSF (optional) and 1 µl per 1 ml pellet volume Benzonase. After addition of 10 µl Lysozyme (10 mg/ml) per 1 ml pellet volume, cells were incubated for 10 min on ice and then sonicated using 1 s pulses for 10 min at 50 % amplitude. After 10 min incubation on ice, the cell debris was removed by centrifugation (58,000 x g, 20 min, 4 °C) and the supernatant was cleared by passing through a 0.45 µm membrane filter.

HEK293 cell pellets were thawed slowly on ice, then resuspended in 5-6 ml Buffer C1 per 1 ml pellet volume and supplemented with 1 mM TCEP, 1 mM PMSF. After addition of 1 µl Benzonase per 1 ml cell suspension, cells were disrupted using a Dounce tissue grinder. The grinder was immersed in ice to prevent warming up the suspension through friction heat. Cells were homogenized by slowly moving the piston up and down 20 times. After 10 min incubation on ice to allow the Benzonase to cleave cellular DNA, cell debris was removed by centrifugation (58,000 x g, 20 min, 4 °C) and the supernatant was cleared by passing through a 0.45 µm membrane filter.

High five insect cells were disrupted analogously to HEK293 cells, with the exception that the pellet was resuspended in 10 ml Buffer B1 and 4 µl Benzonase per 1 ml cell suspension was added. In order to reduce plasma membrane contamination of the samples, 0.1 % (v/v) Tween-20 was added to the lysis buffer.

2.2.4.2 Immobilized metal ion affinity chromatography (IMAC)

Recombinant proteins with a hexa-histidine (His_6) fusion tag were purified by immobilization on an agarose matrix functionalized with nitrilotriacetic acid (NTA) groups. NTA is a potent chelating agent, which coordinates metal ions such as Ni^{2+} and creates a surface that binds poly-histidine stretches in proteins with high affinity. Elution of the target protein is achieved by addition of excess imidazole, which competes with the His-residues for the binding sites on the Ni-NTA resin. The recombinant proteins were purified using either HisTrap HP columns on the FPLC system or Ni-NTA beads for batch purification.

Ni-NTA column purification

Prior to sample application, the column was washed with 5 column volumes (CV) of ddH_2O, followed by 3 CV of elution buffer (500 mM imidazole) to remove potential contaminants. The column was then equilibrated with 3 CV running buffer (0 mM Imidazole). The cleared cell lysates were loaded using a sample pump, passing the sample over the column 2-3 times. The elution was performed in steps of 3-6 CV of increasing imidazole concentration. Typically, the steps used were 0 mM, 20 mM, 50 mM, 100 mM, 250 mM and 500 mM imidazole. The elution profile was adapted for each protein to achieve highest purity. Fractions of 0.5 – 14 ml were collected during the elution phase, depending on column size and expected behavior ("wash" fractions vs. target protein elution fractions). The chromatography was monitored using a multi-wavelength detector at 215 nm (peptide bond), 260 nm (DNA), 280 nm (protein) and optionally 650 nm (647-labeled proteins). The protein composition of the peak fractions was determined using SDS-PAGE and the fractions containing the target protein were pooled and concentrated for following purification steps. After completion of the protein purification, the column was washed again with 5 CV ddH_2O, followed by 2-3 CV 20 % ethanol. The column was stored under 20 % ethanol at 4 °C and re-used until a decrease in purification performance was observed.

Ni-NTA batch purification

For batch purification, an appropriate amount of Ni-NTA beads was used, depending on the expected protein amount produced. (1 ml of Ni Sepharose High Performance beads can immobilize 40 mg protein under optimal conditions). The beads are delivered as "slurry", meaning a suspension in storage solution. This slurry is composed of ~ 50 % (Qiagen) or ~ 80 % (GE) beads, which has to be taken into consideration when estimating the amount of beads needed. The slurry was centrifuged at 600 x g, 2 min, 4 °C to sediment the beads, then the supernatant was removed and discarded. The beads were then equilibrated by adding 5-10 bead volumes of the respective buffer used for purification and then centrifuged again, followed by removal of the supernatant. This step was carried out twice, then the cell lysate was applied on the beads at 4 °C on a rotating wheel for 2 h or over night. The suspension was then centrifuged and the supernatant removed. The beads were washed afterwards with ≥10 bead volumes of buffer containing increasing concentrations of imidazole (0, 20, 50, 100, 250,

500 mM) and the supernatants analyzed by SDS-PAGE. At the expected elution volumes (250 and 500 mM in most cases), the suspension was incubated for 10 min on ice before centrifugation. The fractions containing the target protein were pooled and concentrated for further use.

Affinity tag removal and "reverse" Ni-NTA chromatography

All recombinant proteins were produced with removable affinity tags. For the removal of poly-histidine tags, the fusion protein was cleaved with the appropriate protease, which carried a poly-histidine tag itself. Proteins with His_{10}-SUMO3 tag were treated with 1 U His_6-SenP2 protease per 100 µg recombinant protein and incubated at 4 °C over night. For the production in HEK293E cells a modified (non-cleavable by the mammalian SUMO-protease) His_{10}-SUMOstar tag and His_6-SUMOstar protease (1U per 100 µg protein, 4 °C, over night) were employed. For tags flanked by TEV or PreScission sites, His_6-TEV protease (1 U per 3 µg protein, 4 °C, over night) and His_6-PreScission protease (1 U per 100 µg protein, 4 °C, over night) were used. After cleaving was completed, the samples were incubated on Ni-NTA beads equilibrated with the respective buffer (see batch purification) for 1-2 h at 4 °C on a rotating wheel to immobilize the affinity tag as well as the protease, leaving the tagless recombinant protein in the supernatant. The beads were centrifuged (600 x g, 2 min, 4 °C) and the supernatant was removed carefully for further use. If the samples were obtained from Ni-NTA purification, they still contained high amounts of imidazole, which had to be removed to enable binding to the beads. For this purpose, the sample was concentrated using a centrifugal concentrator, diluted 5- to 10-fold to reach an imidazole concentration of 50-70 mM and concentrated again if SEC was performed afterwards.

2.2.4.3 Cation exchange chromatography (CIEX)

The underlying principle of ion exchange chromatography is the interaction of charged protein side chains with column material carrying opposite charges. For CIEX, the target protein is transferred into a buffer with low salt concentration and a pH value that is at least 1 unit below the theoretical pI of the protein. The theoretical pI can be calculated using the ProtParam tool on the ExPASy website. Since most adhesome proteins do not tolerate dialysis, the buffer exchange was achieved by concentrating the target protein and then diluting it 15 – 20 x with CIEX running buffer,. Elution of the target protein is achieved by increasing the NaCl

concentration of the buffer, since free ions interact with the column material and “shield” it from the charged protein side chains.

For the purification, the column was washed with 5 CV of ddH_2O, followed by 5 CV of elution buffer containing 1 M NaCl to remove potential contaminants. The column was then equilibrated with 3 CV of running buffer and the sample was loaded passing it 3 x over the column using a sample pump. Elution was performed using a stepwise increase of the NaCl concentration, from 0 mM to 1 M. The chromatography was monitored using a multi-wavelength detector and the protein-containing fractions were analyzed by SDS-PAGE. The fractions containing the target protein were pooled and concentrated. After purification, the column was washed with 5 CV ddH_2O and 3 CV 20 % Ethanol for storage.

2.2.4.4 Size exclusion chromatography (SEC)

Size exclusion chromatography separates proteins by their hydrodynamic volumes. Small, globular proteins can easily enter the porous column material and are held back for some time, whereas large particles pass through the column much more quickly. Therefore, aggregates elute first, followed by large proteins or protein complexes and finally small proteins.

Preparative size exclusion chromatography was used as a final “polishing” step in protein purification to remove aggregates and small contaminants and to achieve buffer exchange. Analytical size exclusion chromatography was performed to test for protein-protein interactions or protein complex formation. Columns with a bed volume of 24 ml were used for analytical SEC, while preparative SEC was performed on a 120 ml Superdex200 HiLoad column. The columns were washed with 1.2 CV ddH_2O and equilibrated with 1.2 CV of running buffer.

Table 4: Overview of SEC columns and properties

Column	Bed volume	Separation range	Flowrate
HiLoad 16/600 Superdex200 pg	120 ml	10 - 600 kDa	1 ml/min
SEC70	24 ml	0.5 - 70 kDa	0.7 ml/min
SEC650	24 ml	0.5 - 650 kDa	0.7 ml/min

Samples were concentrated to a final volume of 250 µl for analytical SEC and 3 ml for preparative SEC and passed through a 0.22 µm centrifugal filter prior to application on the columns. The samples were injected into sample loops with 500 µl or 5 ml capacity. For sample application, the loops were emptied with 2 x loop volumes and the chromatography was performed by passing 1.2 CV of running buffer over the column at flow rates of 0.7 (analytical SEC) or 1.0 ml/min (preparative SEC). The fractions containing protein were analyzed by SDS-PAGE and the desired fractions (not the aggregate peak) were pooled and concentrated. The columns were washed with 1.2 CV of ddH_2O and 1.2 CV of 20 % ethanol for storage.

In order to calculate the hydrodynamic volumes of proteins from their retention time on the column, calibration runs using a protein standard were performed. Using the molecular weights and the peak elution volumes of the proteins in the standard, a calibration curve is generated (formula (2)).

$$k_{av} = \frac{(v_e - v_0)}{(v_t - v_0)} \qquad \textbf{(2)}$$

k_{av}: specific partition coefficient of a protein
v_e: elution volume
v_0: dead volume of the column
v_t: bed volume

2.2.4.5 SDS-polyacrylamide gel electrophoresis (SDS-PAGE)

For analytical separation of a protein mixture, SDS-PAGE was performed. The protein sample was denatured by mixing with reducing sample buffer containing sodium dodecyl sulfate (SDS) and applied on a gel. The denatured proteins bind negatively charged SDS molecules, which mask charges in the amino acid side chains, leading to a separation by molecular weight alone. Depending on the size of the protein of interest, gels containing different percentages of acrylamide were used. A higher percentage of acrylamide yields a more densely crosslinked gel, through which proteins need longer to pass leading to a better resolution in the lower molecular weight range and vice versa. The gels used for discontinuous gel electrophoresis consisted of a weakly crosslinked 4 % stacking gel on top of a 10 or 12 % separating gel. Proteins pass quickly through the stacking gel and are concentrated at the top of the separating gel, in which the actual separation according to molecular weight is achieved.

The vertical gel electrophoresis was performed in mini-gel format using the Mini-Protean Tetra cell system. Protein marker and denatured protein samples were applied into the gel pockets and a constant voltage of 100 V in the beginning and 300 V after a few minutes was applied. Electrophoresis was performed until the blue loading dye running front had almost reached the lower end of the gel.

For most samples containing ample amounts of protein, Coomassie staining was used to visualize protein bands. The gels were covered with 0.1 % (w/v) Coomassie staining solution, boiled for 30 s in a microwave at 800 W and incubated at RT on a rocking platform for 20 – 25 min. For destaining, the gels were covered with destaining solution I, boiled shortly in a microwave and incubated for 10 min on a rocking platform. After analogous treatment with destaining solution II and 30 min incubation, gels were covered with deionized H_2O and scanned.

2.2.4.6 Silver staining of SDS gels

For visualization of protein bands in samples of low protein concentration (down to low nanogram levels) a more sensitive staining method was necessary. Silver staining is based on the principle that silver ions bind to proteins and can be reduced under certain conditions to form a visible image of the protein bands. The gels were covered in Fixing solution and incubated at RT for 10 min on a rocking platform (like all following steps), then washed 2x for 5 min with deionized H_2O. Afterwards, the gels were incubated in $Na_2S_2O_3$ solution for 1 min, then washed 2x for 20 s with deionized H_2O. The freshly prepared, cold silver nitrate solution was added then and incubated for 10 min in the dark. After rinsing the gel shortly with deionized H_2O and a small volume of developing solution, the rest of the developing solution was added and the gels were incubated under constant shaking until brownish bands started appearing. As soon as the desired grade of staining was reached, the stop solution was poured onto the gel and mixed briefly. The stained gels were then imaged using a scanner.

2.2.4.7 Tricine SDS-PAGE (Haider et al., 2012)

In order to better resolve proteins in the low molecular weight range (≤ 20 kDa), 16 % tricine gels were used, according to the protocol by Haider *et al.* The discontinuous polyacrylamide gels are cast analogously to the “classical” SDS gels, with the exception that the gels do not contain any SDS. The running buffer used for these gels contains SDS as well as tricine as a

carrier molecule, instead of glycine. Electrophoresis and Coomassie staining were performed analogously to the classical gels.

2.2.4.8 Trichloroacetic acid (TCA) precipitation of proteins

Samples containing low amounts of protein can be concentrated prior to SDS-PAGE by precipitating the proteins with trichloroacetic acid (TCA). This method can also be applied for samples containing high amounts of detergents or other molecules which interfere with gel electrophoresis. The proteins are precipitated by addition of TCA to a final concentration of 20 % (w/v) and 10 min incubation on ice. After centrifugation (5 min, 21,000 x g, 4 °C), the supernatant was removed and the pellet washed twice with 1 ml cold acetone and centrifuged again. After the second washing step, the pellet was dried in a heating block at 50 °C until the remaining acetone had evaporated. The pellet was then resuspended in a small volume of 1x sample buffer and applied onto an SDS or tricine gel.

2.2.4.9 Detection of proteins by Western Blot

The detection of proteins immobilized on a membrane by specific mono- or polyclonal antibodies is referred to as Western Blotting. This method is suitable for the identification of a certain target protein in purified samples as well as cell lysates at much higher sensitivity than Coomassie or silver staining.

Proteins were first separated via SDS-PAGE and then transferred onto a PVDF membrane by electroblotting. The stacking gel was removed and the separating gel was placed onto a slightly larger slip of PVDF membrane, which was activated in 100 % methanol for 5 min prior to assembly. The membrane itself rested on 4 sheets of Whatman paper soaked in transfer buffer and another 4 sheets were placed on top of the SDS gel. Great care was taken at each assembly step to remove any air bubbles trapped between the layers and to properly soak every component in transfer buffer. The assembly was then inserted into the blotting chamber filled with transfer buffer and cooled by an ice block. The transfer was performed at 300 V for 1.5 h. Afterwards, the membrane was incubated for 1 h in blocking buffer containing 4 % (w/v) non-fat dry milk to saturate unspecific binding sites. The membrane was then rinsed with PBS-T and incubated with the primary antibody (usually 1:1000 dilution in PBS with 5 % (w/v) BSA) over night at 4 °C and shaking. The primary antibody was removed and could be re-used for a few weeks. The membrane was washed 3-4 times in PBS-T for 5 min and the secondary

antibody, coupled to horseradish peroxidase (HRP), was added in 1:3000 dilution in PBS-T for 1 h at RT. The membrane was washed again 3-4x in PBS-T and then imaged using a chemiluminescence-based detection kit.

2.2.4.10 Determination of protein concentration

The concentration of a purified protein sample was determined by measuring the absorbance at 280 nm (A_{280}) using a NanoDrop spectrophotometer. By applying the Lambert-Beer law (formula 3), the protein concentration was calculated from the A_{280} value and the protein's molar extinction coefficient ε_{prot}. The latter was determined using the ProtParam tool on the ExPASy website.

$$A_{280} = \varepsilon_{prot} * c * d \qquad \textbf{(3)}$$

A_{280} : absorbance at 280 nm
ε_{prot} : molar extinction coefficient of the protein, [$M^{-1}cm^{-1}$]
c: protein concentration, [mol/l]
d: path length, 1 cm for NanoDrop

From the protein concentration, the total amount of protein in a certain sample volume could be determined using formula 4.

$$m = c * M * V \qquad \textbf{(4)}$$

m: protein amount [g]
M: molar weight of the protein [g/mol]
V: volume of the sample [l]

For proteins labeled with fluorescent dyes, the degree of labeling (DOL) was determined by measuring the absorbance at 280 nm and at the emission maximum of the respective dye. A DOL of 1 corresponds to 100 % labeling of the protein, or a theoretical one dye molecule on each protein molecule. For the DOL calculation, formula 5 was used.

$$DOL = \frac{A_{max} * \varepsilon_{prot}}{(A_{280} - A_{max} * CF_{280}) * \varepsilon_{max}} \qquad \textbf{(5)}$$

A_{max} : absorbance at absorption maximum of dye
ε_{prot} : molar extinction coefficient of the protein, [$M^{-1}cm^{-1}$]
A_{280} : absorbance at 280 nm
CF_{280} : correction factor of the dye
ε_{max} : molar extinction coefficient at absorption maximum of dye, [$M^{-1}cm^{-1}$]

Table 5: Molar extinction coefficients and molecular weights of the proteins and dyes used in this study

Protein/dye	MW (g/mol)	ε [$M^{-1}cm^{-1}$]	CF_{280} (dyes only)
α_5 TMCyto	14,073.2	8,480	
β_1 TMCyto wt	16,304.0	13,980	
β_1 TMCyto NPIA	16,211.9	12,490	
β_1 TMCyto NPKA TT/AA	16,151.8	12,490	
β_1D TMCyto DTQ/V	16,527.3	13,980	
EPLIN	66,134.8	69,900	
FAK	119,242.9	133,620	
ILK	51,313.1	70,930	
kindlin 2	77,800.0	124,790	
His_6- α-parvin	46,058.7	21,430	
paxillin	60,811.0	47,330	
PINCH	37,240.3	32,890	
PINCH-strep	38,481.6	36,900	
PINCH dLIM5	28,707.0	24,410	
RSU-1	31,461.1	15,930	
THD	46,891.0	42,860	
IPP complex	135,877.5	129,260	
Alexa-488 NHS	643.4	73,000	0.11
Alexa-647 Maleimide	1250	265,000	0.03
Alexa-647 NHS	1250	270,000	0.03
Atto-565 NHS	708	120,000	0.12
NT-647	unknown	250,000	unknown

2.2.4.11 Concentrating of protein samples using centrifugal concentrators

Centrifugal concentrator units are simple and efficient tools for reducing the volume of a protein sample and thereby increasing its concentration. Depending on the volume of the sample, concentrators with capacities of 0.5, 4 or 15 ml were used. Concentrators with molecular weight cut-off (MWCO) of 10,000 or 30,000 Da were selected according to the sizes of the proteins to be concentrated. The concentrators were equilibrated with buffer prior to

use and centrifuged at 4000 x g, 10 min, 4 °C (4 and 15 ml) or 9500 x g, 5 min, 4 °C (0.5 ml). The flow-through and remaining concentrate were discarded and the protein sample was added and centrifuged. After each round of centrifugation, the concentrate was pipetted up and down several times to keep it homogeneous and to check for the formation of aggregates. This procedure was repeated until the desired final volume of the sample was achieved or the protein started to aggregate. The concentrate was then flushed a few times over the membrane to remove residual bound protein and removed by pipetting.

2.2.4.12 Chemical labeling of proteins with fluorescent dyes

Proteins were labeled using either thiol-reactive maleimide-conjugated dyes for attachment of fluorophores to cysteine residues, or amine-reactive NHS-ester conjugates for labeling of primary amine groups, predominantly in lysine side chains. 1 mg of fluorescent dye was dissolved in 200 µl water-free DMSO and stored in 10 µl aliquots at -20 °C.

Prior to labeling, the proteins were transferred into a buffer suitable for the intended labeling reaction using desalting columns. For maleimide dyes, all types of buffer (Tris, HEPES, MES, phosphate) can be used, as long as the pH value is between 7.0 and 7.5. In order to ensure that the cysteines to be labeled were in their reduced form, TCEP was added to a final concentration of 2 mM prior to the labeling reaction. Then, the thiol reactive dye was added in 10-20x molar excess, and the reaction carried out at RT for 2 h in the dark. For amino-reactive dyes, the protein was first transferred to NHS labeling buffer (PBS, 10 mM $NaHCO_3$, pH 9.0) and then mixed with 2.5x molar excess of dye. The labeling reaction was carried out for 1 h at 4 °C in the dark.

For removal of excess dye, the samples were either passed through desalting columns or, if carrying a His-tag, bound to Ni-NTA beads, washed with buffer until the supernatant was colorless and then eluted with 500 mM imidazole.

2.2.4.13 Buffer exchange using desalting columns

DextraSEC PRO2 desalting columns were used for buffer exchange at low sample volumes or for removal of free dye after labeling reactions. The columns were equilibrated by letting first the storage fluid and then 5 ml of the desired buffer pass through the column by gravity flow. Then, 200 µl sample were applied to the column, followed by 200 µl buffer. Elution was performed with 350 µl buffer. For removal of unbound dye, separation of two fluorescent

species could be seen on the column. The eluate was collected before the second species reached the bottom of the column and residual eluate was discarded. For applications, which are highly sensitive to perfectly matched buffers, the samples were passed through a column a second time.

2.2.5 Biophysical methods

2.2.5.1 Dynamic light scattering (DLS)

DLS is used for characterization of protein solutions with respect to particle size and polydispersity. By measuring fluctuations in the intensity of scattered laser light, the translational diffusion coefficients of the particles in solution can be determined. Using the diffusion coefficient, the hydrodynamic radius of a particle can be calculated, provided that the sample is monodisperse, i.e. it contains only one species of molecules. This makes DLS a suitable method for detecting and monitoring protein aggregation and thus allows for quality control of protein preparations.

Before conducting a DLS measurement, the sample was centrifuged for 5 min at 21,000 x g and 4 °C to remove dust particles and very large aggregates, which could interfere with the measurement. The DLS instrument was cooled to 4 °C before starting a measurement to avoid temperature-dependent aggregation of the proteins. 6 µl of buffer were pipetted into a disposable DLS cuvette and placed into the sample holder. If the cuvette was not clean or if the buffer contained large particles, a decay curve was visible and the count rate exceeded a value of 80,000. In this case, the cuvette was cleaned thoroughly with ddH_2O and dried with compressed air and the buffer filtered. If the buffer sample was clear, the actual protein sample was loaded into the cuvette and the DLS measurement carried out. The laser power was set to auto-attenuation, the temperature to 4 °C, the acquisition time to 5 s, the number of acquisitions to 15 and the measurement was carried out 3 times. The Dynamics software was used to calculate the hydrodynamic radius of the particles in the sample.

2.2.5.2 Circular dichroism (CD) spectroscopy

Circular dichroism spectroscopy is a valuable tool for rapid determination of protein secondary structures. When circularly polarized light at wavelengths in the far-UV (< 250 nm) spectrum

hits protein secondary structures, the left- and right-handed circularly polarized components of the light are absorbed to a different extent. Thus, the plane of the light wave is rotated, resulting in a shift of the circularly polarized light to an elliptically polarized form. CD is reported in degrees ellipticity at different wavelengths. Secondary structure elements of proteins render distinct CD traces. Proteins with predominantly α-helical structures display negative ellipticity at 222 nm and 208 nm and positive values at 193 nm. Proteins containing mostly antiparallel β-sheets render negative ellipticity at 218 nm and positive values at 195 nm. Disordered proteins display almost no ellipticity at wavelengths ≥ 210 nm and negative values around 195 nm. Since most proteins are composed of a mixture of these secondary structure elements, each protein renders a distinct CD spectrum in the near-UV range. This spectrum can be used to estimate the percentage of each structure element and to determine whether the protein is correctly folded or not. CD spectroscopy can also be used to monitor changes in the secondary structures of a protein, induced by conformational change when binding a ligand or by unfolding of the protein.

CD spectra were acquired using a quartz cuvette with 1 mm path length and a sample volume of 300 µl in a Jasco J-715 spectropolarimeter. Prior to the measurements, a buffer reference was prepared by mixing 30 µl of the protein buffer with 270 µl ddH_2O. Likewise, the sample (protein concentration ≥ 1 mg/ml) was diluted with ddH_2O. First, a CD spectrum of the buffer sample was acquired from 190 nm to 250 nm at 10 °C with 4 repetitions. Afterwards, the buffer was removed from the cuvette and the protein sample was added and measured using the same parameters. The buffer reference spectrum was later subtracted from the protein spectrum to eliminate effects caused by the buffer. The secondary structure estimation on the corrected spectrum was performed with the Spectra Manager II software.

Protein stability was determined by thermal denaturation. From the protein spectrum acquired as described above, the wavelength at which the spectrum displays the lowest ellipticity was selected (usually near 206 nm). At this wavelength, ellipticity was continuously measured while raising the temperature from 10 °C to 90 °C at a rate of 1 °C/min. When the protein unfolds, the secondary structures become disrupted and change the CD spectrum of the protein to a disordered curve. The ellipticity values were plotted against the temperature, rendering a transition temperature around which the protein unfolds. This transition

temperature is an indicator of protein stability and indicates the quality of the protein preparation.

After the measurements, the quartz cuvette was cleaned by incubation with chromosulfuric acid over night and rinsing with methanol, followed by drying with compressed air.

2.2.5.3 Interaction studies on recombinant proteins using pull-down assays on Ni-NTA beads

Pull-down assays on Ni-NTA beads were used as a first indication of proteins binding to each other or as a means to assemble multi-protein complexes for crosslinking studies. Ni-NTA beads were equilibrated with the buffer of the bait protein and then incubated with the His-tagged bait protein on a spinning wheel at 4 °C for 1-2 h or over night. The supernatant was removed and the beads were washed once with buffer. Then the prey protein or proteins were added at a higher amount than the bait protein in order to detect binding also at low affinities. The interaction partners were added to the beads and, if necessary, diluted with buffer to a volume that allows for an adequate suspension of the beads. The mixture was incubated on a rotating wheel at 4 °C for 1 h, then the supernatant was removed and the beads were washed twice with buffer containing 50 mM imidazole to remove non-specifically bound protein. If the beads were subsequently used for crosslinking, the second washing step was carried out with buffer without imidazole to avoid losing the amine-reactive crosslinker to imidazole. The protein complexes bound to the beads were then eluted with 500 mM imidazole and analyzed by SDS-PAGE or Western Blot. As a control to check for non-specific interaction of the prey proteins with the Ni-NTA beads, “empty” beads were incubated with the same amounts of prey proteins as the sample and treated in the same way.

2.2.5.4 Chemical crosslinking of focal adhesion complexes and analysis by LC-MS

Complexes of recombinant focal adhesion proteins were assembled on Ni-NTA beads, crosslinked, enzymatically digested and analyzed by LC-MS/MS to identify protein surfaces, which had been close to each other in the complex. In one approach, the complexes were assembled on beads and eluted with 500 mM imidazole. Afterwards, the sample was passed through a desalting column to reduce the imidazole concentration far enough to not impede the crosslinking reaction. A titration series with increasing concentrations of an equimolar mixture of isotopically light (d0) and heavy (d12) labeled BS3 crosslinker was conducted on

small volumes of the sample in order to find the optimal concentration. The concentration of the eluate was determined via NanoDrop and aliquots of 5 µl were mixed with 2.5x, 2x, 1x, 0.5x, 0.4x or 0.2x molar amount of BS3. An aliquot of BS3 powder was dissolved directly before crosslinking in 35 µl ddH_2O and diluted to the desired concentrations with buffer. As a control, one aliquot was mixed with buffer instead of BS3. The samples were crosslinked on ice for 1 h and then analyzed by SDS-PAGE. The optimal amount of BS3 was selected, where the protein bands started disappearing but were still visible, while larger species at the upper part of the gel started to form.

In another approach, the complexes were not eluted but instead directly crosslinked while still bound to the beads. The pelleted beads were mixed with approximately their volume of buffer to obtain a 1:1 slurry. A titration series following the same principle as described above was conducted on 5 µl aliquots (corresponding to 2.5 µl beads) to determine optimal crosslinker concentration. 1 µl of BS3 dilution was added to the sample and the crosslinking reaction carried out at 35 °C and 1200 rpm for 30 min in a heating block. For SDS-PAGE, 5 µl sample buffer were added to the beads, incubated at 95 °C for 5 min and the entire sample was applied on a gel.

In both approaches, the optimal crosslinker concentration was selected and scaled-up to 170 µl eluate or 100 µl bead-slurry and the crosslinking reaction was carried out analogously to the test samples using a freshly dissolved BS3 aliquot. The crosslinking reaction was quenched by addition of 1 M ammonium bicarbonate solution to a final concentration of 100 mM. After 10 min incubation at 35 °C, 2 sample volumes of 8 M urea (340/200 µl) and 50 mM TCEP to a final concentration of 5 mM were added and incubated at 35 °C and 800 rpm for 30 min. Afterwards, 100 mM iodoacetamide solution was added to a final concentration of 10 mM and incubated at RT in the dark for 35 min. The proteins were digested by adding LysC protease in a ratio of 50:1 ($m_{proteins} : m_{LysC}$) and incubating at 35 °C and 1300 rpm for 2 h. Afterwards, 14 sample volumes (2380/1400 µl) of a 50 mM ammonium bicarbonate solution was added, as well as Trypsin at the same amount as LysC before. The samples were incubated at 35 °C and 1300 rpm over night and then mixed with 100 % acetonitrile to a final concentration of 3 % and 10 % trifluoroacetic acid to a final concentration of 1 %.

The samples were then subjected to peptide clean-up using Sep-Pak columns. After activation with 1 ml 100 % acetonitrile and washing with 2x 1 ml 2 % acetonitrile, 0.2 % formic acid, the sample was loaded onto the column. The flow-through was collected and re-applied to the column to increase binding. Afterwards, the column was washed twice with 2 % acetonitrile, 0.2 % formic acid, letting it run dry after the second wash. The sample was eluted twice with 400 µl 60 % acetonitrile, 0.2 % formic acid and lyophilized using a Speed-vac for storage at -20 °C. For mass-spectrometric analysis, the sample was dissolved in 20 µl 25 % acetonitrile, 0.1 % trifluoroacetic acid while shaking for 20 min at 35 °C and maximum rpm. Crosslinked peptides were enriched on a Superdex Peptide PC 3.2/30 column and the fractions analyzed by LC-MS on an LTQ Orbitrap Elite instrument. The analysis was carried out using the xQuest software.

2.2.5.5 Assembly of Nanodiscs by dialysis

Nanodiscs consist of lipid bilayers encircled by membrane scaffold proteins (MSPs) and have a disc-like shape and a uniform diameter that depends on the MSP variant used. Once assembled, these discs are stable and homogeneous, can be diluted or concentrated and are used for applications such as electron microscopy. During assembly, transmembrane proteins can be added to the mixture and thus be incorporated into the disc, allowing for reconstitution of the membrane protein in a plasma membrane-like environment and removal of the detergent necessary for solubilization.

TMcyto-α5 wt, -β1 wt or -β1 mutant constructs were produced intracellularly in *E. coli,* leading to the formation of inclusion bodies due to the hydrophobic transmembrane domain. The cells were disrupted, the supernatant containing the soluble proteins was discarded and the pellet was washed once in buffer D1, followed by centrifugation (58,000 x g, 20 min, 4 °C). The pellet was resuspended in buffer D2, which contained 3 % (v/v) EMPIGEN BB detergent for solubilization of the TMcyto constructs from the inclusion bodies. The sample was incubated over night on a rotating wheel at 4 °C. Afterwards, the solution should have become more transparent, indicating successful solubilization. If this was not the case, more buffer D2 was added and the EMPIGEN concentration increased to 4 % (v/v), followed by another 1-2 h incubation. The sample was centrifuged again and the supernatant was passed through a 0.45 µm sterile filter and purified by IMAC and CIEX chromatography. If the sample was intended

for single-molecule microscopy, the TMcyto constructs were fluorescently labeled with maleimide-coupled dyes, immobilized on Ni-NTA beads and eluted, maintaining the EMPIGEN concentration at 1.5 % (v/v) to avoid precipitation.

As scaffold proteins, MSP1E3D1 and MSP2N2 were used producing discs with 13 and 17 nm diameter, respectively. Both MSP proteins carry His_6 tags, which are cleavable by TEV protease. If empty Nanodiscs were used for microscopy, the scaffold protein was labeled with amine-reactive dyes prior to Nanodisc assembly.

The lipids used were DMPC, a mixture of DMPC and PIP_2 (9:1 molar ratio) or DMPC with 10 % PIP_3. The lipid powder was dissolved in 100 % chloroform (DMPC, POPC) or a 20:9:1 mixture of chloroform:methanol:H_2O and (PIP_2, PIP_3) to a final concentration of 50 mg/ml. The desired volume of lipid solutions was then transferred to a clean glass tube using a Hamilton glass syringe and dried under N_2-stream. The tube was then incubated in a vacuum desiccator over night and the lipids were solubilized in cholate buffer, rendering a 50 mM lipid stock solution.

For Nanodisc assembly, the TMcyto protein, the scaffold protein and the lipids were mixed in the correct molar ratio to obtain theoretically one TMcyto tail in one Nanodisc. The mixing ratios depended on the type of MSP used. For smaller, MSP1E3D1 discs, a ratio of 1 (TMcyto) : 2 (MSP1E3D1) : 150 (lipid) was used, due to the fact that 2 molecules of MSP1E3D1 form one disc encircling 150 lipid molecules. For larger MSP2N2 discs, a ratio of 1 (TMcyto) : 1 (MSP2N2) : 330 (lipid) was used. Before adding lipids to the mixture, cholate buffer was added to keep the final cholate concentration between 10 and 20 mM to avoid precipitation of the lipids. The samples were then dialyzed three times against 1 l of Nanodisc buffer in dialysis cups (MWCO 10,000), allowing the dialysis to reach equilibrium for 4 h or more per step. The samples were then passed through 0.22 µm centrifugal filters and applied on an analytical SEC650 column to separate assembled Nanodiscs from individual components. The fractions were then analyzed by SDS-PAGE and silver staining.

2.2.5.6 Analytical ultracentrifugation (AUC)

Analytical ultracentrifugation is a versatile method for determining shape, molecular mass and complex formation of proteins in solution. The sample is being centrifuged at up to 250,000 x g while simultaneously being monitored through an optical detection system using light absorbance at a specific wavelength. Using this set-up, the process of sedimentation of

the different components in the sample relative to the axis of rotation can be followed and plotted. From these intensity plots, the sedimentation coefficients and molecular masses of the different particle species can be obtained. These data give hints to protein complex formation, multimerization of proteins and of aggregation.

AUC measurements were performed using either unlabeled proteins and detection at 280 nm, allowing for the simultaneous monitoring of all components in the mixture, or labeling one protein with an amine-reactive fluorescent dye and detection at the absorbance maximum of the dye. The latter approach shows complex formation more clearly, since the sedimentation of only one protein is monitored and every peak appearing in addition to the monomer peak of the labeled protein indicates an interaction with one of the unlabeled components. For one measurement, up to 3 cells could be used simultaneously. Therefore, when using unlabeled proteins, the components expected to form a complex were each sedimented alone in two cells and mixed together in the third. This approach allows for the clear assignment of monomer peaks in the mixed sample and the detection of additional “new” peaks, which indicate complex formation of the two proteins. For measurements with unlabeled proteins, a sample volume of 300 µl was used, while for labeled samples, cells with 130 µl sample volume were used. For calculation of the sedimentation coefficients and the molecular weights, the viscosity of the buffer was determined before the measurement. The AUC runs were performed at 250000 x g for 18 h at 16 °C and the data evaluation was performed using the Sedterp software.

2.2.5.7 Determination of binding constants using microscale thermophoresis (MST)

Microscale thermophoresis (MST) is a method for monitoring and quantifying biomolecular interactions in solution by applying a temperature gradient. One of the interaction partners is labeled using a fluorescent dye (e.g. Alexa 488 or NT-647), making it traceable by exciting the sample with blue or red laser light. Inside thin glass capillaries containing constant amounts of the labeled interaction partner in a titration series of the unlabeled component, a microscopic temperature gradient spanning 2-6 °C is induced by an infrared (IR) laser. Application of the temperature gradient usually leads to a depletion of labeled molecules in this region, which can be quantified by the change in fluorescence intensity. The velocity of movement along the gradient is influenced by the size, charge and hydration shell of a protein.

These attributes usually change when an interaction partner is bound to the protein, altering the MST trace of the labeled molecule. Using the thermophoresis readouts from the titration series, an equilibrium binding constant for the interaction can be calculated.

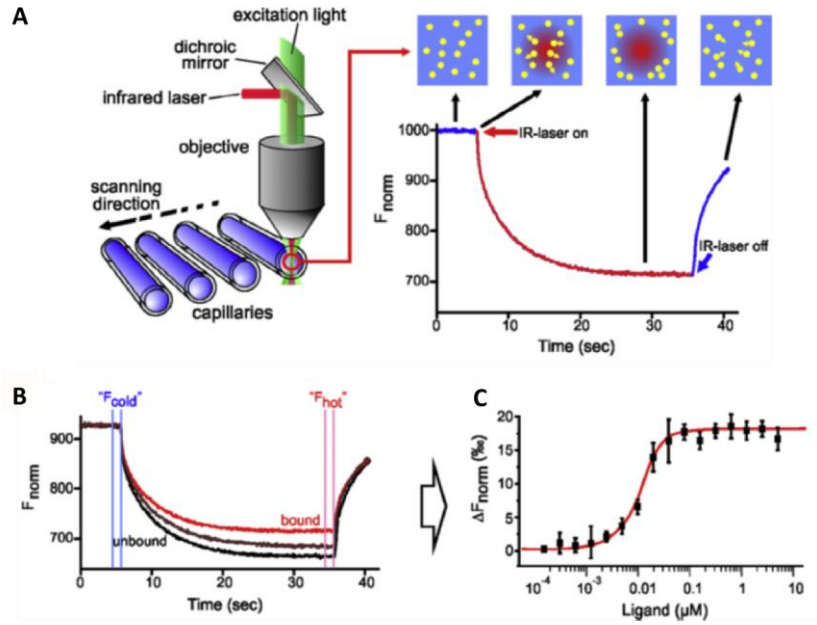

Figure 14: Schematic representation of MST principle (Jerabek-Willemsen et al., 2014)**.** (A) Fluorescently labeled molecules are excited and detected by the same objective in a temperature gradient induced by an infrared laser. At the beginning of the measurement, fluorescent molecules are evenly distributed, resulting in a constant initial fluorescence. When the infrared laser is switched on, a temperature gradient forms and leads to a "temperature jump" caused by a change of the properties of the fluorophore. During the following thermophoresis phase, labeled molecules move out of the heated area until an equilibrium is reached. After the laser is switched off, an "inverse temperature jump" occurs where the fluorescently labeled molecules diffuse back into the heated area. (B) The shape of the MST trace is dependent on the size, charge and hydration shell of the fluorescently labeled molecule and changes upon binding of an interaction partner. (C) Typically, a titration series of 16 different concentrations of the interaction partner is used to determine an equilibrium binding constant. For this purpose, the change in normalized fluorescence ($\Delta F_{norm} = F_{hot}/F_{cold}$) is plotted against the ligand concentration, yielding a binding curve, which can be fitted to obtain a binding constant.

For interaction studies on adhesome components using MST, capillaries with hydrophilic coating ("premium coated") were used to reduce non-specific interaction of the proteins with the glass surface. The interaction partner (ligand) and the fluorescently labeled protein were transferred into the same buffer to avoid artifacts derived from non-matching buffers. The ligand was concentrated to ~10x the expected K_D of the interaction, or as highly as possible and centrifuged at 21,000 x g and 4 °C for 5 min to remove large aggregates.

The interaction partner was labeled and loaded into capillaries in varying dilutions to test for the optimal concentration to be used in the actual experiment. The capillaries were scanned using standard settings (20 % LED power, red or blue laser, depending on the fluorophore) and a concentration was selected which yielded 800-900 fluorescence counts. Then the titration series of the ligand was performed by mixing 10 µl of the concentrated protein with 10 µl buffer, then 10 µl of the first dilution with another 10 µl buffer and so on. From the last dilution, 10 µl was removed and discarded, while the first tube contained 10 µl of undiluted

protein. Great care was taken to pipet exactly 10 µl in each step and low-binding pipet tips were used to reduce sample loss. Each dilution was then mixed with 10 µl fluorescent protein (or 2 µl, if very high ligand concentrations were desired) and loaded into capillaries. Then, a capillary scan was performed and the measurements carried out at 20 % LED power and once 20 % and once 40 % MST power. The binding curves were fitted using the NT Analysis software.

2.2.5.8 Determination of protein stability using differential scanning fluorimetry (Nano-DSF)

Differential scanning fluorimetry is a label-free method for determining thermal and chemical stability of a protein. The underlying principle of this method is the measurement of tryptophan and tyrosine fluorescence of a protein over a temperature gradient or in increasing concentrations of denaturing agents (e.g. urea or guanidinium chloride). When a protein unfolds due to temperature or denaturants, Trp and Tyr residues, which are normally hidden inside the hydrophobic core of the protein, become exposed to the solvent. This leads to a change in fluorescence intensity and emission wavelength, which is determined by measuring the fluorescence emission at 330 and 350 nm. By plotting the F_{350}/F_{330} ratio versus the temperature, protein denaturing curves are derived. Usually, the thermal unfolding process occurs over a narrow temperature range and the mid-point of the transition from folded to unfolded protein is referred to as the melting temperature, T_m. This value can be used as a measure for protein stability, the higher the T_m, the more stable the protein. Due to the measurement of 48 samples at the same time, Nano-DSF is used for buffer screening to determine optimal pH, salt and additives like detergents, which help stabilize the protein.

For conducting a Nano-DSF measurement, the purified protein was concentrated and centrifuged at 21,000 x g and 4 °C for 5 min. The minimal sample concentration should provide 500 nM Trp residues, but in order to ensure high enough signal strength, the protein concentration was adjusted so that at least 5 µM Trp concentration was reached. The protein was mixed in a 1:10 ratio with the 10x concentrated buffer solutions to be tested, in a final volume of 15 µl. The samples were then loaded into glass capillaries, making sure that the whole capillary was filled by tapping on it carefully in order to avoid unwanted effects caused by evaporation. Up to 48 capillaries were placed into the sample holder and fixated by a magnetic clamp. The excitation intensity was adjusted by performing capillary scans at

different laser intensities and choosing a value that gave sufficient fluorescence counts for all capillaries while not exceeding the detection maximum. The thermal unfolding was performed from 15 °C to 95 °C at a rate of 1 °C/min and optionally, a refolding curve from 95 °C to 15 °C at 1 °C/min was measured. The PR.ThermControl software was used to determine the T_m values for the different buffer conditions were determined using.

2.2.5.9 Preparation of complexes using rate-zonal centrifugation

For the preparation of large protein complexes, rate-zonal centrifugation using a sucrose gradient can be used, avoiding high pressures, which occur during column-based purifications. A density gradient of 5-20 % sucrose in buffer B2 at a total volume of 13 ml was mixed using a gradient station. 300 µl of sample was carefully layered as a narrow zone on top of the gradient and centrifuged at 260,000 x g at 4 °C for 16 h. Afterwards, the gradient was fractionated into 500 µl fractions using the gradient station, beginning at the top. The gradient provides a medium of increasing density and velocity, separating the particles in the sample by size and mass. The fractions were then analyzed by SDS-PAGE and Western Blot.

3 Results

3.1 Focal adhesion kinase (FAK)

3.1.1 Production and purification of recombinant FAK

The DNA sequence coding for full-length murine FAK was inserted into the pCoofy55 expression vector (obtained from the Microchemistry Core Facility), optimized for intracellular production in HEK293E cells. This vector contains a His_{10}-SUMOstar tag under the control of a CMV promoter and an EBV origin of replication for enhanced copy number and retention inside the cell. The coding sequence for FAK was amplified from the bacterial expression vector pCoofy18-mFAK (cloned by D. Moik, Fässler department) using the primers PaKa53 and PaKa135 (see Table 4) and inserted into the pCoofy55 backbone, amplified using primers PaKa81/136, by SLIC cloning. This allowed for the insertion of the FAK gene at the C-terminus of the SUMOstar sequence without any additional amino acids. The correct insertion and absence of unwanted mutations was verified by sequencing the entire coding sequence for His-SUMO-FAK on the vector pCoofy55-FAK.

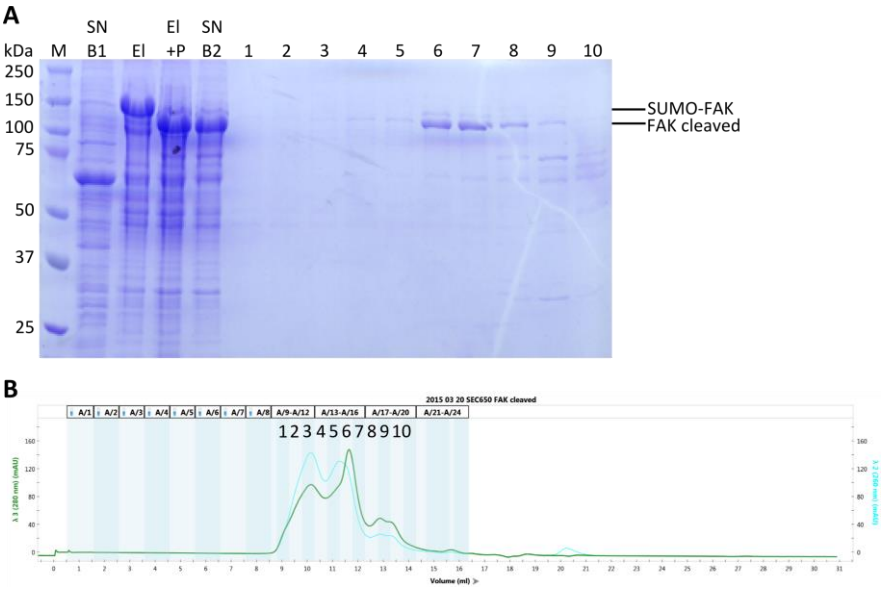

Figure 15: Test purification of His-SUMO-FAK from HEK293T cells. (A) Adherent cells from three T-175 flasks were homogenized in buffer (20 mM Tris, 200 mM NaCl, 1 mM TCEP, 1 mM PMSF, pH 7.5) and recombinant His-SUMO-FAK was enriched by Ni-NTA batch purification (SN B1: unbound protein, El: 500 mM imidazole eluate). The eluate was cleaved with SUMOstar protease and the protease and affinity tag were removed by reverse Ni-NTA chromatography (El+P: eluate after cleaving, SN B2: supernatant after removal of protease and tag). (B) Cleaved FAK was applied to a SEC650 gel filtration column fur further purification and removal of aggregates (lanes 1-10: fractions as indicated in chromatogram; buffer: 20 mM Tris, 200 mM NaCl, 1 mM TCEP, pH 7.5). The elution volume of the FAK-containing peak (6, 7) is 11.6 ml, corresponding to a molecular weight of 267 kDa.

Expression of the construct was first tested in small-scale production in adherent HEK293T cells and then expanded to liter-scale production in suspension - growing HEK293E cells. For first trials, His-SUMO-FAK

was produced by transient transfection of three T-175 flasks of HEK293T cells, which were harvested after 72 h. The protein was then subjected to Ni-NTA batch purification, followed by removing of the His-SUMO tag with SUMOstar protease and “reverse” Ni-NTA chromatography. The affinity tag was removed with ≥ 90 % efficiency, assessed by SDS-PAGE, where the FAK band was shifted from 132 kDa (His-SUMO-FAK) to 119 kDa (FAK cleaved). The cleaved protein was concentrated and applied to an SEC650 analytical gel-filtration column for further purification (Figure 15). The elution volume of FAK is 11.6 ml, which corresponds to a size of 267 kDa. This might indicate a dimeric state of FAK or be due to an elongated conformation of the molecule.

pH 5,5	pH 6,5	pH 7,5	pH 5,5	pH 6,5	pH 7,5	pH 5,5	pH 6,5	pH 7,5	pH 5,5	pH 6,5	pH 7,5
Succinat 50mM NaCl 0mM CaCl2 2mM	Bis-Tris 50mM NaCl 0mM CaCl2 2mM	Tris 50mM NaCl 0mM CaCl2 2mM	Succinat 50mM NaCl 0mM MgCl2 2mM	Bis-Tris 50mM NaCl 0mM MgCl2 2mM	Tris 50mM NaCl 0mM MgCl2 2mM	Succinat 50mM NaCl 0mM Glycerol 10%	Bis-Tris 50mM NaCl 0mM Glycerol 10%	Na-P 50mM NaCl 0mM Glycerol 10%	Succinat 50mM NaCl 0mM Glycin 5% Mannitol 5%	Bis-Tris 50mM NaCl 0mM Glycin 5% Mannitol 5%	Na-P 50mM NaCl 0mM Glycin 5% Mannitol 5%
Succinat 50mM NaCl 350mM CaCl2 2mM	Bis-Tris 50mM NaCl 350mM CaCl2 2mM	Tris 50mM NaCl 350mM CaCl2 2mM	Succinat 50mM NaCl 350mM MgCl2 2mM	Bis-Tris 50mM NaCl 350mM MgCl2 2mM	Tris 50mM NaCl 350mM MgCl2 2mM	Succinat 50mM NaCl 350mM Glycerol 10%	Bis-Tris 50mM NaCl 350mM Glycerol 10%	Na-P 50mM NaCl 350mM Glycerol 10%	Succinat 50mM NaCl 350mM Glycin 5% Mannitol 5%	Bis-Tris 50mM NaCl 350mM Glycin 5% Mannitol 5%	Na-P 50mM NaCl 350mM Glycin 5% Mannitol 5%
Succinat 50mM NaCl 0mM Trehalose 10%	Bis-Tris 50mM NaCl 0mM Trehalose 10%	Na-P 50mM NaCl 0mM Trehalose 10%	Succinat 50mM NaCl 0mM Taurin 0,2M	Bis-Tris 50mM NaCl 0mM Taurin 0,2M	Na-P 50mM NaCl 0mM Taurin 0,2M	Succinat 50mM NaCl 0mM TMAO 50mM	Bis-Tris 50mM NaCl 0mM TMAO 50mM	Na-P 50mM NaCl 0mM TMAO 50mM	Succinat 50mM NaCl 0mM Arginin 0,5M	Bis-Tris 50mM NaCl 0mM Arginin 0,5M	Na-P 50mM NaCl 0mM Arginin 0,5M
Succinat 50mM NaCl 350mM Trehalose 10%	Bis-Tris 50mM NaCl 350mM Trehalose 10%	Na-P 50mM NaCl 350mM Trehalose 10%	Succinat 50mM NaCl 350mM Taurin 0,2M	Bis-Tris 50mM NaCl 350mM Taurin 0,2M	Na-P 50mM NaCl 350mM Taurin 0,2M	Succinat 50mM NaCl 350mM TMAO 50mM	Bis-Tris 50mM NaCl 350mM TMAO 50mM	Na-P 50mM NaCl 350mM TMAO 50mM	Succinat 50mM NaCl 350mM Arginin 0,5M	Bis-Tris 50mM NaCl 350mM Arginin 0,5M	Na-P 50mM NaCl 350mM Arginin 0,5M

pH 5.5	pH 6.5	pH 7.5	pH 5.5	pH 6.5	pH 7.5	pH 5.5	pH 6.5	pH 7.5	pH 5.5	pH 6.5	pH 7.5
48.1°C	49.2°C	52.3°C	50.1°C	51.7°C	52.6°C	51.1°C	52.6°C		54.5°C	56.4°C	**59.1°C**
49.2°C	51.4°C	52.4°C	49.1°C	52.3°C	**51.8°C**		53.4°C	54.7°C	53.5°C	56.0°C	**58.0°C**
53.9°C	53.8°C	**58.6°C**	50.3°C	51.3°C	56.4°C	50.0°C		55.2°C	45.4°C	44.7°C	47.3°C
53.1°C	52.5°C	55.3°C	46.9°C	51.4°C	54.4°C	47.0°C	51.8°C	52.7°C	47.8°C		49.3°C

Figure 16: Buffer optimization of recombinant FAK produced in HEK293T cells using Nano-DSF. FAK was mixed with each buffer indicated in the upper matrix to a final concentration of 50 µg/ml and the transition temperatures during thermal unfolding were compared (lower table). The condition most similar to the buffer FAK was purified in is highlighted in blue, while the conditions with the highest transition temperatures are highlighted in red.

During purification problems concerning the stability of FAK became apparent. Concentrating the protein in centrifugal concentrators and also dialysis into low-salt buffer led to severe aggregation. Furthermore, considerable amounts of protein were lost on the SEC column, either in filters or on the column itself. The losses during SEC were independent of the column material used (S200, Superose-6, SEC650). In order to reduce these effects, the thermal unfolding of FAK was assessed using Nano-DSF and a buffer screen obtained from the Microchemistry Core Facility (Figure 16). FAK was diluted 10-fold with each of the 48 different buffers with varying pH, salt concentrations and additives to a final concentration of 50 µg/ml and the transition temperatures for the different conditions were compared. The best conditions showed a clear shift of the transition temperatures from 51.8 °C (Tris buffer, pH

7.5) to 58.0 °C and 59.1 °C (50 mM Na-Phosphate, 0/350 mM NaCl, 5 % Glycine, 5 % Mannitol, pH 7.5). Therefore, the high-salt variant of the buffer with 1 mM TCEP (C1/C2) was used for larger-scale purifications from HEK293E cells.

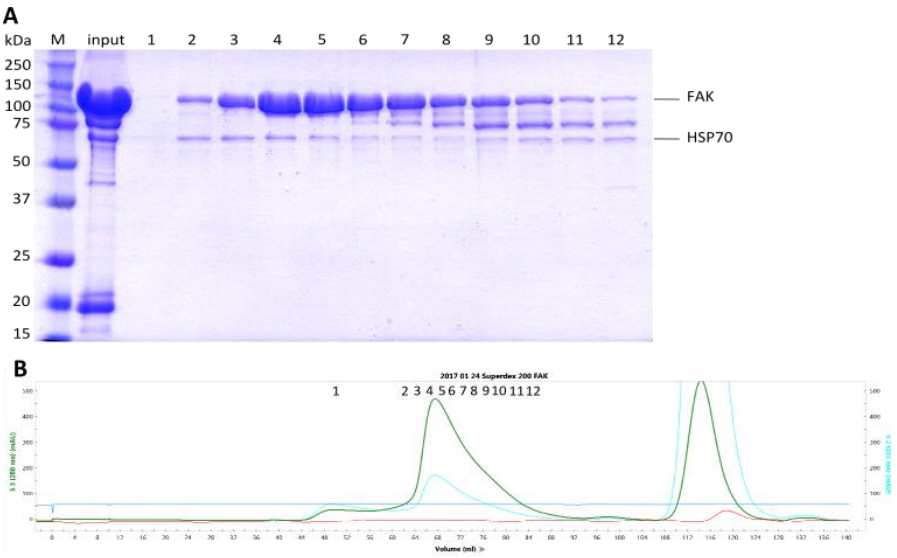

Figure 17: Large-scale purification of recombinant FAK produced in HEK293E cells. (A) After IMAC, FAK was applied to a preparative Superdex200 column for further purification and removal of aggregates and affinity tag (B, right peak). The fractions indicated in the chromatogram were visualized by SDS-PAGE, showing high purity of FAK and the presence of HSP70 protein. This chaperone appears to keep ~5 % of the recombinant FAK in solution and could not be removed by SEC.

Purification of His-SUMO-FAK from one liter of HEK293E suspension culture in buffers C1/2 typically yielded 10 mg of protein after Ni-NTA column purification and 2.5 mg cleaved FAK after SEC. This indicates that, although increasing the thermal stability of the protein, the buffer could not significantly reduce the high losses during SEC. Furthermore, SDS-PAGE shows the co-purification of a second protein of approximately 70 kDa (Figure 17), which was identified by LC-MS analysis as HSP70. The presence of this chaperone indicates that a part of the FAK molecules (~5 %) might not be correctly folded and kept in solution by HSP70. Nevertheless, yield and purity of FAK are satisfactory and sufficient for interaction studies and complex assembly.

3.1.2 Biophysical characterization of recombinant FAK

Purified recombinant FAK was analyzed by CD spectroscopy to ensure that the protein is folded and to determine the distribution of secondary structure elements. Figure 18 shows that FAK displays an estimated secondary structure composition of 55.5 % α-helical, 14.3 % β-sheet and 16.4 % unordered elements, as well as a clear transition temperature at 53.5 °C when thermally unfolded. This transition temperature of FAK purified on Tris buffer (Figure 18B) is in good accordance with the Nano-DSF measurements, where the protein was thermally half unfolded at 51.8 °C in Tris buffer. DLS measurements showed that FAK is monodisperse (23 %

PD) and that the particles measured have an average hydrodynamic radius of 5.4 nm, which corresponds to a globular protein of 174 kDa. Since this is slightly higher than the molecular weight of monomeric FAK (119 kDa) but still well below the weight of a dimer (238 kDa), the measurements might indicate a slightly elongated shape of the protein.

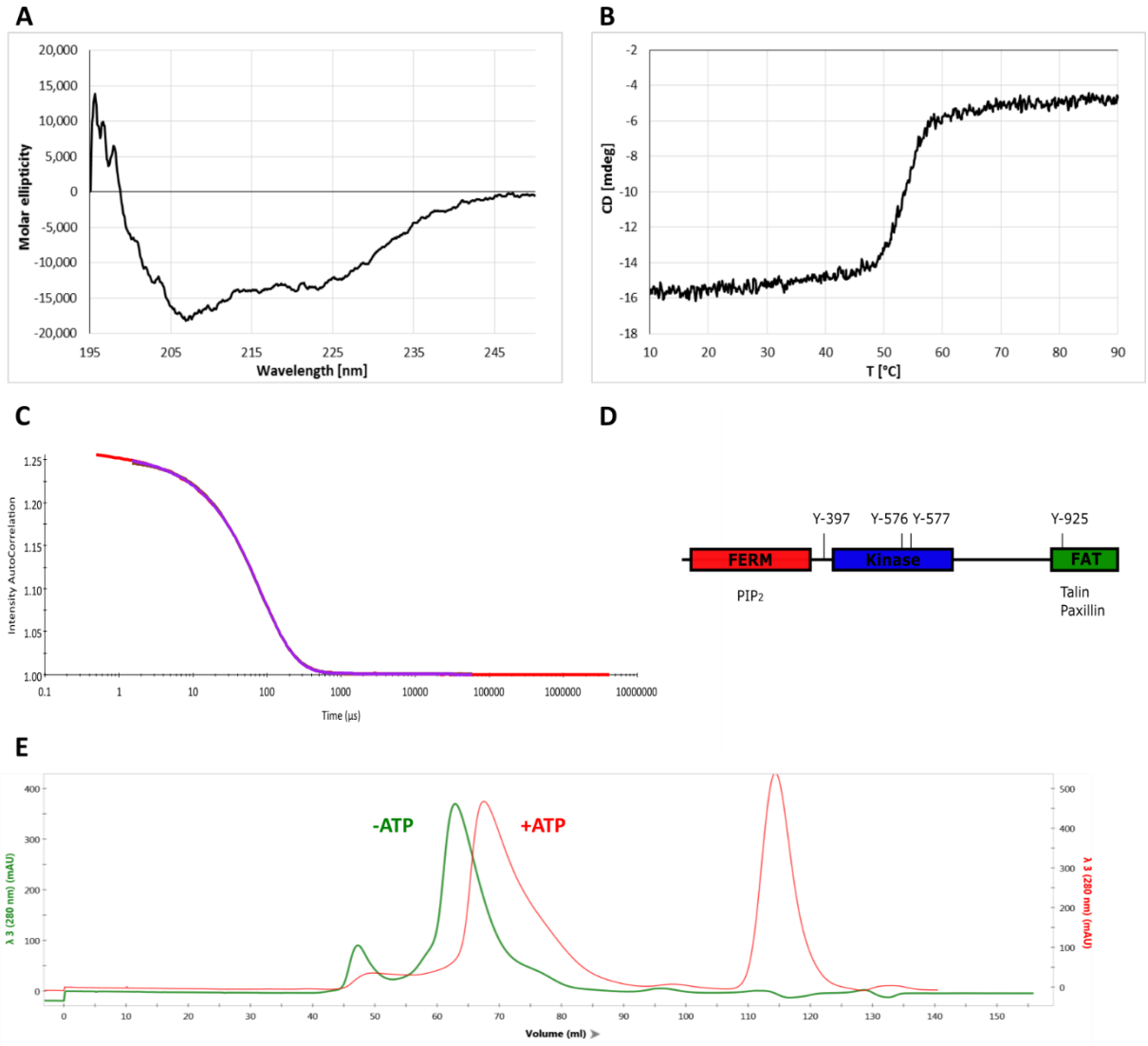

Figure 18: Biophysical characterization of recombinant FAK. (A) CD measurement revealed a secondary structure distribution of 55.5 % α-helical, 14.3 % β-sheet, 13.8 % turn and 16.4 % unordered, RMSD 0.303. (B) The transition temperature was determined by measuring CD at 207 nm over a temperature gradient from 10 to 90 °C. The melting temperature T_M is 51.8 °C. (C) DLS measurements showed a monodisperse protein at 5.4 nm hydrodynamic radius. (D) Recombinant FAK displays 1-3 phosphorylations at the positions Y-397, Y-576, Y-577 and Y-925. (E) Addition of 0.5 mM ATP to the recombinant protein before SEC shifts the elution volume, indicating a conformational change. The green trace represents FAK without addition of ATP and the red trace shows FAK in the presence of 0.5 mM ATP. The second peak in the red trace at 115 ml elution volume represents His-SUMO tag, which was absent in the other sample. Both SEC runs were carried out on a Superdex200 column in Buffer C1.

Analysis of the protein total mass revealed that each molecule carries 1, 2 or 3 phosphorylations, since peaks for the expected mass plus 80, 160 or 240 Da were detected.

Mapping of the phosphorylation sites within the protein (analysis by N. Nagaraj, MPIB Core facility) revealed that the most abundant modification was on Tyr-397, followed by Tyr-925, Tyr-576 and Tyr-577. Modification of Tyr-397 in the linker region between the FERM domain and the kinase domain is achieved by auto-phosphorylation while Tyr-576 and Tyr-577 are phosphorylated by Src kinase. All three modifications are necessary for FAK to adopt the catalytically fully active, elongated conformation. Therefore, the recombinantly produced FAK is expected to be (at least partially) catalytically active.

Upon addition of ATP to a final concentration of 0.5 mM to recombinant FAK for the SEC purification step, a clear shift in the peak elution volume was observed (Figure 18E). FAK without additional ATP eluted at 62.9 ml, corresponding to a globular protein of 292 kDa, while FAK incubated with 0.5 mM ATP eluted at 67.5 ml or 202 kDa. The second peak in the profile of FAK with 0.5 mM ATP corresponds to cleaved His-SUMO tag, which was not removed prior to SEC, while in the sample without ATP it was removed by reverse Ni-NTA chromatography. The shift in FAK elution volume might hint at a conformational change upon ATP binding or at a transition from a dimeric to a monomeric form, resulting in a more compact shape of the protein.

3.1.3 Interaction with paxillin and THD

FAK has been reported to directly interact with paxillin and talin via its C-terminal FAT domain. In order to determine whether this holds true with the recombinantly produced proteins, pull-down experiments were conducted as a first attempt (Figure 19). Either His-SUMO-paxillin (produced in *E. coli*) or His-SUMO-FAK were immobilized on Ni-NTA beads and incubated with tag-less THD or FAK.

A control with FAK and THD on empty beads served as an indicator of unspecific interactions. Immobilized paxillin binds tag-less FAK at much higher levels than the unspecific interaction of FAK with empty beads, confirming interaction and potentially indicating the ability of paxillin to bind more than one molecule of FAK. The stoichiometry of FAK-paxillin binding is the subject of ongoing investigations. Furthermore, THD appears to bind to immobilized FAK, but not at 1:1 stoichiometry, indicating a weaker affinity to FAK than paxillin. Immobilized paxillin does not bind THD and it seems that no ternary complex between FAK, paxillin and

THD is formed either, since paxillin is able to bind a high amount of FAK but still no THD in the presence of FAK. The affinities of FAK towards THD and paxillin have to be determined.

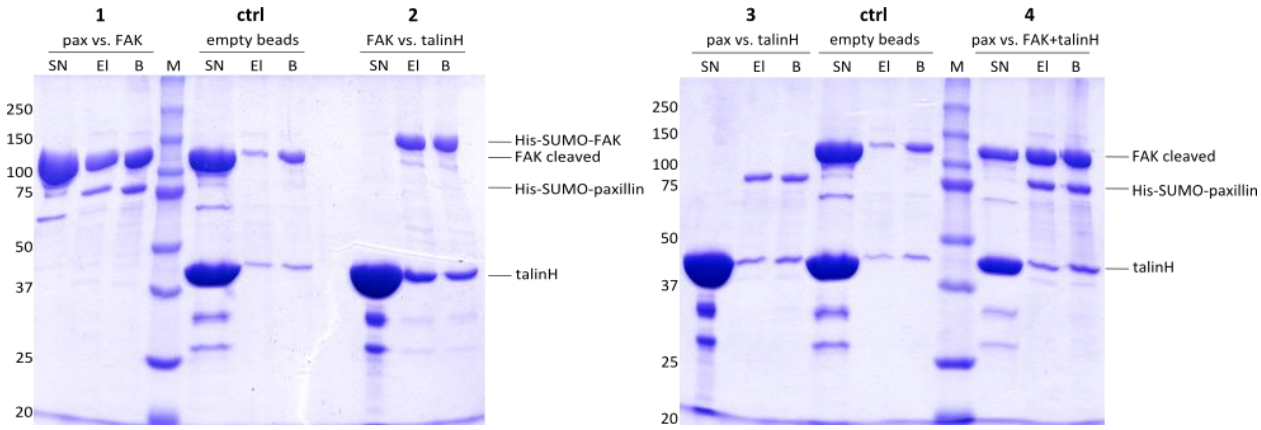

Figure 19: Ni-NTA pull-downs to determine interactions between FAK, paxillin and THD. His-SUMO-paxillin (samples 1, 3 and 4) or His-SUMO-FAK (sample 2) were immobilized on Ni-NTA beads and incubated with tag-less FAK or THD. As a control, empty beads were incubated with the tag-less proteins. The beads were washed twice with 50 mM imidazole-containing buffer to reduce unspecific binding and eluted with 500 mM imidazole. Sample 1 shows interaction of FAK with paxillin, which is more than 1:1 stoichiometry, while sample 2 indicates a sub-stoichiometric interaction with THD. Paxillin does not bind THD directly, nor in a trimeric complex with FAK (sample 3 and 4). SN: unbound interaction partner, El: eluate, 500 mM imidazole, B: proteins still on beads after elution

FAK binding to paxillin was further confirmed by AUC measurements with equimolar concentration of the two proteins (Figure 20). Both proteins were measured separately and in mixture to determine the different sedimentation behaviors. The runs were conducted at 14 °C in Buffer C1 supplemented with 10 µM $ZnCl_2$, which is required to keep all LIM domains in paxillin properly folded. The protein peaks were detected by via light absorption at 280 nm.

FAK renders two peaks at 2.5 S and 3.0 S, which correspond to HSP70 and FAK. Surprisingly, the intensity of the HSP70 peak is significantly higher than the FAK peak (3.0 vs. 0.6 AU), which does not represent the ratio observed in SDS-PAGE (Figure 17) or mass spectrometry and is likely an artifact, potentially caused by the addition of Zn^{2+} ions. Paxillin renders one clear peak at 1.4 S and a smaller one at 0.5 S, which is likely caused by insufficient removal of the His-SUMO tag and of no consequence to the analysis. In the sample containing both proteins, the intensity of the paxillin peak at 1.4 S is reduced and the FAK peak at 3.0 S is shifted to 3.5 S, away from the HSP70 peak, which remains unchanged. This clear shift of the FAK peak confirms the interaction with paxillin.

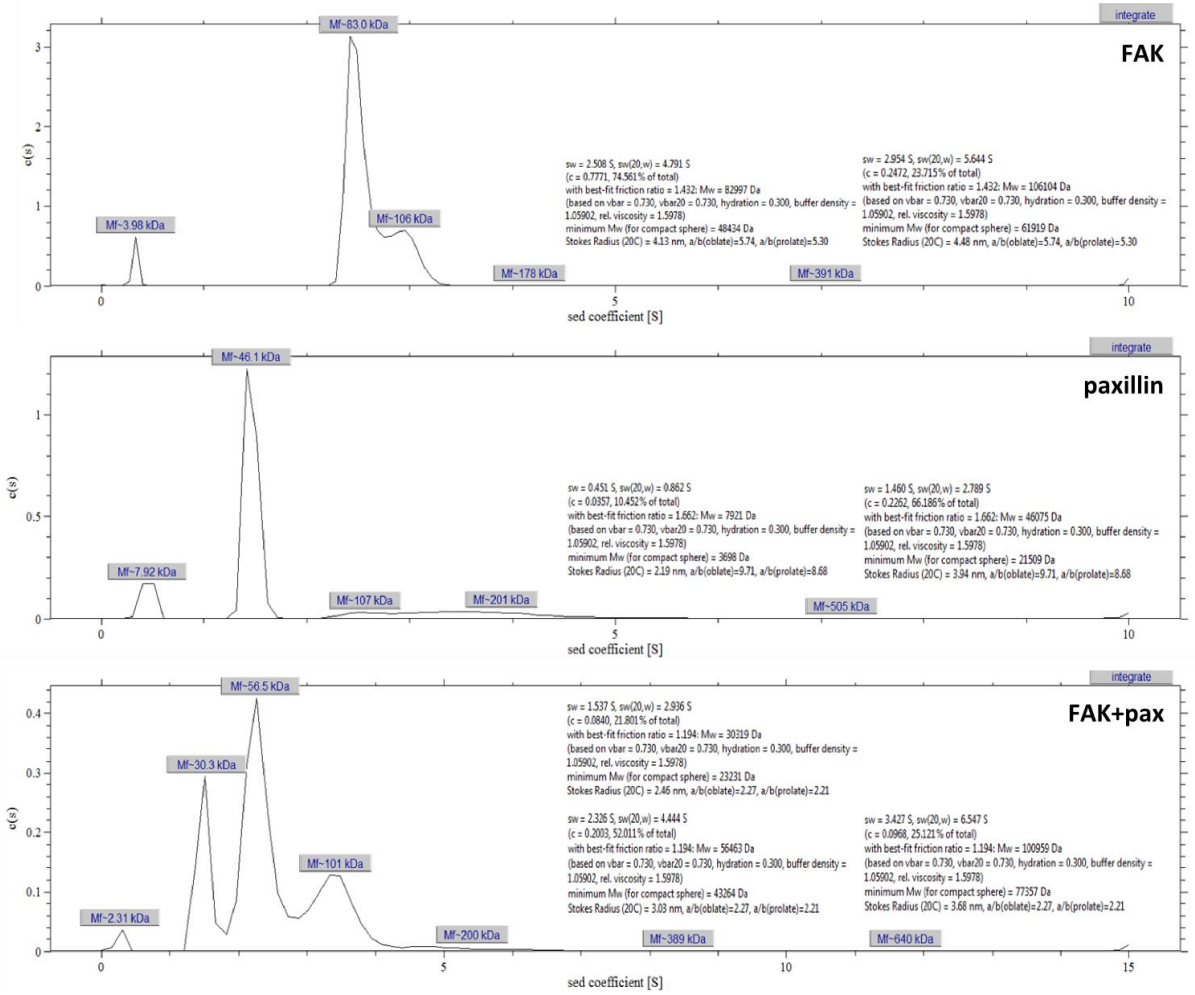

Figure 20: AUC analysis confirms FAK-paxillin binding. Recombinant FAK and paxillin were each diluted to a final concentration of 4.8 µM in Buffer C1 supplemented with 10 µM $ZnCl_2$ and separated at 14 °C. Sedimentation was monitored via A280-measurement. FAK and paxillin were sedimented separately and in equimolar mixture. FAK yields a main peak at 3.0 S, while a second peak at 2.5 S is likely due to HSP70 content in the sample. Paxillin renders a peak at 1.4 S. When both proteins are present, the FAK peak is shifted to 3.5 S, indicating interaction.

3.1.4 Phosphorylation of recombinant paxillin by FAK

Phosphorylation of paxillin by FAK has been studied in cells and two tyrosine residues (Y-31 and Y-118), which are predominantly phosphorylated, have been identified (Bellis et al., 1995). Consequently, kinase activity of FAK could be tested with recombinant paxillin produced in *E. coli* and therefore non-phosphorylated. Furthermore, it can be used to test whether other adhesome components such as talin or kindlin are phosphorylated by FAK. For each phosphorylation reaction, 100 µg of recombinant paxillin, kindlin-2, THD, full-length talin (obtained from Z. Sun, Fässler department), EPLIN or α-parvin were incubated with 1 µM FAK, 10 mM $MgCl_2$ and 0.5 mM ATP. Phosphorylation was allowed to proceed for 20 min on ice, then at room temperature and finally at 37 °C. After each incubation step, samples were taken for Western Blot analysis and the phosphorylation stopped by addition of SDS sample buffer.

The phosphorylation was monitored using a universal phospho-tyrosine antibody (Figure 21A, C). The Western Blots showed clearly that FAK phosphorylates paxillin at low efficiency at 4 °C or RT and at high efficiency at 37 °C, confirming the biological activity of the kinase. Furthermore, in all samples the intensity of the FAK band, which is also detected due to its Tyr phosphorylation, increases after incubation at RT or 37 °C, indicating auto-phosphorylation of FAK and probably further increase in activity.

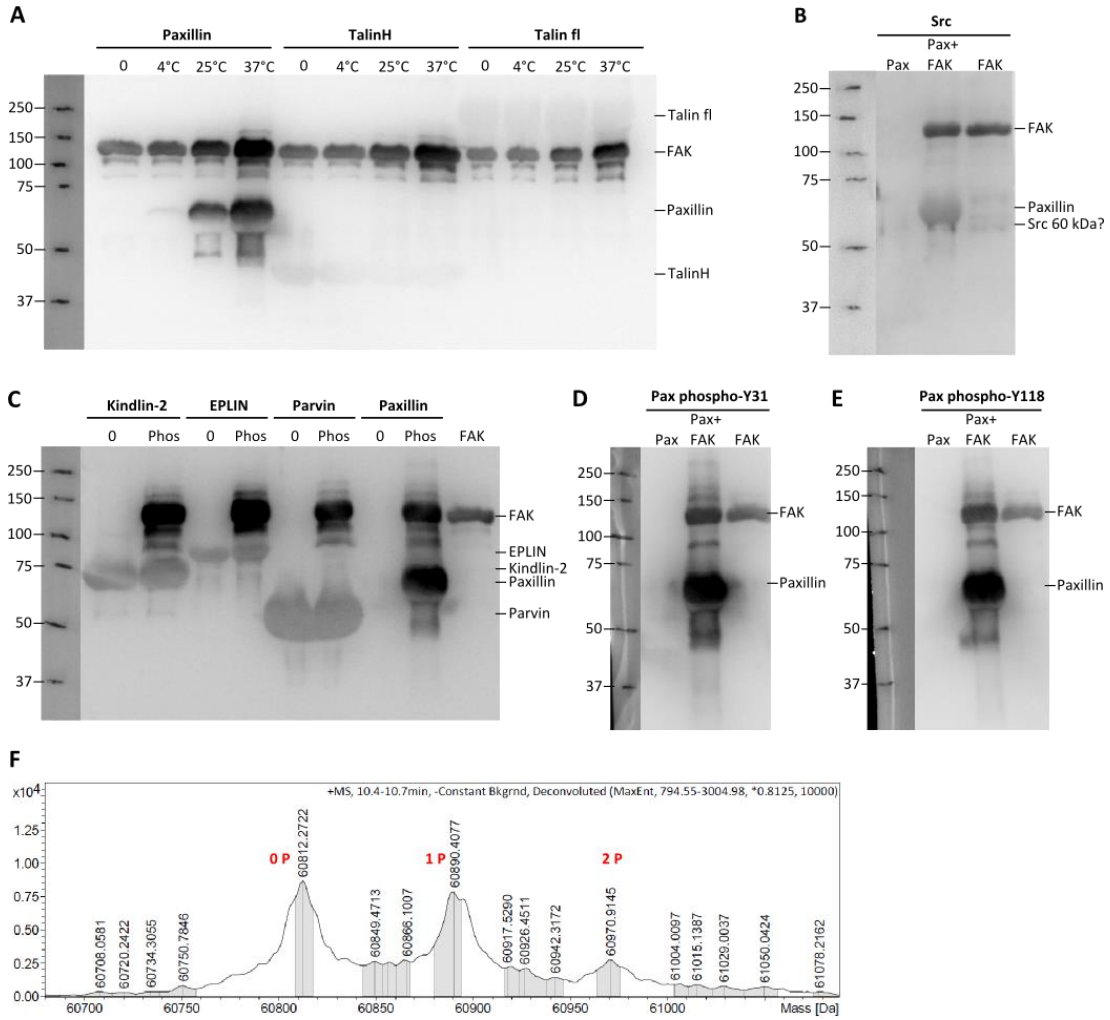

Figure 21: Characterization of paxillin phosphorylation by FAK. (A) Recombinant FAK (1 µM) was incubated with 100 µg of each potential substrate (paxillin, THD, talin fl,) in Buffer C1 supplemented with 10 mM $MgCl_2$ and 0.5 mM ATP at first for 20 min on ice (4 °C), then 20 min at 25 °C and finally 20 min at 37 °C. After each incubation step, a sample was taken for Western Blot analysis. Only paxillin is clearly phosphorylated by FAK. (B) It was further confirmed that no Src is present in the FAK or paxillin samples, which might also account for the phosphorylation. (C) Apart from paxillin, no other protein phosphorylation was detected (kindlin-2, EPLIN, α-parvin). 0 indicates the substrates without FAK addition, Phos indicates FAK addition and 20 min incubation at 37 °C. Detection with antibodies specific for paxillin phosphorylation at position Y31 (D) or Y118 (E) both detected phospho-paxillin but not the non-phosphorylated form, confirming phosphorylation in both positions. (F) Mass spectrometric analysis of phospho-paxillin shows the presence of 0, 1 or 2 phosphorylations on the protein.

None of the other substrates was phosphorylated by FAK, including THD or the full-length variant (forced into the open confirmation with high salt concentration), which seems to interact with FAK. It is possible that kindlin becomes phosphorylated by FAK in the presence of paxillin, which might act as a "bridge" between the two proteins. Paxillin, however, is efficiently phosphorylated in at least two different positions as determined by analysis of the protein full mass of the phosphorylated paxillin sample (Figure 21F). About 40 % of paxillin is still non-phosphorylated (60811 Da expected), while approximately 50 % of the molecules carry one phosphorylation (mass difference of ~80 Da) and 10 % carry two phosphorylations (~160 Da mass difference). Western Blot analysis using antibodies directed against phospho-Tyr31 and phospho-Tyr118 of paxillin both detected the phosphorylated protein, indicating that both known sites are phosphorylated (Figure 21D, E). Enzymatic digest of the protein and analysis of the fragments by LC-MS confirmed that paxillin is primarily phosphorylated on Tyr118 and to a lesser extent on Tyr31. Furthermore, phosphorylation of Tyr40 and Tyr181 was detected, two residues which have been mentioned in the literature but not as extensively studied as Tyr31 and Tyr118.

The phosphorylations might be induced by co-purified Src from HEK293E cells, since FAK is phosphorylated itself at Y-576 and Y-577, which is normally done by Src. However, no Src band at ~60 kDa could be detected in either paxillin or FAK samples, indicating that no Src was co-purified (Figure 21B). FAK, however, is also detected with the Src antibody, indicating that the antibody might not be entirely specific.

In summary, recombinant full-length FAK could be produced and purified in milligram amounts and its activity as a scaffolding protein, which binds to paxillin and, potentially, talin as well as its kinase activity could be demonstrated.

3.2 EPLIN

3.2.1 Purification and characterization of recombinant α-EPLIN

The coding sequence for full-length murine α-EPLIN was amplified from the vector pET15b-EPLIN (by E. Karaköse, Fässler department) using the primers PaKa137/138. The PCR product and the empty pCoofy17 vector were cut with the restriction endonucleases *Bam*HI and *Xho*I.

The ensuing fragments were purified by gel extraction and ligated, yielding the pCoofy17-EPLIN expression vector for His-SUMO-tagged, full-length EPLIN. Correct insertion was confirmed by sequencing of the entire coding sequence.

Recombinant His-SUMO-EPLIN was produced in *E. coli*-Rosetta cells in LB medium supplemented with kanamycin and chloramphenicol at 18 °C for 18 h after induction with 200 mM IPTG. The pellet was resuspended and disrupted in Buffer A1. The recombinant protein was isolated from the cleared lysate via IMAC using buffers A1 and A2, where the main fraction of EPLIN eluted at 250 mM imidazole concentration. The His-SUMO-tag was removed by cleaving with SenP2 protease over night and reverse Ni-NTA chromatography. EPLIN was further purified by SEC chromatography using Buffer A3 supplemented with 10 µM $ZnCl_2$, which is required for proper folding of the central LIM-domain, as is the case for paxillin.

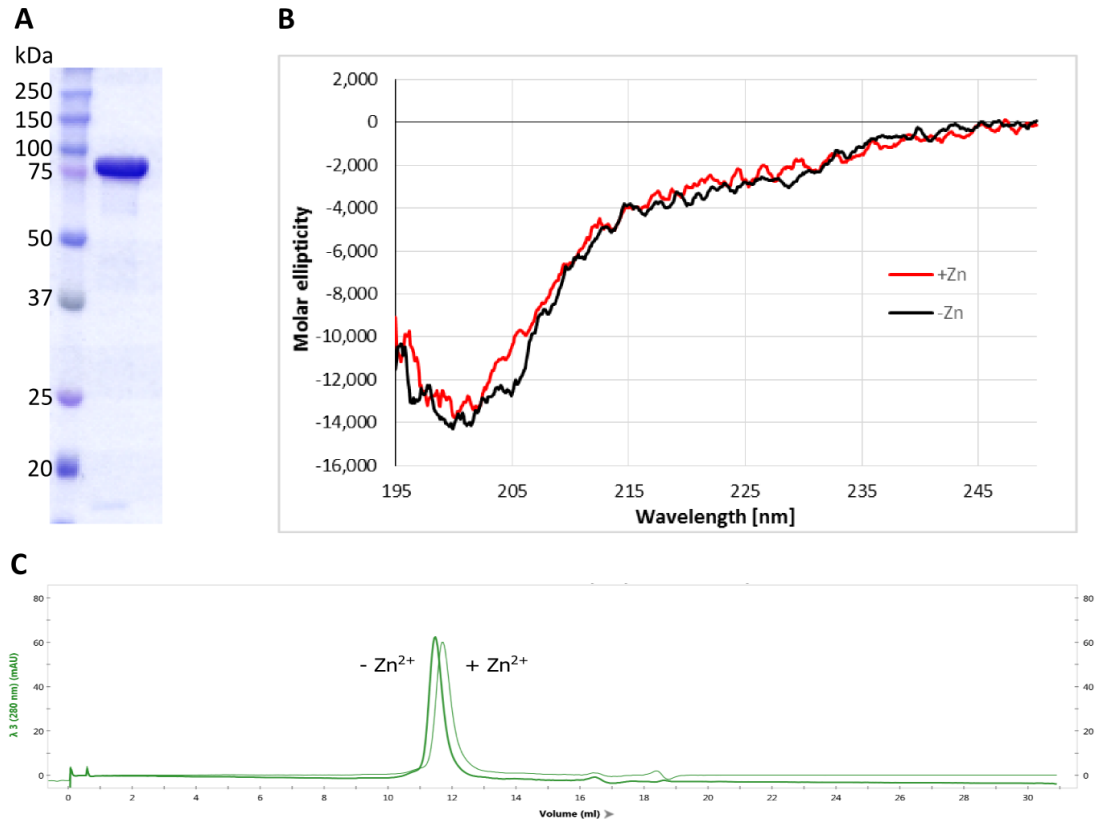

Figure 22: Characterization of recombinant EPLIN. (A) SDS-PAGE shows SEC-purified, tagless EPLIN at an apparent size of 75 kDa, while the actual MW is 66 kDa, confirmed by ESI-TOF mass spectrometry. (B) CD-spectroscopic analysis of EPLIN purified in Buffer A containing 0 or 10 µM ZnCl2. For the measurements the protein was diluted with water to a final concentration of 2.3 µM (+ Zn2+) or 2.5 µM (- Zn2+). The spectra confirm the largely unstructured nature of the protein. (C) Size exclusion chromatography using Buffer A containing 0 or 10 µM ZnCl2 shows a shift of the elution peak, indicating a Zn2+-dependent compaction of the central LIM-domain.

Addition of $ZnCl_2$ already during IMAC causes severe precipitation of His-SUMO-EPLIN, potentially due to interaction of Zn^{2+}-ions with the His_{10}-tag. Incorporation of Zn^{2+}-ions into the LIM-domain could be shown in analytical SEC runs in the absence or presence of $ZnCl_2$ in the buffer. Addition of $ZnCl_2$ causes a clear shift of the elution volume from 11.5 ml to 12.0 ml (295 kDa to 213 kDa), indicating a compaction of the molecule and a reduction of the hydrodynamic volume, probably caused by a conformational change of the LIM domain (Figure 22C). The apparent molecular weight of EPLIN is much higher than its actual weight of 66 kDa, which indicates a largely unstructured protein, as was to be expected from disorder prediction analysis (data not shown). CD spectrometric analysis of EPLIN yielded a secondary structure distribution of 6 % α-helix, 33 % β-sheet, 24 % turns and 37 % unordered elements (Figure 22B), confirming the predictions. It appears that only the central LIM-domain of EPLIN has a distinct structure, while the actin-binding domains at the N- and C-termini are unstructured and flexible. Binding to F-actin might cause these domains to adopt a more distinct structure. It is notable that on denaturing SDS-PAGE, the apparent size of EPLIN is approximately 80 kDa, while analysis of the total protein mass yielded the expected molecular weight of 66132 Da (Figure 22A). This shift might therefore be caused by the large amount of disordered structures. Addition of $ZnCl_2$ does not significantly change the CD spectrum, indicating that binding of Zn^{2+} leads to the compaction observed in SEC but does not lead to the formation of secondary structures.

3.2.2 Recombinant EPLIN does not interact with PINCH and paxillin

EPLIN has been shown to localize to focal adhesions and associate with PINCH and paxillin, which might be responsible for its recruitment to the adhesome. However, in pull-down assays neither full-length His-SUMO-PINCH nor full-length PINCH in complex with α-parvin and ILK bound EPLIN in higher amounts than the negative control.

Furthermore, recombinantly produced PINCH LIM 2, 3, 4 or 5 domains (produced and purified by M. Veelders, Fässler department) failed to bind EPLIN (Figure 23). PINCH LIM 1 domain could not be expressed, therefore binding to it was not tested. Similarly, binding to paxillin was neither observed in pull-down assays nor in MST measurements (data not shown).

These findings suggest that the interaction is indirectly or postranslational modifications such as phosphorylation of EPLIN might be necessary for interaction with either PINCH or paxillin.

It has been reported that in cells, EPLIN is phosphorylated by ERK. This was confirmed by incubating recombinant EPLIN with commercial ERK (New England Biolabs) and then analyzing the protein total mass (Figure 24).

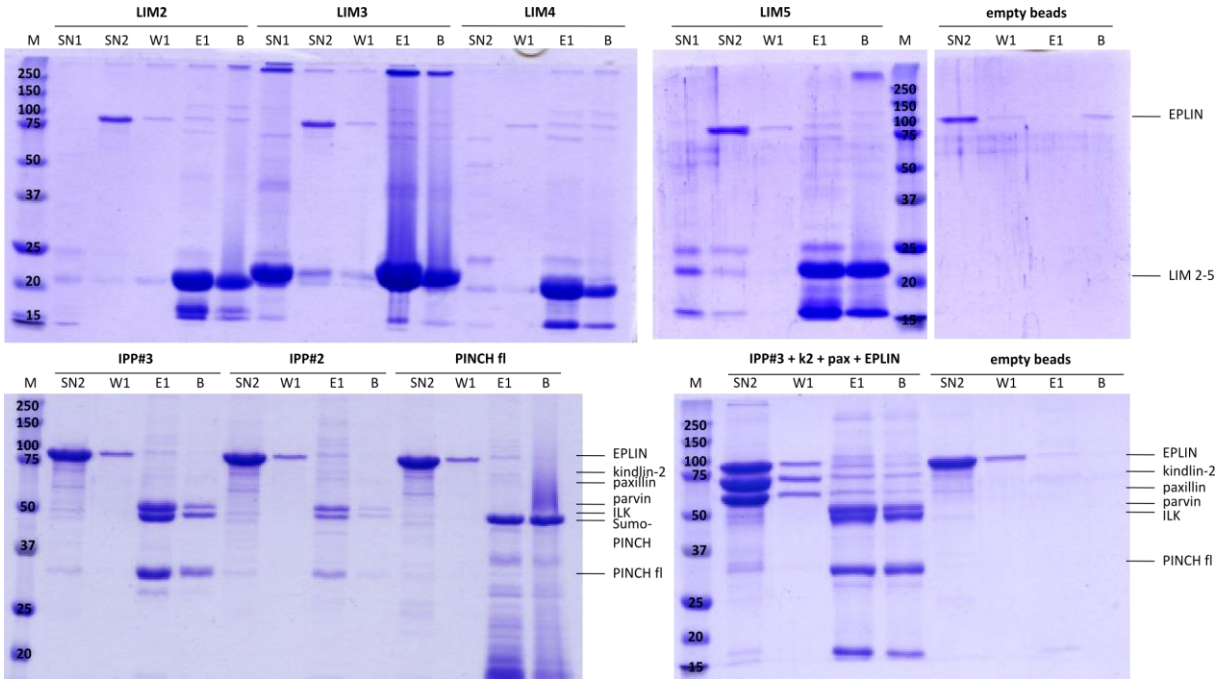

Figure 23: Interaction studies of EPLIN and PINCH using Ni-NTA pull-downs. His-SUMO-tagged PINCH LIM domains 2-5, full-length PINCH or full-length IPP complex (constructs #2, #3 or #3 in complex with kindlin-2 and paxillin) were immobilized on Ni-NTA beads and incubated with recombinant tagless EPLIN. Empty beads were used as a control for unspecific interactions. SN1 refers to unbound tagged protein, SN2 to unbound EPLIN, W1 to the first of two washing steps with 50 mM imidazole, E1 to eluate 1 with 500 mM imidazole and B to beads with residual protein bound to them. Neither full-length PINCH nor the individual LIM domains showed binding to EPLIN. PINCH in complex with parvin and ILK showed no interaction either, even when in complex with kindlin-2 and paxillin.

Besides non-phosphorylated EPLIN at 66132 Da, peaks with masses of 66293 Da and 66374 Da were detected, corresponding to EPLIN with 2 and 3 phosphorylations (~80 Da mass shift per phosphate group). However, direct comparison of phospho-EPLIN (pEPLIN) to the non-phosphorylated form did not yield differences in pull-downs or MST experiments. Therefore, no direct interaction between EPLIN and either paxillin or PINCH was observed. However, it cannot be fully excluded that modifications on PINCH or paxillin are required for interaction or that different phosphorylations on EPLIN from those by ERK are necessary.

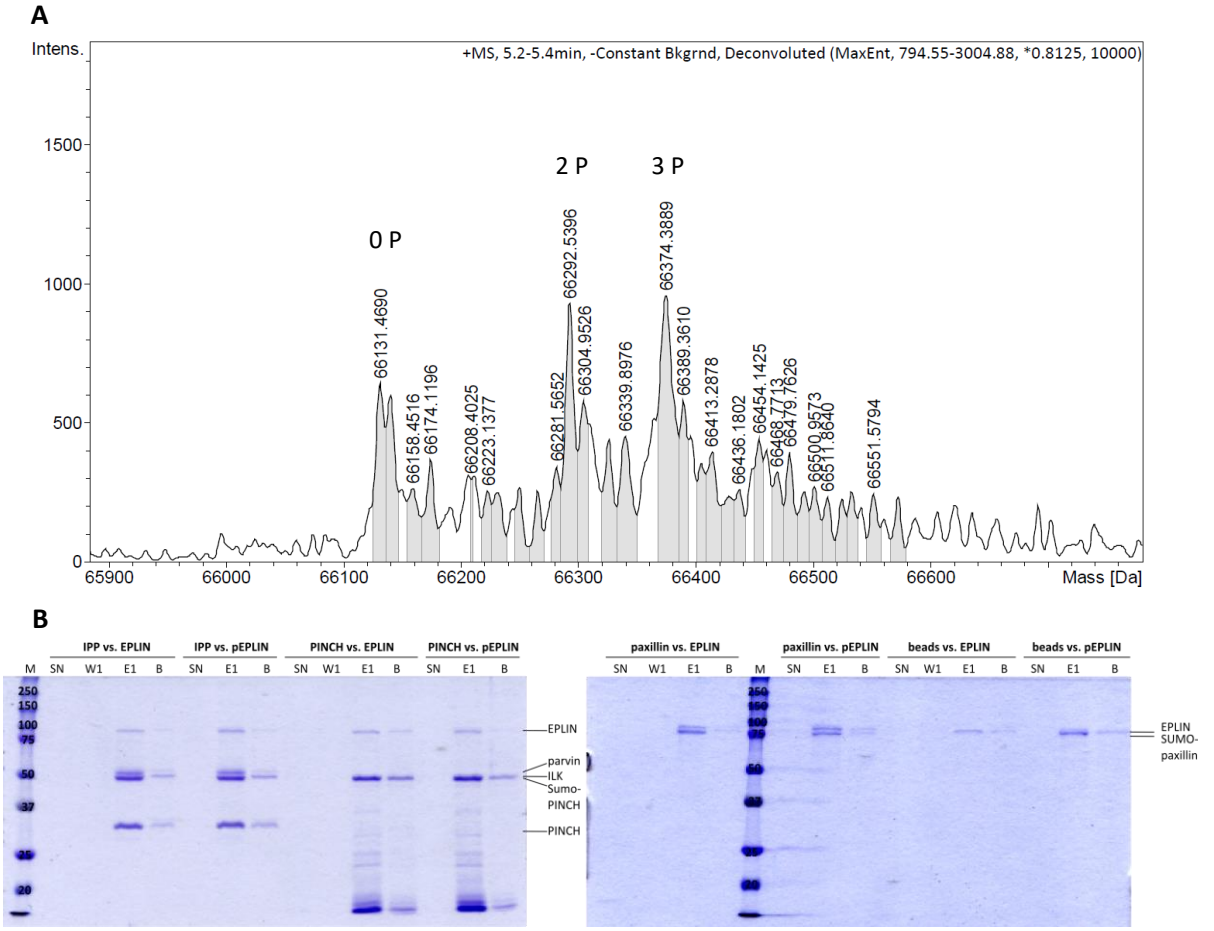

Figure 24: Phosphorylation of EPLIN by ERK has no effect on binding to PINCH or paxillin. (A) EPLIN was phosphorylated by recombinant ERK (NEB) 2 or 3 times, as confirmed by mass spectrometric analysis. Residual non-phosphorylated EPLIN at a molecular weight of 66132 Da was observed as well as species which were 160 or 240 Da heavier, corresponding to 2 or 3 phosphate groups. (B) In Ni-NTA pull-down assays with immobilized His-SUMO-PINCH, His-SUMO-paxillin or His-tagged IPP complex, no difference was observed between phosphorylated EPLIN (pEPLIN) and the non-phosphorylated form. Empty beads were used as a control for unspecific interactions. None of the samples showed increased EPLIN binding compared to the negative control. SN refers to unbound EPLIN, W1 to the first of two washing steps with 50 mM imidazole, E1 to eluate 1 with 500 mM imidazole and B to beads with residual protein bound to them.

3.3 Simultaneous expression of the adhesome core components in the same cell using the MultiBAC expression system

3.3.1 Cloning and assembly of MultiBAC expression vectors

For the study of multi-protein complexes it is often advantageous to co-express all components simultaneously in a single cell, allowing the complex to assemble on its own in native conditions, rather than producing all components separately and then painstakingly assembling them *in vitro*. If a tight complex is formed inside the cell, it can subsequently be purified as an entity with all components present in the correct stoichiometry. One expression

system optimized for multi-protein complex production in insect cells is the MultiBAC system (Bieniossek et al., 2012). It was used for the production of full-length IPP complex by itself or in combination with either kindlin-2 or paxillin or GST-integrin β1 or THD together with FAK or EPLIN together with RSU-1.

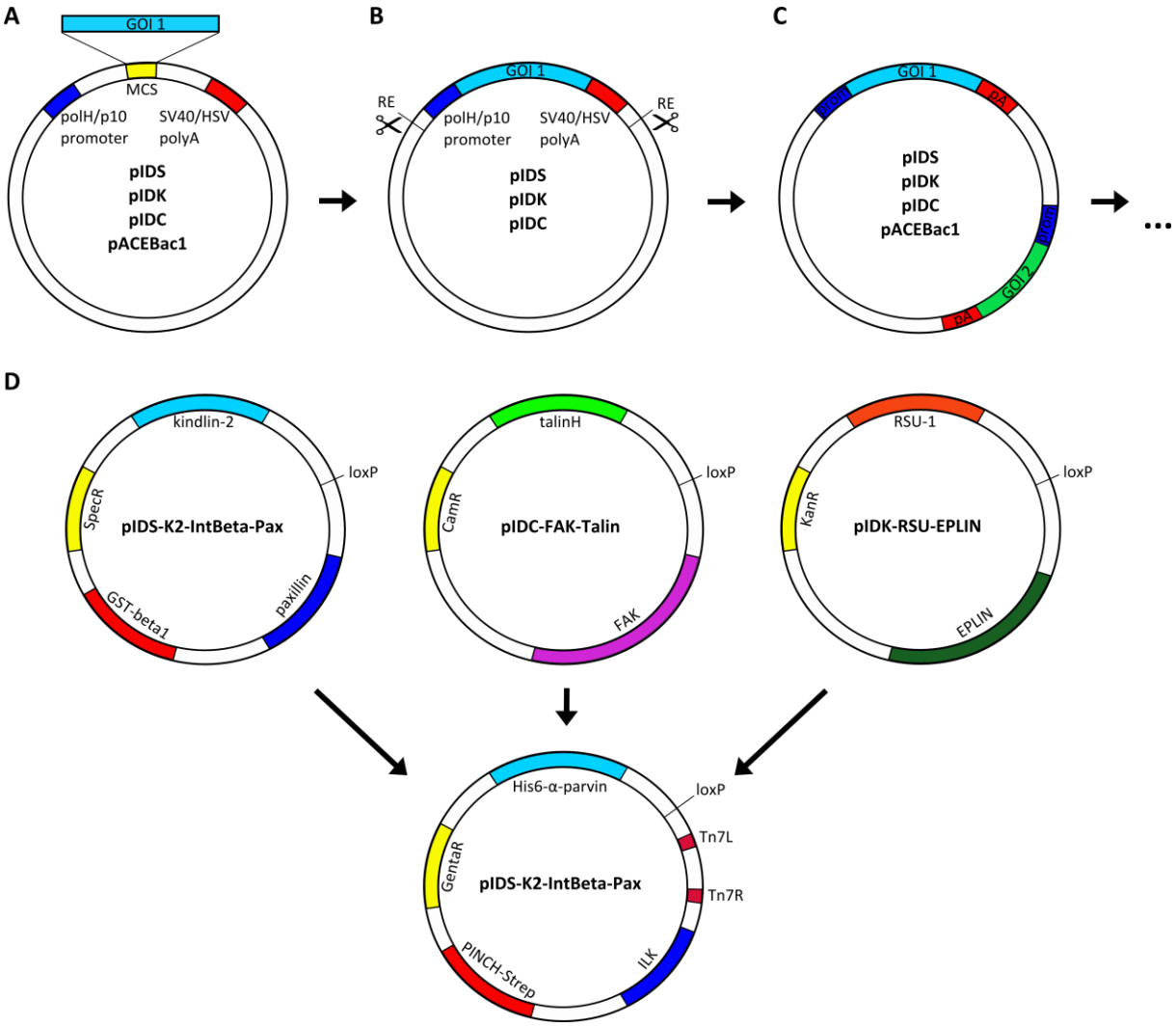

Figure 25: Schematic representation of the MultiBAC expression vector assembly. (A) Each gene to be expressed was first inserted into a donor vector (pIDC/pIDK/pIDS) or an acceptor vector (pACEBac1) to provide a promoter and a polyA sequence for insect cell expression. (B) The expression cassettes were then cut out with restriction enzymes and inserted into another linearized vector carrying another expression cassette (C). (D) This allowed for the assembly of donor and acceptor vectors with 2-3 expression cassettes. The donor vectors can each be merged with the pACEBac1-IPP acceptor vector separately or simultaneously using Cre-mediated recombination at the loxP sites. Correctly fused vectors are selected according to the respective antibiotic resistance markers. The acceptor vector or any fusions with donor vectors can be integrated into the baculovirus genome via the Tn7L and Tn7R sites.

The rationale behind this expression strategy was to start with the IPP complex as a stable "core" of the multi-protein complex, since ILK, PINCH and α-parvin have been reported to form a ternary complex which is pre-assembled in the cytosol prior to recruitment into focal

adhesions (Hoffmann et al., 2014). To this “core”, additional components can be added to test if a larger complex is formed and stable enough to allow co-purification. Ideally, this would have allowed for the isolation of adhesome complexes, which could have been used for chemical crosslinking, cryo-EM studies or even crystallization.

The basic principle of the MultiBAC system is the assembly of all genes to be expressed into one vector, pACEBac1 or 2, which contains Tn7R and Tn7L sequences necessary for transposition into the baculovirus genome. Therefore, the genes coding for ILK, PINCH and α-parvin were inserted into the pACEBac1 “acceptor” vector to provide the complex core. The other components were inserted into pIDC, pIDS or pIDK “donor” vectors, which do not possess Tn7R/L sequences and thus cannot be directly inserted into the virus genome. Instead, they each contain one loxP site, which allows for Cre recombinase-mediated fusion of the donor vectors with the acceptor vector pACEBac1, which also carries a loxP site. Since all vectors carry different antibiotic resistance markers, up to three different donor vectors can be fused to an acceptor vector and the desired expression vector can be identified by selection using a combination of the respective antibiotics. With this approach, different combinations of the adhesome components could be cloned in one single step.

Prior to assembly of the multi-protein expression constructs, each gene to be expressed had to be inserted into the multiple cloning site of pACEBac1, pIDC, pIDK or pIDS in order to provide them with a promoter and a polyA sequence compatible with insect cell expression. The coding sequences for full-length murine ILK, PINCH-1, α-parvin, kindlin-2, FAK, paxillin, integrin β1-CT, EPLIN and RSU-1 were amplified from expression vectors available at the Fässler department. α-parvin carried an N-terminal His_8-tag, cleavable by PreScission protease and PINCH-1 was amplified with primers coding for a C-terminal Strep-tag sequence. In order to increase the size of the integrin β1 tail peptide and to allow for affinity purification, the coding sequence was first cloned into the pGEX-6P-1 vector, adding an N-terminal GST-tag to the tail. The coding sequence for GST- β1 tail was then inserted into the pIDK vector. Apart from the above mentioned, no further affinity tags were added to components of the complex. The details of the construction of the first set of vectors are indicated in Table 6.

Table 6: Overview of MultiBAC donor and acceptor vectors generated. All coding sequences were amplified by PCR using the primers indicated and, if not further specified, vector backbone and PCR product were both digested with the same restriction enzymes prior to ligation.

Name	Template	Primers	promoter/polyA/tag	Restriction enzymes
pGEX-6P-1-Beta1	pET15b-TMCyto-b1-wt	PaKa182/183	-/-/GST	*Bam*HI/*Xho*I
pACEBac1-PINCH	pCoofy17-PINCH1	PaKa184/185	polH/SV40/Strep	*Sal*I/*Not*I
pIDK-ILK	pCoofy50-mILK	PaKa187/188	p10/HSV/-	*Xho*I/*Nhe*I
pIDK-Parvin	pCoofy50-mParva	PaKa189/190	p10/HSV/His_8	*Xho*I/*Nhe*I
pIDS-K2	pCoofy17-Kindlin2	PaKa191/192	p10/HSV/-	*Xho*I/*Nhe*I
pIDC-Paxillin	pCoofy50-Paxillin	PaKa193/194	polH/SV40/-	*Stu*I/*Xba*I
pIDK-IntBeta	pGEX-6P-1-Beta1	PaKa203/204	p10/HSV/GST	*Xho*I/*Nco*I
pIDK-EPLIN	pCoofy17-EPLIN	PaKa195/196	p10/HSV/-	*Xho*I/*Nhe*I
pIDK-RSU	pCoofy17-RSU	PaKa197/198	p10/HSV/-	*Nhe*I/*Nsi*I
pIDC-Talin	pCoofy17-THD	PaKa199/200	polH/SV40/-	*Afe*I/*Xba*I insert *Stu*I/*Xba*I backbone
pIDC-FAK	pCoofy55-FAK	PaKa201/202	polH/SV40/-	*Bam*HI/*Xba*I

After insertion of all coding sequences into donor or acceptor vectors and sequencing of the entire genes, vectors with multiple expression cassettes were generated. Restriction enzymes were selected which cut the vectors before the promoter and after the polyA sequence. The ensuing fragments were blunted when necessary and inserted into a linearized acceptor or donor vector carrying a second expression cassette. Likewise, vectors with three expression cassettes were created. Table 7 lists the multiple expression vectors generated. Figure 25 shows the schematic representation of the cloning steps as well as the final three donor vectors pIDS-K2-IntBeta-Pax, pIDK-RSU-EPLIN and pIDC-FAK-Talin and the acceptor vector pACEBac1-IPP.

Table7: Overview of MultiBAC vectors with multiple expression cassettes. Indicated are the vectors out of which expression cassettes were cut out (Insert) as well as the vectors into which they were inserted (Backbone) and the restriction enzymes used. Whenever the ensuing ends of the fragments did not match, they were blunted using T4 DNA polymerase. The vectors highlighted in green are the final donor and acceptor vectors.

Name	Insert from	Insert RE	Backbone	Backbone RE
pACEBac1-PINCH-ILK	pIDK-ILK	*Spe*I/*Pme*I/*Hind*III	pACEBac1-PINCH	*Spe*I/*Pme*I
pACEBac1-IPP	pIDK-Parva	*Pme*I/*Cla*I/*Pst*I	pACEBac1-PINCH-ILK	*Pme*I
pIDS-K2-IntBeta	pIDK-IntBeta	PI-*Sce*I/*Bst*XI	pIDS-K2	*Bst*XI
pIDS-K2-IntBeta-Pax	pIDC-Paxillin	PI-*Sce*I/*Nru*I	pIDS-K2-IntBeta	*Bst*XI
pIDK-RSU-EPLIN	pIDK-EPLIN	PI-*Sce*I/*Bst*XI	pIDK-RSU	PI-*Sce*I
pIDC-FAK-Talin	pIDC-Talin	*Nru*I/*Msc*I	pIDC-FAK	*Nru*I

The donor vectors were mixed with the acceptor vector and fused using Cre-mediated recombination. After transformation into chemically competent *E. coli* cells, clones carrying correctly fused vectors were selected by testing for the presence of multiple antibiotic resistances. Attempts to generate a fusion construct of pACEBac1-IPP with all three donor vectors were not successful. It is possible that the ensuing vector fusion construct is too large for efficient transformation into chemically competent cells, a problem that might be overcome by electroporation. It was decided, however, to try expression of fusions of pACEBac1-IPP, pIDS-K2-IntBeta-Pax and pIDC-FAK-Talin or pACEBac1-IPP and pIDK-RSU-EPLIN first and upon promising results more efforts could have been made to create a fusion of all four vectors. Five different vector fusions or acceptor vectors were integrated into baculovirus and used for recombinant protein production. For simplicity, they were given numbers as which they are referred to in the following sections.

IPP#1: pACEBac1-IPP + pIDS-K2-IntBeta-Pax + pIDC-FAK-Talin

ILK, His_8-α-parvin, PINCH fl-Strep, kindlin-2, paxillin, GST-beta 1, THD, FAK

IPP#2: pACEBac1-IPP + pIDS-K2-IntBeta-Pax

ILK, His_8-α-parvin, PINCH fl-Strep, kindlin-2, paxillin, GST-beta 1

IPP#3: pACEBac1-IPP + pIDK-RSU-EPLIN

ILK, His_8-α-parvin, PINCH fl-Strep, RSU-1, EPLIN

IPP#4: pACEBac1-IPP

ILK, His_8-α-parvin, PINCH fl-Strep

IPP#5: pACEBac1-IPP-dLIM5 (Stop-codon inserted after PINCH LIM4 via mutagenesis)

ILK, His_8-α-parvin, PINCH dLIM5

3.3.2 Test expression and purification of IPP#1 and IPP#2 and optimization of expression conditions

IPP constructs 1 and 2 were inserted into baculovirus genomes and virus was produced in SF9 insect cells. The virus particles were used to infect small culture volumes (10 ml) of SF9 or High Five insect cells at dilutions of 1:500, 1:1000 or 1:2000. After 72 h post infection, the cells were counted, harvested by centrifugation, flash-frozen in liquid nitrogen and resuspended in PBS (100 µl per $10*10^6$ cells). The lysed cells were mixed by vortexing and samples of the whole

cell lysates as well as of the cleared supernatants after centrifugation were separated by SDS-PAGE and analyzed by Western Blot (Figure 26). Detection of the expected adhesome proteins using specific antibodies revealed that the IPP complex, kindlin-2, paxillin, FAK and THD were successfully produced. Comparison of the whole cell lysates and the soluble fraction revealed no large differences for most of the proteins, indicating that the greater part of the recombinant proteins is soluble and not aggregated. High Five and SF9 cells displayed significant discrepancies in expression levels, especially for α-parvin, PINCH and paxillin. Overall, protein amounts were much higher in High Five cells at all dilutions, suggesting these cells are best suited for large-scale production. In High Five cells, virus dilutions of 1:500 and 1:1000 showed no significant differences, while the 1:2000 dilution resulted in slightly reduced expression levels. Therefore, production in High Five cells at a virus dilution of 1:1000 was determined as optimal condition.

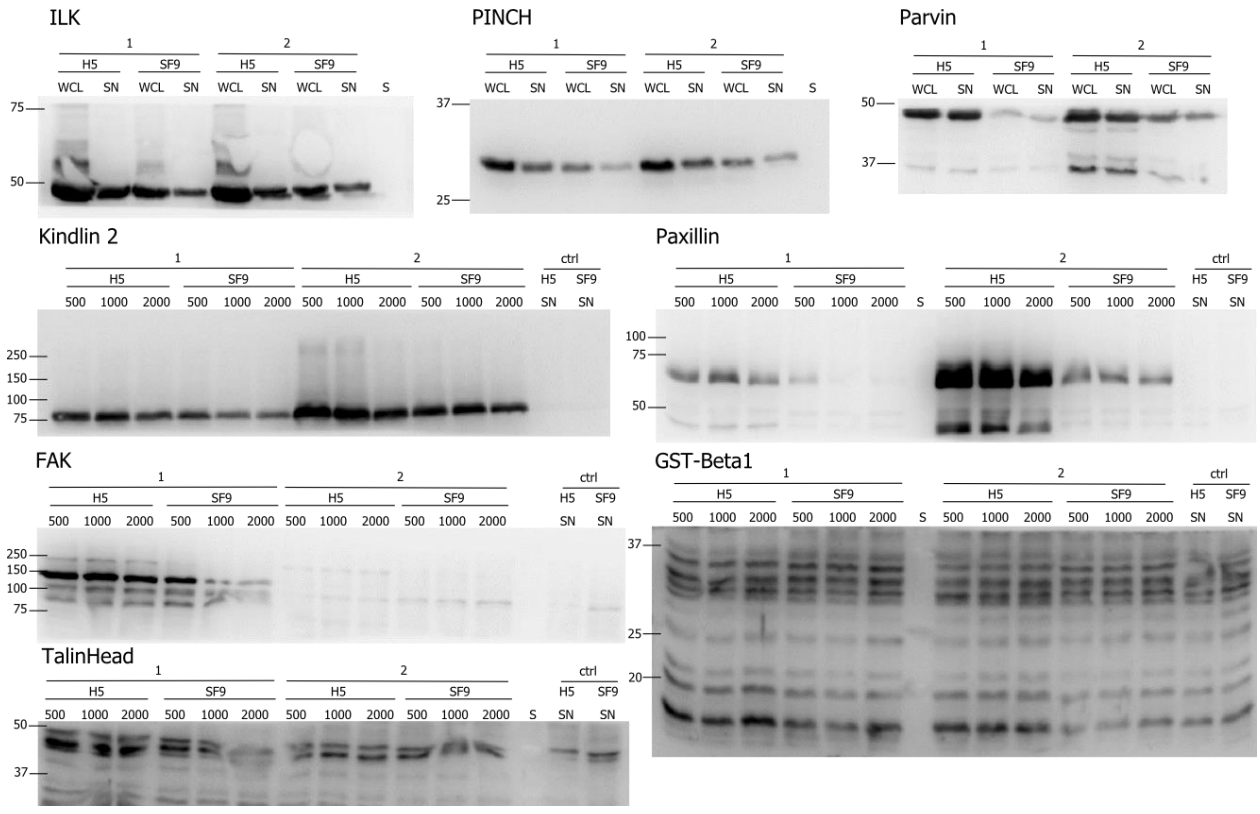

Figure 26: Detection of recombinantly produced proteins in insect cells by Western Blot. IPP#1 and #2 constructs were produced in High Five (H5) and SF9 cells for 72 h and the whole cell lysates (WCL) and soluble fractions (SN or not further specified) were analyzed by Western Blot using specific antibodies against the proteins produced. Optimal virus dilutions (1:500, 1:1000, 1:2000) were tested as well and compared to non-infected SF9 or H5 lysates (ctrl). All proteins were produced in the expected samples, except for GST-Integrin β1, which might be degraded or not produced at all. Protein levels of all components were higher in High Five cells than in SF9 cells and a dilution of 1:1000 yielded optimal expression levels.

None of the samples showed a prominent band at 32 kDa in the anti-GST detection, indicating that either the GST-Integrin β1 fusion construct is not expressed or is being degraded in insect cells. Furthermore, a high amount of unspecific bands indicates that a lot of GST is present in the cells, which might be the reason why GST fusion proteins are degraded. Therefore, integrin tail peptides from other sources have to be added for complex assembly.

FAK and THD were only detected in the IPP#1 samples, as expected. The anti-THD antibody detects some unspecific bands but shows clearly a band at 46 kDa, which is absent in the IPP#2 samples. Paxillin and kindlin-2 levels appear to be significantly higher in the IPP#2 samples than in IPP#1, which might be due to the fact that in #2, the cells do not have to produce FAK and THD and have therefore more capacities for producing the other proteins. However, the levels for ILK, PINCH and parvin appear mostly identical in both constructs. Another explanation could be the fusion of 2 copies of the pIDS-K2-IntBeta-Pax vector to one pACEBac1-IPP vector, resulting in higher expression levels of the two proteins.

After defining the optimal expression conditions, 500 ml culture volume of construct IPP#2 was was used to test purification with a 1 ml HisTrap column. Theoretically, if a tight complex of ILK, PINCH and parvin and optionally of kindlin-2 and paxillin is formed, all components should co-elute if α-parvin is immobilized to the column via its His_8-tag. Since the previous samples were very viscous, the purification of one quarter of the cell lysate each was carried out in Buffer A3 without any additives (1), with 0.1 % NP-40 (2), with 0.1 % Tween-20 (3) or with 10 µM $ZnCl_2$ (4) (Figure 27). The addition of $ZnCl_2$ was expected to increase the amounts of PINCH and paxillin purified, since both proteins require the presence of Zn^{2+} in the buffers when produced in *E. coli*. The protein bound to the column was eluted using stepwise increase of 50, 125, 250 and 500 mM imidazole.

Sample (3) showed by far the purest preparation of ILK, PINCH and α-parvin, indicating that Tween-20 reduces unspecifically bound contaminating proteins or binding to membrane fragments left over from cell lysis. As expected, addition of $ZnCl_2$ to the buffer resulted in a more distinct PINCH band. Therefore, supplementing the buffers used for purification with 0.1 % Tween-20 and 10 µM $ZnCl_2$ appears beneficial. In later purifications, it became evident that including 0.1 % Tween-20 in the lysis buffer and 0.05 % in all other buffers yields equivalent purity and reduces the effects of the detergent on biophysical methods.

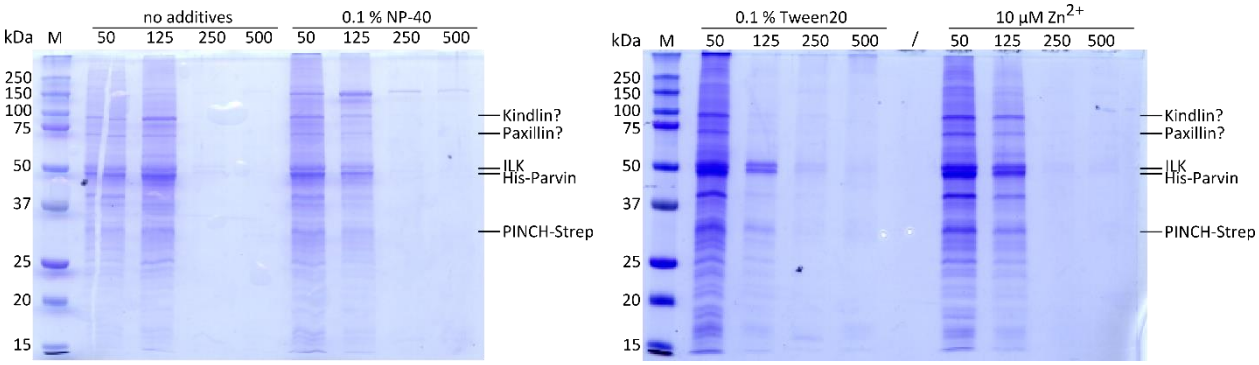

Figure 27: Optimization of buffer conditions for purification of the IPP complex. Cell lysate of IPP#2 was purified via IMAC in Buffer A3 with either no additives, 0.1 % NP-40, 0.1 % Tween-20 or 10 µM $ZnCl_2$. The fractions of the 50, 125, 250 and 500 mM imidazole elution steps were concentrated by TCA precipitation and analyzed via SDS-PAGE. Addition of Tween-20 resulted in the purest preparation of ILK, PINCH and parvin, while addition of $ZnCl_2$ increased PINCH elution.

Unfortunately, none of the samples showed clear bands of kindlin-2 or paxillin bound to the IPP complex. This indicates that the interactions might not be strong enough to retain a larger complex potentially formed inside the insect cells during purification. Therefore, this method was used for purification of only the IPP complex without co-expression of other components.

3.3.3 Purification of recombinantly produced adhesome complexes using rate-zonal centrifugation

Since all of the desired adhesome components were produced in copious amounts inside the same cell, the formation of a larger complex was expected. The reason why no other components than ILK, PINCH and parvin could be co-purified in Ni-NTA chromatography might be that shearing forces are too high when the complexes pass through the column material under constant flow and thus components bound with low affinities or with high k_{off} rates than those between the components of the IPP complex are washed away more easily. To avoid this situation, the more gentle method of purification by rate-zonal centrifugation was applied to cell lysates of IPP#1. Cells were homogenized in Buffer B2 and 300 µl of the centrifuged, unfiltered lysate was applied to a 13 ml sucrose gradient (5-20 %). After 16 h of centrifugation, the gradient was separated into fractions of 500 µl, beginning from the top of the tube. The fractions, especially those representing the first half of the gradient where complexes were expected, were analyzed by SDS-PAGE and Western Blot (Figure 28).

All proteins were present in the cell lysate, as expected. ILK, PINCH and α-parvin were detected in fractions 2-12, with lower fraction numbers corresponding to lower density of the gradient and lower molecular weight of the particles and higher numbers to more density and

heavier particles. Therefore it seems that some IPP complex was formed and could be detected at the expected medium-range density, while the majority of IPP was detected as single proteins. The remaining proteins FAK, THD, paxillin and kindlin-2 were only detected in fractions 2-7 and did not correlate with the IPP complex at higher fractions. Therefore, they were not part of a complex, which would have sedimented further than the first few fractions.

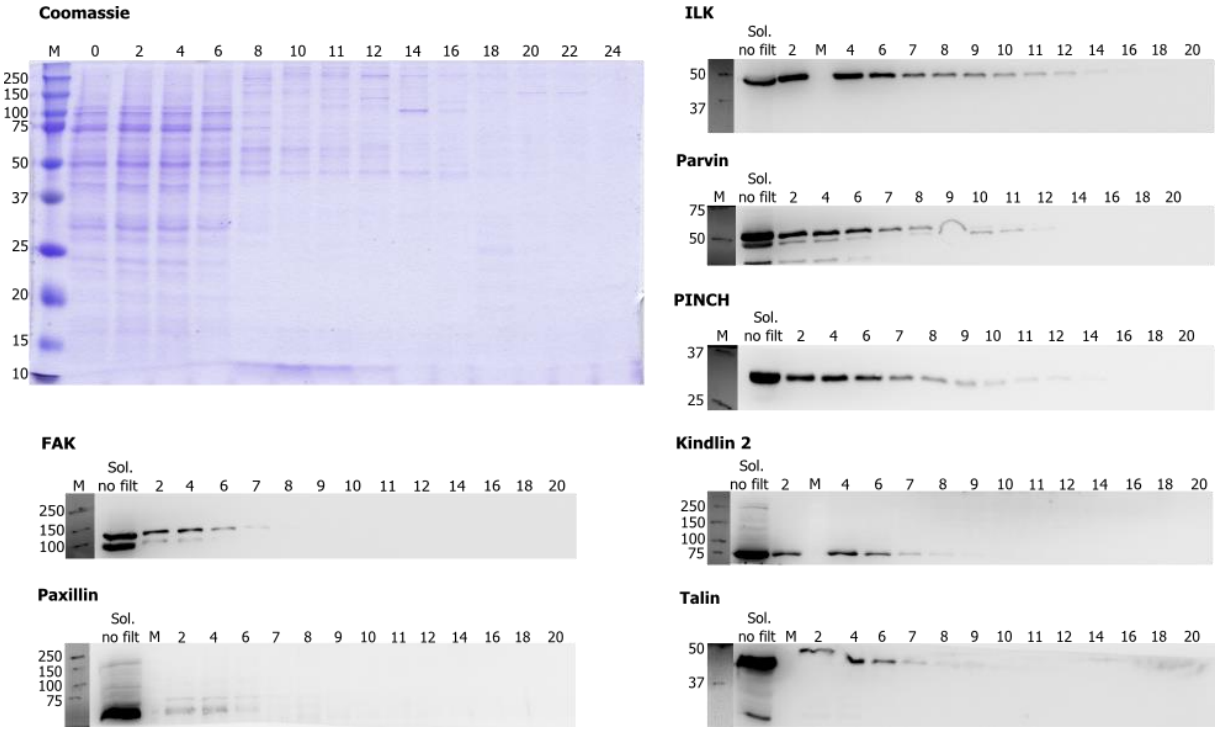

Figure 28: SDS-PAGE and Western Blot analysis of the preparation of adhesome complexes by rate-zonal centrifugation. Lysate of construct IPP#1 was separated using a 5-20 % sucrose gradient and fractions of 500 ml were harvested from the top. 0 indicates the topmost fraction containing the lightest particles, while 24 is the bottom fraction of highest density. The location of the expressed adhesome components was determined by Western Blot using specific antibodies. It is apparent that ILK, PINCH and α-parvin are spread out over fractions 2-12, indicating the presence of a complex at higher fraction numbers and individual proteins at lower numbers. FAK, THD, paxillin and kindlin-2 are only present up to fraction 7, indicating that none of them forms a complex with other proteins. If a large "adhesome" complex had been formed, the individual bands would have been enriched in certain higher fractions due to the increased molecular weight of a complex compared to individual components.

This experiment showed that separation of adhesome complexes in a sucrose gradient is not a suitable tool for obtaining high-quality protein preparations for structural analysis. If there are complexes pre-formed in the cytosol of the High Five cells, they are not stable enough to allow purification, potentially because the affinities of individual components towards each other are too low. It is also possible that FAK, THD, paxillin or kindlin-2 are post-translationally modified (e.g. phosphorylations) by the insect cells in a way that abrogates binding to the IPP complex.

Production and purification of IPP#3, in which EPLIN and RSU-1 are co-expressed with the IPP complex yielded similar results. After purification, only the IPP complex and trace amounts of RSU-1 were detected, suggesting that the affinity of RSU-1 to PINCH is not high enough to form a tight complex in 1:1:1:1 stoichiometry (data not shown).

Taken together co-purification by IMAC or on Ni-NTA beads with large pore sizes failed (data not shown), suggesting that the initial hypothesis of a stable adhesome complex might have to be corrected and that the interactions of the individual components might be more transient.

3.4 The IPP complex

3.4.1 Large-scale expression and purification of recombinant full-length IPP complex from High Five insect cells

Since the initial tests showed that no large adhesome complex could be isolated by this approach, the main focus was shifted towards the production and purification of recombinant full-length IPP complex. Due to instability of the proteins and extremely low expression levels, no purification and characterization of a trimeric complex of all three components in full-length has been reported to date. Since a number of caveats have been observed during production and purification of the complex, a detailed protocol is presented here.

IPP complex can be purified using any of the constructs, but highest yields are obtained for IPP#4, which comprises only the pACEBac1-IPP donor vector. Infection of the cells can be achieved using a P1 virus preparation, which is the “classical” protocol. Alternatively, an appropriate amount of SF9 cells are transfected with the bacmid DNA and the ensuing cleared supernatant, which contains virus particles, is used to infect the final expression culture. The latter protocol omits the P1 virus amplification to shorten the process. It is however critical that the baculovirus used for infection is prepared directly before protein production. The virus can theoretically be stored at 4 °C for several weeks and retain its activity, but it has been observed that with increased age of the virus IPP yields decrease and at a certain point ILK is suddenly no longer produced, while parvin and PINCH are still produced. Therefore, fresh virus should be produced for each expression and it is beneficial to produce a large batch (3-5 l culture volume) once instead of several smaller batches subsequently.

Protein production was maintained for 72 h post infection and yielded copious amounts of IPP complex. Therefore, no variation of the duration of protein production was tested although the yield might still be further increased. The cells were harvested by centrifugation and the pellets flash-frozen in liquid nitrogen. The pellets can be stored for several months at -80 °C until needed, causing no reduction in yield or quality of the purified proteins that could be observed so far.

After thawing the cell pellet was resuspended in buffer to a final volume of 10x pellet volume to lower the viscosity of the ensuing lysate. Cell lysis was carried out in Buffer B1, which contains 0.1 % Tween-20 for efficient removal of membrane fragments. The buffers used for purification contained 0.05 % Tween-20. The lysis buffer and all other buffers were supplemented with 1 mM TCEP to keep the Cysteine residues of the intracellular proteins reduced and to prevent formation of non-physiological disulfide bonds. To prevent proteolytic degradation, 1 mM PMSF was added to the lysis buffer. Since no degradation was ever observed, PMSF can probably be omitted. Furthermore, all buffers contained 10 mM $ZnCl_2$ to allow proper folding and activity of the five PINCH LIM domains. For cell disruption, thawing of the flash-frozen cells and treatment with a Dounce homogenizer was sufficient. Although Tween and high amounts of DNase were added, the cell lysate after centrifugation was still very turbid and probably still contained membrane or other cell fragments. This could not be improved by longer centrifugation, therefore the lysate had to be passed through several 0.45 µm sterile filters (~30 ml per filter before clogging) to remove large particles prior to IMAC.

The cleared lysate was passed 2-3 times over the column for sample application and elution was carried out using a stepwise increase of imidazole concentration (Figure 29). IPP complex eluted at 125 mM and 500 mM imidazole, with the majority of the protein in the 500 mM fraction. Judging from SDS-PAGE analysis, ILK, PINCH and α-parvin are purified in approximately 1:1:1 stoichiometry, indicating that a stable complex is formed. If this were not the case, more His_8-tagged α-parvin would be isolated and tagless ILK and PINCH would be lost. It is noteworthy that despite having lower molecular weight, α-parvin (46 kDa) displays a higher apparent molecular weight in SDS-PAGE than ILK (51 kDa). This was verified by Western Blot analysis and by cleaving His_8-parvin with PreScission protease, which results in a shift of only the upper band, while the ILK band remains unchanged (data not shown). The apparent

molecular weight of PINCH (38 kDa) in SDS-PAGE is lower than expected (~30 kDa), but mass-spectrometric analysis of protein full mass showed all three proteins at the expected sizes.

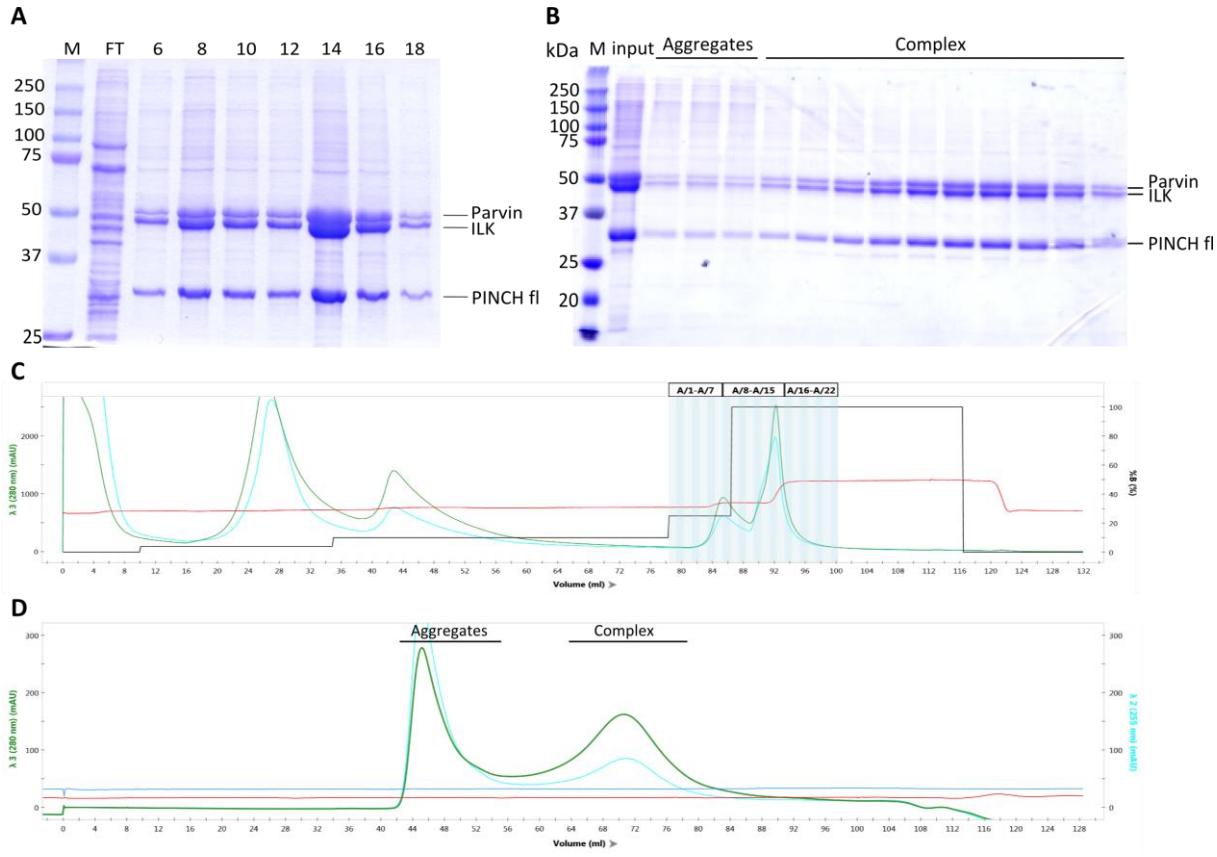

Figure 29: Purification of full-length IPP complex by IMAC and SEC. (A) The cleared lysate from High Five insect cells was loaded onto a 5 ml HisTrap column and the chromatography carried out in Buffer B2 and B3. The fractions were analyzed by SDS-PAGE. (C) Full-length IPP complex in an apparent stoichiometry of 1:1:1 eluted at 125 and 500 mM imidazole. Since only α-parvin carries a His_8 tag, the three proteins evidently form a stable complex that allows co-purification. (B, D) As a second purification step, the IPP complex was separated from aggregates on a Superdex200 column. The peak elution volume of 70 ml corresponds to an apparent molecular weight of 165 kDa, only slightly larger than the actual weight of 136 kDa, indicating monomeric complexes. The IPP complex could be purified to >90 % purity.

PINCH carries a C-terminal Strep-tag, therefore immobilization of the complex on StrepTactin beads was intended as a second purification step to reduce contaminants in the protein sample. However, only very low amounts of IPP complex bound to the beads, indicating that the Strep-tag might not be accessible and hidden inside the complex. Therefore, it cannot be used for further purification.

The fractions containing IPP complex were pooled and concentrated using a centrifugal concentrator to a final volume of 2.5-3 ml and applied on a Superdex200 size exclusion column equilibrated with Buffer B2. The chromatogram showed a clear separation of aggregates near the void volume (~40 ml) and the trimeric IPP complex with a peak at 70 ml elution volume,

which corresponds to a globular protein of 165 kDa. This is very close to the actual size of the complex of 136 kDa, indicating a monomeric form. It is notable, however, that the IPP peak is unusually broad, which might be caused by the presence of oligomers at lower elution volumes and by disassembled complexes towards higher elution volumes. The presence of contaminants, such as HSP70 or other chaperones, can be excluded, as they would have been detected either in SDS-PAGE or mass spectrometric analysis. If the presence of Tween-20 poses a problem for subsequent analyses or assays, SEC can also be performed without the detergent in the running buffer. This seems to slightly reduce yield and stability of the proteins and results in a more “uneven” chromatogram, indicating the presence of multiple species.

The final purified IPP complex displays a purity of >90 %, judging from SDS-PAGE, at a yield of around 5 mg per 1 l High Five cell culture volume. It can be concentrated up to 10 mg/ml and can be flash-frozen in liquid nitrogen without any additives and stored at -80 °C. Upon thawing, aggregates need to be removed by centrifugation at 21000 x g for 5 min at 4 °C.

The main problem when working with the IPP complex is its tendency to form aggregates and to precipitate. Considerable amounts of protein are lost when the IPP complex is concentrated using a centrifugal concentrator, which is noticeable as white precipitate on the membrane. Furthermore, the IPP complex aggregates in a time-dependent manner, resulting in clearly visible precipitate after storage over night at 4 °C. This aggregation process can be accelerated by increasing the temperature to room temperature. Therefore, whenever assays are conducted, aggregates are removed by centrifugation shortly before adding the IPP complex to a sample and all samples are constantly kept on ice or at 4 °C.

3.4.2 Biophysical characterization of recombinant IPP complex

For all assays and for the determination of protein concentration, the IPP complex is treated as one large fusion protein with a molecular mass of 135878 Da and an extinction coefficient of 129260 $M^{-1}cm^{-1}$.

The secondary structure distribution and thermal unfolding of recombinant IPP complex was studied by CD spectroscopy (Figure 30A, B). The spectrum reveals that the complex is folded and contains 38.4 % α-helical, 13.2 % β-sheet, 18.9 % turn and 29.3 % unordered elements. The thermal unfolding curve did not show one clear transition temperature, but rather several "smaller" transitions. This might be due to individual unfolding of ILK, PINCH and α-parvin and could potentially be further influenced by disassembly of the complex. The main transition occurs around 52 °C, while two smaller transitions can be observed around 30 °C and 75 °C. It is notable that thermal unfolding seems to begin at 20 °C already, confirming the observation of increased aggregation at room temperature.

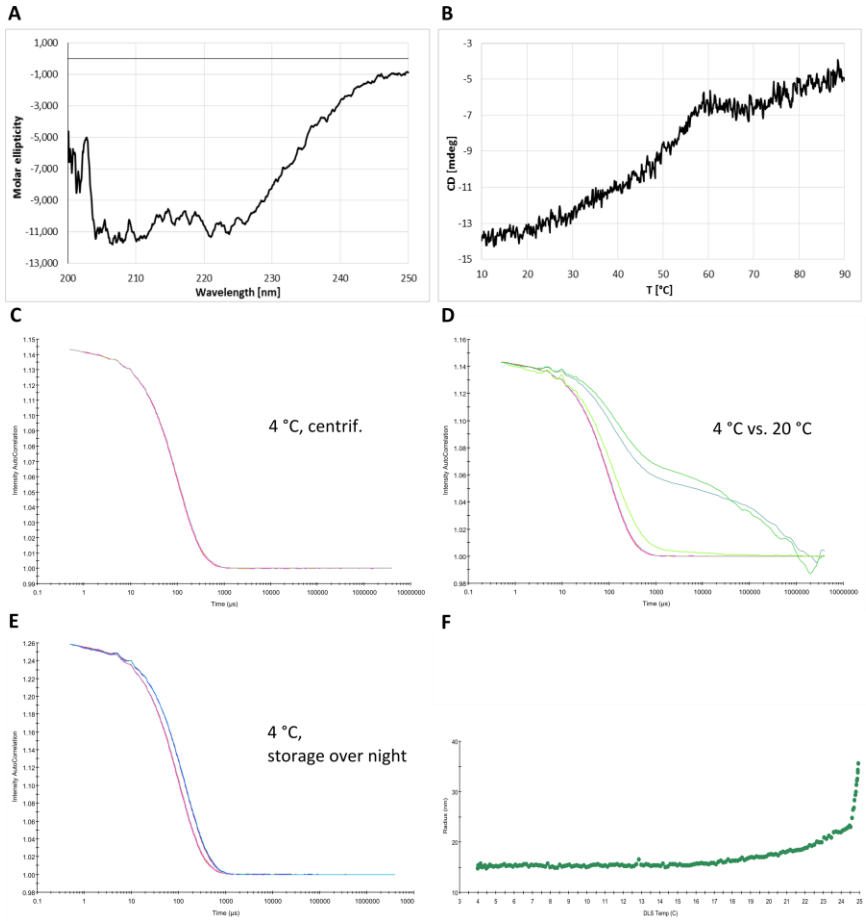

Figure 30: CD and DLS analysis of recombinant IPP complex. (A) CD measurements of 55 µM IPP complex, diluted 1:10 in ddH_2O revealed a secondary structure distribution of 38.4 % α-helical, 13.2 % β-sheet, 18.9 % turn and 29.3 % unordered, RMSD 0.187. (B) The melting curve shows a main transition at 52 °C and two smaller transitions at 30 °C and 75 °C. (C) DLS measurements at 4 °C showed a sharp decay curve which was fitted to a hydrodynamic radius of 5.2 nm (157 kDa) at 50 % polydispersity. (D) DLS measurements at 20 °C (green curves) showed the presence of large particles and aggregation, compared to the same sample at 4 °C (pink curve). (E) Storage at 4 °C over night resulted in a defined increase in hydrodynamic radius to 6.5 nm (269 kDa). (F) A temperature scan from 4 °C to 25 °C revealed that aggregation of the IPP complex begins at a temperature of 17-18 °C, with really large aggregates beyond 25 °C. The measurements were carried out in Buffer B2 without Tween-20.

DLS measurements were conducted in Buffer B2 without Tween-20, since the detergent micelles interfere with the detection of particle species. The measurement revealed a hydrodynamic radius of 5.2 nm, which corresponds to a globular protein of 157 kDa (Figure 30C). This value is very close to the actual molecular weight of 136 kDa and, like SEC

measurements, indicates monomeric complexes. The polydispersity of 50 % was rather high, indicating that the sample was not perfectly homogeneous. DLS analysis also confirms the thermal instability of the IPP complex, since after increasing the temperature to 20 °C the sample already contains large aggregates (Figure 30D). Aggregation begins to increase significantly at 17-18 °C, leaving only very large particles beyond 25 °C (Figure 30F). Therefore, measurements with the IPP complex should be conducted below 17 °C, if possible. Another notable change in the DLS decay curves occurs after storage of the IPP complex over night at

4 °C. Even after centrifugation directly before the measurement, the same sample suddenly shows an increase in hydrodynamic radius, from 5.2 nm to 6.5 nm, corresponding to a globular protein of 269 kDa (Figure 30E). This might indicate the formation of complex dimers over night, but not of large aggregates, since the decay was still very sharp.

From CD and DLS measurements it can be concluded that the IPP complex is folded and monomeric, if freshly purified by SEC. Increasing the temperature to more than 18 °C or incubation over night lead to an increase in size and to the formation of aggregates. Therefore, for critical analyses the IPP complex should be used directly after SEC and kept at lowest possible temperature.

3.4.3 Interaction studies of IPP and other adhesome components

Correct folding and biological activity of the recombinant IPP complex was assessed through interaction studies with its reported binding partners. IMAC-purified IPP complex was concentrated and mixed with other recombinantly produced and purified adhesome components and applied to an analytical SEC650 column. The formation of a quaternary complex of IPP and kindlin-2 (78 kDa, produced in *E. coli*) could be observed by a clear shift of the IPP elution peak from 12.3 ml (197 kDa) to 11.7 ml (293 kDa) (Figure 31A). SDS-PAGE of the peak fraction shows all four proteins at apparently equal amounts, confirming the formation of a quaternary complex (Figure 31D). A second peak at 13.2 ml (109 kDa) contains excess kindlin-2 and disassembled IPP components. The elution volume of the second peak is almost identical to that of monomeric kindlin-2.

The same applies for complex formation with paxillin (66 kDa, *E. coli*), where the IPP peak is also shifted to 11.7 ml (Figure 31B). A shoulder of the peak contains paxillin and IPP complex, which did not bind each other (Figure 31E). Notably, monomeric paxillin elutes at the same

volume as the IPP complex, which is probably due to a high amount of disordered stretches within the protein rather than multimer formation.

THD does not bind to the IPP complex, which results in the formation of two peaks at elution volumes identical to monomeric IPP complex and THD (Figure 31C). Unlike kindlin-2 and paxillin, addition of THD does not cause a shift of the IPP peak and the four proteins were not found within a fraction in SDS-PAGE (Figure 31F).

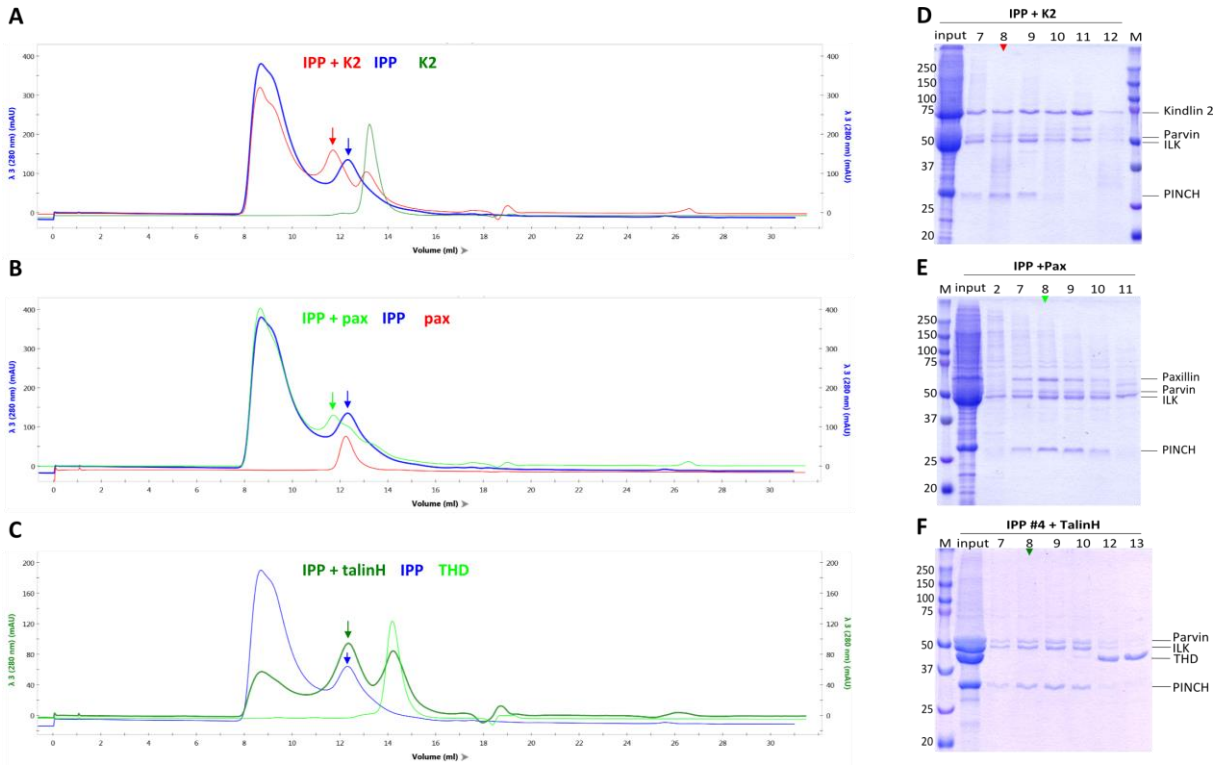

Figure 31: Detection of complex formation of IPP with kindlin-2, paxillin or THD via SEC. (A) To detect protein-protein interactions, recombinant, IMAC-purified IPP complex was mixed with recombinant kindlin-2 (A), paxillin (B) or THD (C) and applied on an analytical SEC column for separation. To confirm complex formation, all proteins were also applied to the column separately and the runs were overlaid to compare peak elution volumes. Arrows depict peak fractions and their positions on the SDS gels (D-F). Kindlin-2 and paxillin both form quaternary complexes with the IPP complex, causing a distinct shift of the IPP peak. THD does not form an additional complex, instead two peaks at the same elution volumes as the monomeric components are observed. The peaks at 8-10 ml elution volume contain aggregates of the IPP complex and are not relevant for complex analysis. SEC was carried out in Buffer B2 at 4 °C on a 24 ml SEC650 column.

Kindlin-2 and paxillin both bind to the IPP complex individually, raising the question whether their binding is mutually exclusive or whether a pentameric complex can be formed. To answer this question, IPP complex was mixed with kindlin-2 and paxillin and applied to an analytical SEC column (Figure 32A). The ensuing chromatogram shows a main elution peak at 11.0 ml (466 kDa), which is clearly shifted from the kindlin-IPP and paxillin-IPP peaks at 11.7 ml, indicating further increase in hydrodynamic volume of the particles and thus complex formation with

both components. SDS-PAGE confirms the presence of all five proteins in apparently equimolar amounts in the peak fraction (Figure 32D).

Overlay of the IPP-kindlin-paxillin chromatogram with those of IPP alone and of kindlin-paxillin show genuine complex formation, since the particles formed are significantly larger than the kindlin-paxillin complex (Figure 32A). It is notable that, although they are of almost equal molecular weight, the kindlin-paxillin complex (11.9 ml, 144 kDa) displays a significantly larger hydrodynamic volume of 257 kDa than the IPP complex (136 kDa actual, 197 kDa apparent). This indicates that the IPP complex is more compact and globular than the kindlin-paxillin complex, which might display a rather extended conformation, possible due to unstructured parts of paxillin.

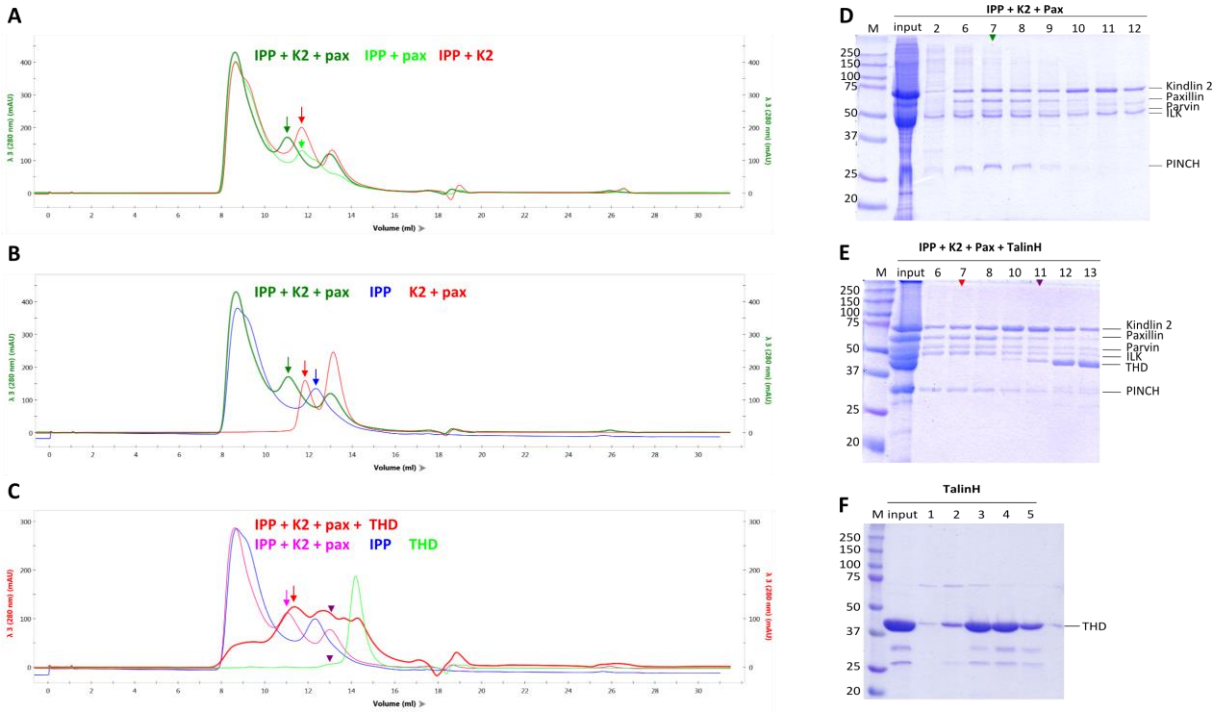

Figure 32: Detection of a pentameric IPP-kindlin-2-paxillin complex but no interaction with THD on SEC. (A, D) Recombinant, IMAC-purified IPP complex was mixed with kindlin-2 and paxillin and separated on an analytical SEC column. Formation of a pentameric complex created a peak at 11.0 ml (466 kDa), which is clearly shifted from the IPP-kindlin and IPP-paxillin peaks at 11.7 ml (293 kDa). (B) The IPP-kindlin-paxillin peak is also clearly shifted from those of the kindlin-paxillin complex (11.9 ml) and the IPP complex (12.3 ml). (C, E) Addition of THD does not lead to formation of a hexameric complex, THD found in the same fraction as the other proteins does not indicate complex formation but is due to an unspecific effect of THD, leading to a second peak at 13 ml in a sample containing only THD (purple arrows, F). The peaks at 8-10 ml elution volume contain aggregates of the IPP complex and are not relevant for complex analysis. SEC was carried out in Buffer B2 at 4 °C on a 24 ml SEC650 column.

Considering that IPP can bind kindlin-2 as well as paxillin individually and that kindlin-2 and paxillin can form a complex themselves, the binding modalities of these complexes are of

particular interest. It is unclear whether in the pentameric complex kindlin and paxillin bind to the IPP complex in the same manner as in the two tetrameric complexes and whether they interact with each other through the same binding interfaces when bound to IPP as in solution. Another scenario is that only paxillin or kindlin can directly bind to IPP and the other protein binds only to the attached partner but not to the IPP complex. These questions are subject of further studies.

It was further tested whether addition of THD to IPP, kindlin-2 and paxillin leads to hexameric complex formation. Although no interaction of THD with either of the proteins has been detected, it might be possible that pentameric complex formation leads to conformational changes and the formation of binding sites, which are not present in the monomeric proteins. However, no further shift of the IPP-kindlin-paxillin peak was detectable (Figure 32C) and no THD appears in the peak fraction when analyzed by SDS-PAGE (Figure 32E). Traces of THD can be seen in the fractions at 13 ml elution volume, significantly before the THD elution peak. However, this is not caused by THD binding to any of the other proteins but is rather an effect of THD itself, since also in the chromatogram of THD alone, a small peak before the main peak appears (Figure 32F). Therefore, SEC analysis indicates that THD does neither bind to the IPP complex nor to the pentameric IPP-kindlin-paxillin complex.

3.4.4 Determination of binding affinity between IPP and paxillin by MST

The paxillin-IPP interaction was further characterized through MST measurements, which allowed determination of the binding affinity and stoichiometry. Recombinant paxillin was labeled with the NT-647 dye (Nanotemper) and diluted to a final concentration of 30 nM in each capillary. IMAC- and SEC-purified IPP complex was concentrated to ~50 µM for each measurement and a 1:1 titration series was pipetted for each measurement. The fluorescence values for all capillaries were similar, within 100 fluorescence units variation caused by pipetting errors. Since the deviations did not follow a defined pattern, fluorescence quench or loss of fluorescent molecules could be excluded as causes.

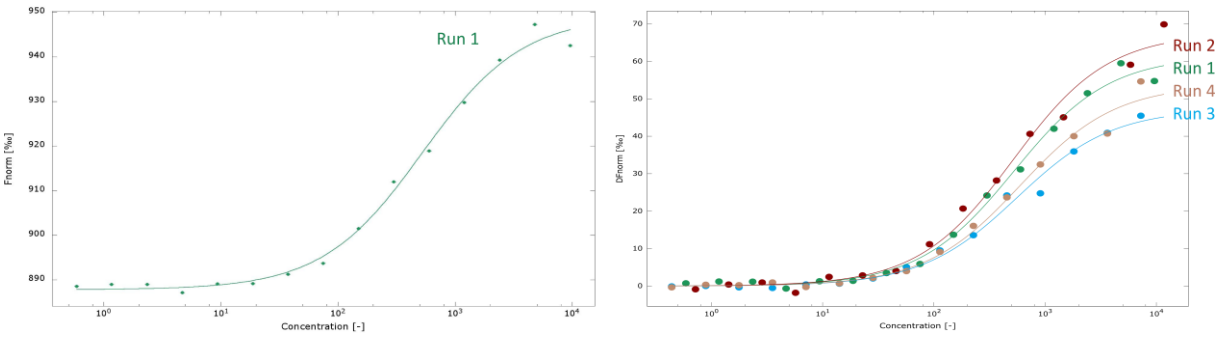

Figure 33: MST measurements of paxillin versus IPP complex. Paxillin-NT-647 was used at 30 nM final concentration, IPP was concentrated to a maximum of 50 µM and diluted in a 1:1 ratio to create a dilution series of 16 concentrations. The normalized fluorescence F_{norm} from thermophoresis and T-jump was plotted against the IPP concentration and a binding curve was fitted through the data points. Reproducibility of the experiment was tested in four independent measurements (Run 1-4). Missing data points were obvious outliers (distorted MST traces) and were removed from the analysis so they would not interfere with the data fitting. The different F_{norm} values of the four experiments at identical fluorophore concentrations are probably due to variations in the IPP sample preparation or in the buffer composition, yet have no effect on the K_D values determined. The measurements were carried out in Buffer B2 at 25 °C, using premium coated capillaries.

For determination of the K_D value the normalized change in fluorescence intensity of thermophoresis and temperature jump were plotted against the IPP concentration and a binding curve was fitted into the data points. From this, the K_D value of paxillin binding to the IPP complex was determined as 535 nM (Table 8). This value represents the average K_D from four independent experiments (Figure 33).

Table 8: Summary of MST measurements to determine the binding constant of paxillin and the IPP complex. The table summarizes four individual experiments conducted at identical settings with slightly varying maximum IPP concentrations.

Run #	K_D [nM]	c (pax-647) [nM]	Std. Error of Regression	Excitation Power	MST Power
1	510.56	30	1.919240761	20%	40%
2	502.85	30	2.769171762	20%	40%
3	544.24	30	1.759375874	20%	40%
4	582.32	30	2.232124671	20%	40%
	ø 535.0				

3.4.5 Interaction of IPP and kindlin-2

Unlike paxillin, determination of the binding affinity of kindlin-2 and the IPP complex turned out to be more difficult. MST measurements conducted with the same setup as for paxillin-IPP with kindlin-2 labeled with NT-647 dye resulted in apparently good-looking binding curves in MST and temperature jumps (Figure 34A). However, a constant increase in fluorescence

intensity was detected with increasing concentration of IPP complex in the capillary scan (Figure 34B) and the fluorescence detected during measurements (Figure 34C). Since this might either indicate a fluorescence enhancement by the IPP complex or be an artifact caused by loss of fluorescent material, an SD-test recommended by the manufacturer was carried out on the remaining samples not loaded into the capillaries. The samples with the three highest and the three lowest IPP concentrations were denatured by addition of SDS and heating, and then their fluorescence values compared to the non-denatured condition. If the change in fluorescence was caused by binding of increasing amounts of IPP to kindlin-NT-647, it should vanish after denaturing of the proteins. However, the denatured samples still showed the same difference in fluorescence between capillaries with high and low amounts of IPP complex, indicating that the measurements are flawed by loss of fluorescent kindlin-2.

This might be due to unspecific interactions of kindlin-NT-647 with pipet tips or plastic tubes in which the samples are mixed. High amounts of IPP complex (50 µM) might "saturate" the surfaces and reduce the probability of kindlin-NT647 (47 nM) interacting with them. This hypothesis was tested by adding 1 mg/ml BSA to the fluorescently labeled kindlin-2 before mixing it with the dilution series of the IPP complex, resulting in a final concentration of 0.5 mg/ml BSA. This should theoretically not interfere with the binding of kindlin-NT-647 to IPP and "saturate" the surfaces to the same amount in all samples.

As expected, BSA reduced the differences in fluorescence intensity to normal levels of ± 50 units without any clear trend of the data points (Figure 34E). However, the resulting binding curve of kindlin-2 towards IPP fluctuates strongly and the fit is not satisfying (Figure 34D, F). This might be because either BSA does unexpectedly interfere with the binding or kindlin-2 stability might be reduced, either by labeling with the NT-647 dye or by using Buffer B2 containing 10 µM $ZnCl_2$, which might lead to aggregation of the protein. Destabilization seems more likely since unlabeled kindlin-2 used in other MST measurements displayed some "stickiness", but to a far less amount which could be countered by using premium coated hydrophilic capillaries. The MST experiment was repeated with unlabeled kindlin-2 and IPP complex labeled with Alexa-647, but no binding could be detected to kindlin-2 in this setup either. This might however be due to problems with the labeled IPP complex, since binding to paxillin could not be detected either.

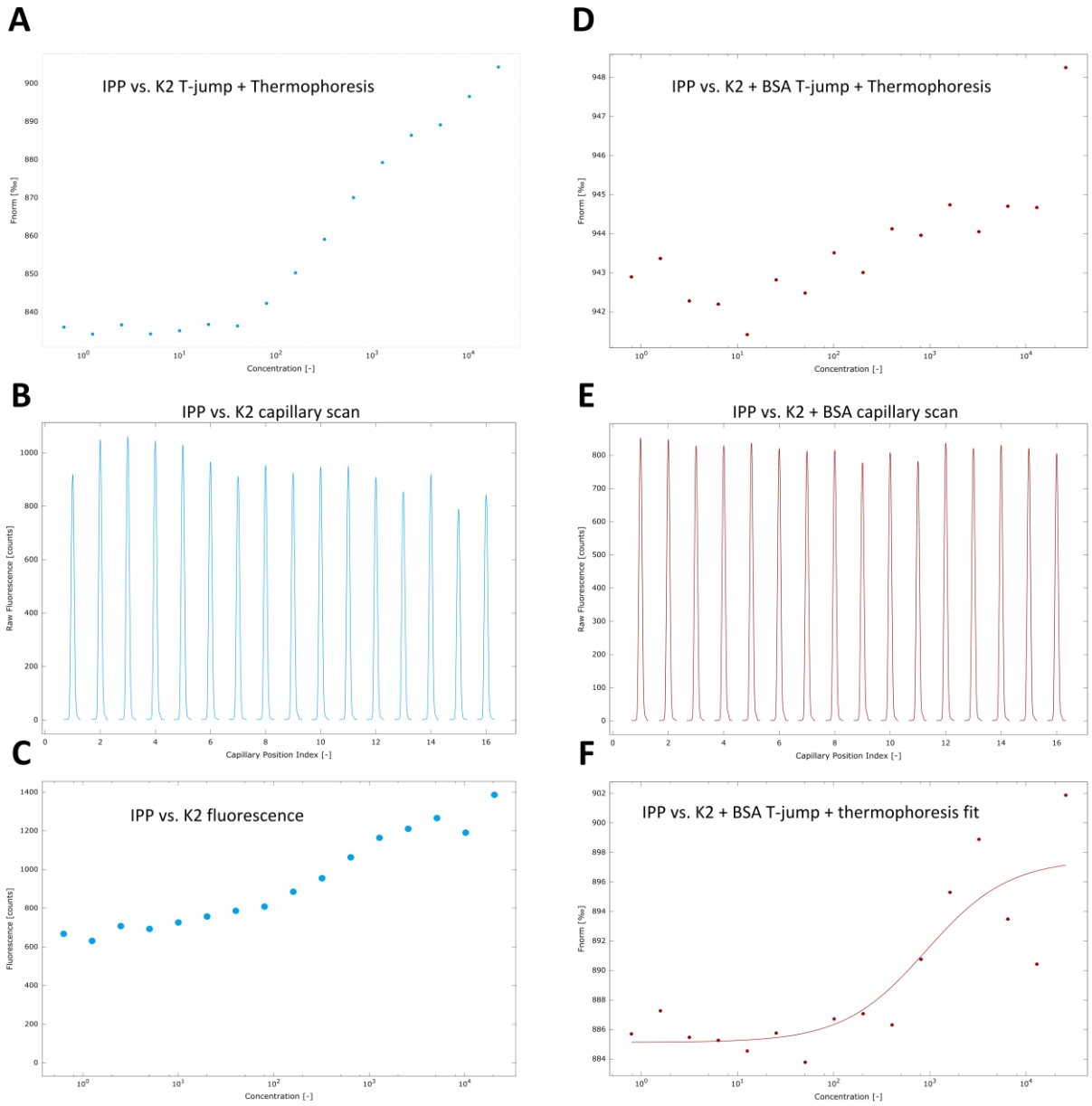

Figure 34: MST measurements to determine the binding affinity of kindlin-2 to the IPP complex. (A) A dilution series of IPP complex (50 µM) with kindlin-2-NT-647 (47 nM) yielded an apparent binding curve in temperature jump and thermophoresis, but also an increase in fluorescence intensity towards high IPP concentrations (B, C). (E) This increase is an artifact caused by loss of kindlin-NT-647, since addition of 1 mg/ml BSA to the fluorescent protein sample removed this difference. (D, F) Addition of BSA also resulted in strong fluctuation of the data points and no clear binding curve. The measurements were carried out in Buffer B2 at 25 °C, using premium coated capillaries.

Conclusively, MST measurements are not suitable for measuring the affinity of kindlin-2 towards the IPP complex. This might instead be achieved by ITC measurements or by ELISA. SPR measurements are also an option. However, in past experiments kindlin-2 displayed a high affinity towards dextrane or polycarboxylate hydrogel surfaces of the SPR chips, interfering with the protein-protein interactions to be detected. Therefore, a passivation of the chip using PEG or PLL-PEG would be necessary.

3.4.6 The IPP complex does not bind directly to integrin tails

Early studies on ILK reported direct interaction of ILK with β1 and β3 integrin tails as well as its ability to phosphorylate the tails (Hannigan et al., 1996). The alleged kinase activity of ILK has since been refuted in several studies and was probably due to co-purification of active kinases together with ILK (Wickstrom et al., 2010). Binding to β1 and β3 integrin tails has been confirmed by GST pull-down assays with recombinant ILK-PKD/α-parvin-CH_2 complex, which was used for crystallization (Fukuda et al., 2009). To test whether this holds true for full-length IPP complex and, if possible, to measure binding affinities, MST, AUC and pull-down experiments were conducted. However, none of the assays showed interaction of IPP with fluorescently labeled or GST-conjugated integrin β1 or β3 tails.

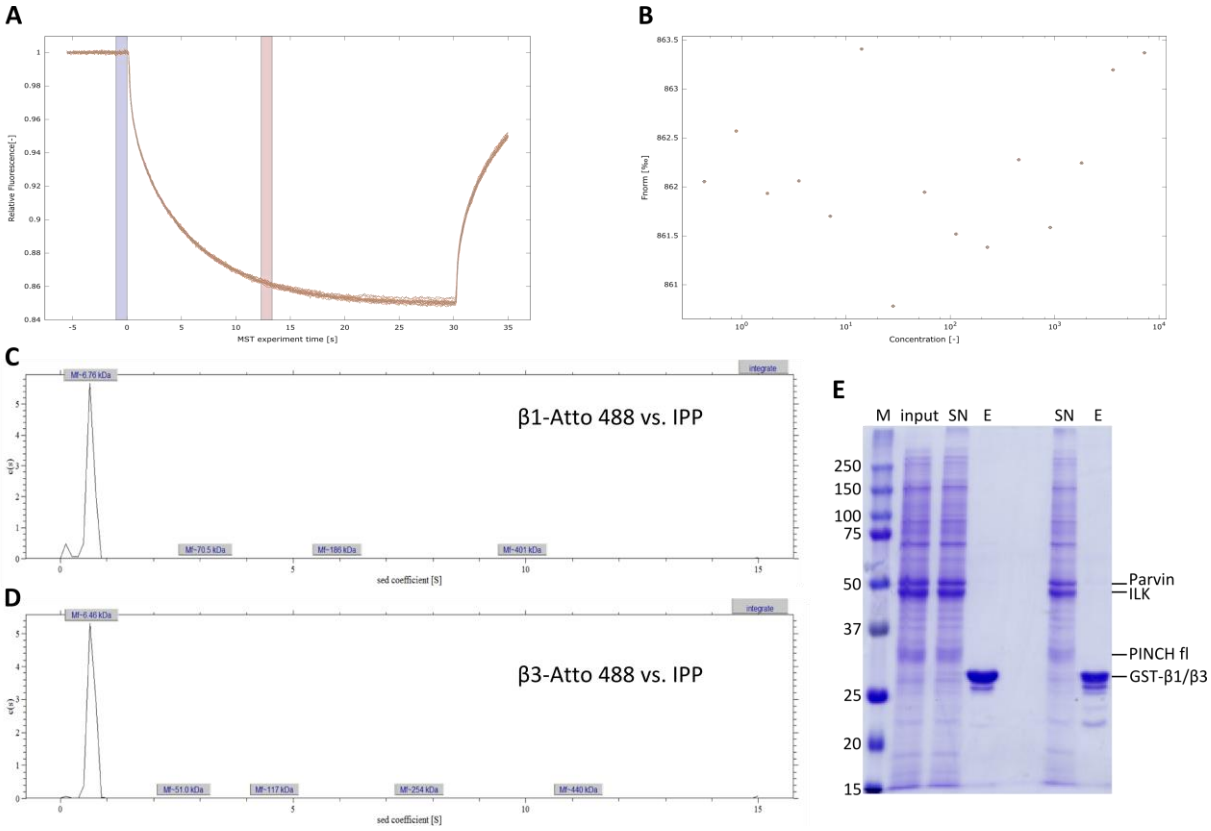

Figure 35: Test for interaction of the IPP complex and integrin β1 or β3 tails by MST, AUC and pull-down experiments. (A, B) In MST measurements with Atto-488-labeled tail peptides (210 nM) versus IPP complex of a concentration up to 50 µM, no interaction could be detected.. The MST measurements were carried out in Buffer B2 at 25 °C, using premium coated capillaries. (C, D) AUC measurements with 10 µM IPP complex and 35/38 µM Atto-488-β1/3 peptide in Buffer B2 were conducted at 14 °C for 16 h and absorption at 503 nm was measured to detect the integrin tail monomers (< 1 S) and a potentially formed complex with IPP. However, no second peak apart from monomeric tail was detected. (E) Pull-down experiments with GST-β1 or –β3 immobilized on GST-beads and IMAC-purified IPP complex also failed to show interactions. SN: unbound proteins, E: eluate

For MST measurements, Atto-488 conjugated β1 tail peptide was dissolved in Buffer B2 and used at a final concentration of 210 nM and added to a 1:1 IPP titration series with a maximum concentration of 50 µM. The fluorescence distribution within the capillaries was within ±50 units without indication of a fluorescence quench or other effect. The MST traces showed no indication of binding, neither in thermophoresis nor in temperature jump analysis (Figure 35A, B). This indicates either no interaction or a K_D value in the very high µM to mM range.

Analytical ultracentrifugation was conducted with Atto-488 conjugated β1 or β3 tail peptide at 35 or 38 µM concentrations in Buffer B2 against 10 µM IPP complex. The samples were adjusted to 400 µl final volume and $A_{503\ nm}$ values of 1.2. The measurements were carried out at 14 °C and detection at 503 nm, ensuring that only the labeled tail peptides are visible in any complexes they might form. Unlabeled peptides are too small (< 5kDa) to cause a detectable shift of the IPP peak, therefore they must be labeled. Like MST, AUC failed to detect any interaction between IPP and either tail peptide (Figure 35C,D). Both AUC traces show only one peak < 1S, representing monomeric unbound tail peptides. Binding of a tail peptide to IPP would have resulted in the detection of a second peak at a much higher sedimentation coefficient. Considering the 3.5-fold excess of integrin tail to IPP complex, even at very low affinity at least a small peak should have been detected (~6 % bound β1 fraction at 500 µM K_D). Therefore, no interaction of IPP and tail peptides could be detected.

In order to reproduce the GST-pull-down assay which was used to show binding by Fukuda *et al*., GST-β1 and GST-β3 fusion proteins were produced in *E. coli* and purified using GST-beads and SEC. Functionality of these fusion proteins was tested by MST measurements with NT-647-labeled GST-β1/3 and unlabeled kindlin-2. The K_D values measured matched those determined with integrin tail peptides (~10 µM range, data not shown). Furthermore, GST-β1/3 immobilized on GST-beads pulled down kindlin-2, confirming its binding activity. However, IPP complex failed to bind to GST-β1/3 on beads (Figure 35E), once more confirming that no interaction takes place between the integrin tails and the IPP complex.

These results contradict the published pull-down experiments with ILK-PKD/parvin CH_2. It is possible that in full-length IPP complex, a potential binding site for integrin tails is hidden by parts of α-parvin or PINCH, which were not present in the published setup. Should this be the

case, ILK would have to be separated from one or both of its binding partners to be able to interact with integrin tails.

3.4.7 Optimization of buffer conditions to reduce aggregation and increase stability of the IPP complex

Considering the thermal instability of the IPP complex and its tendency to form aggregates, which prevents the generation of good samples for cryoEM analysis, an extensive buffer screen was conducted to find conditions, which improve its stability. The screen used was optimized for cryoEM applications and contains 11 different buffer substances at 8 different pH values each (Chari et al., 2015). The buffers were formulated as 10x stock solutions, therefore the protein was diluted in a 10:1 ratio, more or less retaining the salt concentration of the original buffer. Thermal stability in the 88 different buffers was assessed by Thermofluor assay, which yielded very noisy data and no clear thermal transitions and was therefore inconclusive. Additionally, thermal unfolding was determined using NanoDSF measurements, which rendered more reliable transitions (Figure 36B, C).

While the reference sample in the normal purification Buffer B2 and most other buffer sets showed a more or less constant increase in Trp/Tyr fluorescence without a pronounced transition from folded to unfolded, two sets of buffers (Citrate and ADA) showed comparatively clear inflection points. Buffers containing 100 mM ADA (N-(2-Acetamido)iminodiacetic acid) rendered the most pronounced thermal transitions around 52 °C, resulting in the highest final fluorescence values of all samples. This effect was observed for all ADA samples, from pH 6.0 to 7.4, with the highest and sharpest peaks at pH 6.0 and 6.2. However, The ADA samples at pH 6.4 and 6.6 displayed a later onset of thermal unfolding than the other samples, with potentially a second transition around 40 °C. This might indicate more overall stability than just higher final fluorescence values, which could be caused by the ADA itself.

The buffer set containing 100 mM Citrate from pH 5.5 to 7.25 also rendered clear transitions around 50 °C, with the best curves at pH 5.75 and 6.0. In these two conditions, the initial fluorescence values are slightly lower than the reference and stay lower until the first transition point is reached, indicating less unfolding at temperatures below the inflection point. A second transition around 70 °C can be detected in the pH 6.0 and 6.25 samples.

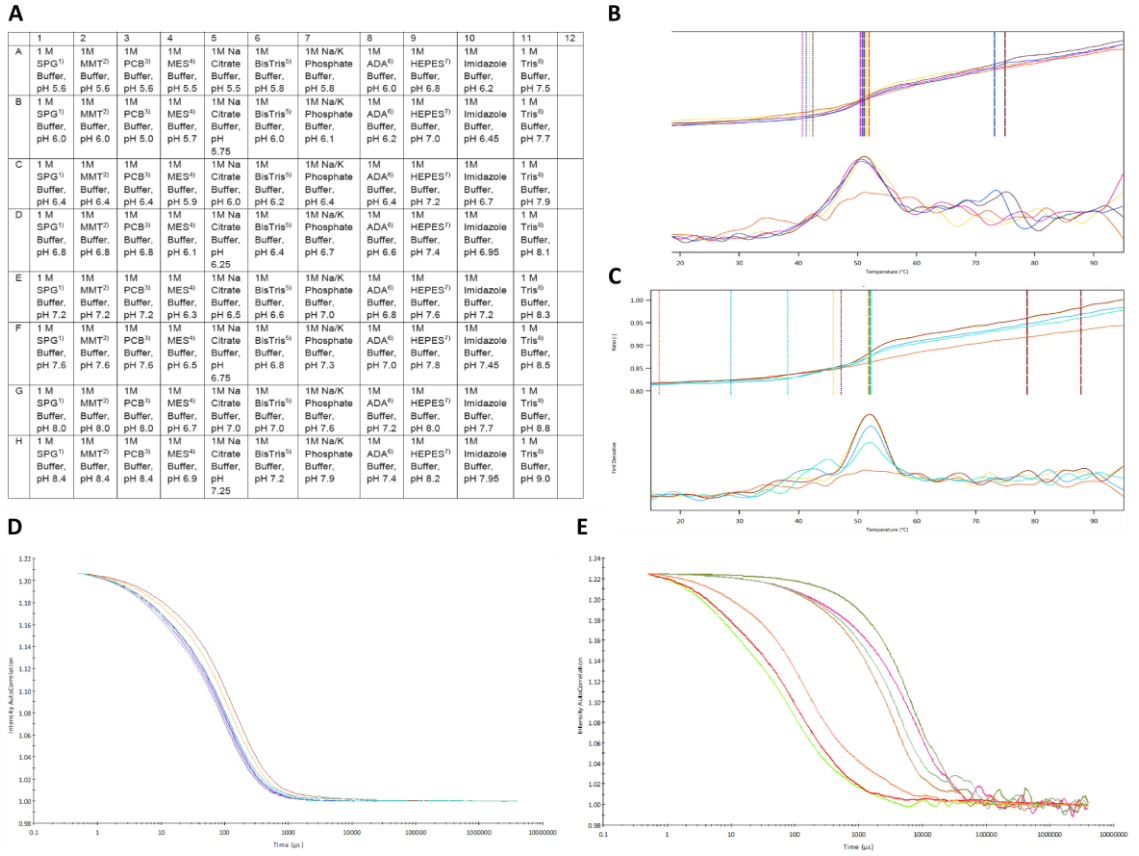

	1	2	3	4	5	6	7	8	9	10	11	12
A	1 M SPG[1] Buffer, pH 5.6	1M MMT[2] Buffer, pH 5.6	1M PCB[3] Buffer, pH 5.6	1M MES[4] Buffer, pH 5.5	1M Na Citrate Buffer, pH 5.5	1M BisTris[5] Buffer, pH 5.8	1M Na/K Phosphate Buffer, pH 5.8	1M ADA[6] Buffer, pH 6.0	1M HEPES[7] Buffer, pH 6.8	1M Imidazole Buffer, pH 6.2	1 M Tris[8] Buffer, pH 7.5	
B	1 M SPG[1] Buffer, pH 6.0	1M MMT[2] Buffer, pH 6.0	1M PCB[3] Buffer, pH 5.0	1M MES[4] Buffer, pH 5.7	1M Na Citrate Buffer, pH 5.75	1M BisTris[5] Buffer, pH 6.0	1M Na/K Phosphate Buffer, pH 6.1	1M ADA[6] Buffer, pH 6.2	1M HEPES[7] Buffer, pH 7.0	1M Imidazole Buffer, pH 6.45	1 M Tris[8] Buffer, pH 7.7	
C	1 M SPG[1] Buffer, pH 6.4	1M MMT[2] Buffer, pH 6.4	1M PCB[3] Buffer, pH 6.4	1M MES[4] Buffer, pH 5.9	1M Na Citrate Buffer, pH 6.0	1M BisTris[5] Buffer, pH 6.2	1M Na/K Phosphate Buffer, pH 6.4	1M ADA[6] Buffer, pH 6.4	1M HEPES[7] Buffer, pH 7.2	1M Imidazole Buffer, pH 6.7	1 M Tris[8] Buffer, pH 7.9	
D	1 M SPG[1] Buffer, pH 6.8	1M MMT[2] Buffer, pH 6.8	1M PCB[3] Buffer, pH 6.8	1M MES[4] Buffer, pH 6.1	1M Na Citrate Buffer, pH 6.25	1M BisTris[5] Buffer, pH 6.4	1M Na/K Phosphate Buffer, pH 6.7	1M ADA[6] Buffer, pH 6.6	1M HEPES[7] Buffer, pH 7.4	1M Imidazole Buffer, pH 6.95	1 M Tris[8] Buffer, pH 8.1	
E	1 M SPG[1] Buffer, pH 7.2	1M MMT[2] Buffer, pH 7.2	1M PCB[3] Buffer, pH 7.2	1M MES[4] Buffer, pH 6.3	1M Na Citrate Buffer, pH 6.5	1M BisTris[5] Buffer, pH 6.6	1M Na/K Phosphate Buffer, pH 7.0	1M ADA[6] Buffer, pH 6.8	1M HEPES[7] Buffer, pH 7.6	1M Imidazole Buffer, pH 7.2	1 M Tris[8] Buffer, pH 8.3	
F	1 M SPG[1] Buffer, pH 7.6	1M MMT[2] Buffer, pH 7.6	1M PCB[3] Buffer, pH 7.6	1M MES[4] Buffer, pH 6.5	1M Na Citrate Buffer, pH 6.75	1M BisTris[5] Buffer, pH 6.8	1M Na/K Phosphate Buffer, pH 7.3	1M ADA[6] Buffer, pH 7.0	1M HEPES[7] Buffer, pH 7.8	1M Imidazole Buffer, pH 7.45	1 M Tris[8] Buffer, pH 8.5	
G	1 M SPG[1] Buffer, pH 8.0	1M MMT[2] Buffer, pH 8.0	1M PCB[3] Buffer, pH 8.0	1M MES[4] Buffer, pH 6.7	1M Na Citrate Buffer, pH 7.0	1M BisTris[5] Buffer, pH 7.0	1M Na/K Phosphate Buffer, pH 7.6	1M ADA[6] Buffer, pH 7.2	1M HEPES[7] Buffer, pH 8.0	1M Imidazole Buffer, pH 7.7	1 M Tris[8] Buffer, pH 8.8	
H	1 M SPG[1] Buffer, pH 8.4	1M MMT[2] Buffer, pH 8.4	1M PCB[3] Buffer, pH 8.4	1M MES[4] Buffer, pH 6.9	1M Na Citrate Buffer, pH 7.25	1M BisTris[5] Buffer, pH 7.2	1M Na/K Phosphate Buffer, pH 7.9	1M ADA[6] Buffer, pH 7.4	1M HEPES[7] Buffer, pH 8.2	1M Imidazole Buffer, pH 7.95	1 M Tris[8] Buffer, pH 9.0	

Figure 36: Determination of the influence of different buffer substances and pH values on thermal stability and aggregation of the IPP complex. (A) 11 different buffer substances at 8 different pH values each were added as 10x stock solutions to the sample, retaining the sample's initial salt concentration. SPG 10x: 0.125 M Succinic acid, 0.5 M NaH_2PO_4, 0.375 M Glycine; MMT 10x: 0.2 M DL-Malic acid, 0.4 M MES, 0.4 M Tris; PCB 10x: 0.4 M Sodium Propionate, 0.2 M Sodium cacodylate trihydrate, 0.4 M Bis-Tris Propane; ADA 10x: 1 M N-(2-Acetamido) iminodiacetic acid. (B, C) NanoDSF measurements were carried out with IPP complex diluted in the respective buffers at a final concentration of 0.1 mg/ml, same as for the DLS measurements. The melting curves for Citrate Buffer pH 5.5-6.25 (B) and ADA buffer pH 6.0-6.6 (C) gave the best results in NanoDSF. Buffer B2, used for purification, is included in the analyses as an orange curve for reference. (D) DLS measurements also identified the Citrate Buffer series as most promising, since it yields nicely defined decays and smaller particles than the reference. (E) The ADA buffer samples all contained very large inhomogeneous particles, which indicate that it is not suited for cryoEM and other sensitive applications.

The limiting factor when working with recombinant IPP is its tendency to form aggregates. Therefore, all samples were additionally analyzed by dynamic light scattering to test how large the IPP particles are in the different buffers. Most buffers tested yielded decay curves that were very similar to the Buffer B2 reference and thus indicated no improvement. Surprisingly, the samples containing ADA which seemed to improve thermal stability all rendered curves

indicating very large particles and high polydispersity, if the curves could be determined at all due to sample inhomogeneity (Figure 36E)

The samples containing Citrate buffer, however, yielded very good decay curves, which indicated smaller particles than the reference in Buffer B2. The best pH conditions are pH 6.0 and 6.25, in accordance with the NanoDSF measurements.

The results from this screen indicate that using citrate as a buffer substance at pH 6.0 or 6.25 might increase thermal stability of the IPP complex as well as reduce aggregation. This has to be tested further and samples purified in citrate buffer analyzed by negative staining to see if they lead to a more homogeneous particle distribution.

ADA seemed to improve thermal properties of the IPP complex but dramatically increases the polydispersity of the sample. Furthermore, it is not an optimal buffer substance for the intended purposes since it chelates divalent metal ions like Zn^{2+}, absorbs light at wavelengths <260 nm and its solubility in H_2O at 4 °C is only 90 mM, which might have caused aggregates of the 100 mM buffer in the DLS samples that are unrelated to the protein.

3.4.8 Chemical crosslinking of focal adhesion complexes

In addition to cryoEM studies and crystallization trials, complexes of IPP, kindlin-2 and paxillin were assembled, crosslinked with the NHS-reactive, isotopically light and heavy labeled BS3 crosslinker, enzymatically digested and analyzed via LC-MS. This approach allows for the identification of protein surfaces which are sterically in close proximity within the complex, so that one Lys residue on each surface can interact with either side of the bifunctional crosslinker. The crosslinks stay intact through enzymatic digest and keep formerly close peptides linked until mass spectrometric analysis. There, the crosslinked peptides are identified and a crosslinking network can be established to represent all protein surfaces within the complex, which are in close proximity. It has to be noted that a crosslink does not necessarily have to indicate the exact interaction surface of two proteins. In many cases, binding of the proteins makes lysines within the binding surface inaccessible or there are simply no lysines involved in the binding. It is more likely that surfaces next to the binding interfaces become crosslinked, where lysines are readily accessible on the protein surface.

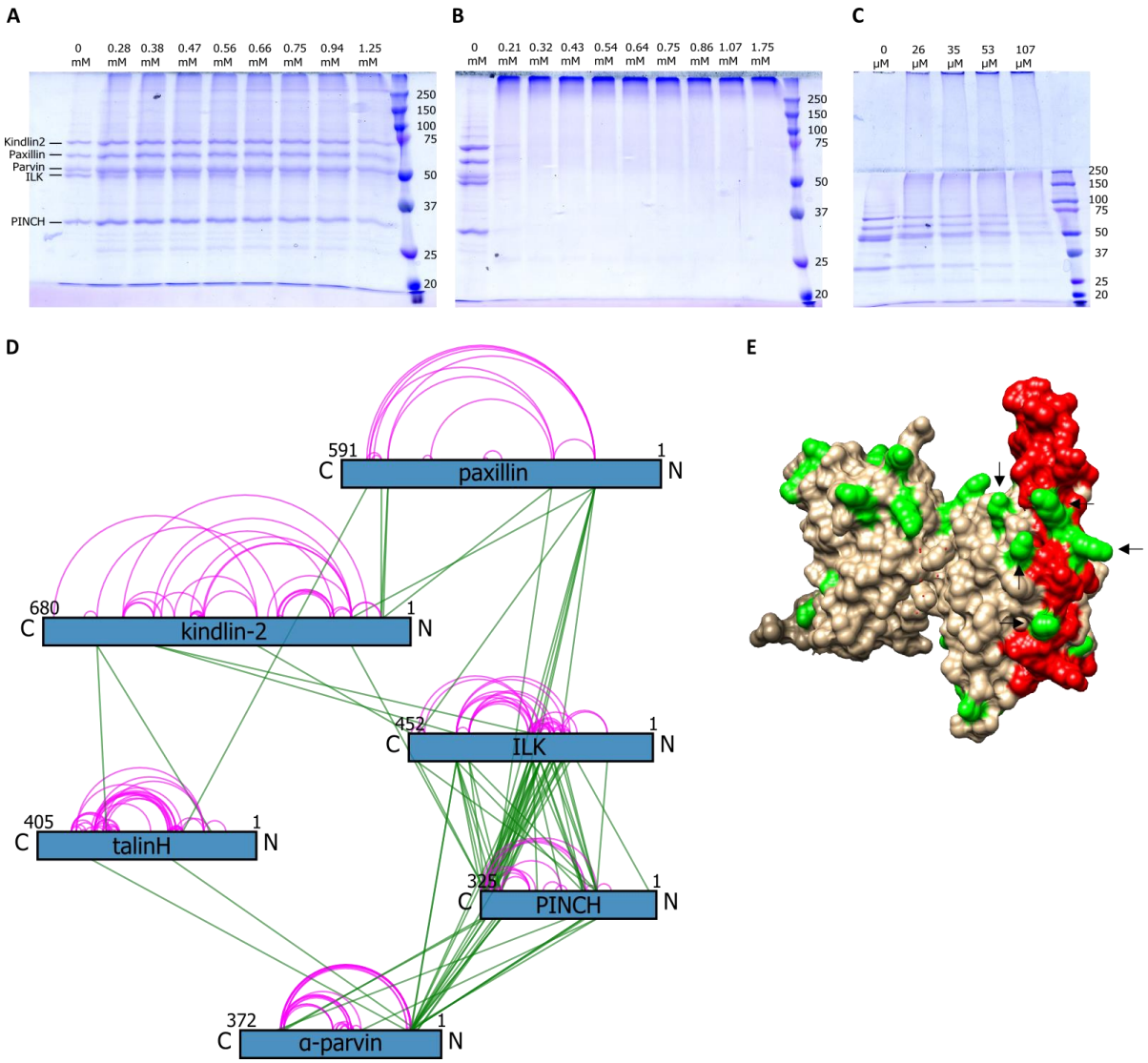

Figure 37: Crosslinking of adhesome complexes with BS3. (A) Ni-NTA immobilized IPP#4 was incubated with kindlin-2, paxillin, THD and integrin β1 tail peptide and eluted with 500 mM imidazole. The eluate was crosslinked with increasing concentrations of BS3, resulting in inefficient crosslinking. (B) Another sample, which was passed through a desalting column prior to crosslinking to reduce the imidazole concentration displayed heavy crosslinking even at the lowest BS3 concentration. (C) The final samples used for digest and LC-MS analysis were crosslinked with 53 and 107 µM BS3. (D) The crosslinks identified in three independent experiments are displayed in a schematic representation of the individual components. Pink lines represent intra-protein crosslinks, green lines are inter-protein crosslinks . (E) No crosslinks between the integrin tail and THD or kindlin were detected, although the THD-β1 complex has several accessible lysines on the surface (marked by black arrows). Depicted is the complex of talin-F2F3 (grey) and integrin β1D tail peptide (red) (PDB: 3G9W). Lysine residues accessible on the surface of the proteins are highlighted in green.

In initial crosslinking trials, recombinant IPP#4 was immobilized on Ni-NTA beads and incubated with excess kindlin-2, paxillin, THD and integrin β1 tail peptide in order to assemble a large complex. After washing with Buffer B4 to remove unbound proteins, the complex was eluted with Buffer B5 and applied on a desalting column to remove most of the imidazole, which reacts with the BS3 crosslinker at high concentrations (Figure 37A, B). In order to obtain

a reasonable amount of inter-protein links but to prevent unspecific crosslinking caused by too high amounts of BS3, for each experiment a titration series was performed on small amounts of the sample prior to the actual crosslinking reaction. Then, the two best concentrations were chosen for the actual sample preparation (Figure 37C).

The samples were denatured and digested with Trypsin and LysC and the crosslinked peptides enriched and analyzed via LC-MS by The PhD student Mia Potočnjak of the Franz Herzog group (LMU Gene Center). For better visualization, the detected crosslinks were displayed in a schematic network (Figure 37D). The crosslinks represent three individual experiments with two different crosslinker concentrations each. A large number of crosslinks have been detected between the components of the IPP complex, as was to be expected since it was used as basis for complex assembly. The most heavily crosslinked region of the entire complex is the PINCH-LIM5 domain (AA 262-325), with many links to ILK and α-parvin and some to kindlin-2 and paxillin. This is surprising, since the LIM5 domain has not been shown to be required for the formation of the IPP complex. The “minimal” IPP complex is comprised of parvin CH2 domain, ILK and PINCH-LIM1 domain and sufficiently stable to be purified (Stiegler et al., 2013). Furthermore, LIM5 appears to be in close proximity to so many surfaces of different proteins that it would have to be at the very center of the complex with all other proteins arranged around it. Another potential explanation is that LIM5 is mostly unstructured and highly flexible and therefore can “reach” many different protein domains without binding to them.

None of the experiments yielded any crosslinks of an adhesome protein to the integrin β1 tail peptide, although the tail was present after the pull-downs and intramolecular crosslinks within the tail were observed. It is possible that the intra links were established in tail peptides, which have become unbound from kindlin or talin due to fast off-kinetics. If there had been a sufficient amount of bound tail in the complex, crosslinks should have formed, as becomes clear from the crystal structure of the THD-integrin tail complex which has several accessible lysine residues on the surface near the binding interface (Figure 37E). To test whether PINCH-LIM5 has a central position in the IPP complex as well as in the IPP-kindlin-paxillin complex or whether it is unstructured and flexible, a mutant IPP complex (IPP#5) lacking the LIM5 domain was produced. If the LIM5 domain were indeed interacting with all proteins the crosslinks imply, its deletion should have consequences on stability of the IPP complex and on complex assembly.

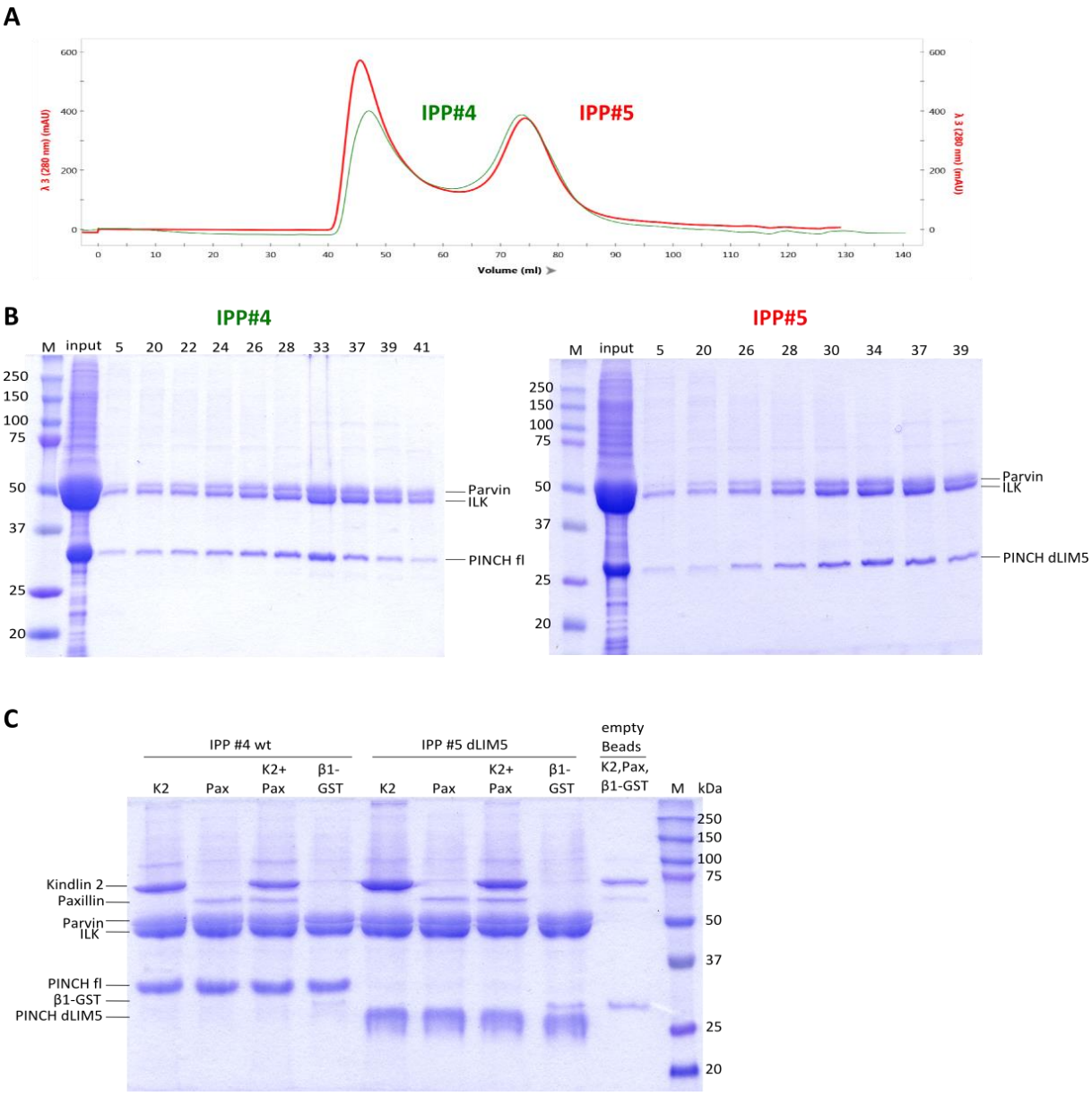

Figure 38: Purification and complex formation of IPP#4 and IPP#5. (A) IPP#4 and #5 were expressed and purified in parallel and their behavior was compared. SEC profiles of both constructs were identical, with a small shift of IPP#5 from 73 to 74 ml elution volume, due to its smaller size (136 kDa vs. 126 kDa). (B) The purity of the SEC fractions was also identical, as well as the yields (~5 mg both). (C) The ability to bind paxillin and kindlin-2 was assessed in pull-down assays with IPP#4 and #5 immobilized on Ni-NTA beads. Both constructs seem to bind equal amounts of kindlin and paxillin and more than is bound unspecifically to the beads. Additionally, the ability of either construct to bind GST-integrin β1 was assessed, but only the same amount of protein as on empty beads was bound.

pACEBac1-IPP-dLIM5 was generated by introducing a stop-codon after the PINCH-LIM4 domain via site-directed mutagenesis using primers PaKa242/243 and the pACEBac1-IPP vector as template. The correct insertion of the desired mutation and the absence of unwanted mutations were confirmed by sequencing the entire coding sequences of ILK, α-parvin and PINCH.

In order to directly compare IPP#4 and #5 they were expressed and purified in parallel, using one liter of insect cell culture each. After performing Ni-NTA purification on beads, both samples were applied on a Superdex200 SEC column (Figure 38A, B). Purity and yield was almost identical for both constructs (~5 mg each), the SEC elution profiles were identical except for a small shift of IPP#5 to higher elution volumes due to the slight reduction in size (10 kDa). This indicates that deletion of LIM5 does not de-stabilize the IPP complex, reduce its solubility or increase losses due to aggregation.

In Ni-NTA pull-down assays the ability of both constructs to bind kindlin-2 and paxillin was tested (Figure 38C). IPP#4 and #5 were immobilized on Ni-NTA beads and incubated with excess tag-less kindlin and paxillin. Both constructs appear to bind similar amounts of the proteins, which are higher than the amounts of unspecifically bound proteins on the beads. This indicates that deletion of the LIM5 domain does not reduce the complex formation with kindlin-2 and paxillin, which would be expected if the domain was truly interacting with both proteins. Furthermore, pull-downs with GST-tagged integrin β1 tail showed no interaction with either construct. There is some protein bound in both samples, but the amounts are identical to that bound to the empty beads control, indicating some stickiness of the GST-β1 but no bona fide binding.

Finally, both constructs were crosslinked with paxillin, kindlin-2, integrin β1 and THD and the crosslinking patterns were compared. For this experiment, the complexes were not eluted from the Ni-NTA beads but instead crosslinked while still bound. Denaturing and enzymatic digest then released the proteins from the beads, which do not interfere with any of the processing steps. Optimal crosslinker concentrations were determined through a titration series performed on small aliquots of the bead-immobilized complexes (Figure 38A).

In the absence of the PINCH-LIM5 domain, previously unobserved inter-protein crosslinks between ILK and α-parvin, paxillin and α-parvin and ILK and paxillin were detected. The intra-protein crosslinks are mostly unchanged, indicating that the conformation of the adhesome proteins is not dramatically changed upon removal of LIM5. Taken together, all experiments with the IPP#5 construct indicate that LIM5 is not the central element holding the complex together but rather an unstructured domain with high flexibility that happens to be in close proximity to several components of the complex. It is possible that the LIM5 domain adopts a

less flexible conformation when it is bound to RSU-1 and then mediates a biological function in adhesome assembly.

3.4.9 Structural information on the IPP-kindlin-paxillin complex gained by crosslinking

The intra-protein crosslinks show that in α-parvin, three regions are mainly crosslinked, the potentially unstructured N-terminus, the central part of the CH1-domain and the N-terminal part of the CH2 domain. The lysine residues in all these regions are crosslinked, suggesting that they face towards each other and possibly form a binding interface. The same residues were also crosslinked to ILK, PINCH and paxillin and thus probably face towards the center of the complex.

The N-terminal residues K56 and K57 were linked to the ILK pseudokinase domain (PKD, K209, K223, K364), as well as to the ANK5 domain. The CH1 domain of parvin (K163) was linked to ILK ANK3 (K85) and the N-terminus of the CH2 domain (K292, 298, 306) was linked to ILK ANK3 (K85) and ANK5 (K154, 165). All three regions in parvin were also linked to PINCH LIM2 (K111) and LIM3 (K132). Furthermore, the CH2 domain showed one crosslink to the C-terminus of paxillin LD4 domain. In the NMR structure of parvin-CH2 in complex with paxillin LD4 (PDB: 2VZI), the crosslinked K277 in paxillin is not included but is only three residues away from the C-terminus of the LD4 peptide and thus in range of K292 in parvin. Therefore, the detected crosslink is in good accordance with the known parvin-paxillin LD4 structure.

Since the PINCH LIM5 domain has been shown to be flexible and probably does not contribute to the stability of the complex, the crosslinks to LIM5 are omitted from the analysis to avoid drawing false conclusions. The intra-protein crosslinks in ILK indicate that ANK3 (K85), ANK5 (K165/170), the linker between ANK5 and PKD (K184) and the central part of the PKD (K209/220) are in close proximity. While ANK3 is linked to α-parvin, ANK5, linker region and PKD are all crosslinked to PINCH LIM2 domain (K84/111) and the linker between LIM2 and LIM3 (K132). The same residues in ILK and in PINCH are involved in binding to parvin CH1 domain and to the N-terminus of the CH2 domain, suggesting a central binding interface within the IPP complex formed by the α-parvin N-terminus, the center of the CH1 domain and the N-terminus of the CH2 domain, the N-/C-terminus and center of the PKD, ANK3 and ANK5 of ILK and PINCH LIM2.

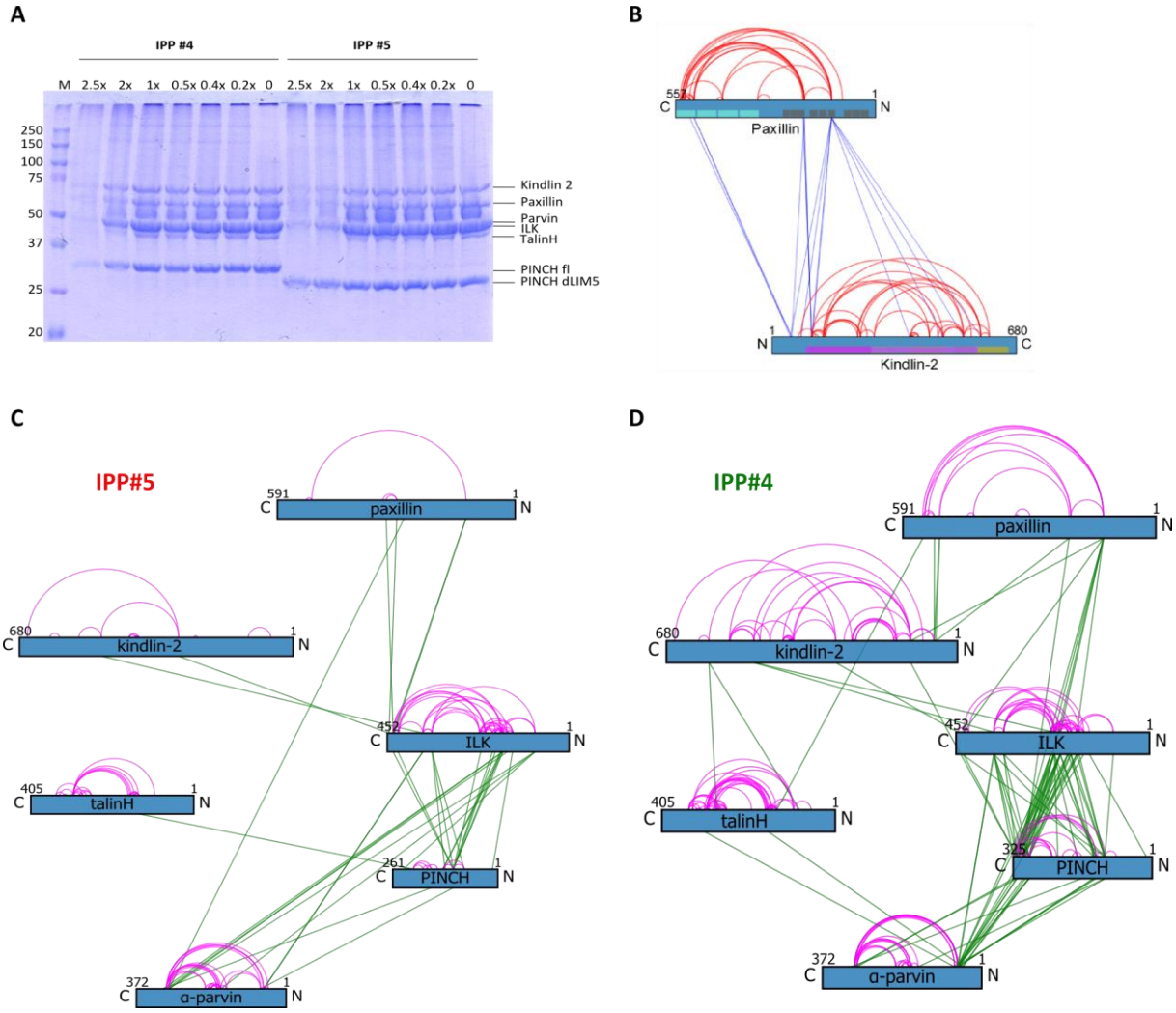

Figure 39: Crosslinking networks of IPP#4 and IPP#5 in complex with kindlin-2, paxillin and THD. (A) Titration series indicated that 2x/1.7x molar excess of BS3 crosslinker for IPP#4/#5 immobilized on Ni-NTA beads and complexed with kindlin-2, paxillin, THD and integrin β1 peptide yielded optimal amounts of linkage between the proteins. (C, D) Direct comparison of the resulting crosslink distributions indicates that the presence of the LIM5 domain in IPP#4 prevents many crosslinks between ILK and parvin or paxillin and parvin, which are observed in IPP#5. This confirms the hypothesis that LIM5 is very flexible and not essential for complex formation. (B) The crosslinks between kindlin-2 and paxillin can be compared to those observed in an experiment with only kindlin and paxillin (data by M. Veelders, P. Rombaut and M. Potočnjak). Crosslinking was carried out on Ni-Sepharose beads in Buffer B4.

The intra-protein crosslinks in paxillin match exactly those observed in crosslinking studies with kindlin-2 and paxillin alone (experiment carried out by M. Veelders and analyzed by P. Rombaut and M. Potočnjak, **Figure 39**B). This indicates that in the pentameric complex with IPP and kindlin-2, paxillin does not adopt a significantly different conformation from that in complex with kindlin-2 alone. The same holds true for the intra-protein links in kindlin-2.

In paxillin, the residues involved in inter-protein crosslinks are limited to K123 at the N-terminus of the LD2 motif, K199/203 between LD2 and LD3, and K506 at the C-terminus of the

LIM3 domain. This indicates that the same areas in paxillin are involved in protein-protein interactions when it is bound to kindlin-2 alone or additionally to the IPP complex.

The inter-protein crosslinks between kindlin F_0 domain (K51/55) and paxillin LIM3 domain (K506/518) are identical in the dimeric and in the pentameric complex, indicating that these protein domains interact in the same manner in both complexes.

Table 9: Overview of adhesome protein domains. All domain boundaries were obtained from the UniProt website. The α-parvin used in this study contains an N-terminal His_8-tag and a PreScission site, adding 32 residues to the protein. The paxillin used is isoform α, however the domain boundaries given at UniProt correspond to the longer, alternatively spliced isoform β and had to be adjusted for correct localization of the crosslinks.

Protein	Domain	Residues	Actual residues wt/iso
ILK	ANK1	2-30	
	ANK2	31-63	
	ANK3	64-96	
	ANK4	97-129	
	ANK5	130-174	
	PKD	193-446	
α-parvin	CH1	127-233	95-201
	CH2	294-401	262-369
PINCH	LIM1	10-62	
	LIM2	71-121	
	LIM3	135-184	
	LIM4	193-243	
	LIM5	252-303	
Kindlin-2	F0	0-96	
	F1	97-276	
	F2-N	277-326	
	PH	380-476	
	F2-C	496-568	
	F3	569-653	
Paxillin	LD1	3-15	3-15
	LD2	144-156	144-156
	LD3	216-228	216-228
	LD4	265-276	265-276
	LD5	299-311	333-345
	LIM1	322-381	356-415
	LIM2	382-439	416-473
	LIM3	440-499	474-533
	LIM4	500-557	534-591
Talin	F0	1-85	
	F1	86-202	
	F2	203-309	
	F3	310-400	

However, the crosslinks between paxillin K199 and K506 and the kindlin PH domain, which represent a second binding site of the two proteins observed in the kindlin-paxillin complex, are absent in the pentameric complex. Instead, K123 is heavily crosslinked to the C-terminus of ANK5 and the N-terminus of the pseudokinase domain of ILK. In kindlin-2, K476 is crosslinked to K223 in ILK PKD, the same residue that is crosslinked to paxillin K123, putting all three residues spatially close together. This explains the absence of the paxillin-K123-kindlin-K476 link, which is replaced by two crosslinks to ILK. A similar observation can be made for paxillin-K123, ILK-K438/448 and kindlin-K285, where the former crosslink between kindlin and paxillin is replaced by two crosslinks to ILK. This indicates that in the pentameric complex, kindlin and paxillin are still attached via the same surfaces as in the dimeric complex but are now both additionally interacting with the N- and C-terminus of ILK PKD. The ILK-

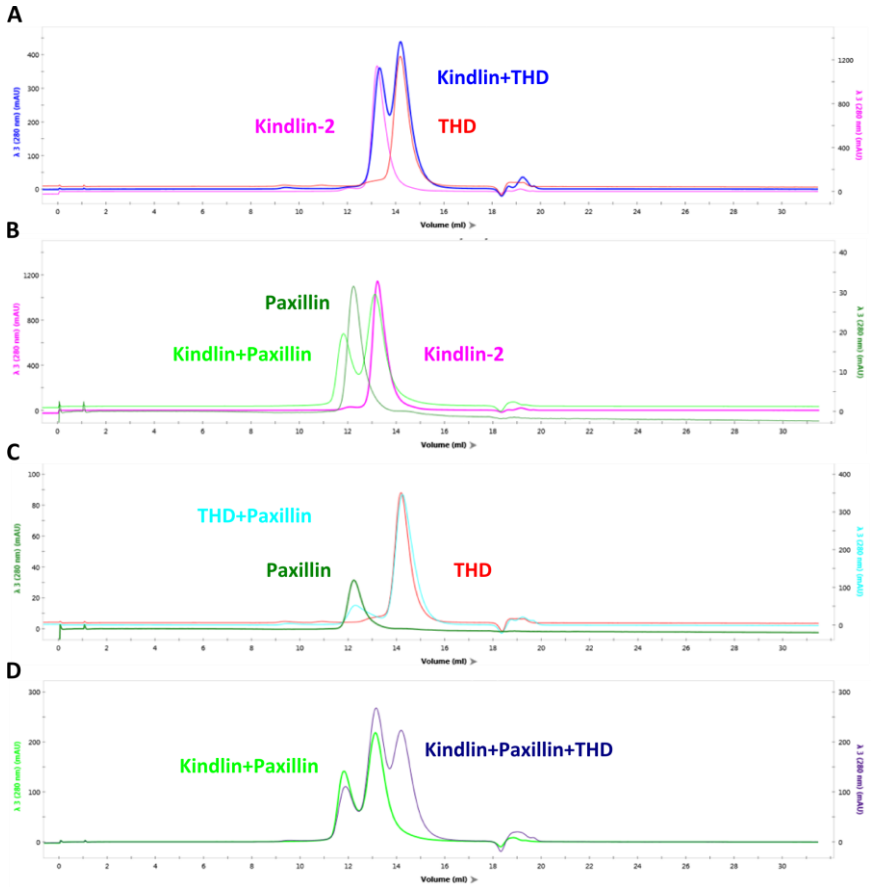

Figure 40: SEC analyses of THD with kindlin-2 and paxillin to test for complex formation. (A) Recombinant THD, kindlin-2 and paxillin were applied on an analytical gel filtration column separately and in combination and the chromatograms were overlaid to detect interactions. Neither kindlin-2 (A) nor paxillin (C) form a complex with THD, which would result in a shift of the elution peak towards lower elution volumes. (B) The interaction of kindlin-2 and paxillin, however, is clearly detectable by a slight shift of the paxillin peak. The reason why the shift is not more pronounced is that paxillin becomes compacted upon binding to kindlin-2. (D) THD cannot bind to the kindlin-2-paxillin complex either, ruling out the possibility that upon complex formation a new binding interface is created by conformational changes. The SEC runs were performed using a SEC650 column in Buffer A3 at 4 °C.

binding interface in kindlin-2 has been mapped to a 38 AA linker sequence between F_2-N and the PH domain (Huet-Calderwood et al., 2014), which fits to the crosslinked residues K476 and K285 in kindlin, which are attached to ILK PKD. In summary, the crosslinks suggest that the kindlin-2 and paxillin interactions are identical in the dimeric and in the pentameric complex and that both proteins bind to ILK PKD at the same time.

The intra-protein crosslinks observed for THD fit perfectly into the crystal structure (PDB: 3IVF), indicating that the protein adopts the same conformation as in the crystal. However, it is not clear whether the observed inter-protein links to α-parvin, kindlin-2, paxillin and PINCH are genuine or an artifact caused by unspecific binding of THD to the beads used for complex assembly. Each inter-protein crosslink involving THD was found only once in several independent experiments, while almost all other inter-links were detected at least twice. Furthermore, since the adhesome proteins studied are all rich in lysines, most inter-crosslinks are “multiplied”, for neighboring lysines tend to be crosslinked with the same partner when

they both are in the vicinity. This is not the case for THD, although it displays a lot of intra-protein crosslinks and thus readily accessible lysines.

Another indication that THD might be only non-specifically linked to the other proteins is that in SEC and AUC analyses, no interaction of THD with any of the other components was detected (Figure 31C, Figure 32C). Therefore, the THD inter-crosslinks might derive from THD sticking to the beads and being in close vicinity to the other proteins without actually binding to any of them. This also explains why there are single, non-reproducible crosslinks to four of the proteins. Another explanation might be that the THD association with the other adhesome components is only very transient and that THD is not included in a tight complex but is constantly dissociating and re-binding to the complex, making its fixation via crosslinks difficult and preventing the co-elution with other proteins on SEC or AUC.

3.4.10 Model of the IPP complex based on existing structural information

The crosslinks identified in the IPP-kindlin-paxillin complex can be displayed in existing NMR or crystal structures using the Xlink Analyzer plug-in for UCSF Chimera (Kosinski et al., 2015). This program inserts crosslinks between specified lysine residues within the same protein or in different components of a multi-protein complex. Depending on the spatial restrictions given by the chemical crosslinker, the crosslinks are displayed in blue if the distance between the lysine residues matches the restriction or in red if this is not the case. The length of one BS3 molecule and two lysine side chains is ~30 Å, therefore the spatial restriction between the backbones of two linked proteins was set to 30 Å.

Of particular interest are the crosslinks found between ILK ANK and ILK PKD, as they might give an indication of how the two halves of ILK are oriented towards each other. To approach this objective, the crystal structures of ILK PKD in complex with α-parvin CH2 domain (PDB: 3KMU) and of ILK ANK in complex with PINCH LIM1 domain (PDB: 4HI8) were merged into one structure. Then the crosslinks were listed in .csv files including the chain names and the absolute positions of the crosslinked lysines (see appendix) and loaded into the Xlink analyzer dialog. The plug-in then displays the crosslinks and facilitates “interactive docking”, where domains can be moved and rotated while the crosslinks are retained and change color from red to blue when the spatial restrictions are met. This allows the rough positioning of ILK PKD/parvin CH2 and ILK ANK/PINCH LIM1 towards each other.

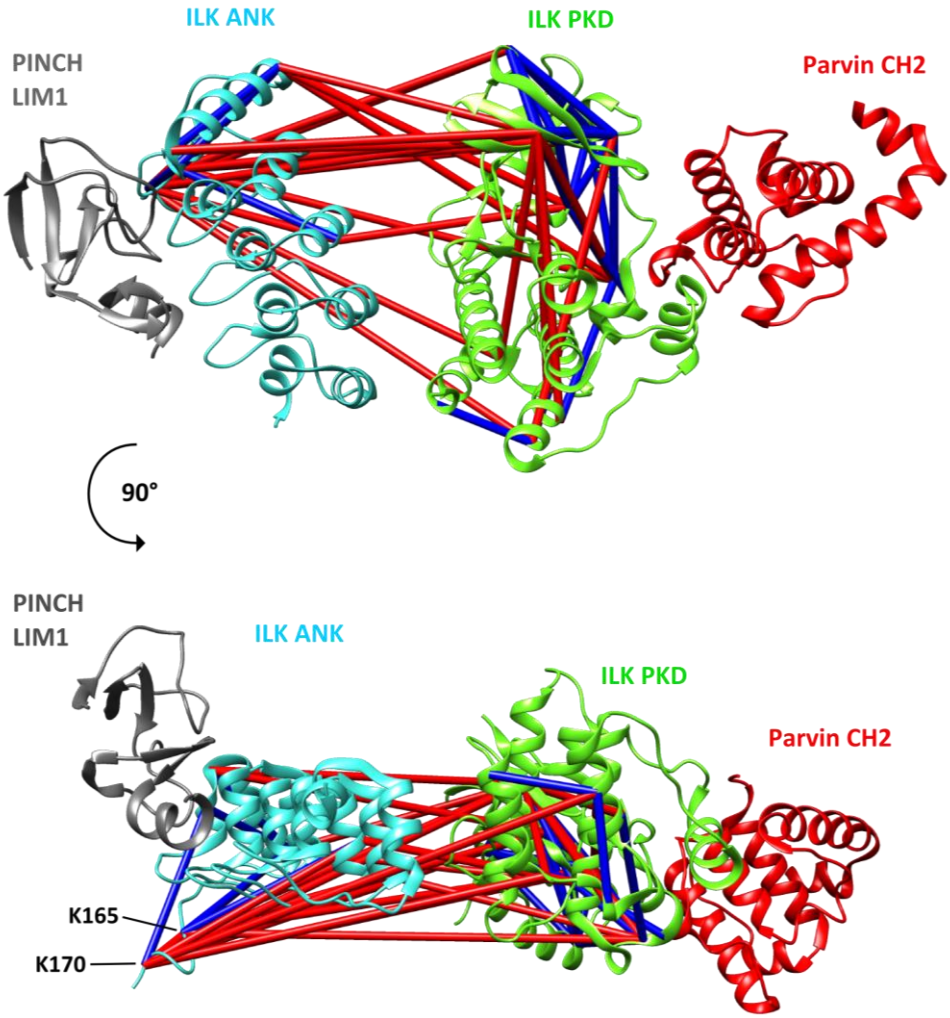

Figure 41: Display of the intra-protein crosslinks of ILK in existing crystal structures of ILK PKD/parvin CH2 (PDB: 3KMU) and ILK ANK/PINCH LIM1 (PDB: 4HI8). The two structures were merged, placed randomly at first and the crosslinks were displayed, with a distance limit of 30 Å. The crosslinks are colored in red (violating the distance restriction) and blue (below restriction). Within ILK PKD, some red crosslinks span the whole domain, indicating that they are not within one molecule but between two neighboring ILK PKD molecules. ILK ANK residues K165 and K170 are heavily crosslinked to a multitude of residues, indicating non-specific links. These links were omitted in further analyses. Grey: PINCH LIM1 domain, blue: ILK Ankyrin repeat domain, green: ILK pseudokinase domain, red: parvin CH2 domain

Of course, this is only a very crude approach to gain structural information on the complex and should by no way be treated as a precise model from which structural insight can be deduced. It can only serve as a tool to roughly positon the domains and to exclude certain orientations which are not supported by the crosslinks. Furthermore, the two separate crystal structures of ILK PKD and ANK do not necessarily have to represent the conformations of the two domains in the full-length IPP complex.

Initially, all intra-protein crosslinks of ILK were displayed in the structures (Figure 41). Especially within the ILK PKD the crosslinks matched the crystal structure very well. However, some

crosslinks spanned the whole domain from one lysine located on the outside of the domain to another. These links are far too long to correspond to genuine crosslinks within the domain but rather appear to have formed between two PKD molecules that were in close proximity. Therefore, these crosslinks were omitted from the analysis, since they do not contribute to the correct positioning of the domains. Furthermore, a multitude of crosslinks from K165 and K170 in ILK ANK to different residues in the PKD and to α-parvin CH2 were observed. These crosslinks appear to be too unspecific to represent genuine spatial proximity of rigid structures. Instead, it seems that the linker region between ANK and PKD where the two residues are located is very flexible and becomes crosslinked to a lot of different residues. Furthermore, the ANK structure ends with a part of this flexible linker, which is not attached to any part of the folded domains and therefore unlikely to be in the exact same conformation as in full-length ILK. For this reason, these crosslinks are likely to lead to a false positioning of ANK and PKD and were omitted from further analyses.

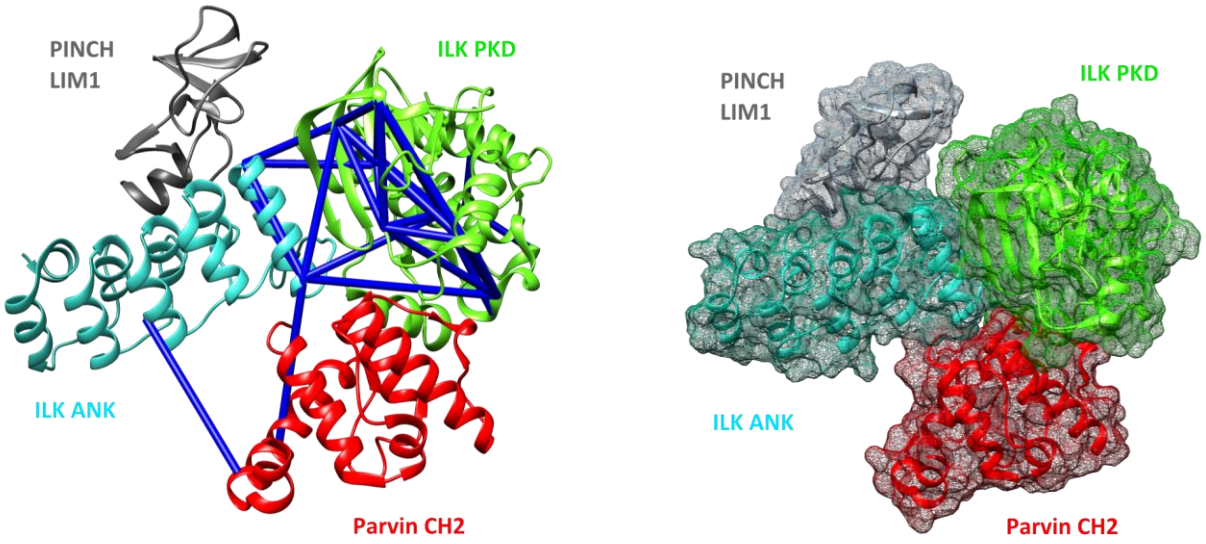

Figure 42: Model of ILK ANK, PKD, α-parvin CH2 and PINCH LIM1 complex based on crosslinking. The two crystal structures 3KMU and 4HI8 were moved and rotated until all distance restrictions of the crosslinks were satisfied. The resulting model was tested for clashes of the domain surfaces and appears to fit quite well. In this model, the four domains form a compacted complex rather than an elongated one. Grey: PINCH LIM1 domain, blue: ILK Ankyrin repeat domain, green: ILK pseudokinase domain, red: parvin CH2 domain

After removing the crosslinks likely to be non-specific, ILK ANK/LIM1 and ILK PKD/CH2 were moved towards each other and rotated until all intra-molecular ILK crosslinks and the two ILK-CH2 inter-links were satisfied and turned blue (Figure 42). For the result of this docking procedure, the surfaces of the four domains were displayed and analyzed for clashes. It

appears that the surfaces fit together quite well and that no domains overlap. The resulting model puts the four domains into a compact shape, with the CH2 domain close to ILK ANK. It has to be emphasized again that this is not a reliable structure but only a crosslink-based approach of gaining an idea of how the domains are oriented within the complex.

3.4.11 Display of all detected crosslinks in crystal structures of individual domains

With the exception of kindlin-2, only partial structures of the crosslinked adhesome components are available, making it difficult to gain structural information only through the crosslinks. Apart from the previously described “minimal” IPP complex of ILK ANK/PKD, parvin CH2 and PINCH LIM1, NMR structures of kindlin-2 PH domain (PDB: 4F7H) and PINCH LIM2-4 (PDB: 2D8X, 2COR, 1NYP) are available, as well as the crystal structure of kindlin-2, in which the flexible loop in the F1 domain and the entire PH domain have been deleted (PDB: 5XPY, 5XPZ, 5XQ0, 5XQZ). The structures of the PINCH LIM domains and the kindlin-2 PH domain have been added to the model of the IPP complex displayed in Figure 42 and the crosslinks to the new domains have been added. Beforehand, all crosslinks involving residues that are either not part of the structures or are located in flexible linker regions at the N- or C-termini of the domains had been omitted from the analysis.

Again, the docking of the LIM2-4 domains and the kindlin-2 PH domain according to the crosslinks is a very crude approach to determine the approximate positions of these domains within the complex. Kindlin-2 PH is located close to ILK PKD, but since only two crosslinks to the same lysine in PH were identified it is impossible to deduce the orientation of this domain towards ILK PKD. For the PINCH LIM domains, more crosslinks have been obtained, which are positioned along the interface between ILK ANK and ILK PKD. The most likely orientations of LIM2 and LIM3 are in a parallel or antiparallel manner to LIM1. For LIM2, it cannot be predicted if the domain is oriented in an antiparallel (Figure 43A) or in a parallel (Figure 43B) manner to LIM1, since both orientations satisfy the crosslinks. It is, however, more likely that the orientation of LIM2 is antiparallel, since the C-terminus of LIM1 and the N-terminus of LIM2 point in the same direction in this configuration. Were it otherwise, the domains would have to be connected by a linker stretching over the distance that is between the two domains. It appears that LIM4 is not positioned in line with the other three LIM domains but has to be located next to LIM2 and LIM3 to satisfy the detected crosslinks. This might indicate that PINCH in complex with ILK and parvin is not completely elongated but folded back on itself. It

might however be the case that the crosslinks are misleading or that the entire model is based on a false positioning of ILK ANK and PKD and therefore other possibilities of positioning the LIM domains have not been considered.

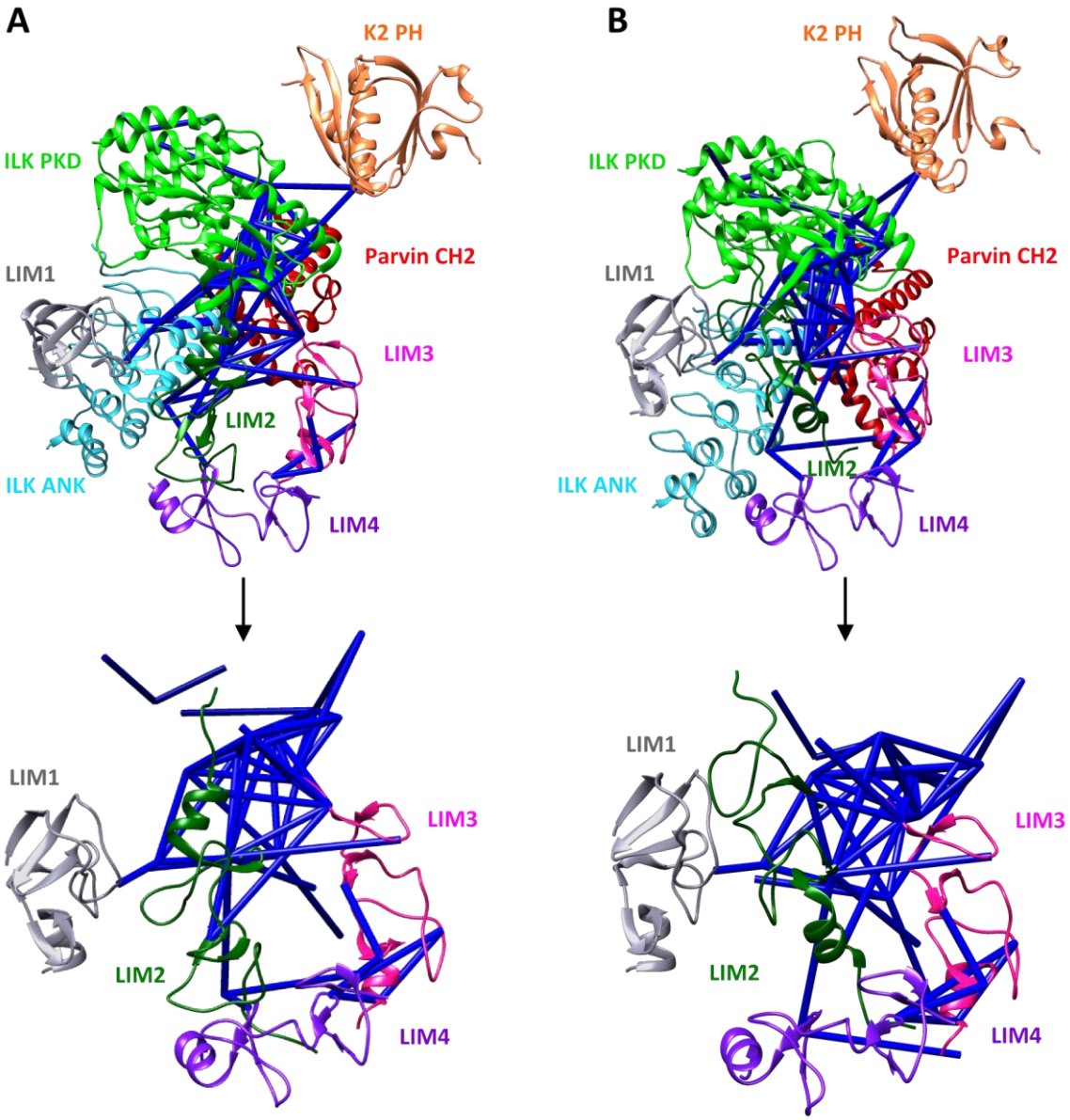

Figure 43: Model of ILK ANK/PINCH LIM1, ILK PKD/parvin CH2, kindlin-2 PH and PINCH LIM2, 3 and 4 based on the detected crosslinks. (A) All components were merged into a single file and the crosslinks displayed by the Xlink analyzer tool (dark blue). Only those crosslinks not involving lysines in flexible loops or between lysines on opposite surfaces of a domain were selected and used for docking of kindlin-2 PH domain and PINCH LIM2-4. The domains were arranged in a manner that satisfies all crosslinks. For LIM2 there are two orientations that satisfy all distance restrictions, one where the domain is arranged antiparallel to LIM1 and where C- and N-termini are close to each other (A) and one where the domain is tilted by 180° so that the domains are parallel but the C- and N-termini on opposing sides (B). The lower pictures show only the LIM domains and the crosslinks for better visualization. Light blue: ILK Ankyrin repeat domain, light green: ILK pseudokinase domain, red: parvin CH2 domain Grey: PINCH LIM1 domain, dark green: PINCH LIM2 domain, pink: PINCH LIM3 domain, purple: PINCH LIM4 domain

Attempts were made to include the kindlin-2 crystal structure into the model of the IPP complex, however only one crosslink between the kindlin-2 “backbone” (F0-F3, without the PH domain and the F1 loop) and ILK PKD was observed, which does not provide enough information for the positioning of kindlin towards the IPP complex. The number of crosslinks between the kindlin-2 “backbone” and the PH domain was also insufficient for creating a model of the entire kindlin molecule. Furthermore, no conformation could be found in which all length restrictions provided by the crosslinks were satisfied. This is mainly due to the missing linker sequences connecting the PH and the F2 domains, which are probably highly flexible and have not been resolved in either structure (PDB: 4F7H, 5XPY). In the structure of the kindlin-2 “backbone”, the entire PH-domain insertion, including the flexible linkers, has been deleted, thus directly connecting the N- and C-terminal halves of the F2 domain (Li et al., 2017a). In the full-length protein, which was used for the crosslinking experiments, the F2 domain is separated by the linkers and PH domain, which might lead to a slightly different arrangement of the F2 domain than was resolved in the crystal structure. This slight distortion might be enough to interfere with the proper positioning of the crosslinks and prevent a correct alignment of the PH domain towards the “backbone”.

Conclusive structural information on the IPP-kindlin-paxillin complex can only be gained by crystallization or EM studies, but the crosslinks can serve as additional information on the overall arrangement of the domains or on conformational changes.

3.5 Study of kindlin-2 and THD interactions with integrin tails in a native lipid environment

3.5.1 Binding of kindlin-2 and THD to integrin tails with low affinity

In order to assemble native adhesome complexes it is most straightforward to begin with immobilized integrin β tails and successively add other proteins. The major prerequisite for this approach is the formation of stable complexes with the integrin tail that allow for washing steps to remove non-specifically bound proteins. However, it became clear in MST and AUC experiments that kindlin-2 and THD, the two proteins that bind directly to the integrin tail and therefore the first components that probably trigger the assembly of adhesome complexes, display surprisingly low affinities towards integrin tail peptides. For kindlin-2 binding to the β1

cytoplasmic tail peptide, the K_D determined by MST measurements and confirmed by AUC experiments is 7 µM, for β3 it is 12 µM. The affinity of THD towards integrin β1 or β3 tail peptide has been placed in the range of 168 µM. Although these values are not as exact as those for kindlin-2 due to problems obtaining high enough THD concentrations to reach saturation of the tail binding reaction. The very low THD affinities are in accordance with those obtained from NMR studies (Anthis et al., 2009).

The very low affinities of the two major integrin activators towards the integrin tails are unexpected and incompatible with the hypothesis that for integrin activation, talin and kindlin are recruited from the cytoplasm to the cytoplasmic tails and initiate the formation of the adhesome complex. This would require the formation of a high affine bond between talin or kindlin and the integrin tail that is stably retained for a given time. Yet, obviously the interaction must be favored by factors within the cell that help overcome the low affinities. One possible explanation might be that the affinities of kindlin and talin are indeed as low as measured, but once they are bound to an integrin tail, the interaction is stabilized by the recruitment of other focal adhesion components. This would mean that although initial binding is limited by the low affinity, once kindlin and talin are at the focal adhesion, other proteins prevent their dissociation. Another potential reason for the high K_D values measured is that inside the cell, talin, kindlin and/or the integrin tail are modified by modifications such as phosphorylation that does not occu in proteins recombinantly produced in *E. coli*. A third explanation is that inside the cell, the integrin tails are inserted into the plasma membrane, which was not done in the solution-based measurements. The lipids might increase the affinity of talin and kindlin to the integrin tail either by ensuring correct orientation of the proteins through a second interaction surface. It is also possible that kindlin and talin are recruited to the membrane through interaction with PIP_2 before attaching to the integrin tail, which leads to a high local concentration and thus increases the number of molecules bound to the tail by reaching concentrations close to the K_D.

To better understand the events at integrin cytoplasmic tails in their native environment and to test the hypothesis that the plasma membrane might be crucial for talin/kindlin-tail interactions, constructs consisting of the integrin transmembrane and cytoplasmic domain

(TMCyto) were embedded into Nanodiscs (lipid bilayers encompassed by scaffolding proteins) and used for interaction studies.

3.5.2 Production and purification of TMCyto constructs and assembly into Nanodiscs

Fusion constructs of the integrin cytoplasmic tail, the integrin transmembrane domain, a Fos/Jun dimerization domain and an N-terminal His_6-tag were expressed in *E. coli* Rosetta cells at 18 °C for 16 h using the expression vectors pET15b-TMCyto-b1-wt and pET15b-TMCyto-a5-wt (obtained from H. Tseng, Fässler department). The constructs were expressed separately, rendering α5 or β1 integrin tails with their native transmembrane helix and a dimerization domain as a means to bring both subunits together if desired. Due to the hydrophobicity of the transmembrane domains, these constructs are insoluble when produced intracellularly and are deposited in inclusion bodies. These can be isolated by centrifugation, washed with Triton X-100 to remove cell debris and membrane fractions and finally be solubilized over night in 3 % EMPIGEN (Buffer D1).

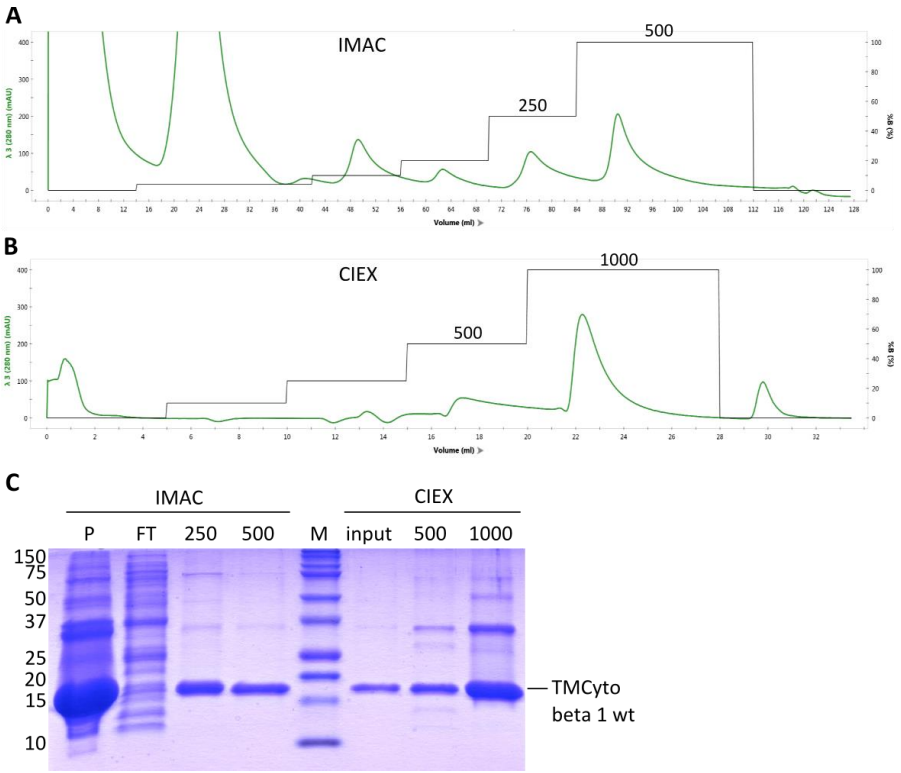

Figure 44: Purification of TMCyto β1 wt by IMAC and cation exchange chromatography. (A)TMCyto β1 wt was produced in E. coli in inclusion bodies, solubilized in 3 % EMPIGEN and purified by IMAC on a 1 ml HisTrap FF column using Buffers D3/D4. (B) The 250 mM (250) and 500 mM (500) imidazole fractions were diluted in Buffer D5 and applied on a 1 ml HiTrap SP HP column and purified using Buffers D5/D6. The 500 mM and 1 M eluates were pooled and flash-frozen. (C) The fractions were analyzed by SDS-PAGE after TCA precipitation to remove the EMPIGEN. P: pellet before solubilization, containing the insoluble TMCyto construct. FT: flow-through IMAC.

The solubilized TMCyto constructs can then be purified by IMAC and CIEX chromatography (Figure 44), as long as the EMPIGEN concentration in the buffers is kept at 1.5 % or higher. The fractions obtained from CIEX chromatography were pooled and flash-frozen in liquid nitrogen without any additives and stored at -80 °C.

The constructs produced were TMCyto β1 for interaction studies and α5 as a negative control, to which talin and kindlin-2 should not bind. As negative controls, mutant β1-NPIY>A and β1-NPKA-TT>AA constructs were also expressed and purified. In TMCyto β1-NPIA, the membrane-proximal NPIY motif essential for talin binding is mutated and should therefore only bind kindlin in interaction studies. Likewise, in TMCyto β1-NPKA-TTAA the membrane-distal NPKY motif is mutated, which should dramatically reduce kindlin binding.

However, MST studies with mutant tail peptides have shown that the NPKA mutation alone is not sufficient to abolish binding but only reduces the K_D tenfold, bringing the affinity to the same range as for talin-integrin tail peptide (personal communication by M. Veelders). Therefore, two Thr residues at the N-terminus of the NPKY motif were additionally mutated to alanines, which should addiotionally lower the affinity. Both binding deficient constructs were generated by site-directed mutagenesis using pET15b-TMCyto-b1-wt as a template and primers PaKa225/226 for generation of pET15b-TMCyto-b1-NPIA and primers PaKa227/228 and, in a second round of mutagenesis, primers PaKa229/230 for generation of pET15b-TMCyto-β1-NPKA-TTAA. All constructs were sequenced to ensure the correctness of the entire coding sequence.

For detection in fluorescence microscopy, the TMCyto constructs were labeled with Alexa-647 dye via maleimide coupling. Since each TMCyto constructs contains a single cysteine at the N-terminus, they can be selectively labeled with one fluorophore per tail. Labeling was carried out by adding the Alexa-647 dye directly to the EMPIGEN solubilized TMCyto constructs (diluted to 0.5 % EMPIGEN) and afterwards removing the excess dye by immobilizing the TMCyto construct on Ni-NTA beads. The eluate was then used for Nanodisc assembly. Unfortunately, the labeling efficiency, determined by LC-MS, could not be raised to more than 50 % and attempts to separate labeled from unlabeled integrin tails failed.

The purified TMCyto constructs were inserted into Nanodiscs by mixing them with cholate-solubilized lipids and commercially available MSP2N2 scaffold protein and then slowly

removing the detergents by dialysis. With decreasing detergent concentrations, the hydrophobic lipids and transmembrane domains become exposed to the hydrophilic solvent and start interacting with each other and with the inside of the membrane scaffold protein. Eventually, stable Nanodiscs are formed with one molecule MSP2N2 enveloping ~330 lipid molecules and one or more TMCyto molecules (Figure 45C). The assembled Nanodiscs were separated from excess MSP2N2 and TMCyto by SEC, which produced two clearly separated peaks. A peak simultaneously in A_{280} and in A_{650} indicates assembled Nanodiscs with Alexa-647-labeled TMCyto incorporated (Figure 45A, B).

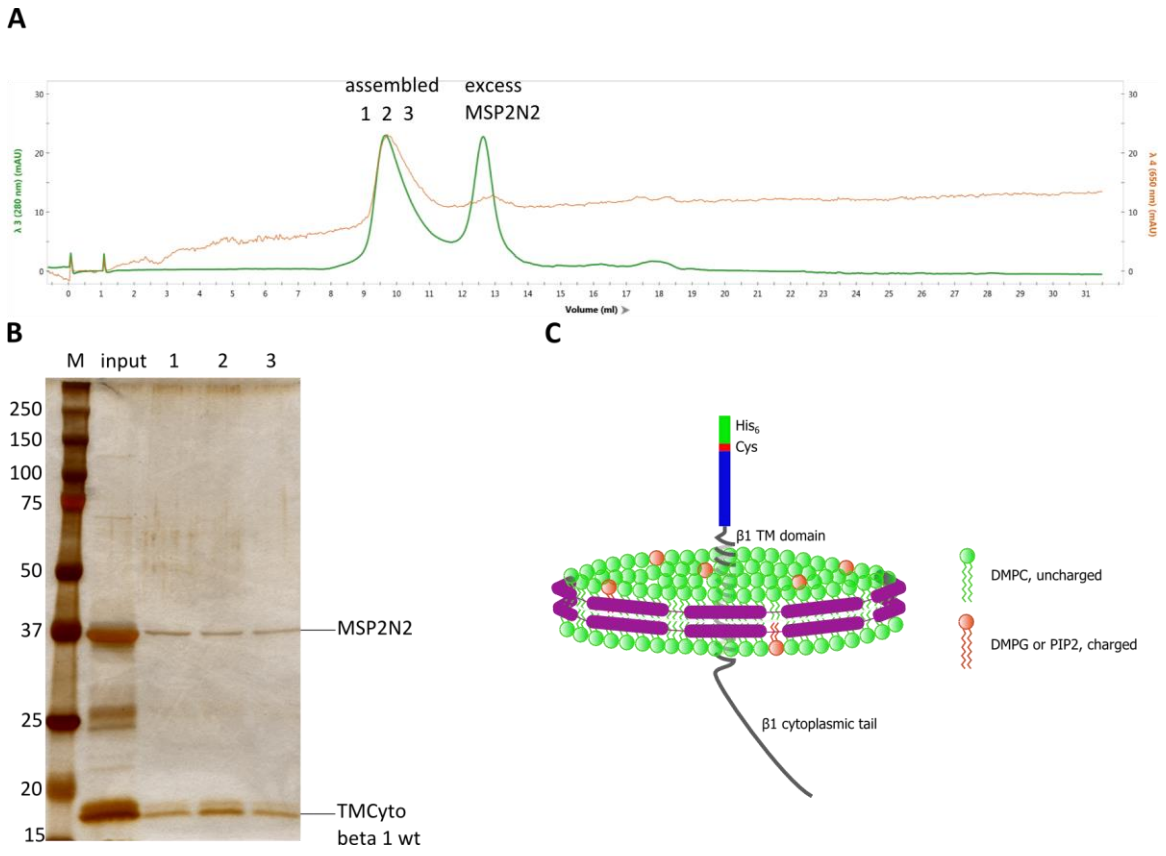

Figure 45: Assembly of MSP2N2 Nanodiscs with incorporated TMCyto constructs. (A) MSP2N2 was mixed with cholate-solubilized lipids and EMPIGEN-solubilized, Alexa-647-labeled TMCyto constructs, dialyzed to remove the detergents and applied on an analytical SEC650 column to separate assembled Nanodiscs from excess MSP2N2 and TMCyto. The green trace shows A_{280}, the brown trace A_{650} to detect labeled TMCyto constructs.. (B) The fractions from the first peak containing assembled Nanodiscs were analyzed by SDS-PAGE and show that both MSP2N2 and TMCyto are present, indicating successful incorporation. Due to low protein amounts, the bands were visualized by Silver Staining, which reveals previously unobserved contaminants at 25 kDa, probably from the commercial MSP2N2. (C) Schematic representation of the final Nanodisc, with MSP2N2 in purple encompassing the lipid surface composed of 90 % uncharged lipids (DMPC) and 10 % charged lipids (DMPG or PIP_2) and the TMCyto construct consisting of the cytoplasmic tail, the transmembrane domain, a FOs/Jun dimerization domain (blue), a single cysteine (red) and a His_6-tag for immobilization.

In order to study interactions of THD and kindlin-2 with the integrin tail, TMCyto constructs α5, β1 wt, β1 NPIA and β1 NPKA TTAA were incorporated into MSP2N2 Nanodiscs.

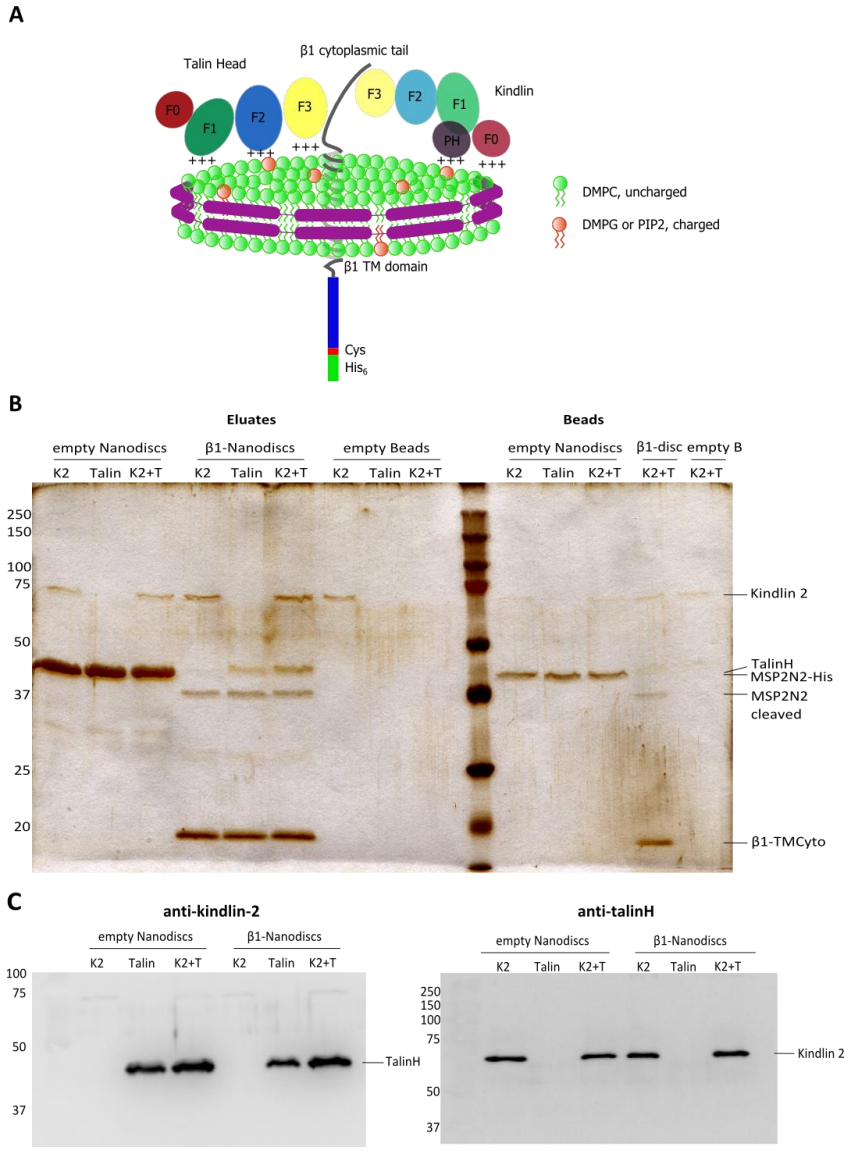

Figure 46: Detection of THD and kindlin-2 binding to empty and TMCyto β1 wt incorporated Nanodiscs. (A) MSP2N2 Nanodiscs have a diameter of ~17 nm, which in theory allows kindlin-2 and THD to bind simultaneously to the same integrin tail located in the middle of the disc. (B) Empty or TMCyto β1-incorporated Nanodiscs with 10 % DMPG were immobilized on Ni-NTA beads (GE) and incubated with THD and/or kindlin-2. After washing twice with 50 mM imidazole, the bound discs were eluted and analyzed by SDS-PAGE and silver staining. For empty Nanodiscs, His-MSP2N2 was used, while for TMCyto containing discs the His_6-tag was cleaved to ensure that only discs containing a tail were immobilized. (C) To check for non-specific binding, empty beads were incubated with THD and kindlin-2 and furthermore the beads after elution were analyzed. The pull-downs were performed in Nanodisc buffer. Since the positions of THD and His-MSP2N2 on the gel overlap, THD and kindlin-2 were detected by Western Blot. Both proteins were present in seemingly equal amounts in all samples.

Furthermore, to determine the effect of different lipid compositions within the Nanodiscs on THD and kindlin-2 binding, Nanodiscs with only uncharged DMPC lipids were compared to discs containing 10 % negatively charged lipids, which should have higher affinity towards the two proteins. At first, a mixture of DMPC with 10 % DMPG was used for establishing purification and assay set-up, while later a mixture of DMPC and 10 % PIP_2 was used. This phosphatidyl-inositide is the natural ligand for THD and kindlin-2 within the plasma membrane. The exact ratio of charged and uncharged lipids at focal adhesions is unknown, therefore 10 % was used as a starting value. Potentially, higher or lower ratios can have an influence on the binding behavior and needs to be tested in the future.

3.5.3 Detection of THD and kindlin-2 binding to Nanodisc-embedded TMCyto constructs

The functionality of the TMCyto-Nanodiscs, i.e. the ability to bind kindlin-2 and talin, was first assessed in pull-down experiments. “Empty” Nanodiscs consisting only of His_6-MSP2N2 and lipids were used as a control for interaction of kindlin and talin with the membrane lipids. Prior to assembly of the TMCyto-incorporated discs MSP2N2 was cleaved with TEV protease to ensure that discs immobilized on Ni-NTA surfaces only attach via the His_6-tag in the TMCyto construct and therefore no empty discs are included. Empty beads, empty Nanodiscs and TMCyto β1 wt-incorporated Nanodiscs immobilized on Ni-NTA beads were incubated with THD, or kindlin-2 or both proteins, washed twice and then eluted. The eluates were compared by SDS-PAGE and silver staining and by Western Blot analysis with antibodies against kindlin-2 or THD (Figure 46).

Both proteins interact with empty and β1 wt Nanodiscs but not or to a lesser extent with empty beads. Since the band representing THD overlaps with that of His_6-MSP2N2, THD had to be additionally visualized by Western Blot. It appears that both THD and kindlin-2 are bound in similar amounts in all samples, regardless of the presence or absence of integrin tails. It has to be noted, however, that the amount of empty discs seems to exceed that of β1 wt Nanodiscs, judged by the strength of the MSP2N2 (cleaved/ uncleaved) bands. Therefore, no reliable quantitative information can be derived from Figure 46B. Instead, it serves as proof that THD and kindlin-2 bind to Nanodiscs with incorporated TMCyto β1 wt as well as to empty Nanodiscs. Therefore, Nanodiscs provide a suitable platform for studying the binding behavior of the two proteins with the integrin β1 tail in a lipid environment of one’s choosing.

3.5.4 Studies on complex formation between THD, kindlin-2 and integrin tail peptides

Having established a platform for studying THD and kindlin-2 behavior towards integrin tails and lipid surfaces it can be used to shed light on the unresolved question whether both proteins can bind to the same cytoplasmic tail. Although the two NPxY motifs are very close together, sterically binding of both proteins might be possible, even in light of the recently published structure of kindlin-2. Attempts to resolve the binding issue using integrin tail peptides and THD and kindlin-2 in solution rendered conflicting results. Analytical ultracentrifugation with Atto-488-labeled β1 tail and unlabeled THD and kindlin-2 or both showed complex formation between THD and β1-488 and kindlin and β1-488, however, no ternary complex of one tail peptide with both proteins (Figure 47A, Data by M. Veelders).

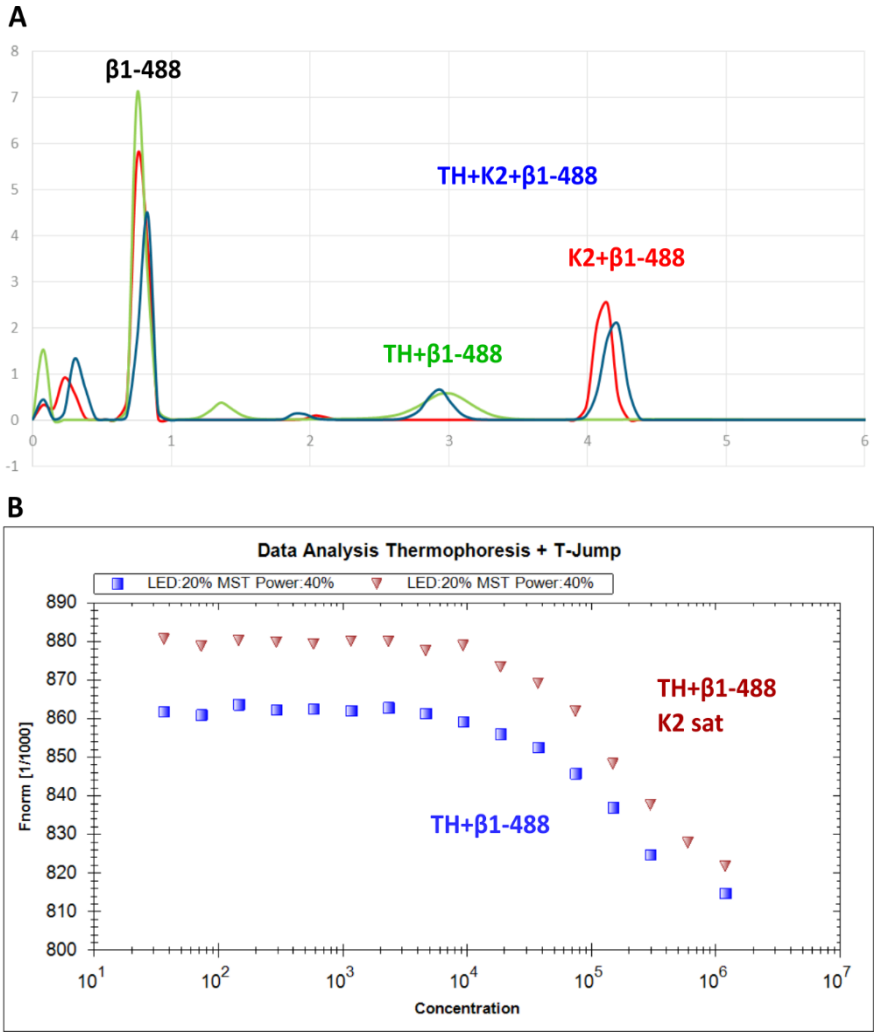

Figure 47: AUC and MST analysis of kindlin-2 and THD interactions with Atto488-labeled integrin β1 tail peptide. (A) Recombinant THD and kindlin-2 were mixed with β1-488 tail peptide and sedimented in Buffer A3. Detection of the labeled tail peptide at 501 nm showed complex formation with both kindlin-2 and THD individually, but no ternary complex with both proteins on the same tail. This would have resulted in the detection of a new peak at a higher sedimentation coefficient (**A**). (B) MST measurement with THD and β1-488 yielded a K_D of 168 µM, while measurements of THD versus 105 nM β1-488 mixed with 28 µM kindlin-2 yielded almost the same K_D value (188 µM). At 28 µM, the tail peptides are saturated to 80 % with kindlin-2, which was expected to change the binding behavior of THD if both proteins are incapable of binding simultaneously. However, neither the shape of the binding curve nor the K_D changed dramatically.

As an orthogonal method, MST measurements were conducted with THD and Atto-488-β1 tail peptide, yielding a K_D of 168 µM. In a second experiment, the β1-Atto-488 tail was mixed with kindlin-2, yielding a final concentration of 105 nM tail peptide and 28 µM kindlin-2. Theoretically, at a K_D of 7 µM, the tail peptides are saturated to 80 % with kindlin-2 in this configuration. Therefore, if THD cannot bind simultaneously to the same tail as kindlin-2, titration of the same THD concentrations should yield a different curve shape than in the absence of kindlin-2. Due to the much lower affinity of THD the binding curve should start to decay at higher concentrations in the presence than in the absence of kindlin-2.

However, the curve measured for THD against kindlin-saturated β1 tail peptide hardly differed from that for THD versus “free” tail peptide (Figure 47B). The K_D was determined at 188 µM, almost identical to that of the interaction without kindlin. At the highest THD concentration

of 1189 µM and a K_D of 168 µM, the tail peptide (105 nM) is saturated to 88 %, while at the same time theoretically being saturated to 80 % with kindlin-2. This strongly indicates that both proteins can bind simultaneously to one tail peptide, which is in stark contrast to the results of the AUC measurements.

A possible explanation for these conflicting observations is that THD somehow displaces kindlin-2 effectively from the integrin tail, potentially due to the different k_{on} and k_{off} values, resulting in an unchanged K_D in MST measurements with only THD attached to a single tail molecule. Another possibility is that the interaction of THD with a kindlin-tail complex is very transient with a fast k_{off} rate, resulting in no observable trimeric complex in AUC. A third possible explanation is that in the AUC measurements an excess of unbound integrin tail was present, resulting in the formation of dimeric THD-tail and kindlin-tail complexes but no trimeric complexes.

Due to the low affinities of both proteins and unspecific interactions with surfaces, biophysical methods with both proteins are difficult to set up, therefore the question whether both proteins can bind to the same tail remains unresolved with the solution-based measurements. Since it is possible that the plasma membrane contributes to the binding of both proteins to the integrin tail, the focus was shifted to the Nanodisc-based approach rather than solution-based methods.

3.5.5 Single-molecule microscopy to analyze binding of kindlin-2 and THD to integrin tails in a lipid environment

One problem of most biophysical methods is that in a system such as the Nanodisc-embedded TMCyto constructs, where THD and kindlin-2 can bind to the integrin tail as well as to the lipid bilayer, it is difficult to distinguish both binding events since they take place at the same time as the binding sites are in close proximity and it is not known to which degree they influence each other. Therefore, a novel approach was developed together with Armin Lambacher (Fässler Department) that allows for the direct observation of all proteins involved as well as their locations and interactions at a single molecule level. Alexa-647-labeled and His-tagged TMCyto constructs incorporated into MSP2N2 Nanodiscs were immobilized on NiNTA-tagged PEG-coated glass slides to yield a density of approximately 100 fluorescent molecules per section and mixed with 1 µM Alexa-488-labeled kindlin-2 and 1 µM Atto-565-labeled THD. The

fluorophores were excited with laser light of their respective excitation wavelengths and the fluorescence was detected using corresponding filter sets in a TIRF microscope. The intensity of the laser light was adjusted to a level that caused stepwise bleaching of the single fluorophores, which were detected during a time-lapse movie. Three channels for the three different fluorophores were measured simultaneously and then overlaid. For a correct alignment of the three channels, their respective offsets were determined using a separate sample containing beads with immobilized antibodies labeled with the different fluorophores. Furthermore, background correction was performed on all channels. The final, corrected time-lapse movies show spots in three different colors representing the three proteins present in the sample (Figure 48A). Each spot can then be analyzed individually and the fluorescence intensity traces over the recorded time can be displayed (Figure 48A, zoom-in). Red spots and traces represent the 647-labeled integrin TMCyto constructs, green ones THD-565 and blue ones kindlin-2-488, according to the laser light needed for their excitation.

The traces show distinct “steps” in fluorescence intensity, indicating the inactivation of one fluorophore. This inactivation is in some cases reversible, causing a fluorophore in one spot to re-appear and disappear again over the time trace (“blinking”). In some traces, two defined steps are visible, indicating the presence of two fluorescent molecules in the same spot. For the TMCyto constructs, each molecule can only carry one fluorophore since they only contain one cysteine residue, while THD and kindlin-2 were labeled via NHS-chemistry to a degree of labeling of ~1.0, which means that most molecules carry one fluorophore and only a few molecules carry two or no fluorophores. However, for analysis and statistics it has to be kept in mind that the labeling efficiency of the TMCyto constructs is only 50 % as determined by LC-MS and it cannot be judged if the ratio of labeled and unlabeled integrin tails after incorporation into Nanodiscs is still unchanged.

To ensure that the presence of steps in two different channels in one spot really indicates interaction of the two proteins control measurements with a fusion protein containing two fluorescent protein domains were performed. These measurements yield a typical distance in the set-up in which two truly interacting fluorophores are positioned towards each other. This distance was used as a restriction for distinguishing true protein-protein interactions from coincidental co-localization. Using this restriction, several different interactions were

identified. Predominantly, spots with a single integrin tail inactivation step and either one THD or one kindlin-2 step are observed (Figure 48A). Additionally, there are spots in which two integrin steps correlate with one kindlin and one THD step, indicating a cluster of two TMCyto constructs bound to the two proteins (Figure 48B). Some spots show only one integrin step and one THD and one kindlin step each, indicating either simultaneous binding of the two proteins to the same tail or the binding to two tails of which only one is detected due to a maximum of 50 % labeling efficiency of the TMCyto constructs. Additionally, a lot of spots show only THD or kindlin-2 steps without integrin tails, indicating either binding of the proteins to unlabeled TMCyto tails or interaction with the lipid surface of the Nanodiscs.

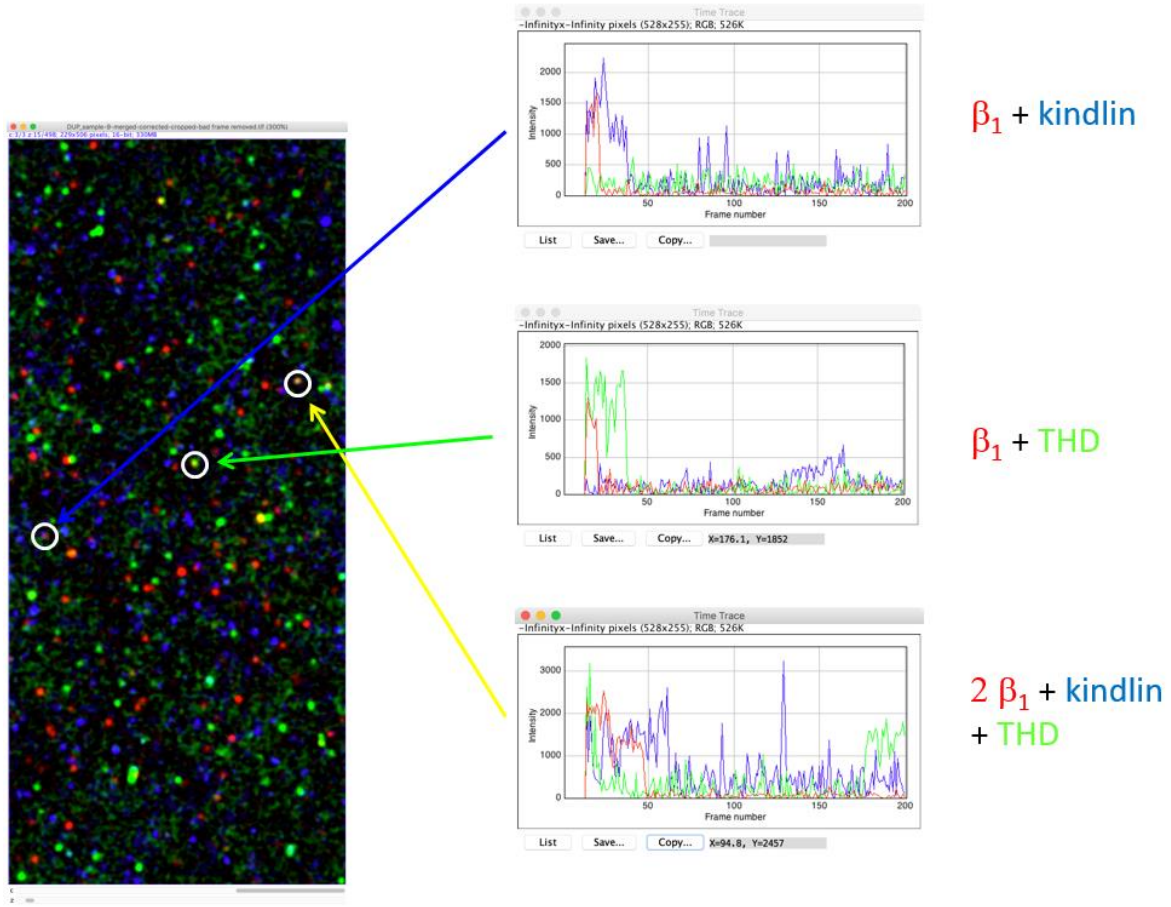

Figure 48: Examples of three-channel single-molecule microscopy to study kindlin-2 and THD interaction with integrin tails in a lipid environment. Alexa-647-labeled TMCyto β1 wt incorporated into DMPC/PIP_2 Nanodiscs (red) were immobilized on PLL-PEG/NTA-passivated glass slides and incubated with 1 µM kindlin-2-Alexa-488 (blue) and 1 µM THD-Atto-565 (green). The three channels were overlaid and for each spot the time-traces of the three fluorophores were analyzed (zoom-in windows). Distinct steps in fluorescence intensity indicate the inactivation of single fluorophores and allow "counting" of the molecules in one spot. Many THD and kindlin-2 molecules are found in spots where there is no integrin tail present, indicating interactions of the two proteins with the lipid surface independent of tail peptides. In other spots, one kindlin-2 or THD step and one integrin step correlate, indicating 1:1 interactions. Spots with two integrin steps and one kindlin and one talin step, indicating a cluster of two integrins with both proteins bound either to one tail each or both to the same tail.

It had been expected that both talin and kindlin attach to the lipid surface, since for both proteins non-specific interactions with a multitude of different surfaces had been observed. For this reason, the glass coverslips used for the single-molecule microscopy have to be passivated with PLL-PEG to create a layer to which non-specific attachment of kindlin and talin is reduced to a minimum. To allow immobilization of the TMCyto-Nanodiscs to the surface some PLL derivatized with NTA groups was mixed with the PLL-PEG. After loading the NTA groups with Ni^{2+} the N-terminal His_6-tag of the TMCyto constructs could bind and ensure a correct orientation of the discs. For immobilization of the empty Nanodisc control the His_6-tag of the Alexa-647-labeled scaffold protein was retained, while it was cleaved off in the TMCyto-samples. Due to the passivation of the glass surface the spots containing only talin or kindlin and no integrin step indicate interactions with the lipids rather than the glass surface.

As control experiments to estimate how many of the binding events are actually due to the integrin β1 tail and to what extent the lipid surface enhances talin and kindlin recruitment Nanodiscs with incorporated Alexa-647-TMCyto α5 as well as empty Nanodiscs were used (Figure 49). The α5 measurements show that kindlin-2 and THD also co-localize with the α-subunit, indicating either unspecific interactions or an enhancement of (in solution) very weak interactions by the lipid surface. The experiments with empty Nanodiscs confirm that both proteins interact with the lipid surface alone, independent of the presence of an integrin tail.

These initial experiments demonstrate that the set-up is working and that it can be used to study the events of THD and kindlin-2 binding to integrin tails in a lipid environment as well as to the lipid surface alone. In order to draw conclusions about the ratio of bound THD and kindlin-2 and whether a statistically relevant number of events involving only one tail and both proteins can be found to prove that a ternary complex is formed, the measurements will have to be repeated several times and evaluated, which will be the subject of further studies.

Furthermore, it is highly interesting to study different lipid compositions within the Nanodiscs, like only uncharged DMPC molecules to test whether the charged head groups of the 10 % PIP_2 included in the first discs increase binding of talin and kindlin to the lipid surface or to the tails. Having established the measurements, the negatively charged lipid will be changed from PIP_2 to PIP_3, which is the component within the plasma membrane with the highest affinity

towards kindlin and which should provide a lipid surface very close to the conditions within the cell.

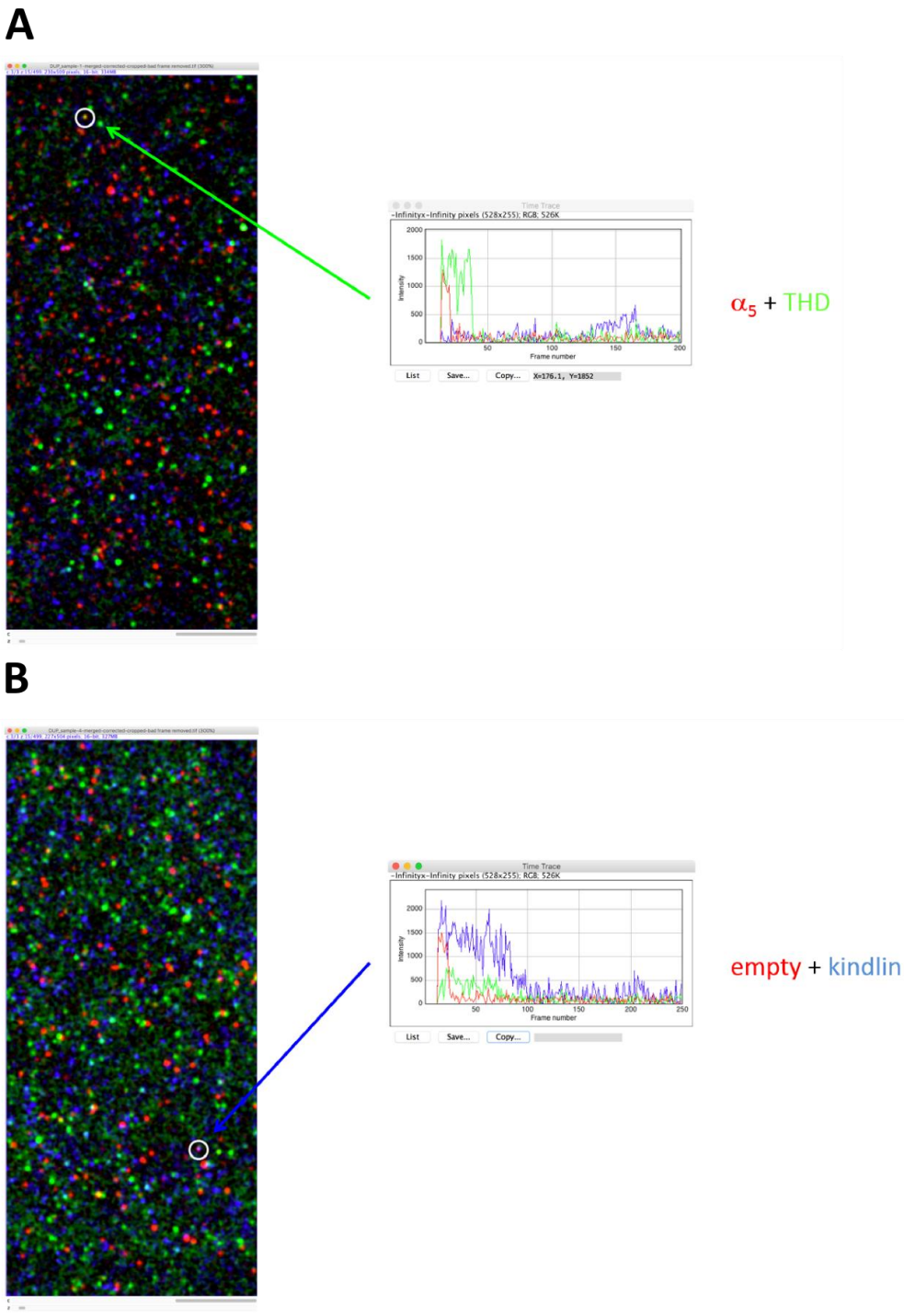

Figure 49: Control measurements with α5-TMCyto-incorporated or empty Nanodiscs in three-channel single-molecule microscopy. (A) Alexa-647-labeled TMCyto α5 incorporated into DMPC/PIP_2 Nanodiscs or empty Nanodiscs with Alexa-647-labeled MSP2N2 (B) were immobilized on PLL-PEG/NTA-passivated glass slides and incubated with 1 µM kindlin-2-Alexa-488 (blue) and 1 µM THD-Atto-565 (green) as negative/lipid-only controls for the β1 interaction. The α5 measurements show that kindlin-2 and THD also co-localize with the α-subunit, to which they do not bind in solution. Furthermore, both proteins co-localize with the scaffold protein of empty Nanodiscs due to interactions with the lipid surface (B).

Another factor that has to be taken into consideration for determining the number of THD and kindlin molecules bound to integrin tails are the labeling efficiencies. For THD and kindlin the labeling reactions could be optimized in order to obtain a degree of labeling of around 1.0, thus placing on average one dye molecule on each protein. For the TMCyto constructs, however, the labeling reaction could not be optimized further and therefore a maximum DOL of 0.5 was achieved. Since there is only one Cys residue in each TMCyto protein, 50 % of the molecules carry one fluorophore and 50 % are unlabeled. Therefore, when counting the bleaching steps for the TMCyto constructs, one has to bear in mind that only 50 % of the molecules give a signal. So when, for example, a TMCyto dimer is observed, it will display two bleaching steps with a probability of 25 %, one bleaching step with a probability of 50 % and no step with a probability of 25 %. These statistical considerations will be included in the data analysis once enough measurements have been performed to provide reliable data.

In the future, the TMCyto-Nanodisc platform can be used to study the behavior of other adhesome components as well, for example paxillin and whether it is recruited to the integrin tail via kindlin-2. Furthermore, FAK can be added as a scaffolding protein or to study its role as a kinase and the effects of its phosphorylation on adhesome components. The potential recruitment of the IPP complex to integrin tails via kindlin or paxillin is another objective that can be studied using this platform. The only limitation is the number of proteins that can be studied simultaneously, since the current set-up only allows for three channels and thus the observation of three proteins labeled with different fluorophores. A fourth channel could be established but requires a lot of effort in hardware and software.

3.6 Study of THD-integrin interactions under force

The surprisingly low affinities of THD to the β1 and β3 integrin tail raise the question how talin is able to transduce actomyosin-mediated forces to the integrin-extracellular matrix bonds with such low affinities for the tail. As discussed before, one possible explanation is a strengthening occurs through the interaction with the plasma membrane, which provides additional binding sites for anchoring talin to focal adhesions. Another hypothesis, which has so far never been tested, is a catch-bond behavior of talin with the integrin tail – a protein-

protein interaction, which increases in strength as force is applied. An example for a catch-bond is the interaction of the a5b1 integrin ectodomain with fibronectin.THD

In order to test the catch-bond hypothesis and to study the kinetics of the talin-F3-integrin interaction, fusion constructs of talin F3 domains connected to the integrin β1 cytoplasmic tail via an unstructured flexible linker was designed and purified by M. Veelders. Since talin1 and integrin β1A are the variants expressed in most cells, they were chosen for this and for other interaction studies. Due to the extremely low affinity of talin1 to integrin β1A (K_D 168 µM) , problems with the detection of binding events were anticipated. Therefore, in addition to a talin1-F3-β1A fusion construct, a talin2-F3-β1D fusion was studied, since this combination has been shown to display the highest affinity of all talin-integrin pairs (Anthis et al., 2009).

The F3 domains of talin1 and 2 used in the fusion proteins were mutated in order to remove all cysteine residues. Instead, two Cys residues were introduced at the N-terminus of the F3 domain and between the end pf the C-terminus of the linker and before the β1 integrin tail. These cysteines are used for the site-directed attachment of maleimide-functionalized oligonucleotides to opposing sides of the fusion protein. These oligonucleotides allow for the attachment to silica beads functionalized with complementary “DNA handles”. The silica beads can then be trapped in a dual-beam optical tweezer-setup, which allows for the stretching of the fusion protein between the beams and thus for the defined application of force on the molecule (Figure 50B). The attachment of the DNA handles, the optical trap measurements and their analysis are carried out by Marco Grison and Mihai Bodescu in Matthias Rief’s group at the TUM.

3.6.1 The talin1-β1A and talin2-β1D constructs with short linkers show no defined two-state behavior

The first measurements were carried out with talin1-F3-β1A and talin2-F3-β1D constructs with 27 AA linker sequences (designed and purified by M. Veelders). Talin2-β1D showed an unexpected behavior upon application of increasing force on the construct. From 1-5 pN the construct was slowly extended but remained in the closed conformation, while at 4 pN a shift was observed, indicating unbinding of the integrin tail peptide from the F3 domain. At 13 pN, a drastic extension represents the unfolding of the entire F3 domain (Figure 50C).

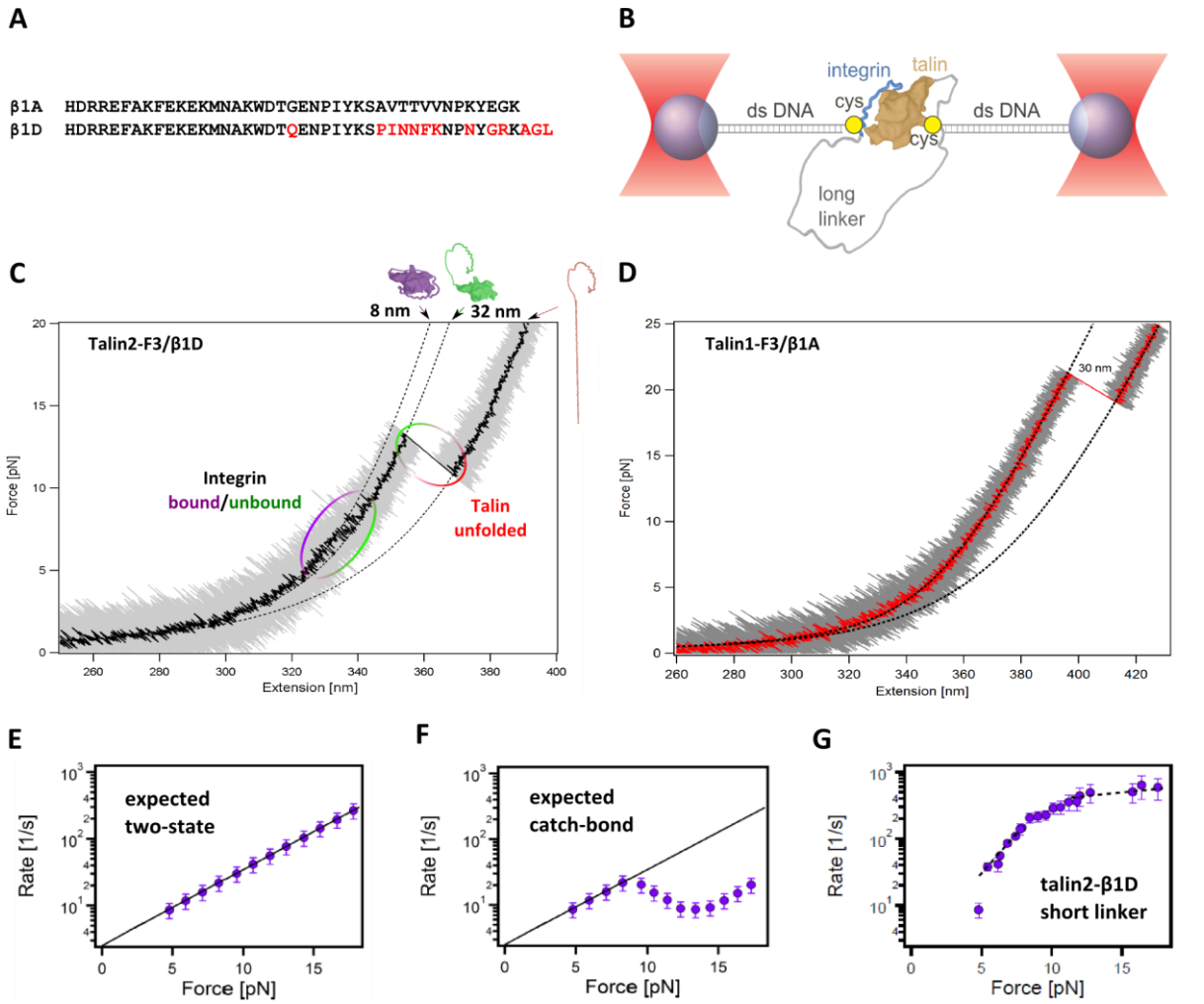

Figure 50: Basic principle of the molecular tweezer set-up and force-dependent elongation traces of talin1-F3-β1A and talin2-F3-β1D (images by M. Grison). (A) The interaction of talin1-F3 domain with integrin β1A as well as the much higher affine interaction of talin2-F3 with β1D were studied using molecular tweezers. (B) Fusion proteins of talin F3 and the integrin tail, connected by a linker sequence were attached to silica beads via DNA handles attached at two cysteine residues at the N-termini of F3 and of the integrin tail. (C) Moving the two laser traps apart creates an increasing force across the molecule, resulting first in unbinding of the integrin tail (purple/green transition) and later in unfolding of the F3 domain (green/red transition) for talin2-β1D. (D) For talin1-β1A no transition indicating unbinding of the integrin tail was observed. (E) Simulatioin of a classical two-step binding curve. In a classical two-step binding, the binding and unbinding rates increase linearly in correlation with the force applied to the molecule. (F) Simulation of a catch-bond binding curve. A catch-bond would manifest itself in a decrease in unbinding events in a certain force range, indicating a force-dependent strengthening of the bond. (G) Actual curve determined for the talin2-β1D construct with short linker. For the talin2-β1D construct with the short 27 AA linker, the observed curve could be fitted to neither model, indicating problems with the linker length.

Therefore, if the construct is maintained at a constant force of around 5 pN a constant binding and unbinding of the integrin tail to the F3 domain can be observed. Surprisingly, the talin1-β1A construct did not display a transition force, only one shift indicating complete unfolding at 20 pN (Figure 50D). Therefore, β1A tail binds with an incredible fast off-rate, which allows

only transient interactions that are detected by the fluctuations observed in a force regime up to 20 pN.

The talin2-β1D construct displays binding and unbinding events in the force range from 5-15 pN. The rates at which this binding and unbinding occurs were determined at different forces and plotted against the applied force (Figure 50E). In a classical two-step system, the unbinding rates should increase linearly with increasing force (simulated curve displayed in Figure 50E). In a system involving a catch-bond, one would expect at first an increase in unbinding rates, followed by a decrease at the force where the catch-bond is formed (simulated curve displayed in Figure 50F). The decrease in unbinding rates corresponds to a strengthening of the bond through the formation of a catch-bond.

At higher forces the unbinding rate increases again (Figure 50F). The curve obtained for the talin2-β1D fusion protein, however, cannot be fitted to any of the two models (Figure 50G). One possible explanation for this could be that the talin-tail interaction does not follow a classical two-step binding model but instead there is an additional binding site in the membrane-proximal region of the integrin tail. This, however could be excluded through a fusion construct in which the membrane-proximal region was replaced by Ser and Gly residues and which still showed the same behavior. Another reason might be that the 27 AA linker between F3 and the integrin tail is too short and therefore induces force on the bond already before it is applied externally. In order to test this hypothesis, talin1-F3-β1A and talin2-F3-β1D constructs with longer linker sequences were produced.

3.6.2 Production and purification of talin-integrin fusion constructs with longer linkers

An expression vector containing the coding sequence for a 72-AA flexible linker containing mainly glycines interspersed with Ser, Thr and Glu residues was obtained from Prof. Dr. Hermann Gaub's group (TUM). The linker sequence was amplified using primers PaKa231/232, while the vector backbone of pCoofy17-Talin2H_7SGGG_b1D_C-link (M. Veelders) was amplified using primers PaKa233/234. The two PCR products were combined by SLIC cloning, creating vector pCoofy17-Talin1-F3-b1A_long_link. Similarly, the backbone of pCoofy17-THD_7SGGG_b1_ dF0F1F2-CYS-C336S-linkerCys was amplified using primers PaKa233/235 and merged with the linker to vector pCoofy17-Talin2-F3-b1D_long_link. The correct insertion of the linker into both constructs was confirmed by sequencing. The cysteine residues at the

N-terminus of the F3 domain and at the C-terminus of the linker region used for attachment of the DNA handles were retained in the same positions.The fusion constructs with longer linkers were produced in *E. coli* with N-terminal His_{10}-SUMO tags and purified via IMAC using Buffer A1 and A2. After removal of the tag with SenP2 protease and reverse Ni-NTA chromatography, the proteins were applied onto a Superdex200 column as a finalizing purification step in Buffer A3 (Figure 51A, B). Both proteins were purified to ≥ 95 % purity and showed identical behavior. DLS measurements showed that both constructs are monodisperse and have a hydrodynamic radius of 3.0 nm, which is slightly larger than that of the constructs with shorter linker sequences (2.7 nm). This is due to the more voluminous longer unstructured linker and hence was expected.

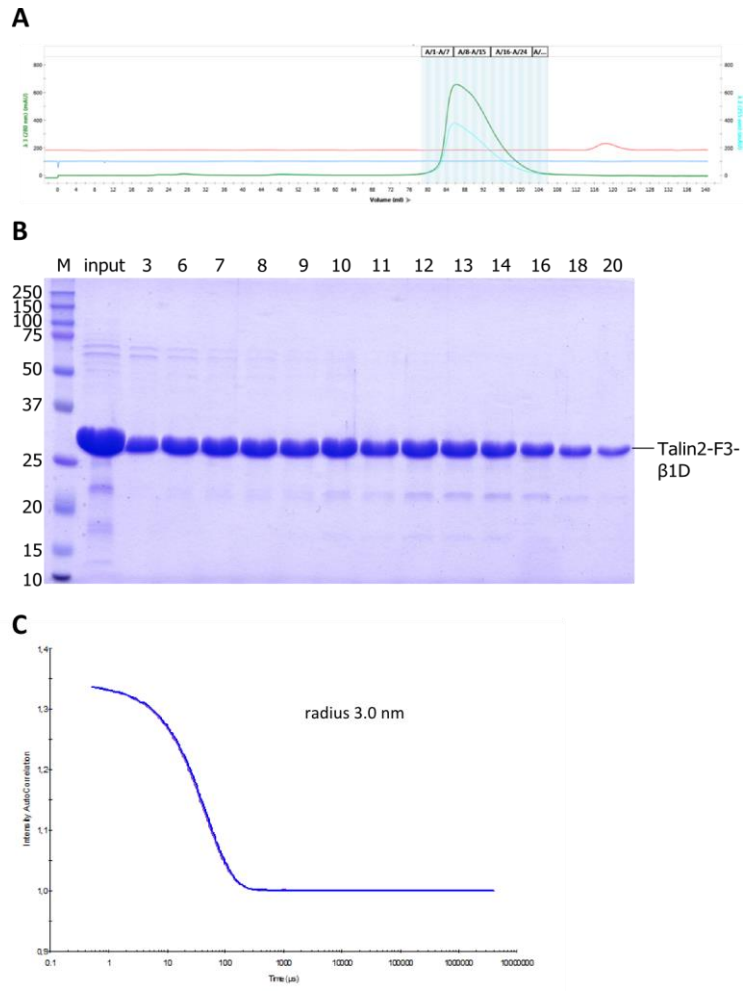

Figure 51: SEC purification and DLS measurements on the talin2-F3-β1D fusion protein with 72 AA linker sequence. The SEC elution profile (**A**) as well as SDS-PAGE of the fractions (**B**) show high purity of the talin2-β1D construct with a longer linker region. DLS analysis shows that the protein is monodisperse and displays a radius of 3.0 nm (**C**), which is slightly larger than the analogous construct with a shorter linker (2.7 nm). SEC was performed on a HiLoad 16/600 Superdex200 pg column at 4 °C using Buffer A3.

As with the construct with the shorter linker, there was no binding and unbinding signal detected for talin1-β1A-long, indicating that the interaction is indeed too weak or transient to be detected and that the shorter linker did not destabilize the bond. For talin2-β1D, a similar elongation, unbinding and unfolding behavior was observed as for the construct with shorter linker. However, the unbinding rates at increasing pN values now match the linear increase expected for a two-state system (Figure 52E). The previously observed effect that distorted the curve is not present in this construct, indicating that it was caused by the shorter linker.

Apparently, this linker applied force on the bond by itself, compromising the measurements. This measurement also rules out the possibility that talin2-F3 forms a catch bond with the integrin β1D tail. All further experiments were carried out with the talin2-F3-β1D construct with the longer linker.

3.6.3 Determination of binding affinities and kinetics of the talin2-F3 interaction with different integrin tail peptides in competition assays

When the talin2-β1D fusion construct is maintained at a constant force between 5-9 pN, the integrin tail is constantly unbinding and binding which is reflected in an oscillation in the signal between the bound state, which is less extended, and the more extended unbound state.

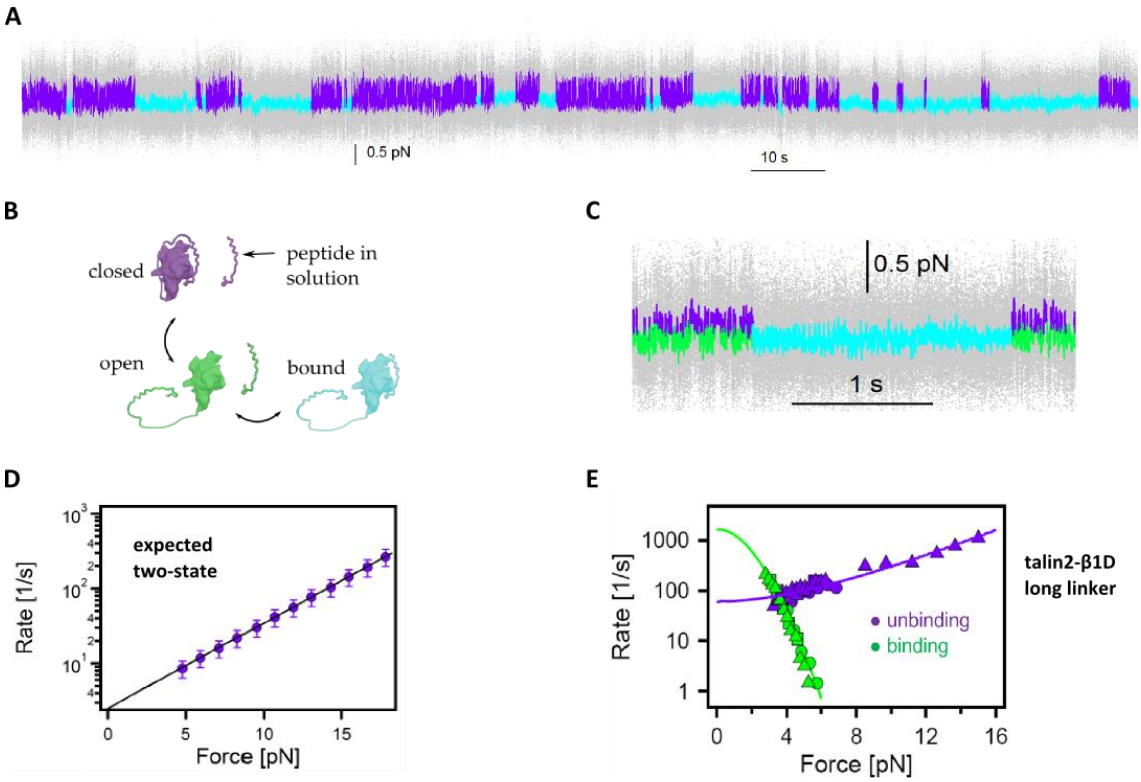

Figure 52: Example of a competition assay between an integrin tail peptide in solution and the talin2-F3-β1D fusion protein (Images from (Grison, 2017)). When maintained at a constant force between 5-9 pN, the integrin tail fused to the F3 domain constantly unbinds and re-binds, causing oscillation of the signal (**A**). Passages colored in purple indicate the "closed" state, in which the fused integrin tail is bound to F3. Green marks the "open" state, in which the fused tail is unbound from F3 and cyan marks the passages in which a competing tail peptide in solution is bound to F3, abolishing the return to the closed state (**B**). A zoom-in of **A** shows the difference between open and closed conformation and the missing assumption of the closed state when a competing peptide is bound (**C**). The fusion constructs with the longer linker sequence show binding and unbinding behaviors as expected for a two-state system, indicating that the previously measured curves were distorted by intrinsic force on the fusion protein, generated by the short linker (**D, E**).

In this state, integrin tail peptides in solution can be added to the set-up for competition assays. When the integrin tail fused to talin F3 dissociates, it can afterwards re-bind, or one of

the peptides in solution can attach to F3 instead (Figure 52B). The bound peptide causes a decrease in the oscillation for a certain time, equal to the lifetime of the F3-peptide bond (Figure 52A). From competition assays with free β1D integrin tail peptide a K_D of 9 µM was determined, three times lower than the K_D determined by NMR.

Furthermore, the on-rate for the binding of free β1D to F3 was estimated at 7 μM^{-1} s^{-1}, the off-rate at 100 s^{-1}. This off-rate indicates an extremely short-lived interaction, independent of the applied force. Further experiments with different tail peptides will show the influence of point mutations on K_D and on-rates.

3.6.4 Production and purification of full-length THD constructs with ybbR-tags for DNA-handle attachment

Since the experiments with the talin2-F3-β1D fusion construct showed no indication for a catch-bond behavior, it is possible that a strengthening of the talin-integrin bond is achieved through the interplay with the other domains of THD or through interactions with the plasma membrane. In order to study this, a construct of full-length THD fused to the integrin tail is required, which can be introduced into the molecular tweezer set-up as well. Since THD contains 6 cysteines, it would take a lot of mutagenesis steps to remove all of them and introduce two new cysteines at the desired positions, while increasing the risk of destabilizing the protein. Therefore, another approach using ybbR tags was chosen for attachment of the DNA handles. The ybbR tag is an 11 AA sequence originating from *B. subtilis*, which is recognized by Sfp phosphopantetheinyl transferase, an enzyme that attaches small molecules via a coenzyme A modification to the target sequence. By introducing two ybbR tags at the end of the linker sequence and at the N-terminus of THD it is possible to apply force onto the entire head domain.

The N-terminal ybbR tag was inserted into the talin2H sequence on pCoofy17-Talin2-Head by restriction digest with *Age*I and insertion of hybridized complementary primers PaKa236/237 carrying the ybbR sequence. The second ybbR tag was inserted into the vector pC17-Talin2-F3-b1D_long by restriction digest with *Msc*I and insertion of the hybridized primers PaKa238/239. The entire linker and tail sequence was then amplified using primers PaKa235/240 and merged with the backbone of the ybbR-talin2H construct amplified with

primers PaKa233/234 by SLIC cloning. The resulting vector was termed pCoofy17-Talin2-Head-b1D-2ybbR-N-link.

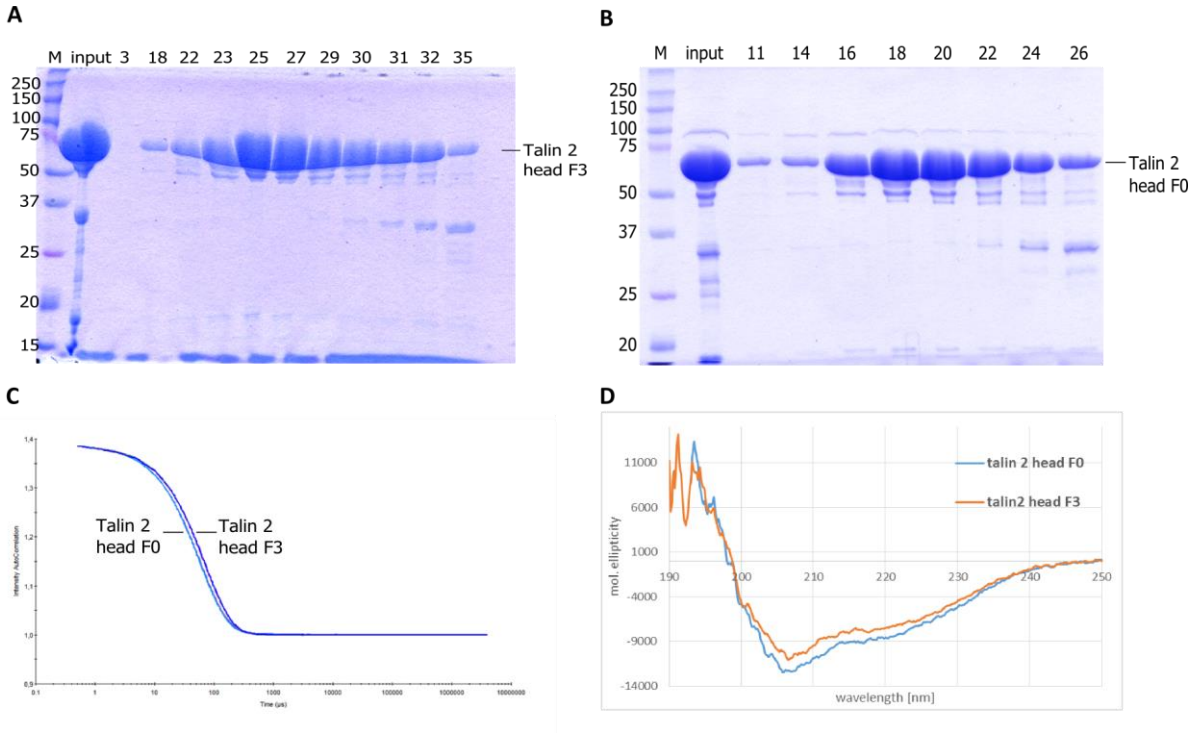

Figure 53: Purification and characterization talin2-head-β1D constructs with ybbR tag on the F0 or F3 domains. Both constructs were purified by IMAC, cleaved and finalized by SEC to ≥ 90 % purity (**A, B**). DLS measurements show that the construct with the ybbR tag inserted between F2 and F3 is larger than that with the ybbR tag at the F0 domain (4.8 vs. 4.2 nm, **C**). This indicates a potential disruption of the THD fold by the ybbR tag at the F3 domain, which also results in changes in the CD profile (**D**). Therefore, the F0 construct should be used for force measurements, since it is properly folded.

An analogous construct for talin1H-β1A was cloned following the same protocol. Additionally, in case the attachment of the ybbR tag to the N-terminus of F0 leads to the unfolding of domains before the integrin-F3 bond is disturbed, another construct was cloned which includes the ybbR tag at the N-terminus of the F3 domain. The three constructs talin1-head-F0-β1A, talin2-head-F0-β1D and talin2-head-F3-β1D were produced and purified analogously to the F3 constructs with longer linkers (Figure 53A, B).

The purified proteins were analyzed by DLS, which showed that all three proteins are monodisperse and that the two constructs with the ybbR tag at the N-terminus of the F0 domain display a hydrodynamic radius of 4.2 nm. The fusion protein with the ybbR tag between the F2 and F3 domains, however, displays a larger hydrodynamic radius of 4.8 nm (Figure 53C). Since all proteins are of the same size and composed of the same domains, this increase in size indicates that the ybbR tag might interfere with proper folding of talin2H by

separating F2 and F3 from each other. The ensuing change in secondary structure distribution was observed in CD spectroscopy (Figure 53D). Conclusively, the construct with the internal ybbR tag at the F3 domain should be used very carefully in optical tweezer experiments, keeping in mind that its stability might be reduced by the inserted tag.

Table 10: Overview of all talin-integrin fusion proteins produced and cloned

Construct #/vector	Talin	Attachment	Location	Status	Producer
#239-pC17-Talin1-F3-b1A_short_linker	1-F3	Cys	N-term F3 C-term linker	measured	M. Veelders
#247-pC17-Talin2-F3-b1D_short_linker	2-F3	Cys	N-term F3 C-term linker	measured	M. Veelders
#249-1-pC17-Talin2H_7SGGG_b1D_C-link-helix-replaced	2-F3	Cys	N-term F3 C-term linker Mutated MP region	measured	M. Veelders
#258-pC17-Talin2-F3-b1D_sh_C-term_Cys	2-F3	Cys	N-term F3 C-term tail	measured	M. Veelders/ P. Kammerer
#259-pC17-Talin1-F3-b1A_long_linker	1-F3	Cys	N-term F3 C-term linker	measured	P. Kammerer
#260-pC17-Talin2-F3-b1D_long_linker	2-F3	Cys	N-term F3 C-term linker	measured	P. Kammerer
#266-pC17-Talin1-Head-b1A-2ybbR-N-link	1-F0, F1, F2, F3	ybbR	N-term F0 C-term linker	purified	P. Kammerer
#268- pC17-Talin2-Head-b1D-2ybbR-N-link	2-F0, F1, F2, F3	ybbR	N-term F0 C-term linker	measured	P. Kammerer
#269-pC17-Talin1-Head-b1A-2ybbR-F3-link	1-F0, F1, F2, F3	ybbR	N-term F3 C-term linker	purified	P. Kammerer
#271-pC17-Talin2-Head-b1D-2ybbR-F3-link	2-F0, F1, F2, F3	ybbR	N-term F3 C-term linker	produced	P. Kammerer
#267-pC17-Talin1-F2F3-b1A-2ybbR-N-link	1-F2, F3	ybbR	N-term F2 C-term linker	cloned	P. Kammerer
#270-pC17-Talin1-F2F3-b1A-2ybbR-F3-link	1-F2, F3	ybbR	N-term F3 C-term linker	cloned	P. Kammerer
#272-pC17-Talin2-F2F3-b1D-2ybbR-F3-link	2-F2, F3	ybbR	N-term F3 C-term linker	cloned	P. Kammerer
#273-pC17-Talin2-F2F3-b1D-2ybbR-N-link	2-F2, F3	ybbR	N-term F2 C-term linker	cloned	P. Kammerer
#274-pC17-Talin1-F3-b1A_long_TM	1-F3	Cys	N-term F3 C-term linker + part of TM helix	cloned	P. Kammerer
#275-pC17-Talin2-F3-b1D_long_TM	2-F3	Cys	N-term F3 C-term linker + part of TM helix	produced	P. Kammerer

Should it be the case that the full-length THD is not suited for the intended experiments, constructs consisting of the talin F2 and F3 domains have been cloned and can be purified. The F2 domain provides a surface for interaction with lipids and might therefore be sufficient to attach the construct to the membrane. An overview of all talin-integrin fusion constructs, including those that have not been purified yet, is presented in Table 10.

3.6.5 Potential use of the talin-integrin fusion constructs for studies on kindlin-2 and the influence of lipids

The purified and characterized full-length talin head fusion proteins will be tested in the molecular tweezer set-up to see whether the binding and unbinding of the integrin tail as well as the unfolding of single domains can be observed. This is especially interesting for talin1-β1A, since for this combination, no binding was detectable so far. Like with the F3 domain constructs, it will be studied whether the full-length head domain shows a catch-bond behavior towards the integrin tail. Furthermore, kindlin-2 will be added to the experiments in order to test whether it competes with talin for the integrin tail or changes the binding behavior. It is also possible that kindlin binds to the fused tail peptide at the same time as talin, stabilizing the complex.

Furthermore, Nanodisc-embedded TMCyto constructs will be added to the fusion proteins, on the one hand in competition assays to measure binding affinities in the same way as it was done for tail peptides in solution. On the other hand, empty Nanodiscs and kindlin-2 can be added to the protein to test whether both proteins need the lipid surface to attach to the same tail. In order to be able to perform measurements with Nanodiscs, the silica beads used for the optical tweezers have to be passivated to avoid non-specific binding of the lipid surface, which interferes with the measurements. A similar passivation approach as for the glass slides used for single-molecule microscopy, using PLL-PEG, could be beneficial.

4 Discussion

The main objective of this thesis was the establishment of a molecular toolkit, which can be used to study the process of adhesome complex assembly *in vitro*. The integrin adhesome is composed of a multitude of proteins linked via an intricate network of protein-protein interactions. Therefore, it is difficult to determine the individual steps that lead to the formation of complexes around integrin tails or the composition of these assemblies in a cellular context, where there might be certain unidentified components or modifications present, which are crucial for adhesome assembly.

For this reason, an approach solely based on recombinant proteins is desirable, in which all components are well characterized and can be modified if necessary, for example by *in vitro* phosphorylation, point mutations, deletion of domains or the introduction of fluorescent labels for visualization. Not only does it allow the detection and quantification of individual protein-protein interactions but also the step-by-step assembly of large complexes. The latter provides insights into the sequence of proteins binding to one another, their stoichiometry and the stability of the complexes formed. Furthermore, structural studies using cryo-EM or crystallography can be conducted on stably assembled adhesome components and provide new insights into the architecture of focal adhesions.

In order to perform the assembly of adhesome complexes in a cell-like, yet controlled environment, an adaptable system that simulates the lipid environment around integrin tails was established. By changing the size and composition of the lipid surface provided by the Nanodiscs as well as the sequence of the integrin TMCyto constructs, the influence of the individual components on complex assembly can be studied. Furthermore, this system is suitable for analyzing, on a single-molecule level, how talin and kindlin behave at integrin tails – whether they can bind to the same cytoplasmic tail or whether their binding is mutually exclusive, which influence the presence of paxillin has on talin or kindlin recruitment and how much the complex assembly differs between β1 and β3 integrin tails.

Lastly, the establishment of a system, which can be used to exert force on talin-integrin fusion constructs, introduces a novel parameter to the *in vitro* studies of adhesome proteins. Traction force, especially across talin, is the one parameter that usually has to be omitted in

solution-based studies, leaving some degree of uncertainty whether a critical factor is missing in the analysis. The optical tweezer-based method allows for the addition of different proteins or peptides, which might compete with the integrin tail binding to talin F3 domain or strengthen the interaction.

Conclusively, a toolkit of recombinant proteins, membrane platforms and biophysical analysis methods has been established and characterized and enables novel *in vitro* approaches to elucidate what is happening around integrin cytoplasmic tails in focal adhesions.

4.1 Focal adhesion kinase and its dual functions in adhesome complexes

4.1.1 Production of recombinant FAK and confirmation of scaffolding function

As one of the key components in integrin signalling and adhesome assembly, functional FAK was considered vital for the intended experiments. An expression system was established which allows for the production and purification of recombinant full-length murine FAK in milligram amounts from HEK293E cells. The His-SUMO tag was found to be beneficial to both yield and stability of the recombinant protein, since earlier constructs with N-terminal His- or Strep-tags were produced as well, yet at lower levels. The thermal stability of FAK could be enhanced by changing the buffers used for purification, however this did not reduce the affinity of the protein towards SEC columns, where a considerable part of each preparation was lost. Furthermore, some HSP70 was co-purifed, indicating some folding problems. However, the final, purified protein is monodisperse and properly folded.

Interestingly, the hydrodynamic volume of FAK observed in SEC seems to decrease upon supplementation with ATP. Furthermore, addition of ATP and incubation at 37 °C leads to increased auto-phosphorylation. It has been shown that in the inactive form, the FAK FERM domain forms dimers (Brami-Cherrier et al., 2014). Therefore, it can be speculated that in a dimer, both FAK molecules phosphorylate each other *in trans* upon additon of ATP and then dissociate, resulting in monomeric, active FAK. It is also possible that binding of ATP leads to a compaction of FAK by binding of the FAT domain to the FERM domain, resulting in a smaller apparent size.

Expectedly, interaction studies have shown that recombinant FAK can bind paxillin as well as THD (Lawson et al., 2012, Hoellerer et al., 2003). Therefore, it can be used as a scaffolding protein in adhesome complex assembly in the absence of ATP, where it associates with paxillin, talin or both. If stable complexes are formed, structural studies using cryo-EM or chemical crosslinking on FAK, paxillin and THD can be conducted. Furthermore, since it has been shown that FAK specifically phosphorylates recombinant paxillin, the effect of these phosphorylations on paxillin binding to kindlin and the IPP complex can be studied.

4.1.2 *In vitro* phosphorylation of paxillin by FAK facilitates study of these modifications on adhesome complex assembly

It could be shown that recombinant full-length FAK phosphorylates paxillin *in vitro* after the addition of ATP and incubation at 37 °C. This indicates that the purified protein is phosphorylated in the HEK293E cells during production, especially at positions Y-397, Y-576 and Y-577, which are crucial for full activation of FAK. The activating phosphorylations were confirmed by mass spectrometric analysis. Apparently, the phosphorylation of Y-397 is not yet present in all FAK molecules after purification, since the level of tyrosine phosphorylation of the FAK band in Western Blot analysis increases after addition of ATP and incubation at 37 °C, indicating auto-phosphorylation.

Paxillin phosphorylation at the well-described positions Y-31 and Y-118 was confirmed by Western Blot and mass spectrometric analysis, the latter revealing additional phosphorylation of Y-40, Y-181, two residues which had been reported as phosphorylation sites in paxillin but not extensively studied. The phosphorylations are entirely accomplished by FAK, since no co-purified Src could be detected in the recombinant protein sample. Interestingly, phosphorylation by FAK is specifically limited to paxillin, as no modification of kindlin-2, THD, full-length talin, EPLIN or α-parvin was observed. Since the phosphorylation of paxillin is accomplished quite fast and can be optimized to ensure quantitative addition of two or more phosphate groups to the molecule, it is possible to generate sizeable amounts of phospho-paxillin for interaction studies. Either by SEC or by using His-SUMO-tagged FAK in the reaction, which can later be easily removed using Ni-NTA beads, phospho-paxillin can be separated again from FAK prior to its use in experiments.

The mechanism by which FAK phosphorylates paxillin is of interest as well, since paxillin binds to the FAT domain of FAK but must come into close proximity of the kinase domain as well to be phosphorylated. Therefore, there has to be either a second paxillin-binding site in the kinase domain or the FAT domain associates with the kinase domain and thus brings paxillin near the catalytic center. The latter would imply that without the FAT domain, paxillin is not phosphorylated by FAK, a hypothesis that can be tested using a FAK construct in which the FAT domain is deleted. If this construct, however, is still able to phosphorylate paxillin it would be interesting to identify the location of the second binding site at the catalytic domain and to determine whether two paxillin molecules can bind to one FAK molecule via the two separate binding sites. Even co-crystallization of FAK and paxillin bound to the catalytic domain, immobilized by an ATP-analogue, could be attempted.

Due to the additional complexity of including FAK in adhesome complex assembly, it was omitted so far. The primary goal was to characterize the IPP complex and its direct interaction partners kindlin and paxillin to better understand the binding modalities of this pentameric complex. The next level of analysis will be to include FAK, with and without the addition of ATP, to test whether it binds to paxillin and creates a stable hexameric complex. It is also possible that FAK binding to or phosphorylation of paxillin results in its dissociation from the IPP complex or in altered binding behavior towards other proteins. Successfully assembled hexameric complexes can be analyzed by chemical crosslinking or cryo-EM to gain structural information.

It is also unclear if the FAK FERM domain, which has been shown to interact with PIP2 in the plasma membrane (Brami-Cherrier et al., 2014), can stabilize the adhesome complex by strengthening its attachment to the membrane. The localization of FAK to the plasma membrane and the co-localization with THD or paxillin there can be studied using the single-molecule microscopy approach on Nanodisc-embedded TMCyto constructs. In the same set-up, the effect of FAK phosphorylating paxillin and a potential change in behavior towards kindlin or THD thereupon can be tested.

4.2 Recombinant unmodified or ERK-phosphorylated EPLIN does not directly interact with recombinant PINCH or paxillin

Recombinant α-EPLIN was produced and purified under the assumption that it binds to both PINCH and paxillin and thus could have a stabilizing effect on the IPP complex or on the IPP-paxillin interaction. It had been shown previously that EPLIN co-localizes with PINCH as well as paxillin inside the cell (Karakose et al., 2015, Tsurumi et al., 2014), therefore a direct interaction that leads to the localization of EPLIN to focal adhesions was suspected. Since these interactions had not been shown *in vitro* and the binding interfaces not identified, recombinant, bacterially produced EPLIN, PINCH and paxillin were intended for this purpose. However, no interaction of unmodified EPLIN with either full-length paxillin, full-length PINCH, individual PINCH LIM-domains or PINCH bound to ILK and parvin in the IPP complex were detected.

Since it has been shown that ERK phosphorylates EPLIN, which leads to a detachment of EPLIN from actin fibers (Han et al., 2007), it was hypothesized that the same phosphorylation might lead to the localozation of EPLIN to focal adhesions. Therefore, EPLIN was phosphorylated by recombinant ERK and used in interaction studies with PINCH and paxillin. However, no interactions of the phospho-protein with either partner could be detected, indicating that ERK phosphorylation is not the “missing link”.

It is possible that EPLIN can be phosphorylated by another kinase and that these different modifications modulate interaction with PINCH or paxillin, or that the interaction partners themselves have to be modified. Since EPLIN is largely unstructured except for the central LIM domain, it is highly probable that interaction with the LIM-domain proteins paxillin and PINCH is mediated via this exact domain. The LIM domain might be inacessible in native EPLIN which is not attached to actin, preventing interactions. This can be tested in interaction studies using only recombinant EPLIN LIM domain. Furthermore, it is possible that EPLIN does not directly interact with PINCH or paxillin but is localized to focal adhesions via a different, unidentified protein and thus brought into close proximity of the two proteins.

4.3 The MultiBAC system is ideal for expression of recombinant IPP complex but does not allow isolation of a fully assembled adhesome complex

Expression of ILK, PINCH and α-parvin from one expression vector in High Five insect cells proved to be the approach that finally led to the production and purification of full-length IPP complex in 1:1:1 stoichiometry. All three components are correctly folded and pre-assemble into the stable IPP complex inside the insect cells. Purification is achieved by IMAC via only one His-tag on α-parvin, which leads to the co-elution of ILK and PINCH, showing that the complex is stable. It also passes SEC with only little dissociation of the components. It is, however, not possible to co-purify any other adhesome components together with the IPP complex, neither by IMAC on column or on beads, nor by a less harsh method like rate-zonal centrifugation.

It appears that the affinities of the other components like kindlin, paxillin or RSU-1 are too low or their off-rates too fast to allow the formation of complexes with lifetimes high enough to withstand purification and dilution. It is possible to form complexes of IPP, paxillin and kindlin on SEC, but for this, kindlin and paxillin have to be used in excess to “force” them to associate with IPP. When the peak fraction obtained from SEC is used for negative staining, it appears that a considerable amount of complexes are dissociating upon dilution, confirming the failed co-purification and complicating cryo-EM analysis.

The fact that, although all adhesome components expressed on the same vector were produced in sufficient quantity, they did not form stable complexes inside the insect cells raises suspicions as to whether there is really a tight adhesome complex around integrin tails which grows over time through the association of additional components. It is possible that focal adhesions are more dynamic than expected and that adhesome components attach for a certain period of time to each other and then some of them dissociate again.

Another possible explanation is that for the proteins to form a stable complex, the integrin tail and the plasma membrane have to be present to localize talin and kindlin as the central proteins and then all other proteins can attach to them. Or a “critical” number of adhesome proteins has to be assembled which form multiple protein-protein interactions and thus stabilize a large complex. Possibly, an approach with Nanodisc-embedded TMCyto constructs

and all recombinantly produced proteins in high concentrations might yield sizeable complexes. This has to be tested in the future.

4.4 Recombinant full-length IPP complex for interaction studies and structural analysis

4.4.1 Interaction of IPP with kindlin-2 and paxillin and pentameric complex formation

The fact that recombinant, full-length IPP complex can be purified and forms a stable complex is in good accordance with published data stating that the three proteins pre-assemble in the cytoplasm and are recruited together to focal adhesions (Hoffmann et al., 2014). This stable trimeric complex is of particular value for structural studies, since no structure of the full-length proteins is available to-date and little is known about the binding modalities of paxillin and kindlin to the IPP complex and to each other in a pentameric complex.

Once purified, the IPP complex has the tendency to aggregate, especially at temperatures beyond 15 °C. Unfortunately, this interferes with many biophysical measurements and with attempts to resolve the structure of the complex by crystallization or cryo-EM. Buffer screens have been conducted in an attempt to find conditions that reduce aggregation and stabilize the complex. However, the interpretation of these measurements was complicated by the fact that the three proteins unfold at different temperatures and the aggregation seems to interfere with the signal as well, resulting in melting curves with no sharp transitions but rather a constant increase in fluorescence. The most promising conditions were in citrate buffer, which will be further tested in aggregation studies and in negative staining.

It could be shown that paxillin and kindlin bind individually to IPP, forming tetrameric complexes, and that their binding is not mutually exclusive. Instead, a pentameric complex is formed when both proteins are added to the IPP complex. Paxillin and kindlin also interact with each other and, judging from the crosslinking data, it appears that they adopt a similar conformation towards each other when bound to IPP, since crosslinks in the same positions as in the sample without IPP were observed. This observation has to be verified by orthogonal methods and by cryo-EM in the best case.

Although it was found in pull-down experiments and consequently also in crosslinking studies, THD does not directly interact with IPP, kindlin, paxillin or the pentameric complex of these proteins. The interaction with Ni-NTA beads is unspecific and can be observed in almost all pull-down experiments and in the controls with empty beads. Therefore it remains speculative if IPP, kindlin and paxillin do not interact with talin at all inside the cell, forming an independent complex or if the interaction is mediated by the integrin tail and the plasma membrane. It is also imaginable that FAK functions as an adapter molecule between talin and paxillin in focal adhesions. This can be tested by the stepwise assembly of complexes on Nanodisc-embedded TMCyto constructs.

4.4.2 Full-length IPP complex does not interact with integrin tail peptides

Contrary to published data on the ILK-PKD/parvin-CH2 complex (Fukuda et al., 2009), full-length IPP complex does not interact with integrin tail peptides. Three orthogonal methods, including pull-downs with recombinant GST-β1 and GST-β3 fusion proteins, which is the only method used by Fukuda et al. to demonstrate interaction with ILK-PKD/parvin-CH2, failed to indicate any interactions. It is possible that in the GST pull-down experiments very low amounts of IPP were bound but not detected by Coomassie staining. Potentially, Western Blot analysis would have shown an ILK band pointing to an interaction with extremely low affinity.

However, it seems more likely that the integrin-binding site in ILK, which has been mapped to residues 293-451 in the pseudokinase domain, is not accessible in the full-length IPP complex. It might be hidden by the parvin CH1 domain or PINCH LIM domains and hence requiring either a conformational change or a dissociation of ILK from its binding partners to allow binding to the integrin tail. The latter, however, seems unlikely since ILK by itself is not very stable and it also has been shown that the IPP complex is pre-assembled in the cytoplasm before being recruited to focal adhesions (Hoffmann et al., 2014). The complex would then have to be disassembled first, allow ILK binding, and re-assemble. It seems more likely that the published data contains an artifact or represents a different structure from that observed in the full-length construct, since binding was demonstrated in only one assay and no affinities were determined.

It is also possible that the ternary IPP complex is recruited to FAs through kindlin-2, which attaches directly to the integrin tail. Being in close proximity to the integrin tail, a

conformational change in ILK might occur that leads to the dissociation of PINCH or parvin, exposing the integrin-binding site in ILK. Kindlin, bound to the integrin tail, might stabilize ILK and facilitate its binding to the tail. This can be tested by assembling kindlin-2 on the surface of Nanodisc-embedded TMCyto constructs and addition of IPP complex. If indeed ILK binds to kindlin-2 and the integrin tail by displacing PINCH or parvin, they should be absent or reduced after washing of the sample.

4.4.3 The PINCH LIM5 domain is flexible and non-essential for IPP function

Initial crosslinking studies on full-length IPP complex with kindlin and paxillin showed that PINCH LIM5 domain becomes heavily crosslinked to lysine residues in several different regions of ILK and parvin. This high number of crosslinks can be derived from high flexibility and the lack of defined structural elements of the LIM5 domain, allowing it to change its position often and reach different surfaces of the complex. Another possible explanation is that LIM5 plays a central role within IPP, re-enforcing the link between ILK and α-parvin by attaching to both of them, and thus is expected to have a high impact on complex integrity.

Therefore, deletion of LIM5 should result in reduced complex stability and yield as well as alterations in biophysical properties and interaction with kindlin and paxillin. Parallel purification of full-length and dLIM5 complex, however, showed almost identical elution profiles and final yield of the two constructs. Furthermore, the tendency to form aggregates is present to the same extent and IPP-dLIM5 is properly folded and monodisperse. The shorter complex also shows no discernible difference in kindlin and paxillin binding compared to the full-length version, in Ni-NTA pull-down experiments as well as in SEC analyses. Crosslinking experiments with IPP-dLIM5 yielded the same crosslinks as full-length IPP, apart from those involving the LIM5 domain, indicating that the overall structure of the complex is identical and not disrupted by the absence of a central link. Instead, several previously unobserved crosslinks were detected, indicating that they were prevented by the presence of LIM5.

All this strongly indicates that PINCH LIM5 domain adopts a very flexible, probably largely unstructured conformation. It is located near the ILK-parvin interface, allowing for the establishment of the numerous crosslinks, but has no apparent structural effect. Another indication that PINCH LIM5 domain is unstructured is the fact that for PINCH LIM1-4 there are NMR structures available (PDB: 1G47, 2D8X, 2COR, 1NYP), while there is no structure

deposited for LIM5. It seems unlikely that LIM5 was omitted from the structural studies when all other LIM domains were analyzed and yielded structures. Therefore, it seems likely that no NMR structure for LIM5 could be obtained, due to its high flexibility. It is possible that PINCH LIM5 domain adopts a more defined and less flexible conformation upon binding of RSU-1 (Dougherty et al., 2005). This can be verified by adding recombinant RSU-1 to the IPP complex and analyzing the crosslinks obtained or by trying to co-crystallize RSU-1 and LIM5.

Conclusively, for structure determination by cryo-EM or crystallization IPP-dLIM5 should be used, since it includes less unstructured elements which are detrimental to the resolution that can be achieved or prevent crystallization or the identification of class averages altogether.

4.4.4 Chemical crosslinking and modelling of substructures

The mass spectrometric analysis of chemically crosslinked complexes is especially suited for proteins of which full or partial structures have already been solved and where the exact orientation of certain domains towards each other needs to be determined. Furthermore, conformational changes occurring upon binding to other proteins in the complex can be detected and mapped. In this case, however, no entire structures of any of the proteins are available, making it exceedingly difficult to gain reliable structural information from crosslinking data. Instead, only a very rough positioning of the single domains is possible and the correctness of this modeling cannot be claimed with any certainty. Therefore, the model depicted in Figure 42 represents by no means a definitive structure of the “minimal” IPP complex but only a suggestion of how the domains might be oriented towards each other satisfiying all valid crosslinks between these proteins.

The obtained crosslinks were inserted into the partial structures of ILK-PKD/parvin-CH2 and ILK-ANK/PINCH-LIM1 solved by x-ray crystallography (Fukuda et al., 2009, Chiswell et al., 2008). Since these structures were solved separately and it is unclear how they are oriented towards each other, Stiegler *et al.* presented an electron density profile for the “minimal” IPP complex consisting of full-length ILK, parvin-CH2 domain and PINCH LIM1 domain, determined by SAXS (Stiegler et al., 2013). This electron density displays a roughly triangular shape, into which the authors positioned the two partial structures, connected by an unstructured linker sequence between ILK ANK and PKD domains which is not present in any of the structures (Figure 54C).

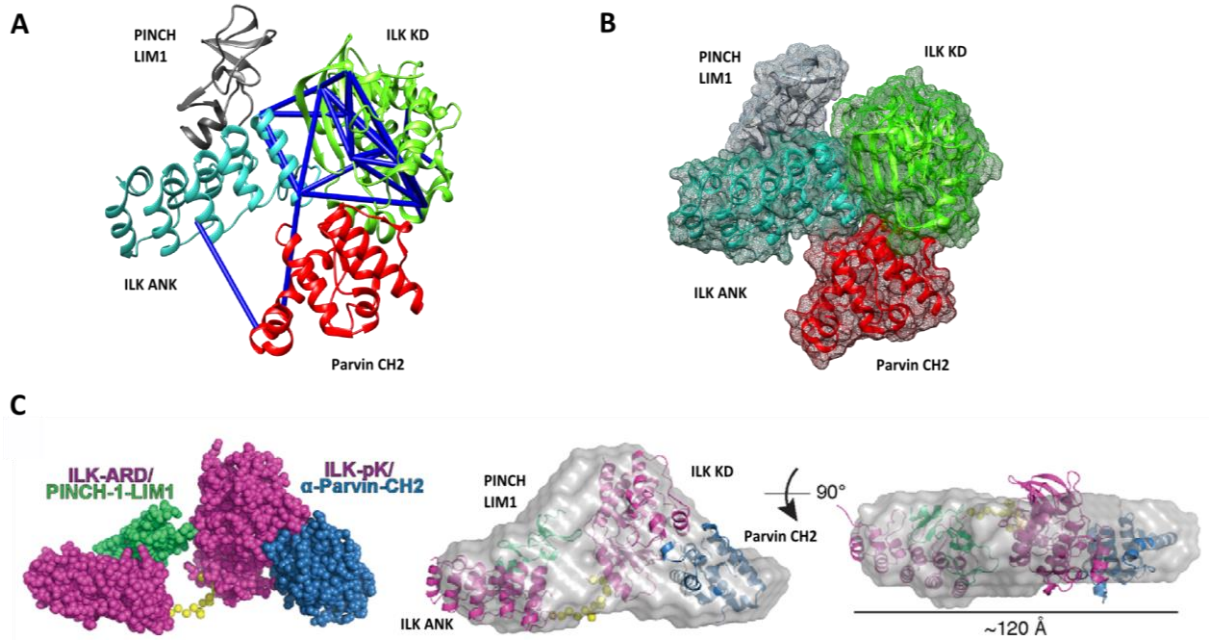

Figure 54: Comparison of published SAXS data of the "minimal" IPP complex (Stiegler et al., 2013) and the model obtained by chemical crosslinking proteomics. The model presented in Figure 42 (**A, B**), which was generated by interactive docking to satisfy all inter-domain crosslinks in ILK-PKD, ILK-ANK, α-parvin CH2 and PINCH LIM1 domain differs from the model obtained by Stiegler *et al.* (**C**). The latter was derived from the insertion of the ILK-ANK/PINCH-LIM1 and ILK-PKD/parvin-CH2 crystal structures (PDB: 3KMU, 4HI8) into the electron density map obtained through SAXS analysis. An unstructured linker between ILK-ANK and ILK-PKD (purple) was inserted (yellow), through which the two domains are shifted away from each other. The resulting model neither fits well into the electron density map, nor would it satisfy the crosslinks obtained for the full-length IPP complex, which indicate that the two ILK domains are much closer together. The model obtained through the crosslinking data does not fit exactly into the electron density either, which might be due to the use of full-length IPP complex for crosslinking and the "minimal" version for SAXS analysis.

It can be claimed with certainty that the crosslinks detected in the full-length IPP complex do not support this model, since the arbitrarily positioned linker separates ILK-PKD and ILK-ANK too far from each other as that the crosslinks could be satisfied. Furthermore, the crosslinks suggest a stronger "tilt" of the two separate structures towards each other, positioning ILK-ANK and parvin-CH2 close enough to be crosslinked, which is not possible in the model presented by Stiegler *et al*.

When looking closely at the model shown in Figure 54C, it becomes obvious that the positioning of the two structures does not fit very well into the measured electron density map, indicating that the orientation of ILK-PKD and ILK-ANK must be different. The most misleading part of the model is probably the linker sequence, which the authors chose to model in an elongated way, with a large distance between ILK-PKD and ILK-ANK. Judging by the observed crosslinks, it seems more likely that the linker is not extended but rather compacted, which brings the two domains closer together.

The model generated from the crosslinking data does not fit exactly into the electron density map of the “minimal” IPP complex either. A potential explanation for this is the fact that the crosslinks were obtained using the full-length IPP complex, whereas the SAXS data was derived from the shortened version. It could be imagined that the presence of parvin CH1 domain as well as PINCH LIM2-4 slightly changes the conformation of ILK, leading to a more compact shape than in the “minimal” complex. Furthermore, it is not entirely certain that the structures of the ILK-PKD/parvin-CH2 and ILK-ANK/PINCH-LIM1 sub-complexes determined by x-ray crystallization represent the structures these domains adopt in the full-length form of the IPP complex. Therefore, in order to determine the exact structure of the IPP complex, cryo-EM or x-ray crystallography will have to be used.

Analogous to the model of the “minimal” IPP complex, the positioning of the PINCH LIM1-4 domains relative to each other and to ILK-PKD and ILK-ANK based on the crosslinking data is very crude and can only serve as an indication of the approximate locations of the LIM domains. It appears that PINCH is not elongated with all LIM domains positioned in a row but rather compacted with the LIM2, 3 and 4 domains forming a cloverleaf-like arrangement. This would bring an unstructured, flexible LIM5 domain to the center of the IPP complex, explaining the multitude of observed crosslinks to this domain. However, this arrangement is also solely based on crosslinking data and might be false due to an incorrect arrangement of ILK-PKD and ILK-ANK.

It is extremely difficult to gain structural information on the IPP-kindlin-paxillin complex from the crosslinking data, since only very small stretches of both proteins have been structurally characterized. Only few crosslinks have been observed involving the kindlin “backbone”, the kindlin-PH domain and the single LD-motifs of paxillin, of which NMR structures are available, therefore a correct positioning of these domains is not possible. In order to gain more structural information on the IPP-kindlin-paxillin interactions, cryo-EM seems the method of choice, if stable complexes can be assembled which do not dissociate upon dilution.

When studying the crosslinks between kindlin-2 and paxillin, it appears that the two proteins interact with each other via the same interfaces as in the absence of the IPP complex. The intramolecular as well as the intermolecular crosslinks indicate no large conformational changes. Therefore, if no pentameric complex stable enough for cryo-EM studies can be established, the dimeric kindlin-paxillin complex could be studied separately. Together, the

two proteins form a complex of approximately 140 kDa, which brings it into the size range observable in negative staining and cryo-EM.

4.4.5 Outlook and future plans for structural studies on full-length IPP complex

As mentioned before, no structural information on full-length IPP complex is available to date. Therefore, it was attempted to gain structural data by x-ray crystallography and cryo-EM studies. Crystallization trials on the full-length IPP#4 construct so far yielded only very thin needle-shaped crystalline particles, which could not be improved by optimization of the buffer conditions. Neither did a seeding approach, for which the needle-like crystals were ground into very small shards and then used for inoculation of a second round of crystallization conditions lead to large, regularly-shaped crystals. However, some conditions appeared to contain a microcrystalline background, which could be analyzed and potentially be used for structure analysis.

Furthermore, crystallization studies on the shortened IPP-dLIM5 construct could lead to better results, since the unstructured PINCH LIM5 domain has been removed in that construct, reducing flexibility. Additionally, considering the results of the buffer optimization screen, purification of the IPP complex in citrate buffer might lead to increased stability or to a slightly different behavior than in Buffer B2, which had been used for previous crystallization trials. The combination of both the shortened IPP-dLIM5 complex and a more stabilizing buffer might lead to an alteration of the crystalline particle shapes and sizes, yielding crystals suitable for x-ray analysis. Furthermore, once stabilizing buffer conditions have been identified, diverse additive screens can be performed. The presence of needle-shaped crystals in numerous conditions in the initial trials indicates that the IPP complex has a tendency to crystallize which, under the right buffer and additive conditions, could lead to crystals with the desired properties.

In parallel to the crystallization trials, the IPP complex was analyzed by negative staining on carbon grids to find optimal purification techniques, dilutions and buffer conditions for the preparation of cryo-EM samples. So far, it is possible to detect single particles in negative staining which represent the IPP complex but, apart from these particles, aggregates are often detected. Since aggregation of the IPP complex is time- and temperature-dependent, the process for generating samples for negative staining so far was to perform SEC, collect the

desired peak fraction as soon as possible, keep the fraction permanently on ice and perform negative staining on ice. However, despite all these precautions, some degree of aggregation could not be prevented.

Another aspect, which complicates the analysis of the IPP complex by negative staining is its relatively small size of 135 kDa (IPP#4, full-length). The recent advances in cryo-EM technology allow for the analysis of particles even smaller than 100 kDa, however the smaller the size of the complex, the more important it becomes that the proteins analyzed form extremely homogeneous and well-defined particles. In order to increase the size of the particles analyzed, attempts were made to visualize the pentameric IPP-kindlin-paxillin complex, at a molecular weight of approximately 270 kDa. As for the IPP complex alone, all five proteins were applied onto an SEC column and the peak fraction containing the pentameric complex was collected and directly used for negative staining on ice.

However, the resulting images indicated that most of the particles detected were too small to be IPP-kindlin-paxillin complexes, raising the concern that the pentameric complex disassembles easily upon dilution. In one sample so far, large, roundish particles were detected which could represent intact pentameric complexes. This will have to be reproduced and subjected to further analysis. One method for stabilizing protein complexes for electron microscopy analysis is the so-called GraFix approach (Kastner et al., 2008). It combines rate-zonal centrifugation in a sucrose density gradient with chemical crosslinking, mostly by a gradient of glutaraldehyde. The aim of this method is the isolation of intact complexes from disassembled single components while at the same time fixating the complex in its assembled state through crosslinks. The GraFix approach has been applied to the IPP-kindlin-paxillin complex using a 5-20 % sucrose gradient with 0-0.1 % glutaraldehyde. However, in the fractions analyzed by SDS-PAGE and silver staining IPP, kindlin and paxillin were detected only separately but not as a defined crosslinked band at 270 kDa. As discussed for the isolation of adhesome complexes by rate-zonal centrifugation, this method seems not suitable for the IPP complex in combination with other proteins as the complexes always seem to disassemble. Therefore, the GraFix approach has been discontinued, but if no other approach is found to stabilize the complex, attempts can be made to optimize the sucrose gradient, the glutaraldehyde concentration or the kind of chemical crosslinker used.

A number of measures will be employed in future preparations to improve the sample quality in negative staining. On the one hand, the IPP-dLIM5 construct will be used for further analysis, since the reduced flexibility might yield more uniform particles. Additionally, purification of the IPP complex and SEC will be performed in citrate buffer, since this might increase its stability and prevent disassembly. In all approaches so far, 0.05% tween-20 was added to the buffer used for purification, as it seems to improve purity and yield of the IPP complex. However, the tween-20 used previously was not of ultra-pure quality and therefore might contain contaminations, which do not interfere with purification of biophysical analyses but are visible in electron microscopy. Therefore, the SEC runs for sample preparation for negative staining will be performed using buffer supplemented with ultra-pure tween-20. Furthermore, the addition of 5-10 % glycerol to the SEC buffer might prove beneficial for complex stability and will be assessed. The sample homogeneity of the IPP preparations might further be improved by performing additional ion exchange or hydrophobic interaction chromatography steps, as possible contaminations or disassembled proteins might be removed better than in SEC alone.

Conclusively, analysis of the IPP complex and the pentameric IPP-kindlin-paxillin complex using cryo-EM seems promising but will require considerable optimization efforts before high-quality structural information can be obtained in order to gain novel insights into the yet unresolved full-length structures and binding modes of the five proteins.

4.5 Establishment of a system to directly visualize adhesome complex formation at integrin tails in a lipid environment

4.5.1 The influence of the plasma membrane on talin and kindlin binding to integrin cytoplasmic domains

It is obvious that the binding modalities of talin and kindlin toward the integrin tail are unusual and in many aspects unexpected. The binding affinities of both proteins towards integrin β1 and β3 tail peptides in solution are extremely low, with 7 µM for kindlin-2 versus integrin β1 being the highest. For proteins, which are the key activators of such important and time-critical processes as integrin activation one would typically expect much higher affinities.

However, the low affinities of talin F3 domain towards integrin tails of 160 – 300 µM had been first characterized by NMR and have been confirmed by MST and AUC measurements (Anthis et al., 2010).

Furthermore, there is the element of traction force, which is conveyed from the extracellular matrix over the integrin and talin to the actin cytoskeleton. In this function, one talin molecule bears 7-10 pN of force (Austen et al., 2015). If the talin F3-integrin cytoplasmic tail interaction were the only binding interface and thus had to bear the entire force it is difficult to imagine how this is possible based on such low affinity. One potential mechanism for reinforcement of the talin F3-integrin bond is the formation of a catch-bond upon force application onto the two molecules, which, however, should have been observable in the optical tweezer measurements.

Another factor, which potentially increases the affinity of talin and kindlin towards integrin tails is the plasma membrane and phosphatidylinositides incorporated therein. Talin binds via its F2 and F3 domains preferentially to PIP2, but also to other negatively charged (phospho)lipids with slightly lower affinity, suggesting that the charge might be the pivotal factor (Martel et al., 2001, Anthis et al., 2009, Moore et al., 2012). Kindlin binds via its PH domain to PIP3 with slightly higher affinity than to PIP2, indicating a similar mechanism for both proteins, which can be fine-tuned by the prevailing phosphatidylinositides (Liu et al., 2011).

There are three mechanisms imaginable for the positive influence of the plasma membrane on the talin/kindlin-integrin interaction. One is a conformational change of talin or kindlin upon phosphoinositide binding, which seems rather unlikely and can be ruled out for kindlin-2 and integrin β1A, since pre-saturation of kindlin-2 with IP4, a soluble PIP3 analogue used for obtaining the crystal structure of kindlin-2 PH domain (Liu et al., 2012), did not change the affinity of kindlin-2 towards an integrin β1A tail peptide in MST measurements (data not shown).

Therefore, a second, more likely explanation is that PIP2 or PIP3, when located in the plasma membrane in close proximity to an integrin tail, offers a second binding site for talin or kindlin besides those on the cytoplasmic tail, strengthening the interaction. For talin F3 domain, this has been demonstrated by NMR measurements using integrin β1 and β3 transmembrane and

cytosolic domains incorporated into bicelles (Lu et al., 2016). However, binding to PIP2 in the plasma membrane does not seem likely to anchor talin more strongly to integrin tails and to help bear the tension forces.

A third hypothesis is that phosphatidylinositides assist in localizing kindlin and talin to the plasma membrane, leading to drastically increased local concentrations in the vicinity of integrin cytoplasmic domains which are high enough to overcome the high K_D values, resulting in a sufficient amount of talin or kindlin bound to integrins to induce and regulate cell adhesion.

Since none of these hypotheses offer an explanation of how talin can bear such high forces at such low affinities, it seems likely that the strengthening effect is derived from additional adhesome proteins binding to the complex, slowing the off-rate of talin binding to integrin tails.

4.5.2 Studies on potential trimeric THD-kindlin-integrin tail complexes in solution yield controversial results

The question whether talin and kindlin, both essential proteins for integrin activation that bind directly to the integrin cytoplasmic domain, can bind to one integrin tail molecule to form a trimeric complex, or whether their binding is mutually exclusive, has been controversially discussed for many years. Due to the low affinities, especially of THD, biophysical assays are often problematic when they require concentrations that allow saturation of the interaction. Bledzka *et al.* presented SPR measurements on integrin tails immobilized on a gold surface with dextrane coating, which seemed to show binding of THD to a surface of tail peptides saturated with kindlin-2 (Bledzka et al., 2012). However, these measurements should not be given too much credit, as the authors fail to present important information and control measurements. For instance, they do not document the strong unspecific interactions of THD and kindlin-2 with the dextrane surface, which was observed in attempts to reproduce the measurements. This makes all the sensorgrams invalid, as it is impossible to tell how much of the signal is derived from non-specific interactions. Furthermore, the authors fail to demonstrate that they can reach saturation of the surface with 2.8 µM THD, upon which they injected kindlin-2, claiming that the resulting binding curve can only be derived from kindlin binding to the talin-saturated integrin tails. Therefore, the results from the study presented

by Bledzka *et al.* should not be taken into consideration when discussing the topic of simultaneous THD and kindlin-2 binding to integrin tails.

The assays presented in Figure 47 render conflicting results, with the AUC measurements clearly showing no formation of a trimeric complex of THD, kindlin-2 and the fluorescently labeled integrin tail peptide. Yet the MST measurements seem to indicate that, while the tail peptide is theoretically saturated to 80% with kindlin-2, the THD titration curve is unchanged compared to "empty" tail peptide, reaching a concentration at which theoretically 88% of the tail is saturated with THD. This indicates either that THD can bind to an integrin tail to which already one kindlin molecule is bound with equal affinity as to a "free" tail peptide or that THD is able to displace kindlin-2 from an integrin tail peptide with extremely high efficiency. Analysis of THD and kindlin-2 binding to integrin cytoplasmic domains in lipid environment by single-molecule microscopy will shed more light on this controversial topic by providing a tool to directly observe events at integrin tails.

4.5.3 Advantages and caveats of the Nanodisc-embedded TMCyto constructs

The newly established Nanodisc-based system for microscopic visualization of single integrin TMCyto molecules opens up a novel approach for studying the assembly of adhesome complexes. The system allows the incorporation of different TMCyto constructs, for example integrin β1 and β3, which makes it possible to test for differences in complex assembly based on integrin type, or α-integrin constructs, on the one hand as a "negative control", for THD and kindlin-2 should not bind to α-tails, and on the other hand for studying α/β-heterodimers. Furthermore, the effect of point mutations within the integrin cytoplasmic sequence on complex assembly can be studied, most prominently the disruption of the two NPxY motifs essential for talin and kindlin binding. Labeling the TMCyto constructs at one defined Cys residue makes it possible to count the bleaching steps in one specific area and deduce how many molecules are present there.

The Nanodiscs have a defined diameter of approximately 17 nm, determined by the membrane scaffold protein used. If desired, smaller Nanodiscs can be produced by employing a different scaffold protein. The discs can be immobilized on a passivated glass surface in a specific orientation using the His_6-tag on either the N-terminus of the TMCyto construct or on the MSP2N2 protein. Furthermore, the lipid composition within the Nanodiscs can be

controlled, for studies on the effect of uncharged or charged lipids on THD and kindlin binding and for determining the influence and concentration dependence of PIP2 or PIP3 on the number of proteins bound to the Nanodiscs.

After characterizing the binding modalities of THD and kindlin-2 to Nanodisc-embedded TMCyto constructs, an increasing number of adhesome components can be added to the system, either labeled or unlabeled. This allows for example the study of kindlin recruitment to the integrin tail by paxillin, as proposed by Theodosiou et al., by testing whether more kindlin is found to co-localize with integrins in the presence of paxillin (Theodosiou et al., 2016). Furthermore, the effect of paxillin phosphorylation by FAK can be directly observed by adding fluorescently labeled paxillin and unlabeled FAK in the presence or absence of ATP to the system.

A few caveats of the Nanodisc-embedded TMCyto constructs have to be taken into consideration when setting up experiments. First, the preparation process is time-consuming and reproducibility depends on the correct adjustment of a number of parameters, such as the volume ratio of EMPIGEN-solubilized TMCyto constructs to that of the lipid and scaffold protein components or the assembly time and temperature during dialysis. In the assembly process, incorporation efficiency of the TMCyto constructs varies with the construct used, and there is always a certain amount of precipitation of the TMCyto constructs, making it difficult to determine their labeling efficiency within the final Nanodiscs. It has to be assumed that equal amounts of labeled and unlabeled TMCyto molecules precipitate, retaining the DOL determined prior to Nanodisc assembly. Furthermore, the yield of one Nanodisc preparation is very limited and depends on the concentration of the TMCyto constructs, which cannot be increased by centrifugal concentrators, as this also increases the EMPIGEN concentration and leads to unpredictable assembly behavior. Therefore, the amount of Nanodiscs obtained from one preparation is more than sufficient for several microscopy sessions or three to four pull-down samples, but barely allows the use of orthogonal biophysical methods. This limitation has to be overcome by preparing multiple samples and combining the Nanodiscs obtained.

Conclusively, the single-molecule approach to observe directly what transpires at integrin tails embedded into lipid bilayers is very promising and has been set up methodically to allow a multitude of different measurements. It will have to be tested how well a measurement can

be reproduced by repeating the Nanodisc preparations and interaction studies with THD and kindlin-2 several times, rendering statistically sound data on the different TMCyto constructs. This will eventually lead to new insights into focal adhesion assembly.

4.6 Production of talin-integrin fusion proteins for force-dependent interaction studies

The application of an optical tweezer set-up to study the effect of traction force on the talin-F3-integrin cytoplasmic tail bond is a novel approach to elucidate the binding modalities of this unusual protein-protein interaction. In all other biophysical methods applied so far to study the talin-integrin interaction, traction force was absent due to solution-based measurements or to complications when using full-length talin and F-actin in the analyses. The new approach facilitates the study of how the talin-integrin interaction changes under force, setting the focus on the talin head domain, while most analyses so far used full-length talin or the rod domain (del Rio et al., 2009, Austen et al., 2015). While initial measurements seemed to indicate an interaction type different from the expected two-step behavior, raising the hypothesis of a catch-bond. The constructs with longer linker sequences between talin-F3 and the integrin tail peptide, however, helped rule out a catch-bond behavior and identifying the effect seen in the initial measurements as an artifact due to the short linker sequence, which itself applied force onto the construct. It is theoretically possible that the entire talin head domain is required for catch-bond formation, but it seems unlikely. Measurements with THD-integrin fusion constructs will provide final evidence for or against a catch-bond behavior.

It is surprising that only the talin2-integrin β1D fusion construct yields detectable interactions, albeit at low affinity and strong fluctuations. The application of traction force onto the talin F3-integrin bond does not increase binding affinity or reduce off-rates. It turned out to be impossible to detect a force range of constant binding and unbinding of the fused integrin tail peptide for any of the talin1 constructs (in fusion with either β1A or β1D). Therefore, either the tails do not bind to the talin1 F3 domain in these constructs at all or the interaction is too transient to be detected, which again raises the question of how this interaction can then bear traction force.

It will be interesting to test whether kindlin-2 can compete with the talin interaction with the fused integrin tail. If this is the case, there should be phases detectable in which there is no un-binding and re-binding, since kindlin is bound to the tail peptide - similar to the competition assays with integrin tail peptides. Furthermore, competition assays with Nanodisc-embedded TMCyto constructs might lead to novel insights into the increase in affinity mediated by the lipid surface as compared to “free” integrin tail peptides. This depends on the passivation of the silica beads used in the optical tweezers to prevent non-specific interaction of the Nanodiscs with the glass surface, which would distort the force measurements.

Conclusively, the novel optical tweezer approach for studying the talin-integrin bond under force adds additional insights, which, combined with the conclusions of the other approaches, will contribute to a more accurate and versatile understanding of this interaction which is so vital for integrin activation and adhesome assembly.

5 Summary

The integrin-proximal adhesome complex is composed of a multitude of proteins which are recruited to the short cytoplasmic tail domain of integrin β-subunits, facilitating diverse signal-transducing and scaffolding functions necessary for the formation of focal adhesion and thus the control of integrin-mediated cell adhesion and motility. Among the innermost components of focal adhesions are talin and kindlin, which directly bind to the integrin tail, as well as paxillin, FAK, the ILK-PINCH-parvin (IPP) complex and EPLIN. All these proteins are essential for integrin function and numerous interactions between them have been identified, however the exact way in which they interact and assemble into a complex has not yet been determined.

In order to observe the formation of adhesome complexes *in vitro*, in a well-defined environment devoid of any unidentified interfering components, the central aim of this study was the establishment of a molecular "toolkit" composed of recombinantly produced and purified proteins. Furthermore, in order to mimic the actual conditions inside the cell as closely as possible, integrin transmembrane and cytoplasmic domains were incorporated into Nanodiscs, which provide an adaptable lipid surface around the integrin tails.

Focal adhesion kinase, as a pivotal factor due to its dual role as a kinase as well as a scaffolding protein, was produced and purified in milligram quantities from HEK293E cells. FAK specifically phosphorylates paxillin at positions Y-31 and Y-118, but not talin or kindlin. Furthermore, binding of FAK to paxillin and THD in the absence of ATP was confirmed. Therefore, recombinant FAK can be used for studying its role in adhesome complex assembly as well as the effect of paxillin phosphorylation by FAK on protein-protein interactions.

The full-length trimeric IPP complex was produced in milligram quantities from High Five insect cells using the MultiBAC system. Obtaining the complex of all three proteins in full-length and in 1:1:1 stoichiometry has never been achieved so far and allows the characterization of protein-protein interactions with other focal adhesion proteins such as kindlin, paxillin and talin. The IPP complex does not bind THD, and, contrary to the literature, no direct interaction with the integrin β1 or β3 cytoplasmic domain could be detected either. Instead, the IPP complex forms a pentameric complex with kindlin and paxillin. The orientation of the proteins within this pentameric complex was studied by chemical crosslinking and mass

spectrometric analysis. Furthermore, the IPP complex will be used for structural studies by cryo-EM and x-ray crystallography.

The interactions of THD and kindlin-2 with integrin cytoplasmic domains, which provide the basis for adhesome complex assembly, were studied in solution, yielding very low affinities and conflicting results on the question whether talin and kindlin can bind the integrin tail simultaneously. In order to elucidate this topic, a novel single-molecule microscopy approach for studying talin/kindlin interactions with integrin tails in lipid environment was established. Integrin transmembrane and cytoplasmic domains incorporated into Nanodiscs, THD and kindlin-2 were fluorescently labeled and studied under single-molecule TIRF conditions. The number of fluorophore bleaching steps at a certain position indicate co-localization of THD and kindlin with the integrin tail. Like this, the binding behavior of these molecules can be studied in the native environment, the effect of point mutations and lipid composition can be assessed and even assembly of adhesome complexes on Nanodiscs can be attempted.

Additionally, fusion proteins of talin head and integrin cytoplasmic domains were produced, which allow the study of this interaction under force, an element which is usually absent in solution-based biophysical studies. The application of optical tweezers to apply traction force onto the bond revealed no catch-bond behavior and low affinities also under force. Furthermore, the bond appears to be very transient, with a high rate of binding and unbinding of the integrin tail to talin F3 domain.

Conclusively, this work demonstrates how to produce elusive protein components for structural studies on integrin adhesome complexes in solution or surface-based in a native lipid environment and a novel approach to study these complexes on the single-molecule level.

6 References

ANTHIS, N. J., WEGENER, K. L., CRITCHLEY, D. R. & CAMPBELL, I. D. 2010. Structural diversity in integrin/talin interactions. *Structure,* 18**,** 1654-66.

ANTHIS, N. J., WEGENER, K. L., YE, F., KIM, C., GOULT, B. T., LOWE, E. D., VAKONAKIS, I., BATE, N., CRITCHLEY, D. R., GINSBERG, M. H. & CAMPBELL, I. D. 2009. The structure of an integrin/talin complex reveals the basis of inside-out signal transduction. *The EMBO journal,* 28**,** 3623-32.

ARNAOUT, M. A., MAHALINGAM, B. & XIONG, J. P. 2005. Integrin structure, allostery, and bidirectional signaling. *Annu Rev Cell Dev Biol,* 21**,** 381-410.

AUSTEN, K., RINGER, P., MEHLICH, A., CHROSTEK-GRASHOFF, A., KLUGER, C., KLINGNER, C., SABASS, B., ZENT, R., RIEF, M. & GRASHOFF, C. 2015. Extracellular rigidity sensing by talin isoform-specific mechanical linkages. *Nat Cell Biol,* 17**,** 1597-606.

BELLIS, S. L., MILLER, J. T. & TURNER, C. E. 1995. Characterization of tyrosine phosphorylation of paxillin in vitro by focal adhesion kinase. *J Biol Chem,* 270**,** 17437-41.

BERGER, I. C., A. 2012. ACEMBL Expression System Series - MultiBacTurbo: Multi-Protein Expression in Insect Cells. *User Manual*.

BERTOLUCCI, C. M., GUIBAO, C. D. & ZHENG, J. 2005. Structural features of the focal adhesion kinase-paxillin complex give insight into the dynamics of focal adhesion assembly. *Protein Sci,* 14**,** 644-52.

BIENIOSSEK, C., IMASAKI, T., TAKAGI, Y. & BERGER, I. 2012. MultiBac: expanding the research toolbox for multiprotein complexes. *Trends Biochem Sci,* 37**,** 49-57.

BLEDZKA, K., BIALKOWSKA, K., SOSSEY-ALAOUI, K., VAYNBERG, J., PLUSKOTA, E., QIN, J. & PLOW, E. F. 2016. Kindlin-2 directly binds actin and regulates integrin outside-in signaling. *J Cell Biol,* 213**,** 97-108.

BLEDZKA, K., LIU, J., XU, Z., PERERA, H. D., YADAV, S. P., BIALKOWSKA, K., QIN, J., MA, Y. Q. & PLOW, E. F. 2012. Spatial coordination of kindlin-2 with talin head domain in interaction with integrin beta cytoplasmic tails. *The Journal of Biological Chemistry,* 287**,** 24585-94.

BOTTCHER, R. T., LANGE, A. & FASSLER, R. 2009. How ILK and kindlins cooperate to orchestrate integrin signaling. *Current opinion in cell biology,* 21**,** 670-5.

BOUAOUINA, M., GOULT, B. T., HUET-CALDERWOOD, C., BATE, N., BRAHME, N. N., BARSUKOV, I. L., CRITCHLEY, D. R. & CALDERWOOD, D. A. 2012. A conserved lipid-binding loop in the kindlin FERM F1 domain is required for kindlin-mediated alphaIIbbeta3 integrin coactivation. *J Biol Chem,* 287**,** 6979-90.

BRAMI-CHERRIER, K., GERVASI, N., ARSENIEVA, D., WALKIEWICZ, K., BOUTTERIN, M. C., ORTEGA, A., LEONARD, P. G., SEANTIER, B., GASMI, L., BOUCEBA, T., KADARE, G., GIRAULT, J. A. & AROLD, S. T. 2014. FAK dimerization controls its kinase-dependent functions at focal adhesions. *EMBO J,* 33**,** 356-70.

BROWN, M. C., PERROTTA, J. A. & TURNER, C. E. 1998. Serine and threonine phosphorylation of the paxillin LIM domains regulates paxillin focal adhesion localization and cell adhesion to fibronectin. *Mol Biol Cell,* 9**,** 1803-16.

BROWN, M. C. & TURNER, C. E. 2004. Paxillin: adapting to change. *Physiol Rev,* 84**,** 1315-39.

CALALB, M. B., POLTE, T. R. & HANKS, S. K. 1995. Tyrosine phosphorylation of focal adhesion kinase at sites in the catalytic domain regulates kinase activity: a role for Src family kinases. *Mol Cell Biol,* 15**,** 954-63.

CALDERWOOD, D. A., CAMPBELL, I. D. & CRITCHLEY, D. R. 2013. Talins and kindlins: partners in integrin-mediated adhesion. *Nature reviews. Molecular cell biology,* 14**,** 503-17.

CALDERWOOD, D. A., FUJIOKA, Y., DE PEREDA, J. M., GARCIA-ALVAREZ, B., NAKAMOTO, T., MARGOLIS, B., MCGLADE, C. J., LIDDINGTON, R. C. & GINSBERG, M. H. 2003. Integrin beta cytoplasmic domain interactions with phosphotyrosine-binding domains: a structural

prototype for diversity in integrin signaling. *Proceedings of the National Academy of Sciences of the United States of America,* 100**,** 2272-7.

CALDERWOOD, D. A., ZENT, R., GRANT, R., REES, D. J., HYNES, R. O. & GINSBERG, M. H. 1999. The Talin head domain binds to integrin beta subunit cytoplasmic tails and regulates integrin activation. *The Journal of biological chemistry,* 274**,** 28071-4.

CARMAN, C. V. & SPRINGER, T. A. 2003. Integrin avidity regulation: are changes in affinity and conformation underemphasized? *Curr Opin Cell Biol,* 15**,** 547-56.

CHARI, A., HASELBACH, D., KIRVES, J. M., OHMER, J., PAKNIA, E., FISCHER, N., GANICHKIN, O., MOLLER, V., FRYE, J. J., PETZOLD, G., JARVIS, M., TIETZEL, M., GRIMM, C., PETERS, J. M., SCHULMAN, B. A., TITTMANN, K., MARKL, J., FISCHER, U. & STARK, H. 2015. ProteoPlex: stability optimization of macromolecular complexes by sparse-matrix screening of chemical space. *Nat Methods,* 12**,** 859-65.

CHEN, N. P., UDDIN, B., HARDT, R., DING, W., PANIC, M., LUCIBELLO, I., KAMMERER, P., RUPPERT, T. & SCHIEBEL, E. 2017. Human phosphatase CDC14A regulates actin organization through dephosphorylation of epithelial protein lost in neoplasm. *Proc Natl Acad Sci U S A*.

CHEN, X., XIE, C., NISHIDA, N., LI, Z., WALZ, T. & SPRINGER, T. A. 2010. Requirement of open headpiece conformation for activation of leukocyte integrin alphaXbeta2. *Proc Natl Acad Sci U S A,* 107**,** 14727-32.

CHISWELL, B. P., ZHANG, R., MURPHY, J. W., BOGGON, T. J. & CALDERWOOD, D. A. 2008. The structural basis of integrin-linked kinase-PINCH interactions. *Proc Natl Acad Sci U S A,* 105**,** 20677-82.

CUTLER, M. L., BASSIN, R. H., ZANONI, L. & TALBOT, N. 1992. Isolation of rsp-1, a novel cDNA capable of suppressing v-Ras transformation. *Mol Cell Biol,* 12**,** 3750-6.

DAS, M., SUBBAYYA ITHYCHANDA, S., QIN, J. & PLOW, E. F. 2013. Mechanisms of talin-dependent integrin signaling and crosstalk. *Biochimica et biophysica acta*.

DEAKIN, N. O. & TURNER, C. E. 2008. Paxillin comes of age. *J Cell Sci,* 121**,** 2435-44.

DEBRAND, E., EL JAI, Y., SPENCE, L., BATE, N., PRAEKELT, U., PRITCHARD, C. A., MONKLEY, S. J. & CRITCHLEY, D. R. 2009. Talin 2 is a large and complex gene encoding multiple transcripts and protein isoforms. *FEBS J,* 276**,** 1610-28.

DEL RIO, A., PEREZ-JIMENEZ, R., LIU, R., ROCA-CUSACHS, P., FERNANDEZ, J. M. & SHEETZ, M. P. 2009. Stretching single talin rod molecules activates vinculin binding. *Science,* 323**,** 638-41.

DOUGHERTY, G. W., CHOPP, T., QI, S. M. & CUTLER, M. L. 2005. The Ras suppressor Rsu-1 binds to the LIM 5 domain of the adaptor protein PINCH1 and participates in adhesion-related functions. *Exp Cell Res,* 306**,** 168-79.

DUROCHER, Y., PERRET, S. & KAMEN, A. 2002. High-level and high-throughput recombinant protein production by transient transfection of suspension-growing human 293-EBNA1 cells. *Nucleic Acids Research,* 30**,** E9.

ELLIOTT, P. R., GOULT, B. T., KOPP, P. M., BATE, N., GROSSMANN, J. G., ROBERTS, G. C., CRITCHLEY, D. R. & BARSUKOV, I. L. 2010. The Structure of the talin head reveals a novel extended conformation of the FERM domain. *Structure,* 18**,** 1289-99.

ENGLER, A. J., SEN, S., SWEENEY, H. L. & DISCHER, D. E. 2006. Matrix elasticity directs stem cell lineage specification. *Cell,* 126**,** 677-89.

FUKUDA, K., BLEDZKA, K., YANG, J., PERERA, H. D., PLOW, E. F. & QIN, J. 2014. Molecular basis of kindlin-2 binding to integrin-linked kinase pseudokinase for regulating cell adhesion. *J Biol Chem,* 289**,** 28363-75.

FUKUDA, K., GUPTA, S., CHEN, K., WU, C. & QIN, J. 2009. The pseudoactive site of ILK is essential for its binding to alpha-Parvin and localization to focal adhesions. *Molecular cell,* 36**,** 819-30.

FUKUDA, K., KNIGHT, J. D., PISZCZEK, G., KOTHARY, R. & QIN, J. 2011. Biochemical, proteomic, structural, and thermodynamic characterizations of integrin-linked kinase (ILK): cross-validation of the pseudokinase. *The Journal of Biological Chemistry,* 286**,** 21886-95.

GOKSOY, E., MA, Y. Q., WANG, X., KONG, X., PERERA, D., PLOW, E. F. & QIN, J. 2008. Structural basis for the autoinhibition of talin in regulating integrin activation. *Molecular cell,* 31**,** 124-33.

GONI, G. M., EPIFANO, C., BOSKOVIC, J., CAMACHO-ARTACHO, M., ZHOU, J., BRONOWSKA, A., MARTIN, M. T., ECK, M. J., KREMER, L., GRATER, F., GERVASIO, F. L., PEREZ-MORENO, M. & LIETHA, D. 2014. Phosphatidylinositol 4,5-bisphosphate triggers activation of focal adhesion kinase by inducing clustering and conformational changes. *Proc Natl Acad Sci U S A,* 111**,** E3177-86.

GONZALEZ-NIEVES, R., DESANTIS, A. I. & CUTLER, M. L. 2013. Rsu1 contributes to regulation of cell adhesion and spreading by PINCH1-dependent and - independent mechanisms. *J Cell Commun Signal,* 7**,** 279-93.

GOULT, B. T., XU, X. P., GINGRAS, A. R., SWIFT, M., PATEL, B., BATE, N., KOPP, P. M., BARSUKOV, I. L., CRITCHLEY, D. R., VOLKMANN, N. & HANEIN, D. 2013. Structural studies on full-length talin1 reveal a compact auto-inhibited dimer: implications for talin activation. *J Struct Biol,* 184**,** 21-32.

GRISON, M. 2017. *Single-Molecule cohesion and adhesion in muscle cells.* Dissertation, Technical University Munich.

HAIDER, S. R., REID, H. J. & SHARP, B. L. 2012. Tricine-SDS-PAGE. *Methods Mol Biol,* 869**,** 81-91.

HAN, M. Y., KOSAKO, H., WATANABE, T. & HATTORI, S. 2007. Extracellular signal-regulated kinase/mitogen-activated protein kinase regulates actin organization and cell motility by phosphorylating the actin cross-linking protein EPLIN. *Mol Cell Biol,* 27**,** 8190-204.

HANNIGAN, G. E., LEUNG-HAGESTEIJN, C., FITZ-GIBBON, L., COPPOLINO, M. G., RADEVA, G., FILMUS, J., BELL, J. C. & DEDHAR, S. 1996. Regulation of cell adhesion and anchorage-dependent growth by a new beta 1-integrin-linked protein kinase. *Nature,* 379**,** 91-6.

HARBURGER, D. S., BOUAOUINA, M. & CALDERWOOD, D. A. 2009. Kindlin-1 and -2 directly bind the C-terminal region of beta integrin cytoplasmic tails and exert integrin-specific activation effects. *J Biol Chem,* 284**,** 11485-97.

HAS, C., HERZ, C., ZIMINA, E., QU, H. Y., HE, Y., ZHANG, Z. G., WEN, T. T., GACHE, Y., AUMAILLEY, M. & BRUCKNER-TUDERMAN, L. 2009. Kindlin-1 Is required for RhoGTPase-mediated lamellipodia formation in keratinocytes. *Am J Pathol,* 175**,** 1442-52.

HAYASHI, I., VUORI, K. & LIDDINGTON, R. C. 2002. The focal adhesion targeting (FAT) region of focal adhesion kinase is a four-helix bundle that binds paxillin. *Nat Struct Biol,* 9**,** 101-6.

HERZOG, F., KAHRAMAN, A., BOEHRINGER, D., MAK, R., BRACHER, A., WALZTHOENI, T., LEITNER, A., BECK, M., HARTL, F. U., BAN, N., MALMSTROM, L. & AEBERSOLD, R. 2012. Structural probing of a protein phosphatase 2A network by chemical cross-linking and mass spectrometry. *Science,* 337**,** 1348-52.

HOELLERER, M. K., NOBLE, M. E., LABESSE, G., CAMPBELL, I. D., WERNER, J. M. & AROLD, S. T. 2003. Molecular recognition of paxillin LD motifs by the focal adhesion targeting domain. *Structure,* 11**,** 1207-17.

HOFFMANN, J. E., FERMIN, Y., STRICKER, R. L., ICKSTADT, K. & ZAMIR, E. 2014. Symmetric exchange of multi-protein building blocks between stationary focal adhesions and the cytosol. *Elife,* 3**,** e02257.

HUET-CALDERWOOD, C., BRAHME, N. N., KUMAR, N., STIEGLER, A. L., RAGHAVAN, S., BOGGON, T. J. & CALDERWOOD, D. A. 2014. Differences in binding to the ILK complex determines kindlin isoform adhesion localization and integrin activation. *J Cell Sci,* 127**,** 4308-21.

HYNES, R. O. 2002. Integrins: bidirectional, allosteric signaling machines. *Cell,* 110**,** 673-87.

ILIC, D., FURUTA, Y., KANAZAWA, S., TAKEDA, N., SOBUE, K., NAKATSUJI, N., NOMURA, S., FUJIMOTO, J., OKADA, M. & YAMAMOTO, T. 1995. Reduced cell motility and enhanced focal adhesion contact formation in cells from FAK-deficient mice. *Nature,* 377**,** 539-44.

ITO, S., TAKAHARA, Y., HYODO, T., HASEGAWA, H., ASANO, E., HAMAGUCHI, M. & SENGA, T. 2010. The roles of two distinct regions of PINCH-1 in the regulation of cell attachment and spreading. *Mol Biol Cell,* 21**,** 4120-9.

JERABEK-WILLEMSEN, M., ANDRÉ, T., WANNER, R., ROTH, H. M., DUHR, S., BAASKE, P. & BREITSPRECHER, D. 2014. MicroScale Thermophoresis: Interaction analysis and beyond. *J. Molstruc.,* 1077**,** 101-113.

KAHNER, B. N., KATO, H., BANNO, A., GINSBERG, M. H., SHATTIL, S. J. & YE, F. 2012. Kindlins, integrin activation and the regulation of talin recruitment to alphaIIbbeta3. *PLoS One,* 7**,** e34056.

KAPUST, R. B., TOZSER, J., FOX, J. D., ANDERSON, D. E., CHERRY, S., COPELAND, T. D. & WAUGH, D. S. 2001. Tobacco etch virus protease: mechanism of autolysis and rational design of stable mutants with wild-type catalytic proficiency. *Protein Eng,* 14**,** 993-1000.

KARAKOSE, E., GEIGER, T., FLYNN, K., LORENZ-BAATH, K., ZENT, R., MANN, M. & FASSLER, R. 2015. The focal adhesion protein PINCH-1 associates with EPLIN at integrin adhesion sites. *J Cell Sci,* 128**,** 1023-33.

KARAKOSE, E., SCHILLER, H. B. & FASSLER, R. 2010. The kindlins at a glance. *Journal of cell science,* 123**,** 2353-6.

KASTNER, B., FISCHER, N., GOLAS, M. M., SANDER, B., DUBE, P., BOEHRINGER, D., HARTMUTH, K., DECKERT, J., HAUER, F., WOLF, E., UCHTENHAGEN, H., URLAUB, H., HERZOG, F., PETERS, J. M., POERSCHKE, D., LUHRMANN, R. & STARK, H. 2008. GraFix: sample preparation for single-particle electron cryomicroscopy. *Nat Methods,* 5**,** 53-5.

KLEINSCHMIDT, E. G. & SCHLAEPFER, D. D. 2017. Focal adhesion kinase signaling in unexpected places. *Curr Opin Cell Biol,* 45**,** 24-30.

KOBE, B. & KAJAVA, A. V. 2001. The leucine-rich repeat as a protein recognition motif. *Curr Opin Struct Biol,* 11**,** 725-32.

KOPP, P. M., BATE, N., HANSEN, T. M., BRINDLE, N. P., PRAEKELT, U., DEBRAND, E., COLEMAN, S., MAZZEO, D., GOULT, B. T., GINGRAS, A. R., PRITCHARD, C. A., CRITCHLEY, D. R. & MONKLEY, S. J. 2010. Studies on the morphology and spreading of human endothelial cells define key inter- and intramolecular interactions for talin1. *Eur J Cell Biol,* 89**,** 661-73.

KORENBAUM, E., OLSKI, T. M. & NOEGEL, A. A. 2001. Genomic organization and expression profile of the parvin family of focal adhesion proteins in mice and humans. *Gene,* 279**,** 69-79.

KOSINSKI, J., VON APPEN, A., ORI, A., KARIUS, K., MULLER, C. W. & BECK, M. 2015. Xlink Analyzer: software for analysis and visualization of cross-linking data in the context of three-dimensional structures. *J Struct Biol,* 189**,** 177-83.

KUO, J. C., HAN, X., HSIAO, C. T., YATES, J. R., 3RD & WATERMAN, C. M. 2011. Analysis of the myosin-II-responsive focal adhesion proteome reveals a role for beta-Pix in negative regulation of focal adhesion maturation. *Nature cell biology,* 13**,** 383-93.

LAU, T. L., KIM, C., GINSBERG, M. H. & ULMER, T. S. 2009. The structure of the integrin alphaIIbbeta3 transmembrane complex explains integrin transmembrane signalling. *EMBO J,* 28**,** 1351-61.

LAWSON, C., LIM, S. T., URYU, S., CHEN, X. L., CALDERWOOD, D. A. & SCHLAEPFER, D. D. 2012. FAK promotes recruitment of talin to nascent adhesions to control cell motility. *J Cell Biol,* 196**,** 223-32.

LEGATE, K. R., MONTANEZ, E., KUDLACEK, O. & FASSLER, R. 2006. ILK, PINCH and parvin: the tIPP of integrin signalling. *Nat Rev Mol Cell Biol,* 7**,** 20-31.

LEGATE, K. R., TAKAHASHI, S., BONAKDAR, N., FABRY, B., BOETTIGER, D., ZENT, R. & FASSLER, R. 2011. Integrin adhesion and force coupling are independently regulated by localized PtdIns(4,5)2 synthesis. *The EMBO journal,* 30**,** 4539-53.

LEITNER, A., WALZTHOENI, T., KAHRAMAN, A., HERZOG, F., RINNER, O., BECK, M. & AEBERSOLD, R. 2010. Probing native protein structures by chemical cross-linking, mass spectrometry, and bioinformatics. *Mol Cell Proteomics,* 9**,** 1634-49.

LI, H., DENG, Y., SUN, K., YANG, H., LIU, J., WANG, M., ZHANG, Z., LIN, J., WU, C., WEI, Z. & YU, C. 2017a. Structural basis of kindlin-mediated integrin recognition and activation. *Proc Natl Acad Sci U S A*.

LI, J. & SPRINGER, T. A. 2017. Integrin extension enables ultrasensitive regulation by cytoskeletal force. *Proc Natl Acad Sci U S A,* 114**,** 4685-4690.

LI, J., SU, Y., XIA, W., QIN, Y., HUMPHRIES, M. J., VESTWEBER, D., CABANAS, C., LU, C. & SPRINGER, T. A. 2017b. Conformational equilibria and intrinsic affinities define integrin activation. *EMBO J,* 36**,** 629-645.

LI, M. Z. & ELLEDGE, S. J. 2012. SLIC: a method for sequence- and ligation-independent cloning. *Methods Mol Biol,* 852**,** 51-9.

LIETHA, D., CAI, X., CECCARELLI, D. F., LI, Y., SCHALLER, M. D. & ECK, M. J. 2007. Structural basis for the autoinhibition of focal adhesion kinase. *Cell,* 129**,** 1177-87.

LIU, J., FUKUDA, K., XU, Z., MA, Y. Q., HIRBAWI, J., MAO, X., WU, C., PLOW, E. F. & QIN, J. 2011. Structural basis of phosphoinositide binding to kindlin-2 protein pleckstrin homology domain in regulating integrin activation. *The Journal of biological chemistry,* 286**,** 43334-42.

LIU, Y., ZHU, Y., YE, S. & ZHANG, R. 2012. Crystal structure of kindlin-2 PH domain reveals a conformational transition for its membrane anchoring and regulation of integrin activation. *Protein & cell,* 3**,** 434-40.

LO CONTE, L., CHOTHIA, C. & JANIN, J. 1999. The atomic structure of protein-protein recognition sites. *J Mol Biol,* 285**,** 2177-98.

LORENZ, S., VAKONAKIS, I., LOWE, E. D., CAMPBELL, I. D., NOBLE, M. E. & HOELLERER, M. K. 2008. Structural analysis of the interactions between paxillin LD motifs and alpha-parvin. *Structure,* 16**,** 1521-31.

LU, Z., MATHEW, S., CHEN, J., HADZISELIMOVIC, A., PALAMUTTAM, R., HUDSON, B. G., FASSLER, R., POZZI, A., SANDERS, C. R. & ZENT, R. 2016. Implications of the differing roles of the beta1 and beta3 transmembrane and cytoplasmic domains for integrin function. *Elife,* 5.

MARTEL, V., RACAUD-SULTAN, C., DUPE, S., MARIE, C., PAULHE, F., GALMICHE, A., BLOCK, M. R. & ALBIGES-RIZO, C. 2001. Conformation, localization, and integrin binding of talin depend on its interaction with phosphoinositides. *J Biol Chem,* 276**,** 21217-27.

MAUL, R. S. & CHANG, D. D. 1999. EPLIN, epithelial protein lost in neoplasm. *Oncogene,* 18**,** 7838-41.

MAUL, R. S., SONG, Y., AMANN, K. J., GERBIN, S. C., POLLARD, T. D. & CHANG, D. D. 2003. EPLIN regulates actin dynamics by cross-linking and stabilizing filaments. *J Cell Biol,* 160**,** 399-407.

MEVES, A., STREMMEL, C., GOTTSCHALK, K. & FASSLER, R. 2009. The Kindlin protein family: new members to the club of focal adhesion proteins. *Trends in cell biology,* 19**,** 504-13.

MILLER, N. L., LAWSON, C., KLEINSCHMIDT, E. G., TANCIONI, I., URYU, S. & SCHLAEPFER, D. D. 2013. A non-canonical role for Rgnef in promoting integrin-stimulated focal adhesion kinase activation. *J Cell Sci,* 126**,** 5074-85.

MITRA, S. K., HANSON, D. A. & SCHLAEPFER, D. D. 2005. Focal adhesion kinase: in command and control of cell motility. *Nat Rev Mol Cell Biol,* 6**,** 56-68.

MONTANEZ, E., USSAR, S., SCHIFFERER, M., BOSL, M., ZENT, R., MOSER, M. & FASSLER, R. 2008. Kindlin-2 controls bidirectional signaling of integrins. *Genes Dev,* 22**,** 1325-30.

MOORE, D. T., NYGREN, P., JO, H., BOESZE-BATTAGLIA, K., BENNETT, J. S. & DEGRADO, W. F. 2012. Affinity of talin-1 for the beta3-integrin cytosolic domain is modulated by its phospholipid bilayer environment. *Proceedings of the National Academy of Sciences of the United States of America,* 109**,** 793-8.

MOSAVI, L. K., CAMMETT, T. J., DESROSIERS, D. C. & PENG, Z. Y. 2004. The ankyrin repeat as molecular architecture for protein recognition. *Protein Sci,* 13**,** 1435-48.

MOSER, M., LEGATE, K. R., ZENT, R. & FASSLER, R. 2009. The tail of integrins, talin, and kindlins. *Science,* 324**,** 895-9.

MOSER, M., NIESWANDT, B., USSAR, S., POZGAJOVA, M. & FASSLER, R. 2008. Kindlin-3 is essential for integrin activation and platelet aggregation. *Nature medicine,* 14**,** 325-30.

NIKOLOPOULOS, S. N. & TURNER, C. E. 2000a. Actopaxin, a new focal adhesion protein that binds paxillin LD motifs and actin and regulates cell adhesion. *J Cell Biol,* 151**,** 1435-48.

NIKOLOPOULOS, S. N. & TURNER, C. E. 2000b. Actopaxin, a new focal adhesion protein that binds paxillin LD motifs and actin and regulates cell adhesion. *The Journal of cell biology,* 151**,** 1435-48.

NISHIDA, N., XIE, C., SHIMAOKA, M., CHENG, Y., WALZ, T. & SPRINGER, T. A. 2006. Activation of leukocyte beta2 integrins by conversion from bent to extended conformations. *Immunity,* 25**,** 583-94.

PASQUALI, C., BERTSCHY-MEIER, D., CHABERT, C., CURCHOD, M. L., AROD, C., BOOTH, R., MECHTLER, K., VILBOIS, F., XENARIOS, I., FERGUSON, C. G., PRESTWICH, G. D., CAMPS, M. & ROMMEL, C. 2007. A chemical proteomics approach to phosphatidylinositol 3-kinase signaling in macrophages. *Mol Cell Proteomics,* 6**,** 1829-41.

PRIDDLE, H., HEMMINGS, L., MONKLEY, S., WOODS, A., PATEL, B., SUTTON, D., DUNN, G. A., ZICHA, D. & CRITCHLEY, D. R. 1998. Disruption of the talin gene compromises focal adhesion assembly in undifferentiated but not differentiated embryonic stem cells. *J Cell Biol,* 142**,** 1121-33.

QIN, J. & WU, C. 2012. ILK: a pseudokinase in the center stage of cell-matrix adhesion and signaling. *Current opinion in cell biology,* 24**,** 607-13.

QU, H., TU, Y., SHI, X., LARJAVA, H., SALEEM, M. A., SHATTIL, S. J., FUKUDA, K., QIN, J., KRETZLER, M. & WU, C. 2011. Kindlin-2 regulates podocyte adhesion and fibronectin matrix deposition through interactions with phosphoinositides and integrins. *J Cell Sci,* 124**,** 879-91.

REES, D. J., ADES, S. E., SINGER, S. J. & HYNES, R. O. 1990. Sequence and domain structure of talin. *Nature,* 347**,** 685-9.

REVERTER, D. & LIMA, C. D. 2004. A basis for SUMO protease specificity provided by analysis of human Senp2 and a Senp2-SUMO complex. *Structure,* 12**,** 1519-31.

ROCA-CUSACHS, P., GAUTHIER, N. C., DEL RIO, A. & SHEETZ, M. P. 2009. Clustering of alpha(5)beta(1) integrins determines adhesion strength whereas alpha(v)beta(3) and talin enable mechanotransduction. *Proc Natl Acad Sci U S A,* 106**,** 16245-50.

SCHALLER, M. D., OTEY, C. A., HILDEBRAND, J. D. & PARSONS, J. T. 1995. Focal adhesion kinase and paxillin bind to peptides mimicking beta integrin cytoplasmic domains. *J Cell Biol,* 130**,** 1181-7.

SCHESWOHL, D. M., HARRELL, J. R., RAJFUR, Z., GAO, G., CAMPBELL, S. L. & SCHALLER, M. D. 2008. Multiple paxillin binding sites regulate FAK function. *J Mol Signal,* 3**,** 1.

SCHILLER, H. B., FRIEDEL, C. C., BOULEGUE, C. & FASSLER, R. 2011. Quantitative proteomics of the integrin adhesome show a myosin II-dependent recruitment of LIM domain proteins. *EMBO reports,* 12**,** 259-66.

SCHMEICHEL, K. L. & BECKERLE, M. C. 1994. The LIM domain is a modular protein-binding interface. *Cell,* 79**,** 211-9.

SEDGWICK, S. G. & SMERDON, S. J. 1999. The ankyrin repeat: a diversity of interactions on a common structural framework. *Trends Biochem Sci,* 24**,** 311-6.

SHATTIL, S. J., KIM, C. & GINSBERG, M. H. 2010. The final steps of integrin activation: the end game. *Nature reviews. Molecular cell biology,* 11**,** 288-300.

STIEGLER, A. L., GRANT, T. D., LUFT, J. R., CALDERWOOD, D. A., SNELL, E. H. & BOGGON, T. J. 2013. Purification and SAXS analysis of the integrin linked kinase, PINCH, parvin (IPP) heterotrimeric complex. *PloS one,* 8**,** e55591.

THEODOSIOU, M., WIDMAIER, M., BOTTCHER, R. T., ROGNONI, E., VEELDERS, M., BHARADWAJ, M., LAMBACHER, A., AUSTEN, K., MULLER, D. J., ZENT, R. & FASSLER, R. 2016. Kindlin-2 cooperates with talin to activate integrins and induces cell spreading by directly binding paxillin. *Elife,* 5.

TOM, R., BISSON, L. & DUROCHER, Y. 2008a. Transfection of Adherent HEK293-EBNA1 Cells in a Six-Well Plate with Branched PEI for Production of Recombinant Proteins. *Cold Spring Harb Protoc,* 3.

TOM, R., BISSON, L. & DUROCHER, Y. 2008b. Transfection of HEK293-EBNA1 Cells in Suspension with Linear PEI for Production of Recombinant Proteins. *Cold Spring Harb Protoc,* 3.

TSURUMI, H., HARITA, Y., KURIHARA, H., KOSAKO, H., HAYASHI, K., MATSUNAGA, A., KAJIHO, Y., KANDA, S., MIURA, K., SEKINE, T., OKA, A., ISHIZUKA, K., HORITA, S., HATTORI, M., HATTORI,

S. & IGARASHI, T. 2014. Epithelial protein lost in neoplasm modulates platelet-derived growth factor-mediated adhesion and motility of mesangial cells. *Kidney Int,* 86**,** 548-57.

TU, Y., WU, S., SHI, X., CHEN, K. & WU, C. 2003. Migfilin and Mig-2 link focal adhesions to filamin and the actin cytoskeleton and function in cell shape modulation. *Cell,* 113**,** 37-47.

TURNER, C. E. 2000. Paxillin and focal adhesion signalling. *Nat Cell Biol,* 2**,** E231-6.

USSAR, S., WANG, H. V., LINDER, S., FASSLER, R. & MOSER, M. 2006. The Kindlins: subcellular localization and expression during murine development. *Exp Cell Res,* 312**,** 3142-51.

VAN KOOYK, Y. & FIGDOR, C. G. 2000. Avidity regulation of integrins: the driving force in leukocyte adhesion. *Curr Opin Cell Biol,* 12**,** 542-7.

VELYVIS, A., YANG, Y., WU, C. & QIN, J. 2001. Solution structure of the focal adhesion adaptor PINCH LIM1 domain and characterization of its interaction with the integrin-linked kinase ankyrin repeat domain. *J Biol Chem,* 276**,** 4932-9.

VICENTE-MANZANARES, M. & HORWITZ, A. R. 2011. Adhesion dynamics at a glance. *Journal of cell science,* 124**,** 3923-7.

VICENTE-MANZANARES, M., MA, X., ADELSTEIN, R. S. & HORWITZ, A. R. 2009. Non-muscle myosin II takes centre stage in cell adhesion and migration. *Nat Rev Mol Cell Biol,* 10**,** 778-90.

WANG, X., FUKUDA, K., BYEON, I. J., VELYVIS, A., WU, C., GRONENBORN, A. & QIN, J. 2008. The structure of alpha-parvin CH2-paxillin LD1 complex reveals a novel modular recognition for focal adhesion assembly. *J Biol Chem,* 283**,** 21113-9.

WEGENER, K. L., PARTRIDGE, A. W., HAN, J., PICKFORD, A. R., LIDDINGTON, R. C., GINSBERG, M. H. & CAMPBELL, I. D. 2007. Structural basis of integrin activation by talin. *Cell,* 128**,** 171-82.

WICKSTROM, S. A., LANGE, A., MONTANEZ, E. & FASSLER, R. 2010. The ILK/PINCH/parvin complex: the kinase is dead, long live the pseudokinase! *The EMBO journal,* 29**,** 281-91.

WOZNIAK, M. A. & CHEN, C. S. 2009. Mechanotransduction in development: a growing role for contractility. *Nature reviews. Molecular cell biology,* 10**,** 34-43.

XIONG, J. P., STEHLE, T., DIEFENBACH, B., ZHANG, R., DUNKER, R., SCOTT, D. L., JOACHIMIAK, A., GOODMAN, S. L. & ARNAOUT, M. A. 2001. Crystal structure of the extracellular segment of integrin alpha Vbeta3. *Science,* 294**,** 339-45.

YANG, J., MA, Y. Q., PAGE, R. C., MISRA, S., PLOW, E. F. & QIN, J. 2009. Structure of an integrin alphaIIb beta3 transmembrane-cytoplasmic heterocomplex provides insight into integrin activation. *Proc Natl Acad Sci U S A,* 106**,** 17729-34.

YATES, L. A., FUZERY, A. K., BONET, R., CAMPBELL, I. D. & GILBERT, R. J. 2012. Biophysical analysis of Kindlin-3 reveals an elongated conformation and maps integrin binding to the membrane-distal beta-subunit NPXY motif. *The Journal of Biological Chemistry,* 287**,** 37715-31.

YE, F., KIM, S. J. & KIM, C. 2014. Intermolecular transmembrane domain interactions activate integrin alphaIIbbeta3. *J Biol Chem,* 289**,** 18507-13.

YE, X., MCLEAN, M. A. & SLIGAR, S. G. 2016. Phosphatidylinositol 4,5-Bisphosphate Modulates the Affinity of Talin-1 for Phospholipid Bilayers and Activates Its Autoinhibited Form. *Biochemistry,* 55**,** 5038-48.

ZAIDEL-BAR, R. & GEIGER, B. 2010. The switchable integrin adhesome. *Journal of cell science,* 123**,** 1385-8.

ZAIDEL-BAR, R., MILO, R., KAM, Z. & GEIGER, B. 2007. A paxillin tyrosine phosphorylation switch regulates the assembly and form of cell-matrix adhesions. *J Cell Sci,* 120**,** 137-48.

ZHANG, Y., CHEN, K., TU, Y., VELYVIS, A., YANG, Y., QIN, J. & WU, C. 2002. Assembly of the PINCH-ILK-CH-ILKBP complex precedes and is essential for localization of each component to cell-matrix adhesion sites. *J Cell Sci,* 115**,** 4777-86.

ZHOU, J., APONTE-SANTAMARIA, C., STURM, S., BULLERJAHN, J. T., BRONOWSKA, A. & GRATER, F. 2015. Mechanism of Focal Adhesion Kinase Mechanosensing. *PLoS Comput Biol,* 11**,** e1004593.

7 Publications

Kammerer, P., Aretz, J., Fässler, R.; *Lucky Kindlin: a cloverleaf at the integrin tail*; PNAS, Sep 2017

Chen, N., Uddin, B., Hardt, R., Ding, W., Panic, M., Lucibello, I., **Kammerer, P.**, Ruppert, T., Schiebel, E.; *Human phosphatase CDC14A regulates actin organization through dephosphorylation of epithelial protein lost in neoplasm (eplin)*; PNAS, May 16, 2017

Tseng, H., Böttcher, R., Samarelli, V., **Kammerer, P.**, Ziegler, T., Nagaraj, N., Zent, R., Sanders, C., Fässler, R.; *A proteomics-based approach for the identification of conformation-specific cytoplasmic integrin interactors*; Manuscript in preparation

8 Acknowledgments

First and foremost, I would like to thank Prof. Dr. Reinhard Fässler for the opportunity to work on this challenging and versatile project and for his support and guidance. I especially appreciate that he encouraged me to apply many different state-of-the-art technologies to this project and to broaden my knowledge in biochemistry and biophysics (on a sailing boat in Croatia). The last four years have taught me a great deal about protein biochemistry, cell biology and academic research in general. I am very grateful for that experience.

I would further like to thank the members of my thesis committee, Prof. Dr. Reinhard Fässler, Prof. Dr. Axel Imhof, Dr. Franz Herzog, Prof. Dr. Christian Wahl-Schott, Prof. Dr. Martin Biel and PD Dr. Stylianos Michalakis.

Special thanks go to Dr. Franz Herzog, Prof. Dr. Axel Imhof and Dr. Carsten Grashoff, who, as members of my TAC committee, always supported me with advice, new approaches and valuable discussions throughout my PhD.

I would like to thank Dr. Maik Veelders for everything he taught me while we were working on this very special and stubborn set of proteins and for the good times we had during those three years. Furthermore, my thanks go to Simone Bach without whom I would not have managed to purify so many proteins and would probably have despaired throughout the last year. I would also like to thank Dr. Armin Lambacher for the good collaboration and the excellent, yet slightly homicidal ideas.

This work would not have been possible without the support of the Microchemistry Core Facility, especially Dr. Stephan Uebel, Dr. Sabine Suppmann, Judith Scholz, Claudia Straßer, Elisabeth Weyher-Stingl and Dr. Nagarjuna Nagaraj. Thank you for being always open for fruitful discussions and for sharing your considerable experience with me.

Furthermore, I would like to thank all our collaborators, Dr. Naoko Mizuno, Stephanie Schumacher and Dirk Dedden for valuable discussions, Dr. Franz Herzog, Mia Potočnjak and Dr. Pascaline Rombaut for the crosslinking proteomics analysis and Prof. Dr. Matthias Rief, Marco Grison and Mihai Bodescu for the optical tweezer measurements.

Finally, I would like to thank my parents, Helmut and Evi Kammerer for their love and support throughout the last ten years I spent studying, traveling, studying some more and finally obtaining a PhD degree. Don’t worry, I’ll get a proper job now. Furthermore, I would like to thank Andrea, Marcus and Hannah Clemente and all my friends for their unwavering support and listening to my constant complaints.

And, of course, Dr. Lucas Clemente, the love of my life.